SAPP XXIV

24th Symposium on Application of Plasma Processes and 13th EU-Japan Joint Symposium on Plasma Processing

Book of Contributed Papers

Štrbské Pleso, Slovakia
27 Jan - 1 Feb, 2023

Edited by J. Országh, B. Stachová, D. Mészáros, P. Papp, Š. Matejčík

Book of Contributed Papers: 24th Symposium on Application of Plasma Processes and 13th EU-Japan Joint Symposium on Plasma Processing, Štrbské Pleso, Slovakia, 27 January – 1 February 2023.

Symposium organised by Department of Experimental Physics, Faculty of Mathematics, Physics and Informatics, Comenius University in Bratislava and Society for Plasma Research and Applications in hotel SOREA TRIGAN***.

Editors: J. Országh, B. Stachová, D. Mészáros, P. Papp, Š. Matejčík

Publisher: Society for Plasma Research and Applications, Bratislava, Slovakia

Issued: January 2023, Bratislava, first issue

ISBN: 978-80-972179-3-8

URL: https://neon.dpp.fmph.uniba.sk/sapp/

Local Organizers

Department of Experimental Physics
Faculty of Mathematics, Physics and Informatics
Comenius University in Bratislava
Mlynská dolina F2
842 48 Bratislava, Slovakia
URL: http://www.fmph.uniba.sk/
Tel.: +421 2 602 95 686
Fax: +421 2 654 29 980

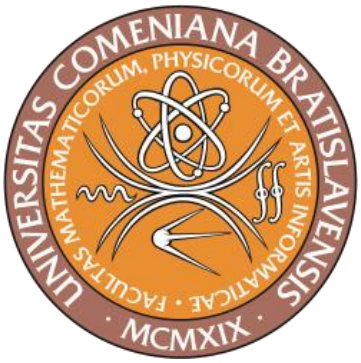

Society for plasma research and applications
Faculty of Mathematics, Physics and Informatics
Comenius University Bratislava
Mlynská dolina F2
842 48 Bratislava, Slovakia
E-mail: spvap@neon.dpp.fmph.uniba.sk
Tel.: +421 2 602 95 686

SPVAP

Local Organizing Committee

Štefan Matejčík (chair)
František Krčma
Peter Papp
Juraj Országh
Ladislav Moravský
Veronika Medvecká

International Scientific Committee

24th Symposium on Application of Plasma Processes

Prof. J. Benedikt	Christian-Albrechts-University, Kiel, Germany
Dr. R. Brandenburg	INP, Greifswald, Germany
Dr. Z. Donkó	Hungarian Academy of Sciences, Budapest, Hungary
Dr. T. Field	Queen's University, Belfast, United Kingdom
Prof. S. Hamaguchi	Osaka University, Japan
Prof. F. Krčma	Brno University of Technology, Brno, Czech Republic
Prof. N. Mason	School of Physical Sciences, University of Kent, United Kingdom
Prof. Š. Matejčík	Comenius University in Bratislava, Slovakia
Prof. J. Pawlat	University of Technology, Lublin, Poland
Prof. M. Radmilović-Radjenović	Institute of Physics, Belgrade, Serbia
Prof. P. Scheier	Leopold-Franzens University, Innsbruck, Austria

13th EU-Japan Joint Symposium on Plasma Processing

Prof. S. Hamaguchi	Osaka University, Japan
Prof. N. Mason	School of Physical Sciences, University of Kent, United Kingdom
Prof. Z. Petrović	Institute of Physics, Belgrade, Serbia

Reading Committee

Prof. Š. Matejčík	Comenius University in Bratislava, Slovakia
Prof. F. Krčma	Brno University of Technology, Brno, Czech Republic
Prof. N. Mason	University of Kent, United Kingdom
Assoc. Prof. P. Papp	Comenius University in Bratislava, Slovakia
Assoc. Prof. J. Országh	Comenius University in Bratislava, Slovakia
Assoc. Prof. V. Medvecká	Comenius University in Bratislava, Slovakia

Conference Topics

1. Electrical discharges and other plasma sources
2. Elementary plasma processes and plasma-chemical reactions
3. Theory and modelling of plasmas and plasma processes
4. Plasma-surface interactions
5. Plasma surface treatment for applications
6. Plasmas for nanomaterials
7. Plasma diagnostics
8. Ion mobility and mass spectrometry

Table of Contents

INVITED LECTURES

INVITED LECTURES

EFFICIENT DEPOSITION AND TRAPPING OF REACTIVE SPECIES IN LIQUIDS AND HYDROGELS

Kinga Kutasi[1], Péter Hartmann[1], Slobodan Milošević[2]

[1]*Wigner Research Centre for Physics, POB 49, H-1525 Budapest, Hungary*
[2] *Institute of Physics, Bijenička cesta 46, 10000 Zagreb, Croatia*
E-mail: kutasi.kinga@wigner.hu

The presentation discusses the methods that make possible the deposition and trapping of reactive oxygen and nitrogen species in liquids and hydrogels in a controlled way. The reactive species are deposited with the use of the plasma plume of a surface-wave microwave discharge, whose composition can be tuned in a wide density range. The reactive species are trapped by making use of the characteristics of the biopolymers, of the Fenton-type reactions and the high reduction potential metals, respectively.

1. Introduction

Reactive oxygen and nitrogen species (RONS) are deposited into the liquid through the interaction of the active or afterglow plasma with the liquid. In the last decade it has been demonstrated that these RONS can have anti-tumour/cancer, antibacterial and antimicrobial effect, and can induce oxidative stress to cells [1]. Although physiological solutions have been proven to kill selectively cancer cells and allow for local delivery by injection into the tumor, they can be quickly washed away by body fluids. To overcome this, Labay et al.[2] have proposed the use of plasma-activated hydrosols such as the gelatin solutions. As the collagen, from which the gelatin is derived, is the most abundant extracellular matrix protein in humans and the main component of connective tissues, it makes the gelatin highly biocompatible, and thus, a great candidate for implantable biomaterials. In the field of agriculture, it has been shown that the RONS enriched liquids have potential in seed disinfection, and in improving seed germination, the growth and stress tolerance of plants [3]. Furthermore, it is hypothesized that due to the nitrate/nitrite ions deposited into the plasma-activated liquids (PAL) the RONS enriched liquids can be used as green fertilizer by providing nitrogen nutrient for plants. In order to be able to produce well designed RONS enriched liquids and hydrogels for the targeted applications, it is essential to achieve the control of the species deposition and their lifetimes.

2. Deposition of RONS

The plasma system used (shown in Fig. 1) is an atmospheric pressure surface-wave microwave discharge ignited with the help of a *surfatron* (Sairem, Surfatron 80) in a quartz tube of outer diameter 7 mm and I.D. 4 mm, using Ar gas at 2000 sccm flow rate and MW input power of 25 W. The characteristics of the plasma plume can be tuned with the initial gas mixture composition, input power and the treatment distance (discharge tube to the water surface). By tuning the concentration of electrons and nitrogen and oxygen content species at the plasma-liquid interface, the creation of NO_2^-, NO_3^- and H_2O_2 species in the liquid can be controlled [4]. The electrons play role in the formation of the long-lived H_2O_2 molecules in the liquid phase through the creation of OH molecules by the dissociation of H_2O. The plasma column of the surface-wave microwave discharge is characterized with a decreasing electron density profile, thus by increasing the distance between the discharge tube and the liquid surface, the deposition of H_2O_2 in the liquid is decreased. Along the plasma plume, there is an air influx into the discharge, which influences the self-sustainment of the discharge and the plasma characteristics (such as evolution of electron density along the plume), while it results in the creation of the NO and NO_2 molecules. The NO and NO_2 molecules when dissolved into the liquid, contribute to the formation of the long-lived nitrite and nitrate ions in the liquid phase. As a consequence, the deposition of nitrite and nitrate ions into the liquid can be increased by increasing the treatment distance. In this way the system makes possible to create different plasma-activated liquids ranging from hydrogen peroxide dominated to nitrate/nitrite

dominated. By treating 32 ml of liquid in a 35 ml Berzelius beaker for 5 min, RONS with a total concentration of about 100 mg l^{-1} can be deposited.

Into hydrosols RONS can be deposited by direct atmospheric pressure plasma treatment [2] or by indirect plasma treatment. This latter method relies on the use of plasma-activated water (or physiological solution) to prepare the hydrosol. For example, the gelatin solution is prepared by mixing the 40°C swelled gelatin with freshly prepared 40–45°C plasma-activated water [5]. The indirect treatment has the advantage to prevent the cross-linking of the gelatin that may occur by plasma treatment, and it can also overcome the diffusion-limited deposition of RONS due to the gelation of the gelatin solution, which starts at about 20–27°C, depending on the solution concentration.

Fig. 1: Treating liquid with the surface-wave microwave discharge.

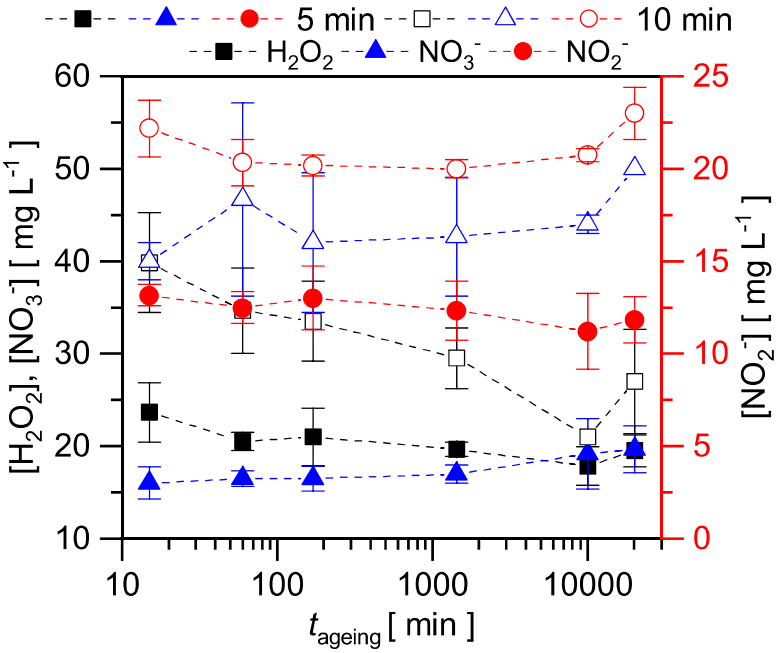

Fig. 2: The concentration of RONS in the filtrated PA(W+Mg) as a function of the storage time in the case of 5 min (closed symbol) and 10 min (open symbol) treatments performed at 12 mm distance. [7]

3. Trapping of RONS

It is well known that the composition of plasma-activated liquids changes during storage, and the total recombination of RONS can also occur. The lifetime of the PALs—followed either through the lifetime of different RONS or the PAL's activity retention time—has been found to vary from days to months, depending on the plasma source used, i.e. on its initial composition, and on the storage temperature. Since the RONS enriched liquids are predominantly acidic, the early stage of ageing is determined by the $NO_2^- + H_2O_2 + H^+ \rightarrow$ products reaction. As a consequence, in liquids with high H_2O_2 concentration the fast disappearance of NO_2^- is expected. It is shown, that by introducing in the system a Fenton-type reaction the kinetics of the H_2O_2 can be controlled, and the lifetime of NO_2^- can be increased [6].

The rate of the $NO_2^- + H_2O_2 + H^+ \rightarrow$ products reaction can also be controlled with the pH of the solution. This can be achieved by introducing into the system metals with high reduction potential, which in liquid (aqueous solution) can reduce H+ ions into H atoms, which escape from the liquid phase leading to the increase of the pH. It is shown, that adding Mg and Zn powder into the liquids during plasma treatment can neutralize the acidification induced by the plasma treatment and ensure the stability of RONS during several weeks of storage (as shown in Fig 2. in the case of Magnesium) [7].

In the case of hydrosols, it is shown that the stability can be achieved even at acidic conditions, as illustrated in Fig. 3 in the case of gelatin. Gelatin is denatured collagen that forms gel through the formation of hydrogen bond stabilized helices (renaturation) as it is cooled, starting from the critical gelation temperature of about 20–27ºC [5]. In the case of gelatin the trapping of RONS by the protein network is suggested.

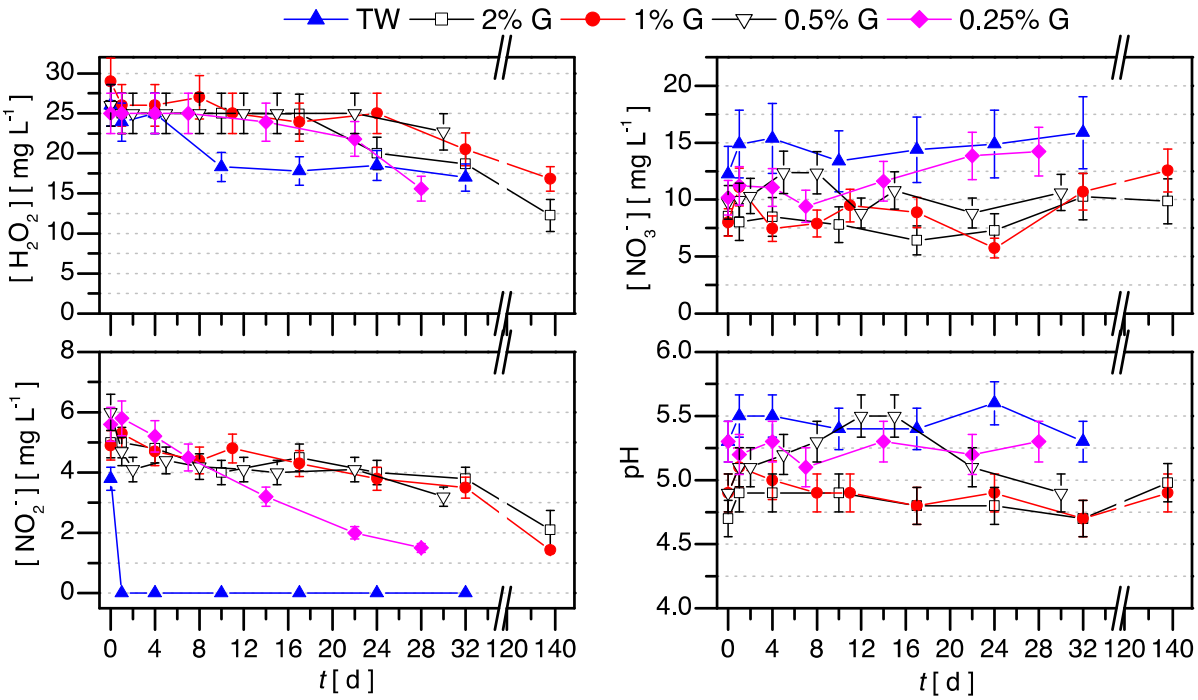

Fig. 3: Evolution of the species concentrations and the pH during storage in treated water (TW) and different percentage gelatin (G) solutions prepared with plasma-activated water produced with the surface-wave microwave discharge using 5 mm treatment distances. The TW and gelatin solutions are prepared by adding 60 ml plasma-activated water to 20 ml purified water and 20 ml water-based gelatin solutions, respectively.

4. References

[1] Bauer G 2019 *Redox Biology* **26** 101291.; Labay C *et al.* 2020 *ACS ppl. Mater. Interfaces* **12** 47256.; Schmidt M *et al* 2019 *Appl. Sci.* **9**, 2150.

[2] Labay C *et al.* 2019 *Scie. Rep.* **9** 16160.

[3] Gierczik K *et al.*2020 Plasma-activated water to improve the stress tolerance of barley *Plasma Process. Polym.* **17** e1900123.

[4] Kutasi K *et al.* 2019 Tuning the composition of plasma-activated water by a surface-wave microwave discharge and a kHz plasma jet *Plasma Sources Sci. Technol.* **28** 095010.

[5] Kutasi K, Tombácz E 2022 Efficient trapping of RONS in gelatin and physiological solutions *Plasma Process. Polym.* **19** 2100077.

[6] Kutasi K *et al.* 2021 Controlling: The composition of plasma-activated water by Cu ions *Plasma Sources Sci. Technol.* **30** 045015.

[7] Kutasi K *et al.*, The role of metals in the deposition of long-lived reactive oxygen and nitrogen species into the plasma-activated liquids 2022 *Plasma Process. Polym.* e2200143.

SPATIOTEMPORAL SPECTROSCOPIC CHARACTERIZATION OF ASYMMETRIC LASER-INDUCED PLASMAS

Erik Képeš[1], Igor Gornushkin[2], Pavel Pořízka[1,3], Jozef Kaiser[1,3]

[1]*Central European Institute of Technology, Brno University of Technology, Purkyňova 656/123, CZ-61200 Brno, Czech Republic*
[2]*BAM Federal Institute for Materials Research and Testing, Richard-Willstätter-Strasse 11, 12489 Berlin, Germany*
[3]*Institute of Physical Engineering, Faculty of Mechanical Engineering, Brno University of Technology, Technická 2, Brno, Czech Republic*
E-mail: kepes@vutbr.cz

The spectrally resolved optical emission of a plasma is a primary (and often only) source of information used for its characterisation. In general, the plasma's emission is collected in a spatially integrated manner, i.e., the spatial distribution of the plasma properties is lost. This talk presents several approaches to attaining spatially (and temporally) resolved characterisation of laser-induced plasmas (LIPs). The presented techniques range from spectrally resolved plasma imaging to inverse integral transforms, such as the inverse Abel transform [1] for rotationally symmetric LIPs and the inverse Radon transformation [2,3] for asymmetric LIPs. These techniques are demonstrated on case studies: non-orthogonal laser ablation and orthogonal double-pulse laser ablation.

The first case study [4] deals with changing ablation geometries. Ablation geometry, including the ablation angle, significantly affects the parameters of laser-induced plasmas. Consequently, the resulting spectroscopic observations are also affected. Non-orthogonal ablation is prominent in stand-off applications, such as the various Mars rovers where the orthogonality of the ablation laser pulse cannot be always secured. As a result of the non-orthogonal ablation angle, the induced plasma exhibits rotational asymmetry. Thus, spectrally resolved plasma imaging must be extended with tomography (inverse Radon transformation) to characterize such LIPs. Using tomography, we confirmed that non-orthogonal ablation leads to a laser-induced plasma that consists of two distinct parts: one expanding along the incident laser pulse and one expanding perpendicularly the sample surface. The former emits mainly continuum radiation, while the latter emits mainly sample-specific characteristic radiation. Furthermore, non-orthogonal ablation affects principally the ionic emissivity of LIPs.

The second case study [5] is concerned with the temporal evolution of LIPs induced by two orthogonal laser pulses, which are frequently used to improve the analytical performance of laser-induced breakdown spectroscopy. Both the pre-ablation mode and the re-heating geometries are explored. In the former an air spark is induced above the sample surface prior to delivering the ablation pulse. Meanwhile, the latter arrangement delivers additional energy into the LIP created by the ablation pulse. We show that the pre-ablation geometry yields a more temporally stable and spatially uniform plasma. On the contrary, the plasma generated in the re-heating geometry exhibits significant variations in electron density and temperature along its vertical axis.

References

[1] I.B. Gornushkin, S. v. Shabanov, U. Panne, Abel inversion applied to a transient laser induced plasma: implications from plasma modeling, J Anal At Spectrom. 26 (2011) 1457. https://doi.org/10.1039/c1ja10044k.
[2] H.H. Barrett, III The Radon Transform and Its Applications, in: 1984: pp. 217–286. https://doi.org/10.1016/S0079-6638(08)70123-9.
[3] I.B. Gornushkin, S. Merk, A. Demidov, U. Panne, S.V. Shabanov, B.W. Smith, N. Omenetto, Tomography of single and double pulse laser-induced plasma using Radon

transform technique, Spectrochim Acta Part B At Spectrosc. 76 (2012) 203–213. https://doi.org/10.1016/j.sab.2012.06.033.
[4] E. Képeš, I. Gornushkin, P. Pořízka, J. Kaiser, Spatiotemporal spectroscopic characterization of plasmas induced by non-orthogonal laser ablation, Analyst. 146 (2021) 920–929. https://doi.org/10.1039/D0AN01996H.
[5] E. Képeš, I. Gornushkin, P. Pořízka, J. Kaiser, Tomography of double-pulse laser-induced plasmas in the orthogonal geometry, Anal Chim Acta. 1135 (2020) 1–11. https://doi.org/10.1016/j.aca.2020.06.078.

DNA ORIGAMI NANOSTRUCTURES FOR STUDIES OF RADIATION DAMAGE

Jaroslav Kočišek, Leo Sala

J. Heyrovský Institute of Physical Chemistry of the CAS, Dolejškova 3 18223, Prague, Czechia
E-mail: kocisek@jh-inst.cas.cz

The talk overviews our recent efforts in implementation of DNA origami nanostructures to study fundamental mechanisms of radiation damage to DNA.

DNA origami nanostructures are made by folding DNA single strand scaffold into desired shape by the use of staples – designed set of short complementary strands. Full control over shape of the nanostructures, functional sites for chemical modifications or high biocompatibility makes the DNA origami nanostructures emerging in the fields like pharmacology, materials research or biophysics. [1].

The use of DNA origami nanostructures in fundamental studies of radiation damage was pioneered by Keller and Bald in 2012 [2]. Since then, a variety of studies confirmed advantages of the technique for *in singulo* studies of precisely defined DNA sequences in vacuum experiments. In 2021, we demonstrated, in collaboration with the Bald group, that stability of the DNA in biological buffers and its high resistivity against ionizing radiation makes them suitable for studies at realistic conditions of buffer solutions [3]. Since then, we are exploring stability of DNA origami under various types of irradiation and environmental conditions, e.g. for drug delivery [4]. However, plasma modifications of DNA origami on surfaces via cross linking, etching or carbonizing could be used also for surface nanopatterning and bottom-up building of materials. Fig. 1 represents some of our trial experiments towards this direction.

The second direction of our research is focused on fundamental reaction mechansimin chemo-radiation therapy. Here we implemented a frame DNA origami design of Endo [5] to study radiation damage to defined DNA sequences. The platform in its current form allows for direct evaluation of relative damage to two strands with approximately 60 unique basepairs allowing for wide range of studies. In our recent study, we demonstrated different mechnaisms of radiosensititzation for radiosnesitizers in a form of nucleoside halogenated at nucleobase and sugar moiety respectively [6]. Particulalry interesting is then observation of proximity effects, when unmodified DNA strand is broken due to radiosensitizer presence in parallel fully separated strand. Here, well characterized plasma sources of UV light and radicals could be used to disentangle the most fundamental mechnisms of radiation damage.

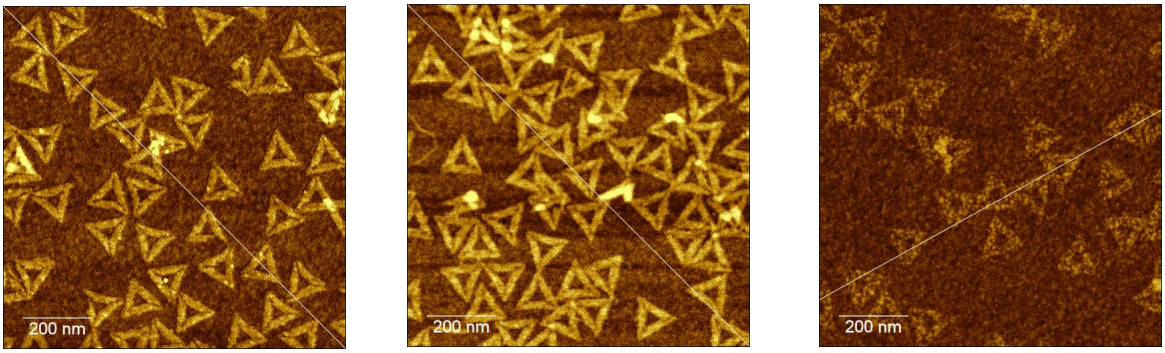

Fig. 1 AFM Images of DNA origami triangles treated by diffuse coplanar surface barrier discharge DCSBD in air (Roplass), 0.2mm from electrode surface. Treatment times from left to right 0, 30 and 60s.

References

[1] Endo M. ed. 2022, DNA Origami: Structures, Technology, and Applications, Wiley
[2] Keller, A.; 2012 ACS Nano **6**, 4392.
[3] Sala L. et al. 2021 *Nanoscsale* **13**, 11197.
[4] Sala L. et al, 2022 *ACS Appl. Nano Mater.* **5**,13267.
[5] Endo, M. et al, 2010 *J. Am. Chem. Soc.* **132,** 1592.
[6] Sala L. et al. 2022 *J. Phys. Chem. Lett.* **13**, 3922.

PLASMA JET INTERACTIONS WITH TARGETS : PHYSICS AND APPLICATIONS

Jean-Michel Pouvesle, Augusto Stancampiano, Éric Robert,

GREMI, UMR7344 CNRS/Orleans University, Université d'Orléans, Orléans, France

E-mail: jean-michel.pouvesle@univ-orleans.fr

In the context of fast development of atmospheric pressure plasma jet, a better understanding of the role of the different plasma components is needed. Among diagnostic experiments, many are performed on plasmas developing freely in the air, away from the conditions of use. However, the plasma/target interactions are of considerable importance as they lead to simultaneous changes in the produced plasma and the treated target. We will address this issue and give some perspectives.

1. Context

The two last decades have seen an impressive increase of the research dedicated to applications of low temperature atmopheric pressure plasmas, especially in biology and medicine related domains. Biological applications are also now extending to agriculture and, more recently, to cosmetic. Despite the huge number of *in vitro* and *in vivo* experiments there are still numerous challenges to overcome linked to the nature of the encountered target (biological tissues and materials, organs and their direct environment, liquids) that have a direct effect on the produced plasma itself and on the generated species. That must therefore be taken into account in the applied treatments and it complicates the definition of a "plasma dose" expected by many. It appears also very important to always take into account the complete electric circuit represented by the plasma reactor, the plasma itself and the target, which electrical characteristics can vary over the time, to properly adjust the plasma parameters. Development of Artificial Intelligence and Machine Learning can also bring new solutions in the quest of reliable routinely applied plasmas treatments.

2. Plasma/target interactions

The extremely strong coupling between the characteristics of the plasma and those of the target, as already shown (e.g. ref. [1, 2]), will play a very important role in the results observed during the treatments. A variation in the chemical or physical characteristics of the target will involve significant differences in the gas flow, the local temperature, or the induced electric field, resulting *de facto* in variations in the production of the reactive species. It also concerns the transposition of the results between the *in vitro* and the *in vivo/in field* experiments [3] that are carried out under extremely different conditions, especially concerning the equivalent electric circuit of the reactor / plasma / target assembly. These problems directly affect the identification of the processes involved and currently limit the possibility of a definition of a "dose" in plasma treatments. In this talk, after a presentation of the context, we will focus on the different problems linked to the plasma/target interaction, including treatments of tissues and liquids. We will emphasize on the fact that plasma diagnostics must be performed in real treatment conditions and discuss the main issues, challenges and opportunities linked to the control of the multimodal action of low temperature non-equilibrium plasmas.

Aknoledgments The work realized at GREMI was supported in part by ANR BLANC 093003 PAMPA, by CNRS PEPS project ACUMULTIPLAS, by the ITMO Cancer in the frame of the Plan Cancer, project PLASCANCER N°17CP086-00, by ARD2020 Cosmetosciences project PLASMACOSM and by GDRs ABioPlas and HAPPYBIO. Involved PhD students have been supported by TFS INEL/Région Centre Val de Loire, MENSR, and ANRT/LVMH PhD fellowships

3. References

[1] Darny T, Pouvesle JM, Fontane J, (…), Robert E *2017 PSST* **26** 105 001
[2] Darny T, Pouvesle JM, Puech V, (…), Robert E *2017 PSST* **26** 045 008
[3] Stancampiano A, Chung TH, Dozias S, (…), Robert E *2020 IEEE TRPMS* **4** 355

DEVELOPMENTS OF PLASMA ACTIVATED LIQUIDS FOR AGRICULTURAL AND WATER TREATMENT APPLICATIONS

Nikola Škoro[1], Olivera Jovanović[1], Amit Kumar[1], Andjelija Petrović[1] and Nevena Puač[1]

[1]*Institute of Physics, University of Belgrade, Pregrevica 118, 11080 Belgrade, Serbia*
E-mail: nskoro@ipb.ac.rs

In recent years many applications of cold atmospheric plasmas (CAP) are focused on treatment of liquid samples. CAP induces rich chemistry in active plasma volume creating short and long lived reactive species that penetrate and/or react with molecules in the liquid-phase producing short and long-lived species [1]. From the application point of view, the plasma treatment could be used for liquid activation and creation of plasma activated water (PAW) and plasma activated medium (PAM), or for destruction of dissolved pollutant molecules – for decontamination processes. For the latter case, plasma can be used as a chemically free advanced oxidation process (AOP) that can efficiently remove various organic micropollutants (OMP) from water. The major area of interest for PAW and plasma decontamination lie within the field of plasma agriculture [2]. Apart this field, liquid activation has a high potential in plasma medicine. For all these applications, clear knowledge of the entangled connection between plasma properties, plasma chemistry and interaction with the liquid target is necessary in order to tune the plasma for different outcomes of the liquid treatment [3,4]. In this work we will present several kinds of plasma treatments featuring investigation of both plasma and treated liquid properties and their dependence on the plasma jet type, operating parameters etc. Results of treatments of pure and contaminated water (with organic contaminant) were performed by using high-frequency pin-type atmospheric pressure plasma jet operating with He and Ar. For PAW creation, we demonstrated how the plasma operating in different regimes with He as working gas yield different concentrations of reactive nitrogen and oxygen species. Moreover, we investigated the influence of the working gas as well as sample volume to the RONS concentration in the activated water. We observed much higher production of H_2O_2 in case of Ar plasma than in He. For treatments of the cell media used in plasma medicine applications, we used a dielectric barrier discharge (DBD) jet configuration that operated at 80 kHz. We showed that the power deposited to the plasma in contact with target was the key parameter for monitoring the production of RONS in the PAW and PAM. Thus precise power determination is crucial for fine tuning of the produced species.

Acknowledgement: This work was supported by MSTDI Republic of Serbia grant number 451-03-68/2022-14/200024, NOWELTIES project - EU H2020 MSCA ITN No. 812880 and the Science Fund of the Republic of Serbia, grant No. 3114/2021 - Project APPerTAin-BIOM.

References

[1] Vanraes P and Bogaerts A 2018 *Appl. Phys. Rev.* **5** 031103.
[2] Puač N, Gherardi M and Shiratani M 2017 *Plasma Process Polym.* e1700174.
[3] Tomic S, Petrovic A, Puac N, Škoro N, Bekic M, Petrovic Z Lj and Colic M 2021 *Cancers* **13** 1626.
[4] Kumar A, Škoro N, Gernjak W, Jovanović O, Petrović A, Živković S, Cuervo Lumbaque E, José Farré M and Puač N 2023 *Sci. Total Env.* **864** 161194.

CONTRIBUTION OF NON-THERMAL PLASMA IN AGRICULTURE: FOCUS ON PRE-HARVEST TREATMENT

P. Attri[1]*, T. Okumura[1], Y. Ishibashi[1], K. Koga[1,2], and M. Shiratani[1]

[1]*Kyushu University, Fukuoka, Japan*
[2] *National Institutes of Natural Sciences, Tokyo, Japan*
E-mail: attri.pankaj.486@m.kyushu-u.ac.jp

The use of non-thermal plasma treatment of seeds benefits over conventional treatments due to short treatment time and low-temperature operations [1,2]. During plasma interacts with the oxygen, nitrogen, water, etc., in air, they produce various radical and non-radical species [3]. It is a general fact that reactive species like reactive oxygen and nitrogen species (RONS) can influence plant growth and development. The increased nitrogen nutrients level influences growth hormones, activation of growth-related gene expression, and other physiological processes to understand the plasma effect on seedling growth. Additionally, the presence of RONS can disrupt redox homeostasis and cause mild oxidative stress in plants during vegetative and reproductive stages. Electron paramagnetic resonance (EPR) spectroscopy is optimal for interpreting any change in paramagnetic defect centers. The detection of the change in paramagnetic species before and after seed treatment is of great interest. Therefore, we used EPR spectroscopy in this study to detect the changes that occurred in seeds before and after plasma treatment. Further, we treated seeds that matured under heat stress with plasma and found that subsequent germination was significantly restored; genes involved in ABA biosynthesis were downregulated, whereas genes involved in ABA catabolism and α-amylase genes were upregulated [4]. We suggest that plasma treatment can significantly improve the germination of rice seeds affected by heat stress by affecting epigenetic regulation.

This work is supported by Japan Society of the Promotion of Science (JSPS)-KAKENHI grant number 22H01212. Additionally, partly supported by JSPS Core-to-Core Program JPJSCCA2019002, JSPS KAKENHI Grant Number JP16H03895, JP19H05462, JP19K14700, JP20H01893, JP20K14454, Plasma Bio Consortium, and Center for Low-temperature Plasma Sciences, Nagoya University.

References

[1] Attri P, Okumura T, Koga K, Shiratani M, Wang D, Takahashi K and Takaki K, 2022 *Agronomy*, **12**, 4.
[2] Attri P, Ishikawa K, Okumura T, Koga K and Shiratani M, 2020 *Processes* **8**, 1002.
[3] Kaneko T, et al., 2021 *Jpn. J. Appl. Phys.* **60**, 040502.
[4] Suriyasak C, et al., 2021 *ACS Agric. Sci. Technol.* **1**, 5-10.

TECHNOLOGICAL 3D PLASMA SOURCES SCALING AND COMPUTATION

Jozef Brcka

Tokyo Electron America, Inc.
2400 Grove Boulevard, Austin, TX-78741-6500, U.S.A.
E-mail: jozef.brcka@us.tel.com

Advanced plasma processing is an integral part of semiconductor devices high-volume manufacturing. State of the art devices consist of the structures with dimensions that are approaching several nanometers in scale. Congruently, with increasing device density per die the elemental variety and materials composition of the novel structures is growing as well as. Fabricating such complex strutures, therefore, calls for selective processes, utilization of new chemistries and precursors, temporal or spatial process separation, and multi-step processing schemes. In this situation, the plasmas could be very complex to understand and control at atomic scale. Indeed, this complexity is challenging to address using experimental techniques and sophisticated diagnostics. Recent reviews have stressed the insights that mathematical modelling can bring knowledge to our understanding of the plasmas processes and their control in semiconductor technology. Plasma simulation is becoming an essential tool for designing and developing a new semiconductor manufacturing equipment. Multiphysics coupled computational models are powerfull tools to help us in understanding of the conceptual models. They enable simulation of complex reaction mechanisms to test hypothesis *in silico* and enable further innovation.

The following factors are current challenges of plasma simulation: Firstly, innovative concepts that are embedding plasmas into nonsymetric configurations. In such cases, computationally demanding 3D plasma transport simulation is necessary. Additionally, 3D plus motion (e.g. 4D plasma simulations) are required. Secondly, the chemistry in large-scale plasma simulation requires a sensitive assessment of the dominant reactions and species to be included in the models. On the other hand, the production and transport of reactive species can be affected under the changes in spatio-temporal situation. Furthermore, operation modes have the potential to control the reaction chemistry. Obviously, reduction of the species and reactants speeds up the computation. However, it is not always the case that optimal runtime performance is the most suitable objective. Thirdly, a major challenge is using simulation data instantly and effectively in the process design and development. This raises many concerns such as how to couple the first principles models, reactions and transport within plasma and their interaction with processed surfaces, correlation with process and equipment data, and as a result delivering an optimized predictive outcome for device fabrication. The discussion and examples in this talk will be mostly related to plasma sources utilized in semiconductor high-volume manufacturing to address briefly described topics. Modelling and simulations are used to test hypotheses that are difficult to address with other experimental techniques. They can help to interpret experimental data or support and connect diversefied types of data obtained by different experimental techniques.

TRANSPORT OF COLD PLASMA REACTIVE SPECIES INTO WATER AND BIO-RELEVANT EFFECTS OF PLASMA-ACTIVATED WATER

Zdenko Machala, Mostafa E. Hassan, Robin Menthéour, Radoslav Jankovič, Patrik Štípala, Karol Hensel, Mário Janda

Faculty of Mathematics, Physics and Informatics, Comenius University Bratislava, Slovakia
E-mail: machala@fmph.uniba.sk

Atmospheric air plasma produces a cocktail of reactive oxygen and nitrogen species (RONS) with multiple functions. The transport of RONS to the liquid phase through plasma–liquid interface can be significantly enhanced by converting bulk water to aerosol microdroplets [1]. The expected solubility of various RONS does not fully match Henry's law solubility coefficients. We verified the applicability of Henry's law coefficients under strongly nonequilibrium conditions characteristic of plasma–liquid interaction, with water in the form of bulk vs. microdroplets. This fundamental understanding can lead to optimized designs of plasma–water interaction systems for multiple applications in biomedicine, environment, and agriculture.

Figure 1 shows the schematic diagram of elementary processes of ionization, excitation and dissociation in air plasma, and formation of radicals and other RONS, and their mutual reactions in the gas phase. Then it shows their transport into the liquid water based on their solvation, indicating the Henry's law coefficients. Finally, in the liquid, the plasma-formed, as well as the new ionic RONS diffuse and undergo further reactions. The RONS transport processes in water are compared in the bulk and in two types of microdroplets, charged microdroplets produced by electrospray (ES), and nebulized non-charged microdroplets. The amount of H_2O_2(aq) and NO_3^-(aq) (mainly from gaseous HNO_3) dissolved in the nebulized microdroplets was ~1 order of magnitude higher compared to that in the ES microdroplets because it was enhanced by their smaller size, providing larger plasma–water interface area. On the other hand, the production of NO_2^-(aq) (mainly from HNO_2 [2]) is higher in the charged ES microdroplets, which indicates the importance of the charge effects.

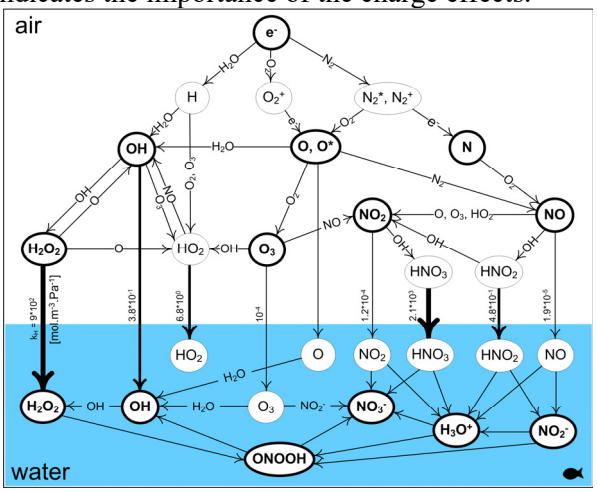

Fig. 1. Schematic of the elementary plasma-chemical and transport processes at the plasma-liquid interface [3].

This work was supported by Slovak Research and Development Agency APVV-17-0382, APVV-20-0566 and Slovak grant agency VEGA 1/0596/22, 1/0822/21.

References

[1] M.E. Hassan, M. Janda, and Z. Machala, Water, 13, 182 (2021).
[2] M. Janda, et al., Appl. Sci., 11, 7053 (2021).
[3] Z. Machala, et al., J. Phys. D Appl. Phys. 52, 340023 (2019).

COLD ATMOSPERIC PRESSURE PLASMA TECHNOLOGY FOR ECOLOGICAL AGRICULTURE

Anna Zahoranová[1], Veronika Medvecká[1], Juliána Tomeková[1], Sandra Ďurčányová[1], Stanislav Kyzek[2], Ľudmila Slováková[3], Renáta Švubová[3], Silvia Mošovská[4], Eliška Gálová[2], Dušan Kováčik[1]

[1]*Department of Experimental Physics, Faculty of Mathematics, Physics and Informatics, Comenius University, Mlynská dolina F2, Bratislava 842 48, Slovakia*
[2]*Department of Genetics, Faculty of Natural Sciences, Comenius University, Ilkovičova 6, Mlynská dolina B-2, Bratislava 842 15, Slovakia*
[3]*Department of Plant Physiology, Faculty of Natural Sciences, Comenius University, Ilkovičova 6, Mlynská dolina B-2, Bratislava 842 15, Slovakia*
[4]*Department of Nutrition and Food Quality Assessment, Faculty of Chemical and Food Technology, Slovak University of Technology, Radlinského 9, 812 37 Bratislava, Slovakia*

E-mail: zahoranova1@uniba.sk

The effect of cold atmospheric pressure plasma treatment on the germination and growth parameters of several types of plant seeds (wheat, corn, soybean, barley, hazelnuts, peanuts) and as well as the inhibition of pathogens on the surface of the seeds were studied. The surface treatment was realized using a Diffuse coplanar surface barrier discharge, which represents a suitable plasma source for generating low-temperature plasma also in ambient air at atmospheric pressure. The effect of plasma treatment was studied under different parameters to optimize the conditions of plasma treatment for a given type of seed. Plasma-induced changes were studied by surface diagnostic methods, such as contact angle measurement to determine hydrophilicity, ATR-FTIR, XPS to determine possible changes in chemical composition and bonds on the surface. Plasma source properties were investigated by measurements of the electrical characteristics. Plasma parameters were investigated using the optical emission spectroscopy and the chemical composition of the plasma gaseous products using Fourier transform infrared spectroscopy.

1. Introduction

Cold atmospheric pressure (CAP) plasma has become the subject of significant research efforts in recent years. In addition to common areas of plasma applications, such as surface treatments, many scientific teams focus on the study of plasma interactions with biomaterials (wound treatment, preparation of biocompatible materials for medical purposes, plant seed treatment in agriculture). The advantage of CAP plasma is its low temperature approach, minimizing of chemicals and no need of vacuum systems at atmospheric pressure [1,2].

Over the last two decades, a lot of scientific knowledge has been obtained declaring the positive effect of CAP plasma on various types of seeds. It was found that plasma treatment of seeds has a decontamination effect on commonly occurring undesirable pathogens on the surface of seeds, which are currently mainly solved by coating the seeds with fungicides. The decontamination effect can be of considerable practical importance, since it is well known that phytopathogenic microorganisms have a negative impact not only on seed quality, but also on the subsequent production of agricultural crops. Pathogens can be transmitted from the seed to the whole plant during its growth and development phase, causing significant economic losses in crop yields. In addition to the reduction of phytopathogenic microorganisms, many scientific studies have confirmed the positive effect of plasma on seed germination (higher germination rate, shorter germination time and improvement of seedling vitality) and plant growth (improvement of physiological parameters, growth dynamics and crop quality) [3,4,5].

Experimental research in the field of plasma processing of biological samples at atmospheric pressure, as well as the first applications in practice, most often prefer two basic groups of plasma sources - *dielectric barrier discharges* (DBD) and *atmospheric pressure plasma jets* (APPJ). Both types of plasma sources include a relatively large number of configurations of electrode systems that allow the

generation of suitable plasma with the required properties for specific applications [6,7,8].
In our contribution, we present an overview of the results achieved by our research group within several scientific projects focused on the application of plasma in agriculture. Our effort is to look for conditions suitable directly for use in seed treatment in practice. We used a plasma source based on dielectric barrier discharge, which generates cold plasma at atmospheric pressure in the surrounding air, or in oxygen, nitrogen and their mixtures. Of course, due to their multidisciplinary nature, the studies are the result of collaboration with several experts in plant physiology, genetics and microbiology from the Faculty of Natural Sciences. We also focus on the use of appropriate diagnostic methods to investigate changes on the surface of seeds after plasma treatment. The evaluation of changes in the physical and chemical surface properties of biological samples after plasma treatment is significantly more complex than in the case of inorganic, polymeric or other samples. Established methods therefore require innovative approaches in determining the surface energy, elemental composition and chemical bonds, or surface morphology of biological samples. The evaluation of the plasma treatment on the physical and chemical properties of the surface was carried out using modern procedures and equipment suitable for the analysis of biological samples. Equally important for the study of the interaction of plasma and its individual components with the surface of biomaterials is appropriate plasma diagnostics using optical emission spectroscopy, determining the composition of plasma products using FTIR spectroscopy, as well as electrical measurements in the plasma to determine the effectiveness of plasma treatment.

2. Experimental

Plasma Source and treatment of seeds
Diffuse Coplanar Surface Barrier Discharge (DCSBD), which we used as a source of cold atmospheric pressure plasma for the treatment of seeds, is composed of many parallel electrodes of 1.5 mm wide and 20 cm long placed in mutual distance of 1mm. Electrodes were embedded in dielectric material (Al_2O_3 96% purity), cooled by oil flowing in cooling circuit. DCSBD was powered by AC high frequency sinusoidal voltage (14 kHz, up to 20 kV peak-to-peak) generated by LIFETECH VF 700 generator, described in more detail in [9]. Schematic layout of DCSBD together with experimental set-up for treatment of seeds, OES and electrical measurement is shown in Fig.1.

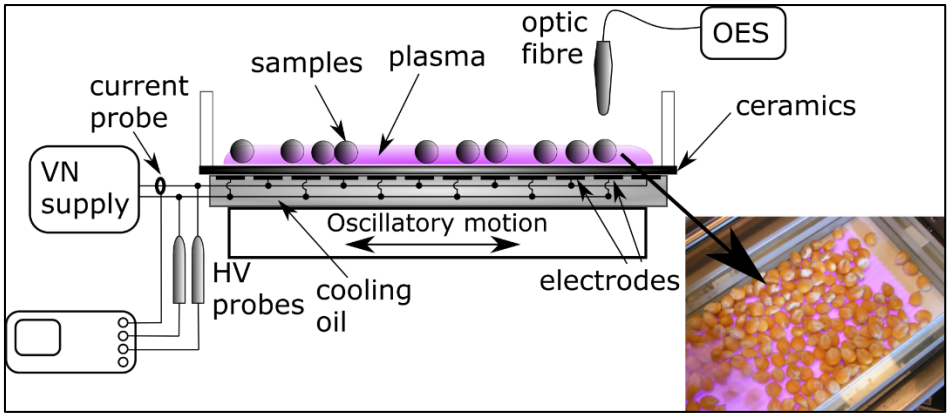

Fig. 1: Experimental set-up for plasma seed treatment, OES and electrical measurements and scheme of DCSBD electrode system.

Tested seeds (maize, wheat, barley, soybean, pea, and others) were treated in LTP of DCSBD discharge ignited in ambient air (or in oxygen, nitrogen, and their mixture) at atmospheric pressure at input power of 400 W and at the different exposure times (from 5 s to 120 s) accordingly on the type of seed, their dimension, hardness and surface properties. The DCSBD plasma panel was placed on the orbital shaker (PSU-10i, f. Biosan) to achieve the movement of the seeds in plasma layer for the purpose of homogeneous treatment of the seeds. Plasma parameters were monitored by voltage and current measurements and by optical emission spectroscopy and FTIR spectroscopy.

Seed Germination

For estimation of plasma effect on vigor of seeds, there were used 50 seeds, which were rolled in the sterile filter paper placed in glass pots and moistened with sterile deionized water. Seeds for germination were cultivated in the incubator at 24 °C in the dark for 5 days. The percentage of germination was calculated using the equation: final germination percentage = number of germinated seeds multiply by 100 and divided by total number of seeds. Germination potential was calculated as number of germinated seeds in 3 days divided by total number of seeds and multiplied by 100. Index of germination was calculated as a sum of germinated seeds on day *x* divided by days of germination [10,11].

Surface Diagnostics

The studied surface properties related to improved germination and physiological parameters of the seeds were:

- Wettability – measurement of water contact angle (WCA) depending on treatment time and water uptake (imbibition)
- Seed surface morphology observed using scanning electron microscopy (SEM)
- Changes in chemical composition and chemical bonds on the surface analyzed by ATR-FTIR spectroscopy and XPS

3. Results and discussion

Seeds Surface Changes

As shown in Fig. 2, experimental measurements of the water contact angle (WCA) of maize seeds after plasma treatment confirm a decrease in the value compared to the reference sample, i.e. an increase in the hydrophilicity of the seed surface. The results of the imbibition measurement confirm that, especially in the first hours, the samples treated with plasma absorb more water [8]. Increasing plasma treatment time is positively correlated with more intense water intake. It turns out that one of the primary mechanisms of increasing germination is the creation of so-called functional (polar) groups, which leads to an increase in the surface energy of the material, thereby causing an increase in wettability and a subsequent increase in ability of water absorption. The changes in characteristic chemical groups and chemical composition can be shown using ATR FTIR spectroscopy and XPS analysis, respectively. As we can see from decrease of C-H stretching peaks and increase of bands attributed to starch and proteins in spectra of treated and untreated samples (Fig. 2), we can assume that plasma treatment in the case of maize surface can cause the activation of surface, due to the removal of lipids from the surface of seeds. This effect is usually occurring on the seeds treated by DCSBD and can be related to further increase of wettability of the surface.

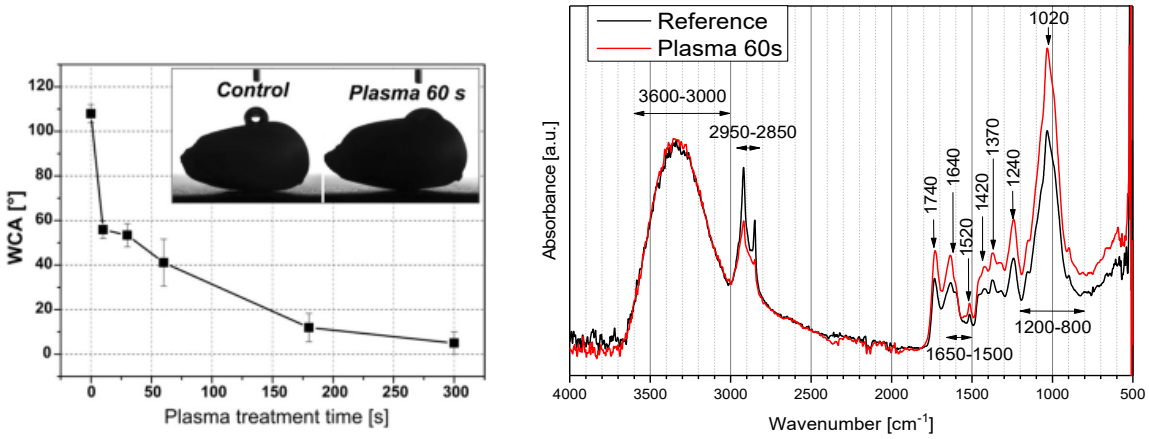

Fig.2: Effect of treatment time on the water contact angle measured on maize seeds samples treated by ambient air plasma at atmospheric pressure, the discharge power was 400 W (left), ATR-FTIR spectra of maize seeds before and after plasma treatment (60 seconds, ambient air, 400 W) (right). Values are the mean ± SD, n = 3, for 50 pieces of seeds in each repetition. [8]

Improvement of Germination

Plasma can interact with the surface of seeds and change the surface characteristics that lead to faster germination and greater yields. The effectiveness of the plasma treatments for seed germination can vary on the type seeds, the condition of the seeds and the environmental factors such as climate, soil conditions and water availability. The effect of plasma treatment on maize seed germination varied with the treatment time as illustrated in Fig. 3. The CAP plasma treatment of maize seeds also affected the characteristics of seedlings growth, including root and shoot length, fresh and dry weight (Fig. 3 right). The maize is monocotyledonous plant with radicle root and two lateral roots. The treatment time of 60 seconds stimulated root length by 12% and shoot length by 35% compared to the control. The seedling vigor index I and II combine the growth parameters and germination rate. The response to 60 seconds plasma exposition increased vigor index I (by 23%) and II (by 32%) compared to the untreated maize seeds (Fig. 3)

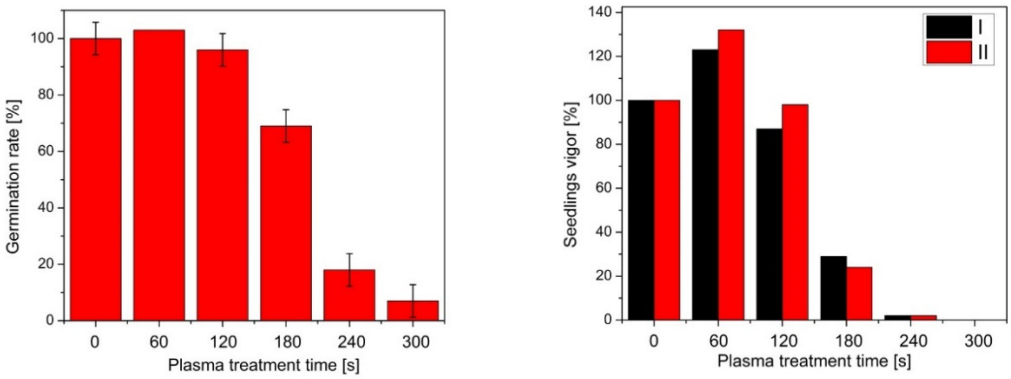

Fig. 3: Effect of CAP plasma treatment on germination rate of maize seeds (left). Effect of a CAP plasma treatment on seedlings vigor I (shoot and root lengths) and vigor II (shoot and root fresh weights) of 5-days old maize seedlings (right) [10] .

Decontamination of seeds

We studied the inhibition of unwanted pathogens on the surfaces of cereals, nuts, and spices [10-13]. As an example, the results of the study of the effects of plasma treatment of corn seeds contaminated with both native contamination occurring naturally on the surface and artificially infected surfaces with pure cultures of toxinogenic *Aspergillus flavus*, phytopathogenic *Alternaria alternata* and *Fusarium culmorum* can be cited. The decontamination effect was different for different pathogens. The most resistant fungus was *Alternaria alternata* (Fig. 4), on the other hand, plasma treatment had the strongest effects on *Fusarium culmorum*. Based on the obtained results, the effectiveness of plasma treatment on fungal contamination on the surface of corn seeds was as follows: *Alternaria alternata* < native contamination < *Aspergillus flavus* < *Fusarium culmorum*.

Since the longer plasma treatment times required for complete decontamination of the seed surface can cause a decrease in germination, we focused on the combination of plasma treatment in a shorter time with chemical fungicide treatment. Plasma treatment of seeds led to increased surface wettability and therefore better germination and fungicide penetration. The synergistic effect of fungicide and CAP plasma treatment used against seed-borne phytopathogens present on the surface seeds was more effective than when each of them was used individually. An optimal combination of plasma treatment time and chemical fungicide dose can significantly reduce the use of harmful chemicals in practice but at the same time stimulate germination via plasma treatment [14].

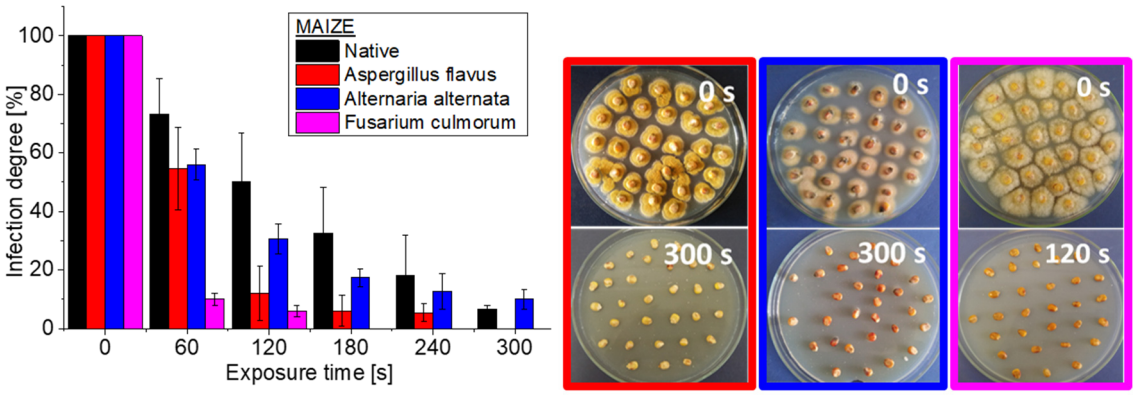

Fig. 4: Growth inhibition of *Aspergillus flavus, Alternaria alternata, Fusarium Culmorum and native contamination* on the maize seeds surface after plasma treatment, a) unterated control samples, b) 300 seconds plasma exposed samples [10].

Genotoxic efect and adaptive response

In our study, we first verified that the influence of CAP plasma pre-treatment of pea seeds can induce a positive adaptive response and improve the seedling resistance to adverse growth conditions [15, 16]. In first, we investigated the effect of pea seeds plasma treatment at different times to estimate the optimal plasma exposure time and determine the interval for safe use of plasma for seed treatment. The DNA damage of pea seedlings was studied using the alkaline comet assay method and seedling-negative conditions were simulated using toxic concentrations of zeocin. CAP plasma was shown to have a positive effect on reducing DNA damage in pea seedlings at all exposure times used via initiation of positive adaptive response when the seeds are treated by plasma before application of zeocin. Even at lower exposure times, which were too short to trigger mechanisms involved in the regenerative phase of the adaptive response, such as protein synthesis or antioxidant production, other defense mechanisms of the adaptive response were activated. Our results showed that plasma pretreatment of pea seeds can increase the defense mechanisms of seedlings and help overcome various stresses caused by adverse growth conditions, such as drought, the presence of heavy metals or toxic chemicals in the soil. Plasma diagnostics using OES confirmed the non-equilibrium, low-temperature character of CAP plasma. FTIR analysis of gaseous products from the DCSBD plasma showed the presence of NO_2, N_2O, NO, HNO_3 and HNO_2, which may play an important role in the interaction with seeds.

4. Conclusion

Experimental results obtained as part of the research in the plasma application on seeds indicated that low-temperature plasma generated by DCSBD at atmospheric pressure in ambient air can be successfully used for plant seeds treatment to reach various positive effects. Plasma treatment of the seeds led to an increase in surface wettability, which helps better germination and also capture of the disinfectant. The application of CAP plasma in the field of agriculture and food industry is a promising way to stimulate and protect plants and food products on the one hand, while reducing unwanted xenobiotics in the environment on the other. A significant advantage of the used type of plasma source (DCSBD) is that it does not need low pressure or any stabilizing working gas, moreover, it can work in continuous mode only in ambient air, which means low operation and maintenance costs. The high power plasma density is advantageous for more efficient processing with treatment times reduced to seconds.

5. Acknowledgement

This work was supported by the Slovak Research and Development Agency under the contract No. APVV-21-0147 and by Slovak Grant Agency for Science VEGA 1/0688/22. This publication is the result of support under the Operational Program Integrated Infrastructure for the project: Advancing University Capacity and Competence in Research, Development and Innovation (ACCORD), co-financed by the European Regional Development Fund.

6. References

[1] Laroussi M. 2005 *Plasma Process Polym.* **2** 39
[2] Laroussi M, Leipold F (2004). *Int J Mass Spectrom* 233:81–86
[3] Bourke P, Ziuzina D, Boehm D, et al. (2018) *Trends Biotechnol* 36:615–626
[4] Randeniya, L.K., De Groot, G.J.J.B., A Review. *Plasma Process. Polym*. 2015, 12, 608–623.
[5] Los A, Ziuzina D, Boehm D, et al. (2017) *InnovFood Sci Emerg Technol* 44:36–45 [12]
Puač N, Gherardi M, Shiratani M (2018) Plasma agriculture: a rapidly emerging field. Plasma Process Polym 15:1700174
[6] Šimončicová, J.; Kryštofová, S.; Medvecká, V.; et al. (2019) *Appl. Microbiol. Biotechnol.* 103, 5117–5129.
[7] Ehlbeck, J., Schnabel, U., Polak, M., Winter, J., et al., *J. Phys. D. Appl. Phys*. 2011, 44, 013002.
[8] Hati, S., Patel, M., Yadav, D., *Curr. Opin. Food Sci*. 2018, 19, 85–91.
[9] Černák M, Černáková L, Hudec I, Kováčik D, Zahoranová A (2009) *Eur Phys J Appl Phys* 22806
[10] Zahoranová A, Henselová M, Hudecová D et al. 2016 *Plasma Chemistry and Plasma Process* **36** 397
[11] Zahoranová A, Hoppanová L, Šimončicová J et al (2018) *Plasma Chem Plasma Process* 38:969–988.
[12] Stolárik T, Henselová M, Martinka M et al. 2015 *Plasma Chemistry and Plasma Processing*. **35** 659
[13] Mošovská S, Medvecká V, Halászová N, et al. (2018). *Food Research International* 106:862–869. doi: 10.1016/j.foodres.2018.01.066
[14] Hoppanová, L., Medvecká, V., Dylíková, et al. *Acta Chimica Slovaca*, *13*(1), 26-33.
[15] Kyzek S, Holubová Ľ, Medvecká V et al (2018) *Plasma Chem Plasma Process* 39:475–486
[16] Tomeková, J.; Kyzek, S.; Medvecká, V. et al. (2020) *Plasma Chem. Plasma Process.* **2020**, 40, 1571–1584.

DIAGNOSTICS AND CHARACTERIZATION OF A NOVEL MULTIPURPOSE RF ATMOSPHERIC PRESSURE PLASMA JET FOR MATERIAL PROCESSING

Mehrnoush Narimisa[1], Yuliia Onyshchenko[1], Ivana Sremački[1], Olivier Van Rooij[2], Anton Nikiforov[1], Ana Sobota[2], Rino Morent[1], Nathalie De Geyter[1]

[1]*Research Unit Plasma Technology (RUPT), Department of Applied Physics, Faculty of Engineering and Architecture, Ghent University, Ghent, Belgium*
[2] *Eindhoven University of Technology, Department of Applied Physics, PO Box 513, 5600 MB Eindhoven, The Netherlands*
E-mail: Mehrnoush.Narimisa@Ugent.be

In this work, a newly designed atmospheric pressure plasma jet (MPPJ3) is introduced and characterized for a potential plasma-assisted material processing application. The proposed device overcomes the typical issues concerning plasma jet efficiency by its specific design that allows the use of three separated gas channels. Essential properties of the discharge such as rotational and plasma temperature by means of optical emission spectroscopy (OES) and laser scattering are determined, and fluid dynamics are examined through Schlieren imaging. The outcomes of this work show that the MPPJ3 set-up provides a plasma with a rich chemistry, a controllable size and temperature, and a superior gas mixing between channels.

1. Introduction

Despite the usefulness of atmospheric pressure plasma jets (APPJs) due to their superior features, a higher performance of these plasma generating sources for practical purposes is still looked for. Many studies have focused on the improvement of APPJ efficiency by alteration of plasma processing parameters [1-3], modifying the APPJ configuration [4-6], switching to a different discharge gas [7], and controlling the ambient environment [8]. In contrast to the extensive investigations of APPJ efficiency enhancement, the existing APPJs are suffering from many issues such as lack of control over the plasma size, temperature, and the chemistry. Therefore, the goal of this work is to introduce an APPJ source to increase the volume of the plasma, to provide an elevated mixing between gases, and at the same time to maintain the temperature of the plasma jet effluent low enough to avoid damaging of heat-sensitive materials. Therefore, a parametric observation of the newly configured RF plasma jet, named MPPJ3, will be reported through a series of diagnostic methods such as optical emission spectroscopy (OES), laser scattering technique, and schlieren imaging.

2. Methods and materials

The MPPJ3 reactor is designed in a 3-layer coaxial geometry illustrated in Figure 1 a). The set-up contains an inner quartz (internal diameter (ID)=1.3 mm) capillary inside which an RF powered tungsten rod with a diameter of 0.5 mm is centered. Coaxial to the inner capillary, another quartz tube (ID=4 mm) for possible monomer introduction is placed. Finally, a grounded outer hollow aluminum cylinder (ID=8 mm) has been arranged to act as outer gas channel maintaining the coaxial symmetry. Furthermore, an aluminum cap with a circular opening of 4.5 mm has been adjusted via a thread on the aluminum cylinder. The plasma jet set-up was powered with an RF generator (CESAR 136, Advanced Energy), operating at 13.56 MHz using a matching box. The RF input power during the complete experiment was fixed at 10 W. Plasma was first generated in pure argon (Air Liquide, Alphagaz 1), flowing through the inner channel, between the centered RF powered tungsten rod and the grounded nozzle, with a flow rate of 0.5 slm. If only this first gas flow is introduced, applying RF power to the tungsten wire leads to typical plasma ignition on the tip of the high voltage electrode (see Figure 1 b)). The gas flow through the second capillary could be used as a potential channel for monomer introduction into the plasma effluent. In this work, the argon gas flow rate through the second channel was fixed at 250 sccm. Finally, through the third external channel, an argon flow rate of 2 slm was applied. The latter channel grants the

following advantages to the jet: 1) it acts as shielding curtain limiting the atmospheric impact on plasma formation, 2) it increases the plasma volume, and 3) it enhances the homogeneous mixing of the monomer containing middle gas stream with the plasma.
For the purpose of plasma characterization, first plasma temperature was determined by analyzing the OH and N_2 bands using optical emission spectroscopy (OES) and the results were compared with the laser scattering technique at 532 nm used for detection of the Rayleigh signal of the heavy species in the discharge effluent 0.7 mm underneath the jet opening. The laser scattering technique was also used to examine the plasma structure. Finally, fluid dynamics were visualized using a single mirror Schlieren set-up.

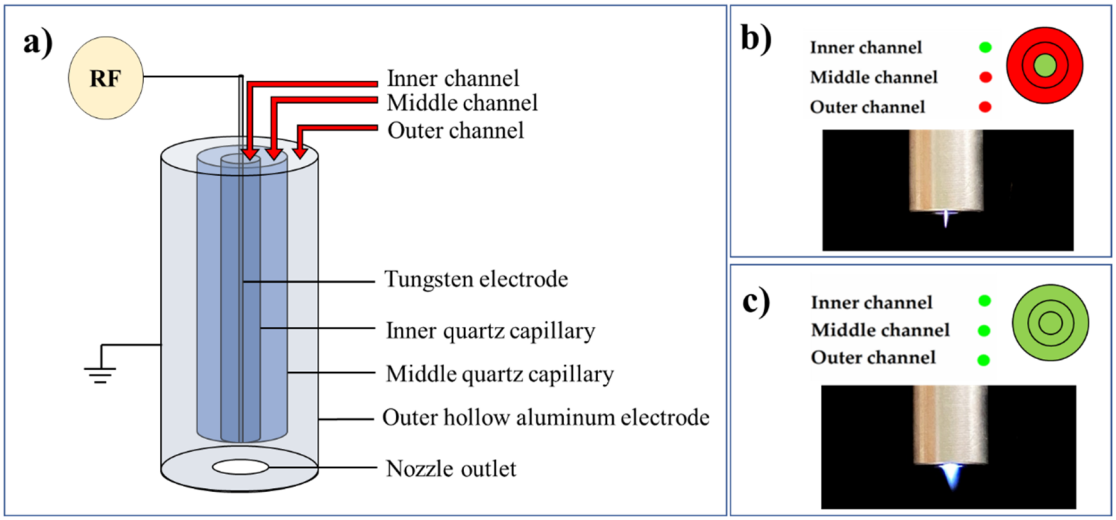

Figure 1. a) Schematic representation of the MPPJ3. b) MPPJ3 image while operating with only the inner active channel, and c) with all the channels active.

3. Results and discussions

The device included three gas layers, each with its own distinctive purpose. Two plasma modes were discernable by activating: 1) the inner and the inner + middle channels and 2) all three channels. When all three channels were fed by argon gas, the plume was wider and filled the volume inside the cap and thus the diameter of the plasma jet followed the nozzle outlet revealing the increased plasma size in this mode (see Figure 1 b)). In addition, the generated plasma inside the semi-closed cap ensures efficient gas mixing in the active plasma region.
A precise determination of the plasma temperature is very important to optimize the plasma performance based on the application. Therefore, using different methods, the plasma temperature has been determined. Figure 2 demonstrates the plasma temperature identified by the laser scattering technique, and by the OH, and N_2 rotational temperatures. The temperature overestimation by N_2 (C-B) can be justified by the effective energy transfer between the Ar reactive states and the nitrogen species of the ambient air resulting in N_2 (C) overpopulation and leading to a non-Boltzmann distribution. In case of the OH rotational temperature, two independent mechanisms are responsible for OH(A) radical formation: 1) electron impact excitation of ground state OH and 2) direct dissociation of water vapor, where OH(A) produced in the latter case are at highly excited levels. These two mechanisms result in the overpopulation of the rotational states of OH(A) with high rotational numbers and subsequent temperature overestimation.
As shown in Figure 2, injection of argon in the outer gas channel significantly influences the gas temperature in case of all used methods. For instance, the gas temperature measured by laser scattering when the inner argon channel is active is 314.3 ± 2.5 K. Adding 250 sccm gas to the middle channel slightly reduces the temperature which is more pronounced in the rotational temperature values. In this case, the energy per molecule is lower due to the excess amount of the gas. As soon as 2 slm of argon is fed to the system through the outer channel, a sharp elevation in temperature up to 360 ± 5 K occurs. This outcome can be explained by the prolonged stay of the gas mixture inside the reusable cap which is filled with argon gas in this case.

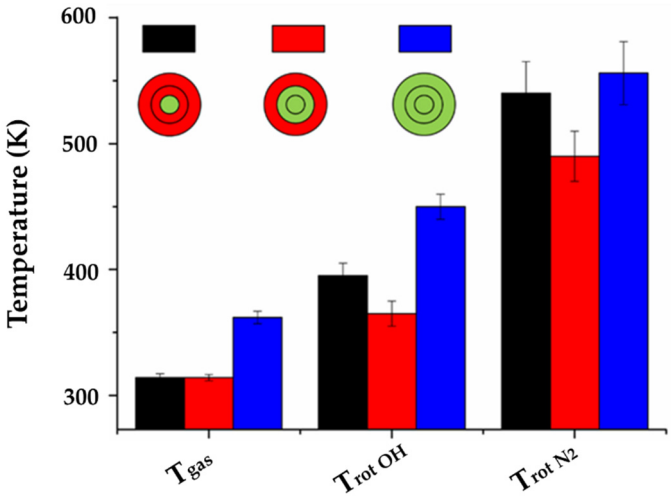

Figure 2. Plasma temperature obtained with different methods.

Aside from the plasma temperature, the plasma profile is another useful characteristic that can be obtained using the laser scattering technique, which can show the plasma expansion for different experimental set-ups. Using Rayleigh scattering, the plasma intensity in the vicinity of the plasma jet outlet is determined in a circular area having a 30 mm radial distance from the plasma core. Figure 3 shows the effect of different experimental conditions on the resultant plasma profiles. Comparing the curves suggests that the injection of gas to the middle and the outer channel enlarges the width of the plasma in the afterglow region. This width depends on the diameter of the capillary which is being fed by argon or in the case of three active channels this width depends on the nozzle outlet diameter. Therefore, if the plasma generation channel is active, the diameter of the plasma effluent is 1.3 ± 0.1 mm, analogous to the inner diameter of the inner capillary. When additional gas is being injected through the middle channel, the plasma effluent diameter increases to 2.3 ± 0.3 mm. Although the inner diameter of the middle capillary is 4.5 mm, this observation can be justified considering that the gas flow rate of the middle channel is small (250 sccm). Finally, adding gas to the outer channel results in a plasma effluent possessing the same diameter the nozzle outlet diameter. Slightly enhanced intensity in the central point of the curves in Figure 3 also appears, which is induced by the presence of the tungsten rod placed within the inner capillary having a diameter of 0.5 mm which influences the gas flow pattern. Particularly, when the inner channel is the only active channel, the impact of the tungsten rod is more pronounced.

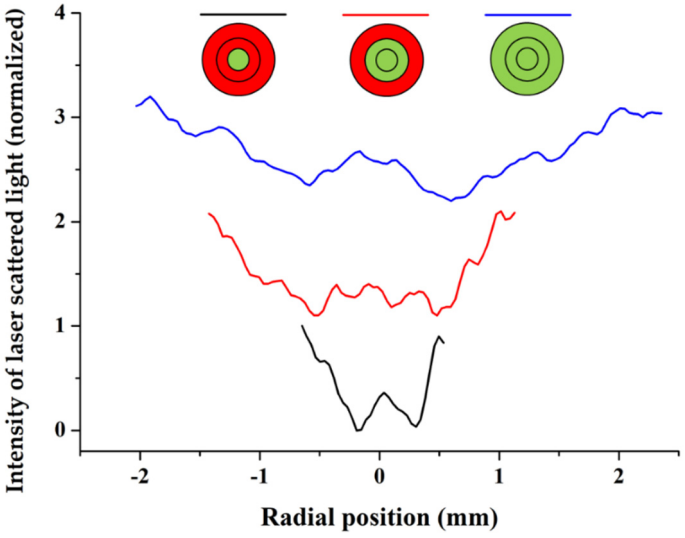

Figure 3. Plasma profiles analyzed by laser scattering.

Depending on the final application of plasma jets, the gas fluid dynamics become relevant. In the turbulent regime, the ambient air species such as oxygen can mix with the reactive plasma species, absorb their energy, and further expand the plasma. For some applications, the presence of these oxygen atoms in the plasma afterglow is advantageous. In this case, the turbulent regime can assist in oxidation and/or higher plasma propagation. On the other hand, if a pure plasma gas for material processing is desirable, the laminarity of the fluid is of great importance. Therefore, flow visualization can provide useful information on the plasma patterns and plasma propagation. The right image of Figure 4 depicts the plasma propagation pattern when only the inner channel is fed by argon gas. Based on the shown images, the laminar region is very extended (around 33 mm). This length however decreases to 27 mm as soon as the second gas layer is activated. The right image of Figure 4 shows that by injecting gas in the outer channel, the transition to the turbulence regime occurs closer to the nozzle outlet compared with the other two experimental conditions mentioned above. For this set of experiments, due to the special design of the RF plasma jet, the main gas mixing and outflow stream forming occurs before the plasma leaves the nozzle. Indeed, under this condition, the gas receives additional thrust due to the semi-closed volume in the reusable cap, where it circulates for a while meaning that the transition to the turbulent regime occurs faster.

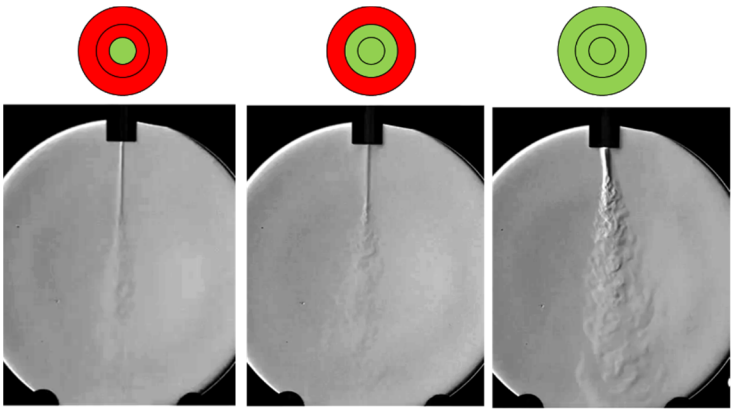

Figure 4. Images of the plasma stream dynamics using the Schlieren technique.

4. Conclusion

This work presents a novel APPJ set-up with improved performance enabling a good control over the plasma size, temperature, and chemistry. Due to its special configuration, the MPPJ3 can operate in two modes depending on the active gas channel. The three-channel configuration enables effective gas mixing in the plasma active region before escaping from the jet outlet. When all three channels are active, the plasma temperature in the core of the afterglow was found to reach a maximum of 360 ± 5 K indicating the potential of the set-up for treatment of heat-sensitive materials. The plasma profiles determined by laser scattering method indicate that, based on the active gas channel, the effluent diameter can vary from 1.3 mm up to the size of the nozzle outlet. Schlieren imaging provided a comprehensive view over the gas distribution over the effluent and proved that the laminarity of the plasma can also be controlled as desired. The acquired findings assure that the innovate MPPJ3 is a multifunctional APPJ system, as it enables control over some plasma features that could be exploited in various material processing domains.

5. References

[1] B. Liu, T. Zhang, and D. Gawne, "Computational analysis of the influence of process parameters on the flow field of a plasma jet," *Surface and Coatings Technology,* vol. 132, no. 2-3, pp. 202-216, 2000.

[2] A. Van Deynse, P. Cools, C. Leys, N. De Geyter, and R. Morent, "Surface activation of polyethylene with an argon atmospheric pressure plasma jet: Influence of applied power and flow rate," *Applied Surface Science,* vol. 328, pp. 269-278, 2015.

[3] C. Wang, Y. Liu, H. Xu, Y. Ren, and Y. Qiu, "Influence of atmospheric pressure plasma treatment time on penetration depth of surface modification into fabric," *Applied Surface Science,* vol. 254, no. 8, pp. 2499-2505, 2008.
[4] I. Onyshchenko, N. De Geyter, and R. Morent, "Improvement of the plasma treatment effect on PET with a newly designed atmospheric pressure plasma jet," *Plasma Processes and Polymers,* vol. 14, no. 8, p. 1600200, 2017.
[5] A. H. R. Castro, K. G. Kostov, and V. Prysiazhnyi, "Influence of nozzle shape on the performance of low-power Ar plasma jet," *IEEE Transactions on Plasma Science,* vol. 43, no. 9, pp. 3228-3233, 2015.
[6] Q.-Y. Nie, C.-S. Ren, D.-Z. Wang, and J.-L. Zhang, "A simple cold Ar plasma jet generated with a floating electrode at atmospheric pressure," *Applied Physics Letters,* vol. 93, no. 1, p. 011503, 2008.
[7] A. Y. Nikiforov, A. Sarani, and C. Leys, "The influence of water vapor content on electrical and spectral properties of an atmospheric pressure plasma jet," *Plasma Sources Science and Technology,* vol. 20, no. 1, p. 015014, 2011.
[8] C.-Y. Chou *et al.*, "Atmospheric-pressure-plasma-jet processed nanoporous TiO 2 photoanodes and Pt counter-electrodes for dye-sensitized solar cells," *Rsc Advances,* vol. 5, no. 57, pp. 45662-45667, 2015.

DETECTION OF PLANT HORMONES BY ION MOBILITY SPECTROMETRY

Vahideh Ilbeigi, Štefan Matejčík

Department of Experimental Physics, Comenius University in Bratislava, Mlynská dolina F2, 84248 Bratislava, Slovakia

E-mail: vahideh.ilbeigi@fmph.uniba.sk; stefan.matejcik@fmph.uniba.sk

1. Introduction

Plant hormones (PHs) are signalling molecules produced within plants that influence plant growth, seed germination, fruit maturation and ripening and pathogen defence [1,2]. Hence, the quantitative analysis of the PHs and determination of their concentrations in different tissues is crucially important to understand the role of these molecules in physiological processes occurring in plants.

Several analytical methods have been developed for analysis of PHs in different parts of fruits and plants using LC and GC, in combination with mass spectrometry.

Methyl salicylate (MeSA), synthesized in plants from salicylic acid, is a plant hormone that plays an important role in the resistance of plants to pathogens, thermogenesis in some flowers, and flower durability [1-3].

In this work, an analytical method was developed to exploit the advantages of solid phase microextraction (SMPE), Multicapillary column (MCC), and ion mobility spectrometry (IMS) for fast and sensitive analysis of MeSA in tomato leaves.

2. Experimental

Fresh tomato leaves were taken, frozen in liquid nitrogen and ground to fine powder. A similar method as reported in reference [4] was used to treat the tomato leaves by tomato ringspot virus (ToRSV) and prepare the leaf samples. The ToRSV inoculation buffer was obtained from Institute of Virology, Biomedical Research Center of Slovak Academy of Sciences (store at -20 ºC) [5]. The lower leaves of the tomato plants with an age of 5 weeks were inoculated by ToRSV.

The SPME fibers used in this work were commercially available SPME Arrow (Restek PAL, Switzerland) coated with (i) Polydimethylsiloxane (PDMS), (ii) Divinylbenzene (DVB)/PDMS, (iii) Carbon Wide Range (WR)/PDMS, and (iv) DVB/carbon WR/PDMS.

In the SPME experiments, the fiber was exposed to head space of 100 µL (standard solution) or 100 mg ground leaves (real sample) in a 20-mL sealed vial. To desorb the adsorbed compounds, the SPME fiber was put in an injection port with a temperature of 220 °C. The desorbed compounds were transferred to the MCC by a carrier gas (zero air) with a flow rate of 50 mL min^{-1}. After separation, the compounds were analysed by an IMS.

MCC columns including OV1, OV5, OV17, and OV20 (Multichrom Ltd. Russia) of 20 cm length were used for pre-separation of the volatile compounds released from tomato leaves. The stationary phases for the MCCs were as OV1: 100% - polydimethylsiloxane (non-polar), OV5: 5% - diphenyl, 95% - dimethylpolysiloxane (non-polar), OV17: 50% - diphenyl, 50% - dimethylpolysiloxane (weak-polar), and OV20: 20% - diphenyl, 80% - dimethylpolysiloxane (weak-polar).

The MCC was heated by heating elements powered by a power supply with a voltage of 30 V. The temperature of MCC was kept constant during the measurements at 100±1 °C. The MCC was put between an injection port and the inlet of IMS. The desorbed compounds from the SPME fiber are separated in MCC before entering to the ionization region of IMS. Experimental set-up is shown in Figure 1.

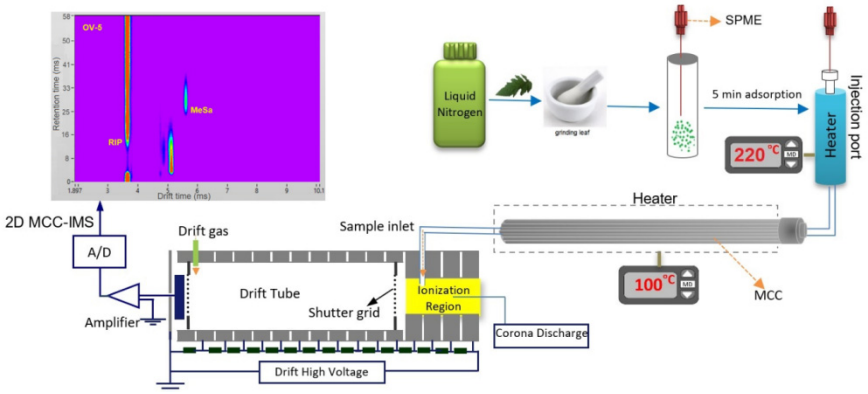

Figure 1. Schematic presentation of the experimental set-up.

3. Results

In the positive polarity, ionization of MeSA resulted in $[MeSA+H]^+$ formation while in the negative $[MeSA-H]^-$ and $[MeSA+O_2]^-$ were formed.

Four different SPME fibers were used for head space analysis and four MCC columns (OV1, OV5, OV17 and OV20) were investigated. Although all fibers can adsorb MeSA successfully, the maximum signal intensity was achieved for the SPME needle with PDMS fiber.

To find the optimal condition for SPME sampling, the effects of concentration, extraction time, and temperature were investigated. The optimal extraction time of 5 min was selected as to avoid saturation in the real sample measurements. With the increasing extraction temperature, signal intensity for the standard sample decreases. This may be due to the vaporization of solvent and its liquification on the SPME fiber. So the room temperature was used for the SPME experiments.

Results of MCC show that in the positive mode, OV1 cannot separate MeSA peak, partial separation is achieved using OV5 and OV20, while with OV17 complete separation is achieved. In the negative polarity, complete separation was achieved for all the MCCs columns. In the real sample analysis, the negative polarity operation resulted in the suppression of many matrix molecules and thus in the reduction of interferences. Hence, the performance of an MCC depends to some extent on the IMS polarity. Since in the negative polarity, fewer matrix interferences appear, the separation is easier in this polarity.

The limits of detection (LODs) of 0.1 µg mL^{-1} and linear range of 0.25-12 µg mL^{-1} were obtained for measurement of MeSA in a standard solution (H_2O:CH_3OH, 50:50) by the SPME-IMS method with 5 min extraction time using an SPME with a PDMS fiber and OV5 column, in negative mode of IMS. The MeSA content of fresh tomato leaves were determined as 1.5-9.8 µg g-1, 24-96 h after inoculation by ToRSV. Figure 2 show that MeSA content reaches its maximum level for both the upper and lower leaves, 48 h after inoculation, then, its amount decreases.

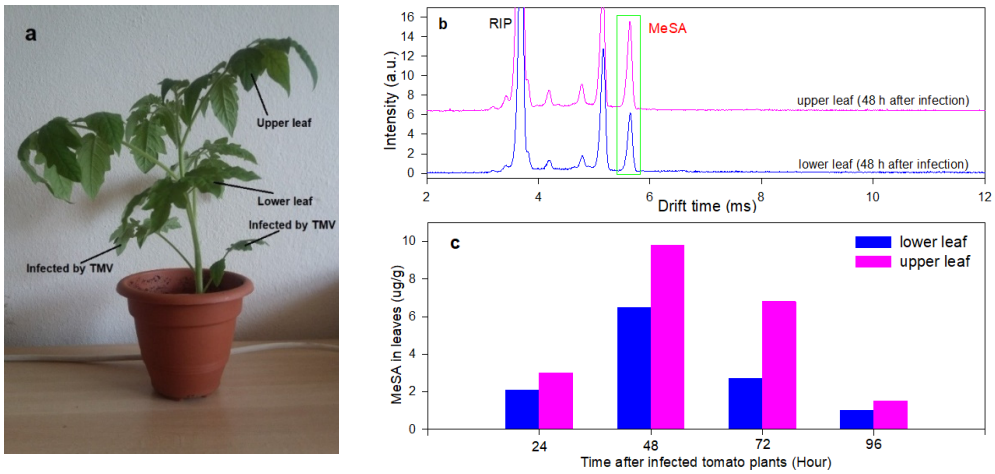

Figure 2. (a) The ToRSV inoculated, lower and upper leaves in a typical tomato plant. (b) The MCC-separated IMS spectra obtained 48 h after inoculation by ToRSV. (c) The measured MeSA content of upper and lower leaves 24 to 96 hours after inoculation.

References

[1] Li, J.; Li, C.; Smith, M. Hormone Metabolism and Signaling in Plants. 1st Ed.; Academic Press, Elsevier Ltd, 2017.

[2] Weyers, J. D. B.; Paterson, N. W. Plant Hormones and the Control of Physiological Processes. New Phytol. 2002, 152, 375-407.

[3] Shulaev, V.; Silverman, P.; Raskin, l. Airborne Signalling by Methyl Salicylate in Plant Pathogen Resistance. Nature 1997, 385, 718-721.

[4] Deng, C.; Zhang, X.; Zhu, W.; Qian, J. Gas Chromatography-Mass Spectrometry with Solid-Phase microextraction method for determination of methyl salicylate and other volatile compounds in leaves of Lycopersicon Esculentum. Anal. Bioanal. Chem. 2004, 378, 518–522.

[5] Sihelská, N.; Vozárová, Z.; Predajňa, L.; Šoltys, K.; Hudcovicová, M.; Mihálik, D.; Kraic, J.; Mrkvová, M.; Kúdela, O.; Glasa, M. Experimental Infection of Different Tomato Genotypes with Tomato mosaic virus Led to a Low Viral Population Heterogeneity in the Capsid Protein EncodingRegion. Plant Pathol. J.2017, 33, 508-513.

PLASMA ASSISTED POLYMER BIOFUNCTIONALIZATION

Marián Lehocký[1,2], Kateřina Štěpánková[2], Miran Mozetič[3]

[1]*Faculty of Technology, Tomas Bata University in Zlín, Vavreckova 275, 76001 Zlin, Czech Republic*
[2]*Centre of Polymer Systems, University Institute, Tomas Bata University in Zlin, Nam. T.G.M. 5555, 76001 Zlin, Czech Republic*
[3]*Department of Surface Engineering, Jozef Stefan Institute, Jamova Cesta 39, 1000 Ljubljana, Slovenia*
E-mail: lehocky@post.cz

In this work, the plasma discharge was selected for surface activation of polymer substrates as a first operation in the multistep approach. After surface modification the monomer was grafted onto the surface to create polymer brush structure via radical "surface from" reaction in gaseous or liquid phase. The last step is connected with the anchoring of the active antibacterial species into the surface structure.

1. A multistep process for polymer biofunctionalization

The direct immobilization of biomolecules onto polymeric surface is difficult and surface pre-activation, followed by a multistep procedure is necessary. Several modification methods are commonly used to modify the polymer surface. One of the most frequent consists in an immersion in the strong acid solution. Nevertheless, such wet chemical methods are technologically complicated and environmentally unfriendly especially because hazardous chemical substances are often used. Recently, a plasma treatment is a preferred procedure considered as a progressive technique for polymer surface modification without the use of aggressive chemicals. Moreover, the plasma treatment enables surface modifications without changing the bulk properties of treated material. The low-temperature plasma belongs to a clean, dry, eco-friendly method of the surface modification and it is often used in various applications, such as in automotive, electronic, aeronautic, textile, optical and paper industry. The main effect of the low-temperature plasma application consists in an increase of a surface free energy as a result of the incorporation of polar functional groups to the treated surface making the surface of polymers more hydrophilic.[1,2] The reactions produced by plasma at polymer surfaces are due to various plasma components such as electrons, ions, radicals, metastables, as well as photons of various wavelength. In practice, plasma can modify the surface chemistry of polymers by incorporating various functional groups, for example, hydroxyl, carboxyl, carbonyl, and peroxide in case of using air as a carrier gas. Incorporation of such functional groups onto polymer surfaces allows for efficient conjugation with further reagents. In addition, plasma induced free radical polymerization is a useful technique for acrylic acid grafting (AAc) onto the surface of several polymeric substrates. Nevertheless, several other monomers can be used and will be discussed in this contribution.

The multistep approach consists in several operations. Firstly, the grafting was initiated by a low-temperature plasma treatment of polymeric substrate. Immediately after the plasma treatment, the samples were subjected to the reaction with reactive monomers in order to create grafted polymer brush. Such a polymer brush is consequently capable to adequately interact with active biomolecule. The scheme is shown below in Fig. 1.

Active biomolecule is chosen according to the final application. The most of applications are targeted to antibacterial or anticoagulant properties. However, accelerated wound treatment approaches are also applications where surfaces of this kind can be applied, what will be shown in real systems and their interaction with fibroblasts or keratinocytes cell systems.

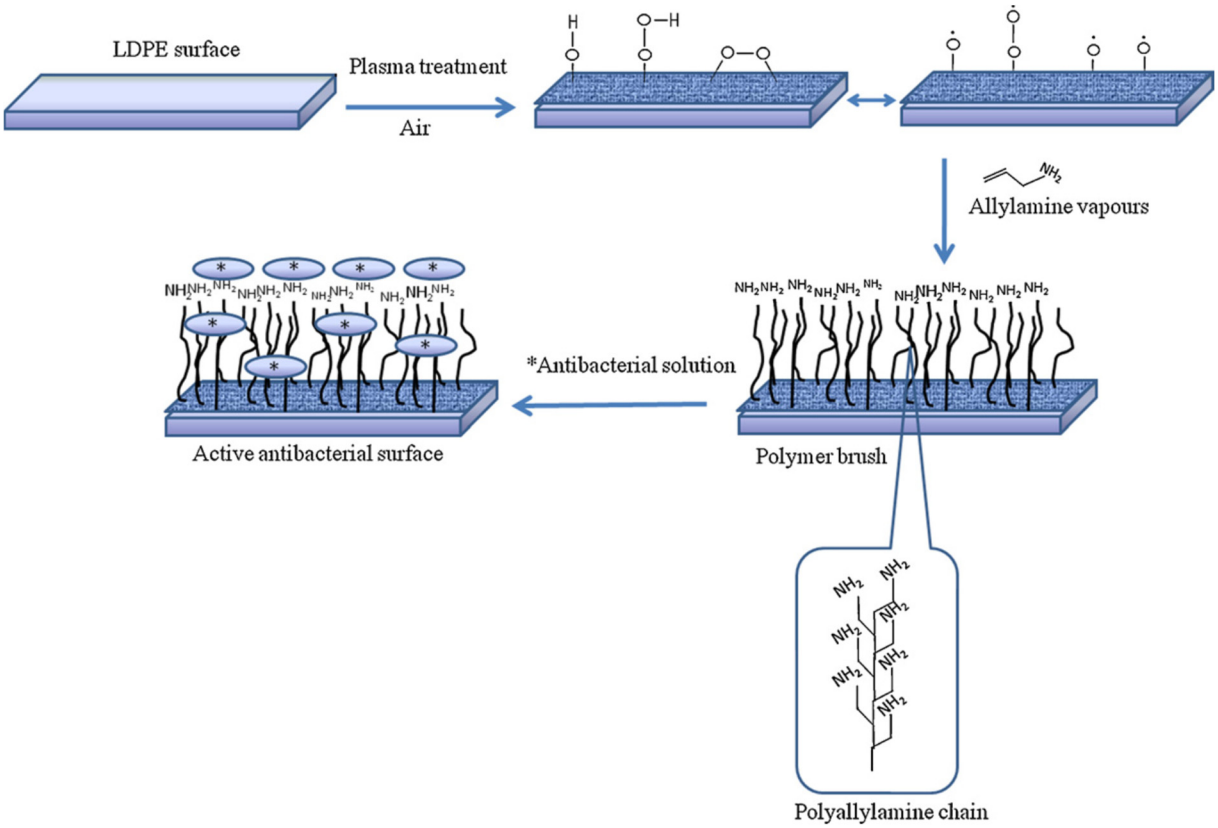

Fig. 1. Scheme of multistep physico-chemical plasma-initiated procedure.

2. References

[1] Desmet T, Morent R, Geyter ND, Leys C, Schacht E, Dubruel P. Nonthermal plasma technology as a versatile strategy for polymeric biomaterials surface modification: A review. Biomacromolecules 2009;10:2351–2378.

[2] Mozetič M, Primc G, Vesel A, Zaplotnik R, Modic M, Junkar I, Recek N, Klanjsek-Gunde M, Guhy L, Sunkara MK, Assensio MC, Milosevic´ S, Lehocky M, Sedlarik V, Gorjanc M, Kutasi K, Stana Kleinschek K. Application of extremely non-equilibrium plasmas in the processing of nano and biomedical materials. Plasma Sources Sci Technol 2015; 24:15–26.

DIAGNOSTIC CHALLENGES IN ATMOSPHERIC PRESSURE PLASMAS FOR PLASMA CATALYSIS

Judith Golda[1], David Steuer[1], Steffen Schüttler[1], Robin Labenski[1], Henrik van Impel[1], Maike Kai[1], Lara Boeddinghaus[1], Volker Schulz-von der Gathen[2], Marc Böke[2]

[1]*Plasma Interface Physics, Ruhr-University Bochum*
[1]*Reactive Plasmas, Ruhr-University Bochum*
E-mail: judith.golda@rub.de

The diagnostics of atmospheric pressure plasmas for use in plasma catalysis is challenging due to the specific reactor designs. Here, we give insights into the diagnostic challenges of plasmas for catalysis as well as possible approaches to overcome them.

1. Introduction

A central challenge of our time is the energy transition from fossil energy sources to renewable ones. Plasma catalysis is one of the promising techniques that has been proposed to contribute to this transition. Research shows that synergies between classical catalysis and plasma processes can be obtained. However, the underlying mechanisms are hard to entangle as typical reactor designs for plasma catalysis are packed bed reactors. While advantageous for industrial processes, the diagnostics of these reactors is challenging. Here, we give insights into the diagnostic challenges of plasmas for catalysis as well as possible approaches to overcome them.

2. Diagnostic challenges

We will discuss alternative reactor designs for fundamental studies [1,2] and give an overview of global and local diagnostic techniques: Current-voltage characteristics for dissipated plasma power and an estimation of electron densities [3], emission-based techniques for reactive species densities such as atomic oxygen [4] or electric fields [5].

As an example, Fig. 1 shows spatially and temporally resolved profiles of a micrometre-sized cavity in an surface dielectric barrier discharge operated in a helium/oxygen mixture which were obtained using an advanced actinometry approach.

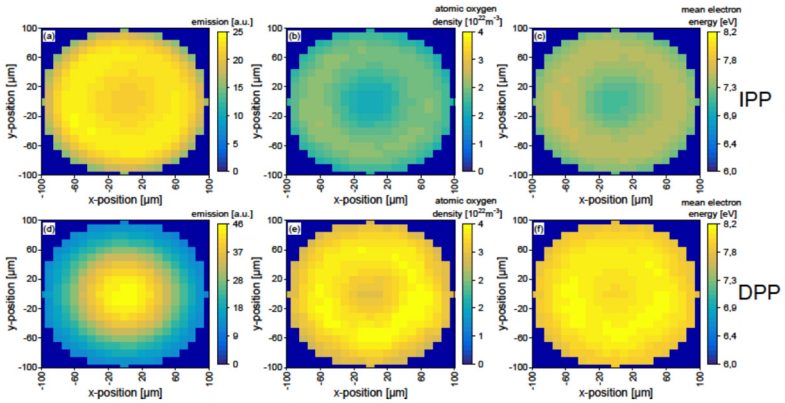

Fig. 1. Emission profiles (a,d), electron density (b,e) and mean electron energy (c,f) in a micro cavity of a dielectric barrier discharge obtained using state-enhanced actinometry in the increasing (upper row) and decreasing (lower row) voltage half-phase of the excitation cycle. [4]

3. References

[1] Stewig C et al. 2020 *J. Phys. D: Appl. Phys.* **53** 125205.
[2] Dzikowski S et al. 2020 *Plasma Sources Sci. Technol.* **29** 035028.
[3] Golda J et al. 2049 *Plasma Sources Sci. Technol.* **28** 095023.
[4] Steuer S et al. 2022 *submitted to Plasma Sources Sci. Technol.*
[5] Dzikowski S et al.2022 *Plasma Sources Sci. Technol.* **31** 065014.

LABOATORY VERSION OF THE ORBITRAP MASS ANALYZER WITH SEVERAL TYPES OF ION SOURCES

HANKA - SPACE INSTRUMENT

Ján Žabka[1], Miroslav Polášek[1], Ylja Zymak[1], Michal Lacko[1], Barnabé Cherville[1], Juraj Jašík[1], Nikola Sixtová[1]

[1]*J. Heyrovský Institute of Physical Chemistry of the CAS, Dolejškova 3, Prague, Czech Republic*
E-mail: jan.zabka@jh-inst.cas.cz

Application of mass spectrometry for asteroid exploration has recently become a hot topic. It is interesting both in orbit and on the asteroid. It can be used for the analysis of space dust, micrometeorites and particles from larger objects.

For the Czech ***SLAVIA*** satellite project was designed the ***HANKA*** (***H***motnostný ***AN***alyzér pre ***K***ozmické ***A***plikace) space instrument - a high-resolution Orbitrap-based electrostatic ion trap mass analyser. The instrument is based on a commercial mass analyser [1] established in biology and medicine research, the so-called Orbitrap™ and the space CosmOrbitrap prototype (developed by LPC2E Orleans [2]). ***HANKA*** will bring this new technology into space to combine a small CubeSat space version of this ion trap analyzer, with an innovative in-situ hypervelocity impact ionization source for micrometeoroids.

A laboratory version of this instrument (***CIARA***) is currently under construction, where ions can be generated by three different methods:

1. Photons with molecules in the liquid phase (coupled with experiment ***LILBID*** (Laser Induced Liquid Bead Ion Desorption)
2. Electrons with molecules in the gas phase (***EI*** source)
3. Photons with solid-phase molecules (***MALDI*** or Laser Ablation)

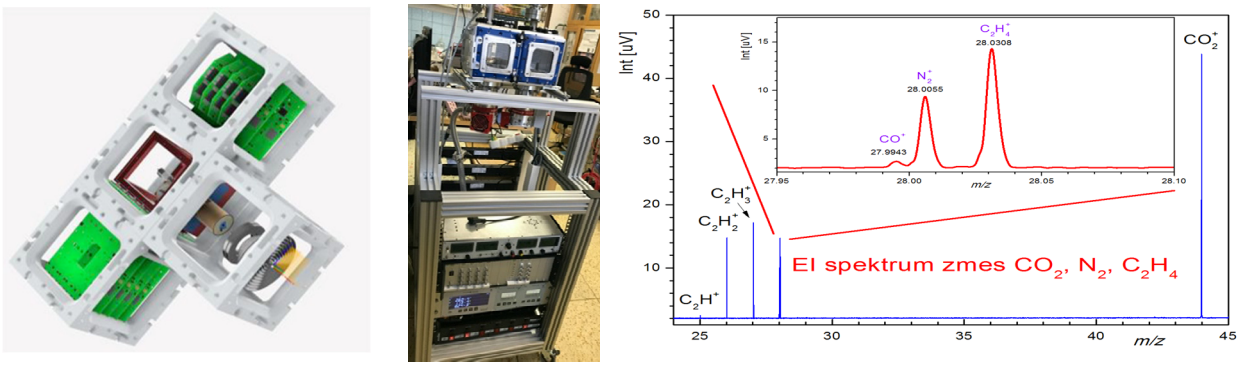

Fig. 1. ***HANKA*** - proposal instrument, laboratory prototyp, preliminary data from EI source

Based on the results obtained on the laboratory prototype, a miniature version of the high-resolution space mass spectrometer - ***HANKA*** - will be constructed.

References

[1] Makarov, A.; *Anal. Chem*. **2000,** 72, 1156–1162.
[2] Briois C, Thissen R, Thirkell L, et al.; *Planet Space Sci.* **2016**, 131, 33-45.

FUNDAMENTAL PROCESSES OF ATMOSPHERIC PRESSURE DARK-CURRENT DISCHARGE IONIZATION

Kanako Sekimoto

Yokohama City University, Yokohama, Japan
E-mail: sekimoto@yokohama-cu.ac.jp

A dark-current discharge state created by combining argon flow with a needle electrode in ambient air is described that has an ionization efficiency and mechanism comparable to those of conventional helium direct analysis in real time (DART), without requiring dopants and DART glow discharge. Polar compounds were mainly (de)protonated dominantly in this discharge, indicating that the present dark-current discharge efficiently generates resonance-state argon with an internal energy of ~14 eV.

1. Introduction

Direct analysis in real time mass spectrometry (DART-MS) was first reported by Cody et al. in 2005 [1]. It is a versatile technique that operates in open air, allowing rapid, non-contact analysis of solid, liquid and gaseous materials without any pre-treatment of samples. In common DART, excited helium (mostly the metastable 2^3S state, He(2^3S)) is generated inside a ceramic flow chamber by an atmospheric pressure glow discharge. The dominant positive-ion formation process is protonation, which results from the Penning ionization of atmospheric water molecules by He(2^3S). He(2^3S) has an internal energy of 19.8 eV, which is higher than the ionization energy of water (12.6 eV). Penning ionization results in the generation of oxonium ion H_3O^+, and its water clusters $H_3O^+(H_2O)_n$, followed by proton transfer to analytes with proton affinities greater than that of water (691 kJ/mol). In negative-ion mode, analyte ionization can be attributed to proton transfer involving superoxide anion water clusters $O_2^-(H_2O)_n$.

Although helium DART has been performed with a great amount of success, helium gas is quite difficult to obtain recently, which makes it hard to sustain its use. Argon is a possible alternative gas for DART. Several research groups have investigated how argon works for DART compared to helium [2-4]. Excited argon stably exists in discharges (including DART glow discharge) in metastable states, such as the $^3P_2$ and $^3P_0$ states, with internal energies of 11.6 and 11.7 eV, respectively [3]. These energies are lower than the ionization energy of H_2O, which results in the formation of fewer $H_3O^+(H_2O)_n$ ions and give rise to quite low analyte ionization efficiency in argon DART [3]. Thus, dopant-assisted protonation based on atmospheric pressure photoionization has been used for the effective operation of argon DART [3,4].

Herein, a novel argon discharge ionization technique under atmospheric pressure is reported in which the analyte ionization efficiency and mechanism are comparable to those of conventional helium DART.

2. Results and Discussion

The present discharge system was easily established by modifying the conventional DART source: (1) a needle, whose tip end was formed into a hyperboloid of revolution, was placed in the sampling area, (2) heated ground state argon was flowed through the sampling area and (3) low DC voltage was applied to this needle. Notably, the use of dopants and a DART glow discharge were not required. The resulting discharge state in the sampling area is referred to as a "dark current discharge (DCD)", a very low electric current (0.2~1 micro A) compared to the DART glow discharge. Ar-DCD, i.e., argon excited by DCD, ionized polar compounds such as α-amino acids (A) to (de)protonated molecules $[A\pm H]^{\pm}$, molecular anions A^-, oxygenated (de)protonated molecules $[A\pm H+nO]^{\pm}$, dehydrogenated deprotonated molecules $[A\text{-}2H\text{-}H]^-$, fragment ions $[A\pm H\text{-}F]^{\pm}$ (F: neutral fragment) and negative ion adducts $[A+R]^+$ (R^-: negative background ion). The absolute intensities of the (de)protonated molecules were found to be 1.1-8.1 times higher than those observed using the helium DART technique. In contrast, using Ar-DCD, non-polar compounds (e.g., *n*-alkanes; Alk) were detected as $[Alk+O\text{-}3H]^+$ and $[Alk+2O\text{-}H]^+$ ions via hydride abstraction and oxidation processes. Major background ions observed using Ar-DCD were $H_3O^+(H_2O)_n$, O_2^+, $O_2^-(H_2O)_n$, and CO_3^-, while argon-related ions were not observed. These results indicate that Ar-DCD efficiently generates excited state argon with an internal energy higher than those of well-known metastable states (~11.6 eV), e.g., resonance states such as 5S $^3P_1$ with an internal energy

of 14.1 eV and 5S $^1P_1$ at 14.3 eV. Therefore, this suggests that ionization reactions occurring in the Ar-DCD method can be attributed to the Penning ionization of atmospheric H_2O and O_2 by resonance-state argon, in a similar manner to that in the helium DART method.

3. References

[1] Cody R B, Laramee J A and Durst H D 2005 *Anal. Chem*. **77** 2297.
[2] Dane J A and Cody R B 2010 *Analyst* (Lond.) **135** 696.
[3] Cody R B and Dane A J 2016 *Rapid Commun. Mass Spectrom*. **30** 1181.
[4] Yang H, Wan D, Dong F, Liu Z and Liu S 2013 *Anal. Chem*. **85** 1305.

DEVELOPMENT OF THERMAL PLASMA SOURCES WITH DIODE-RECTIFICATION AND THEIR APPLICATIONS TO NANOMATERIAL FABRICATION

Manabu Tanaka, Ryo Takenaka, Takafumi Okuma, Takayuki Watanabe

Department of Chemical Engineering, Kyushu University, Japan
E-mail: mtanaka@chem-eng.kyushu-u.ac.jp

Innovative thermal plasma generation with high-current switching by diode-rectification has been successfully developed. High-speed visualization of fluctuated temperature field in thermal plasmas was clarified. Feasibility of silicon nanopowder processing by thermal plasma system was investigated. Obtained remarks suggested that the thermal plasma is a promising tool to establish high-throughput material process.

1. Introduction

Innovative thermal plasma sources have been successfully developed on the basis of diode-rectification technique. Thermal plasmas can offer unique advantages such as high temperature, high chemical reactivity, and rapid quenching rate. Industrialization of thermal plasma processing can be realized by further development of thermal plasma sources in terms of the energy efficiency, scaling up, etc. Recent improvement of semiconductor switching device enables to develop innovative thermal plasma sources. Diode-rectified thermal plasma generation will be presented here. First one is a multiphase AC arc (MPA) with bipolar electrode divided through the diode technique, as presented in **Fig. 1**. Another one is generation of planar thermal plasma jet.

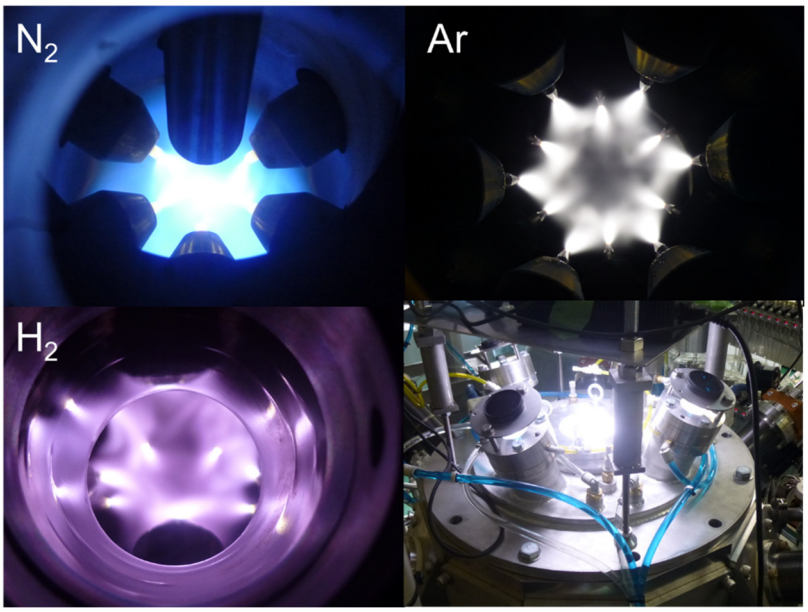

Fig. 1. Representative snapshots of thermal plasmas in diode-rectified AC arc system at different atmospheres.

2. Diode-rectified multiphase AC arc for nanomaterial synthesis

2.1. background

A multiphase AC arc (MPA) is one of the most attractive thermal plasmas. This is because the MPA has following advantages compared with conventional thermal plasma system such as higher energy efficiency, larger plasma volume, lower gas velocity, availability of the scaling-up, and so on [1].

The MPA has been applied to an innovative in-flight glass melting technology due to the above-mentioned advantages [2-4]. In order to achieve the practical use of the MPA in industry, fundamental research in terms of arc stability [5], the temporal and spatial characteristics of the arc discharge [6, 7], and the electrode phenomena [8–10] has been conducted. However, the understanding of the fundamental phenomena in the MPA remains to be explored. In particular, the electrode erosion phenomenon is one of the most important issues to be understood, because it determines the electrode lifetime and purity of the products.

Electrode erosion of the multiphase AC arc was a severe problem. In general, the required properties for the cathode and anode in arc discharge are different. Low work function and high melting point as well as sufficient electrical conductivity are important cathode properties for stable thermionic emission. In contrast, high thermal and electrical conductive material is suitable for the anode as the electron recipient. This originates from larger anode heating due to electron condensation. However, there is a lack of appropriate electrode material, which satisfies the required properties at both the cathodic and anodic periods. In terms of stable thermionic emission, tungsten-based electrodes are commonly used as the AC electrode, although their thermal conductivity is not sufficiently high, resulting in severe erosion in conventional single-phase AC arc [11] or the MPA [12, 13].

The electrode erosion mechanism in the MPA has been investigated based on high-speed visualization. Erosion due to ejection of metal droplets larger than 100 μm in diameter is dominant at the cathodic period [12], while electrode evaporation at the anodic period is the dominant mechanism [13]. The droplet ejection at the cathodic period is basically caused by the electrode melting due to high heat transfer from the arc to the electrode at the anodic period.

To separate each AC electrode into cathode and anode pairs could lead to a breakthrough in the AC electrode erosion issue. Therefore, an innovative diode-rectified MPA (DRMPA) to improve the electrode erosion characteristics has been developed [14].

Table 1 summarizes the comparison between conventional MPA and the innovative DRMPA. Electrode erosion has been successfully degraded in DRMPA. In this paper, feasibility of DRMPA in nanomaterial synthesis process is discussed from the plasma arc temperature measurement and preliminary test of silicon nanomaterial synthesis.

Table 1. Comparison between conventional multiphase AC arc (MPA) and diode-rectified multiphase AC arc (DRMPA) in the case of 6-phase AC arc.

	Electric Circuit	Electrode Configuration	Waveform of arc current per unit electrode	High-speed snapshots of electrode region
Conventional MPA	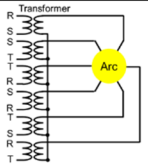	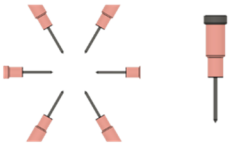	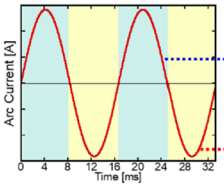	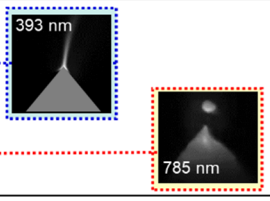
Innovative DRMPA	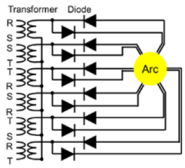	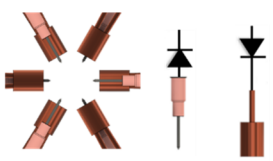	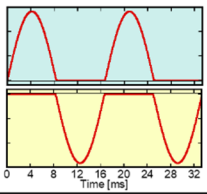	

2.2. Experimental setup

Figure 2 shows the schematic illustration of the experimental setup for thermal plasma generation. Twelve diodes are placed between the electrodes and transformers. Thus, the electrodes were divided into pairs of cathode and anode, namely bipolar electrodes. Representative waveform of arc current in Table 1. Each electrode consists of cathode made of water-cooled 2wt%-La_2O_3 W rod with 6.0 mm in

diameter and anode made of water-cooled Cu. Twelve pairs of electrodes are symmetrically arranged at angle of 30 deg. DRMPA was generated among 12 bipolar electrodes in the chamber which was filled by Ar-N_2 mixture at atmospheric pressure. Nitrogen concentration was changed from 0 to 40vol% to investigate the N_2 addition effect on arc characteristics. Temperature field and its fluctuation under different N_2 concentration was clarified. Measurement method will be explained in Section 2.3.

Feasibility test of the multiphase AC arc for Si nanomaterial synthesis was conducted. Silicon powders with 5 μm in diameter were directly injected into thermal plasma by Ar carrier gas at feeding rates of 10-50 g/min. Arc current for each electrode was adjusted at 200 A, whereas arc power was about 80 kW. Argon was used as main plasma forming gas.

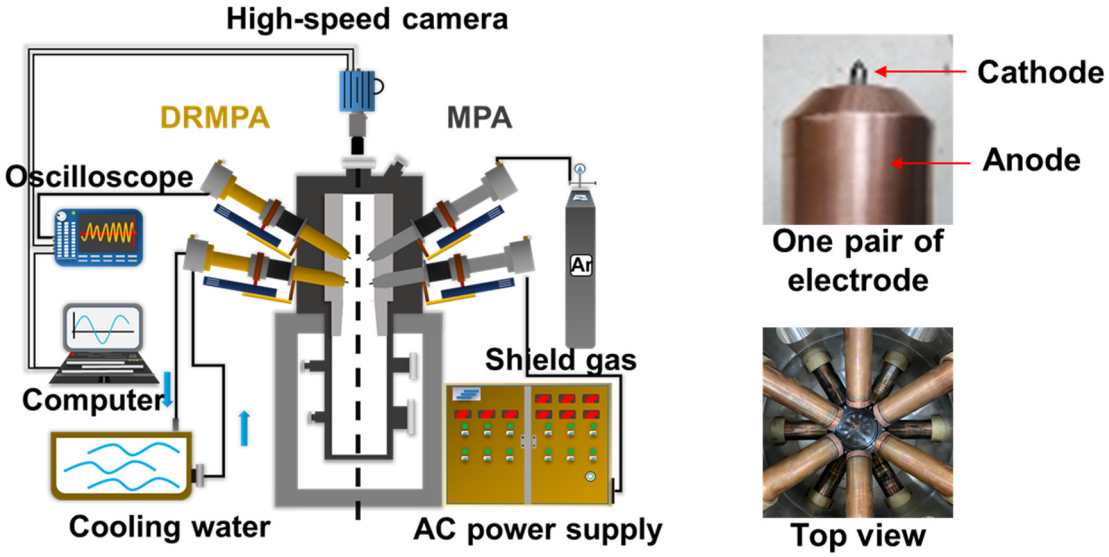

Fig. 2. Experimental setup for diode-rectified 12-phase AC arc generation.

2.3. Measurement method of arc temperature

The arc temperature was measured from emission intensity ratio method assisted by high-speed camera combined with optical band-pass filters under the assumption of local thermal equilibrium. The total arc emission from thermal plasma can be classified into line emission and continuous emission.

Line emission coefficients due to electron transitions of Ar I, Ar II, Ar III, N I, N II, and N III are calculated in temperature range from 5,000 to 30,000 K while no self-absorption is considered due to its low importance in this case. Moreover, continuum emission coefficients due to recombination radiation and Bremsstrahlung radiation were also calculated to evaluate total emission coefficients for two different wavelength ranges of band-pass filters. Two filters with centre wavelengths of 795 nm and 675 nm at 5 nm band-width were selected on the basis of our previous research [15]. **Figure 3** shows examples of the calculated results for 795 nm and 675 nm at 90% Ar-10% N_2 condition. Temperature can be measured from the ratio of total emission coefficient at 795 nm to that at 675 nm because the ratio is a function of temperature.

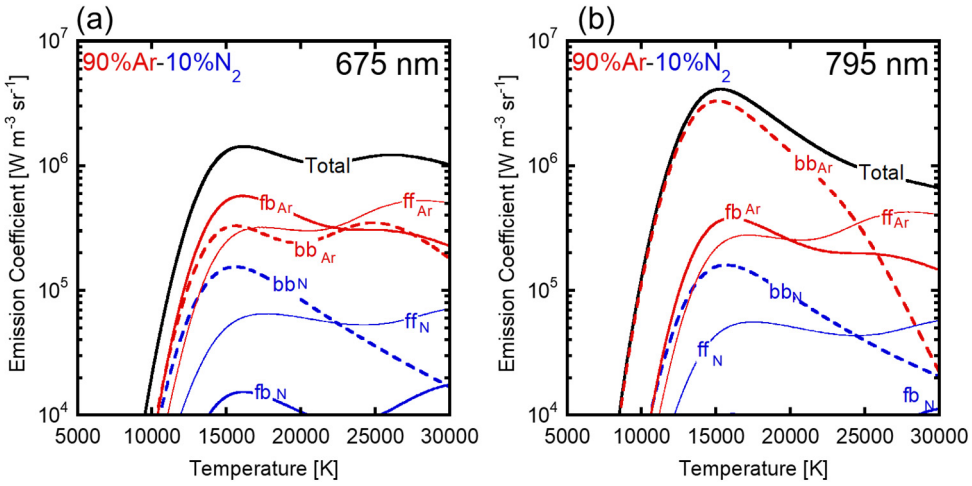

Fig. 3. Total emission coefficients at two different wavelength range; (a) 675±5 nm and (b) 795±5 nm. The expressions of bb, fb, and ff correspond to line emission (bound-bound radiation), continuum due to recombination (free-bound radiation), and Bremsstrahlung emission (free-free radiation), respectively.

A high-speed camera combined with suitable BPFs is used to visualize fluctuated temperature fields. The schematic illustration of high-speed visualization system is shown in **Fig. 4**. Typical frame rate and shutter speed are 5,000fps and 1 μs, respectively.

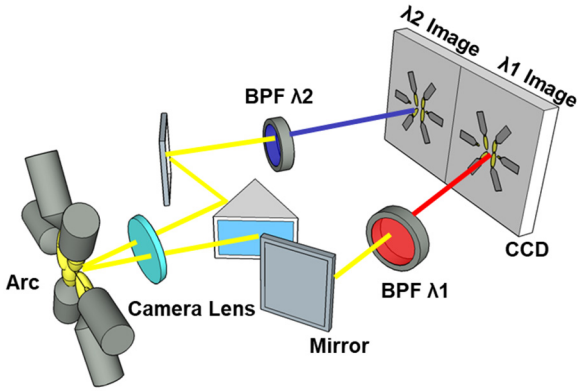

Fig. 4. Schematic illustration of visualization system with band-pass filter optics and high-speed camera.

2.4. Experimental results and discussions

Figure 5 shows the visualized temperature distribution during 10 ms under 10% N_2 condition. Complicated and fluctuated arc can be observed. Temperature near the electrode is higher than other regions. **Figure 6** shows the comparison of the arc temperature distributions in different N_2 concentrations. The arc temperature at the centre is fluctuated in the range from 6,000 to 14,000 K. Higher temperature region than 6.000 K was obviously became larger with an increase of arc current. Addition of N_2 into Ar leads to temperature decrease, while the temperature is still higher than 6,000 K. As a conclusion, the arc temperature in the DRMPA is sufficiently high to melt and/or evaporate the raw material in powder processing.

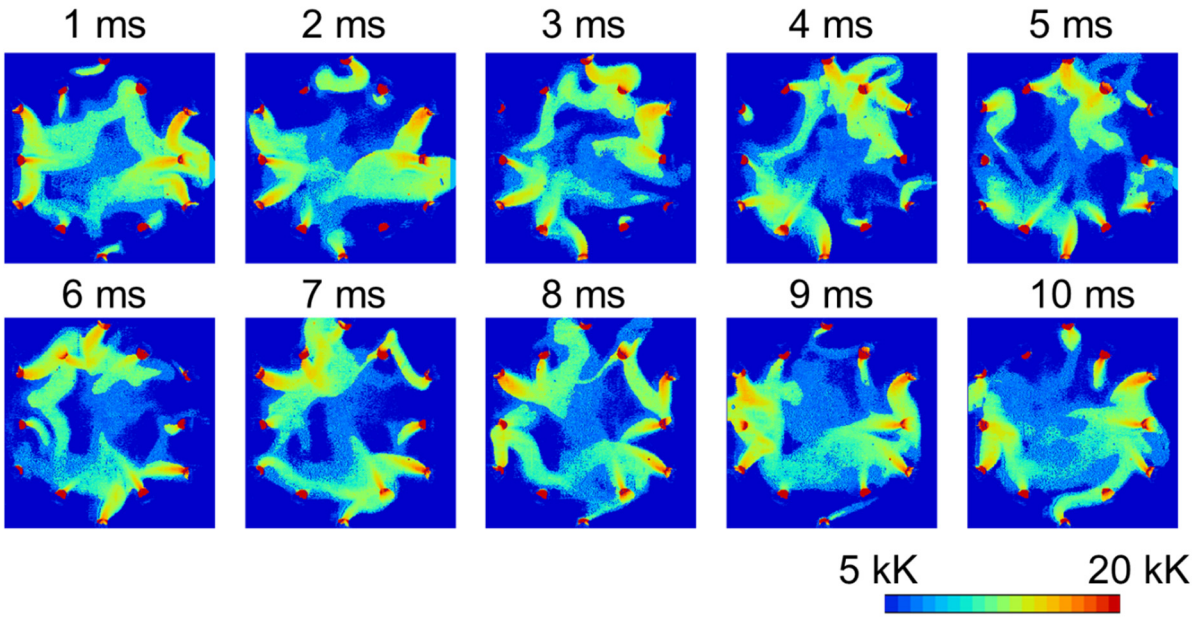

Fig. 5. Representative snapshots of obtained arc temperature distributions during 10 ms. Nitrogen concentration was 10vol%.

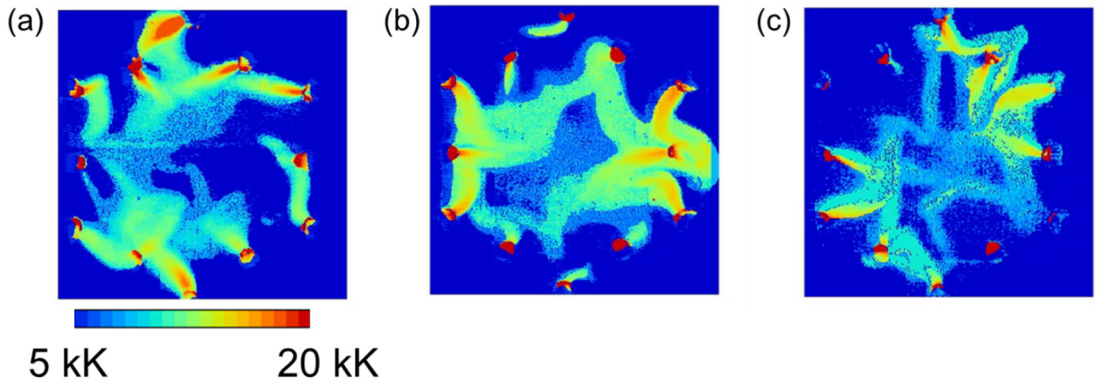

Fig. 6. Representative snapshots of obtained arc temperature distributions at different nitrogen concentrations; (a) 0vol%, (b) 10vol%, and (c) 40vol%.

Silicon nanoparticles were successfully synthesized via thermal plasma method. Representative SEM images and size distribution are summarized in **Fig. 7**. Average particle size was about 80 nm, while sizes are largely distributed.

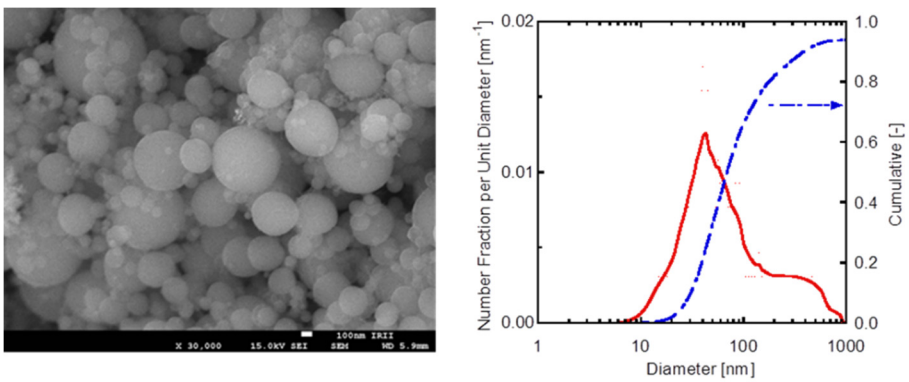

Fig. 7. SEM image of synthesized silicon nanoparticles and their particle size distribution.

3. Diode-rectified AC arc for generation of planar thermal plasma jet

3.1. Background

Generation of planar-shaped thermal plasma jet is one of the most important approaches to expand the applicability of thermal plasmas for materials processing, surface treatment, and waste treatment at high processing rate. A few approaches using radio frequency inductively-coupled plasma [16] or DC arc discharge [17] have achieved enlarged treatment area with plasma jets, although many limitations such as insufficient temperature still remain. Here, an innovative thermal plasma source based on the diode-rectified AC arc has been developed to overcome the afore-mentioned difficulties.

3.2. Experimental setup for planar thermal plasma generation

Schematic of thermal plasma source is shown in **Fig. 8**. Arc discharge was generated using 10 electrodes placed in a linear array. These 10 electrodes were configurated by AC electrodes, diode-rectified electrodes, cathodes, and anodes. Figure 1 shows the schematics of the plasma source. Electrode positioned at locations 1 and 3 have the role of AC electrode, corresponding to negative-positive cycle and positive-negative cycle, respectively. Diode-rectified electrodes are located at 2 and 4. Location 2 has the role of anode, while 4 works as cathode. Planar-shaped thermal plasma jet was successfully generated owing to this unique configuration of electrodes with diode-rectification technique.

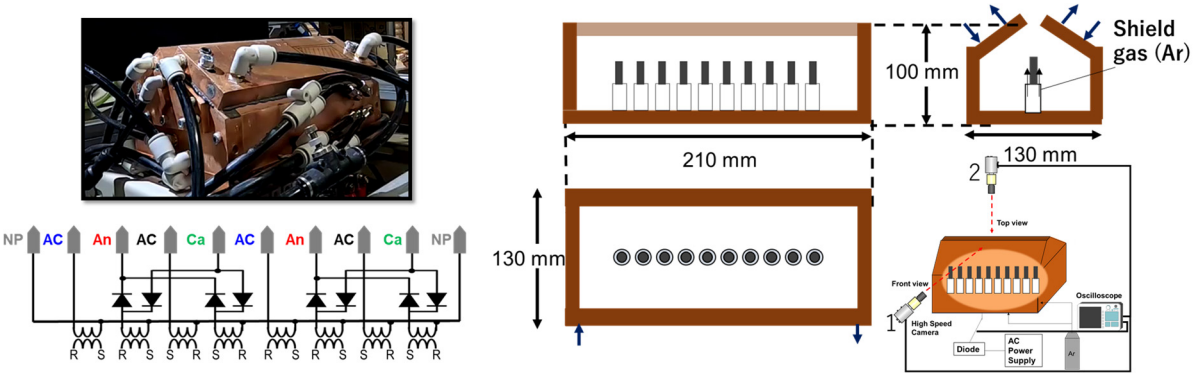

Fig. 8. Experimental setup of planar thermal plasma generation with diode-rectified AC arc system. Schematics from multi-views and a photograph.

3.3. Experimental results and discussions

Representative snapshots of the plasma jet is presented in **Fig. 9**. Corresponding waveforms of current and voltage are also shown as Fig. 9(a). The plasma jet existence probability was analysed from the high-speed images for 5 AC periods. This existence probability was defined as the ratio of the time during which the plasma jet existed to total time. Therefore, “1” indicated that the plasma jet always existed and “0” does not exist. Analysed image shown in **Fig. 10** indicates that time-averaged existence region of plasma jet exhibits planar-like shape as originally designed. Obtained remarks suggests that the plasma jet is a promising plasma source and might replace the conventional DC arc in many applications.

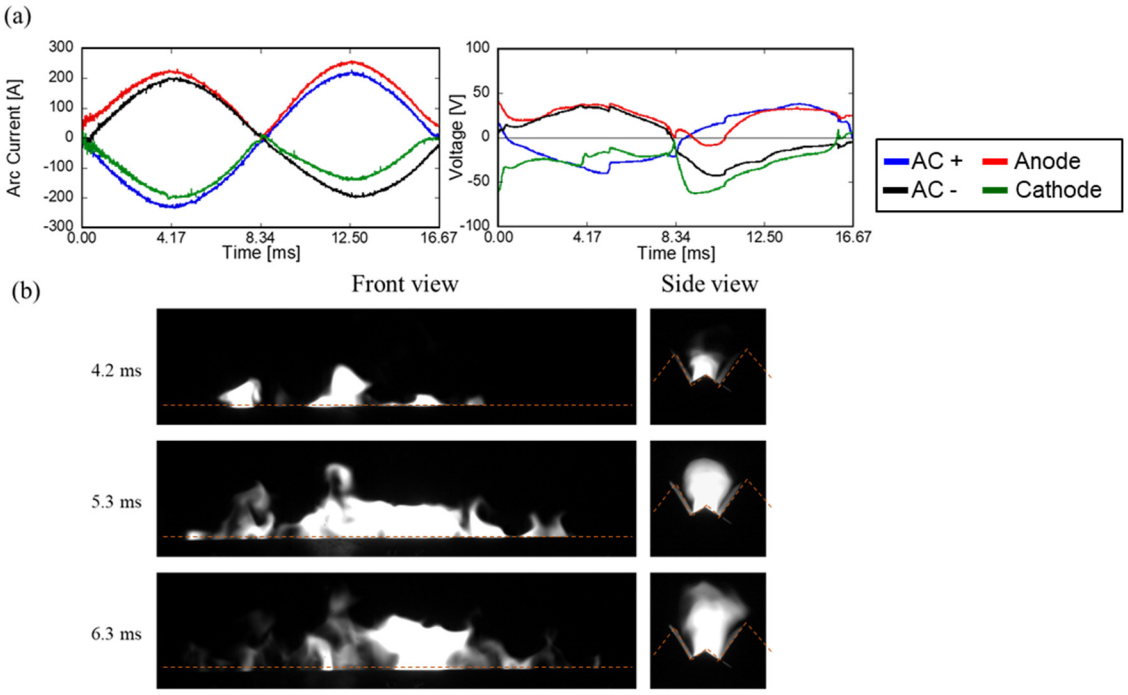

Fig. 9. (a)Waveform of arc current and voltage and (b) synchronized high-speed snapshots.

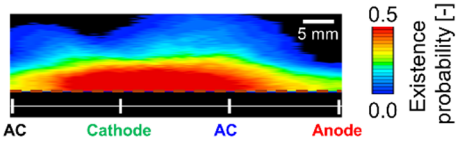

Fig. 10. Representative existence probability of plasma jet during 5 AC period.

4. Conclusion

Innovative thermal plasma generation based on diode-rectification technique has been successfully developed. Fundamental phenomena and feasibility in material processing were investigated. Obtained remarks suggests that thermal plasma based on diode-rectification is a promising plasma source in material processing at high throughput.

Acknowledgments

The paper is based on the results obtained from a project, JPNP20004, subsidized by the New Energy and Industrial Technology Development Organization (NEDO). supported by Supporting Industry Project, Japan. The present research was partially supported by Supporting Industry Project, Japan. This is also supported by JSPS KAKENHI Grant Number JP19K03808 and JP22K03587. The study was partially supported by Grant-in-Aid for "Initiative for Realizing Diversity in the Research Environment" through the "Diversity and Super Global Training Program for Female and Young Faculty (SENTAN-Q)", Kyushu University from MEXT. The authors thank to Mr. Naoki Terada and Mr. Hideki Touzaki, Tamada Industry, Japan, for their help to fabricate the diode-rectified multiphase AC arc system.

5. References

[1] Matsuura T et al., 2007 *Thin Solid Films* **515** 4240.
[2] Watanabe T et al., 2010 *Pure Appl. Chem.* **82** 1337.
[3] Liu Y et al., 2012 *J. Thermal Spray Technol.* **21** 863.
[4] Liu Y et al., 2014 *Int. J. Appl. Glass* **5** 443.
[5] Tanaka M et al., 2011 *Curr. Appl. Phys.* **11** S35.
[6] Tanaka M et al., 2011 *IEEE Trans. Plasma Sci.* **39** 2904.

[7] Liu Y et al., 2012 *J. Phys.: Conf. Ser.* **406** 012015.
[8] Tanaka M et al., 2013 *J. Phys.: Conf. Ser.* **441** 012022.
[9] Tanaka M et al., 2013 *J. Fluid Sci. Technol.* **8** 160.
[10] Watanabe T et al., 2014 *Plasma Chem. Plasma Process* **34** 443.
[11] Hinata T et al., 1988 *J. Light Met. Weld.* **26** 97.
[12] Hashizume T et al., 2015 *Quert. J. Jpn. Weld. Soc.* **33** 44s.
[13] Tanaka M et al., 2016 *Jpn. J. Appl. Phys.* **55** 07LC01.
[14] Tanaka M et al., 2017 *J. Phys. D: Appl. Phys.* **50** 465604.
[15] Okuma T et al., 2018 *IEEE Trans. Plasma Sci.* **47** 32.
[16] Tanaka Y et al., 2017 Plasma Chem. Plasma Process **37** 857.
[17] Segawa K et al., 2020 *Jpn. J. Appl. Phys.* **59** SJJF01.

HOT TOPICS

SPARK CHEMISTRY: CAN WE CONTROL THE ENERGY OF THE ELECTRONS?

Tom A Field,[1] Leonidas Asimakoulas,[1] Ciara Harkin,[1] Mario Janda[2], Karol Hensel[2], Zdenko Machala,[2]

[1]*Centre for Light Matter Interactions, School of Maths and Physics, Queen's University Belfast, BT71NN, Northern Ireland, U.K.*

[2]*Division of Environmental Physics, Department of Astronomy, Earth Physics and Meteorology, Faculty of Mathematics, Physics and Informatics, Comenius University in Bratislava, Mlynska dolina, 84248 Bratislava, Slovakia*

E-mail: t.field@qub.ac.uk

It appears that the energy distribution and density of electrons can be influenced in a self-pulsing spark discharge by a simple modification to the driving circuit. This may be a strategy to control the chemistry in the discharge.

Self-pulsing transient spark discharges can be generated with simple driving circuits with a high voltage DC power supply, but without any pulsing electronics. In the circuit a capacitor is charged 'slowly' up to a high voltage before it 'rapidly' discharges through a spark gap. The typical time scale for charging is in the region of 100 μs to 1 ms, but the typical time scale for the discharge is 10 ns to 1 μs.

A simple modification to the driving circuit will be described. UV/Visible spectra indicate that the distribution of atomic excited states changes in the discharge due to this modification. The change in excited state populations suggest that the energies/density of electrons may be affected by the modification and suggest that this may be a route to exerting some control over the chemistry in the discharge.

USAGE OF MICROWAVE PLASMA TORCH FOR TREATMENT OF DIFFERENT TYPES OF MATERIALS

Michal Hlína[1], Tomáš Mates[2], Dominik Kralik[1], Kateřina Märzová[1], Alan Mašláni[1], Jakub Pilař[1], Jafar Fathi[1], Michal Jeremiáš[1]

[1]*Institute of Plasma Physics of the Czech Academy of Sciences, U Slovanky 2525/1a, 182 00 Prague 8*
[2]*Institute of Physics of the Czech Academy of Sciences, Cukrovarnická 10/112, 162 00, Prague 6*
E-mail: hlina@ipp.cas.cz

A microwave plasma torch (up to 100 kW input power) was used as the source of energy in the reactor where different types of materials (polypropylene, solid recovered fuel and simulated hospital waste) were fed to. Air was used as a working gas for the torch. The analysis of gas products was performed.

1. Introduction

Plasma gasification of materials with high hydrocarbon content has been studied for decades [1]. Municipal solid wastes, sludges, hazardous and industrial wastes are typical materials convenient for plasma gasification, because high plasma temperature limits the production of unwanted species such as dioxins, toxic residues or tars in produced gas and higher price of the plasma facilities is justified by the character of input materials.
Thermal plasma torches suitable for gasification can be divided into two groups: electric arc discharge and radio-frequency/microwave induction torches. The radio-frequency/microwave induction torches have the advantage in not having electrodes, which corrode and lower their lifetimes [2].

2. Microwave plasma torch

The microwave plasma torch used during experiment was supplied by company Muegge (Germany). The torch consists of four major components which are: an AC power supply, a water cooling system, a 2450MHz microwave generator and a 3-stub tuner. Maximum input power of 100 kW (with total output power of 75 kW) was adjusted during some of described experiments and air was used as a working gas.

3. Experimental

The plasma torch, together with the inlet of treated material, is mounted at the top of a reactor with ceramic thermal insulation of 400 mm thickness. The inner volume of the reactor is 220 L. Produced gas flows into a quenching chamber, where temperature is reduced to 300°C by a water spray, then enters a filter chamber, a water ejector for controlling the underpressure in the reactor and subsequently is burnt in the flare with a propane butane stabilizing burner. Temperature is monitored by thermocouples and ranged between 1000°C and 1200°C during experiments. A sampling probe for composition measurements was located at the reactor output and was cooled down by passage through the quenching chamber. A quadrupole mass spectrometer Pfeiffer Vacuum Omnistar GSD 301 with direct inlet and Matrix MG01 spectrometer Bruker Optik GmbH were used as gas analyzers. A freezing unit had to be placed into the sampling line to avoid water condensation.
Three different types of material were treated: polypropylene (PP), simulated hospital waste (SHW) and solid recovered fuel (SRF) with main elemental composition CH_2, $C_{5.5}H_{10}O$ and $C_{1.9}H_3O$, respectively. SHW and SRF contain also small amounts of N, S and Cl.

4. Results

The analysis of produced gas and basic parameters of experiment are summarized in Tab. 1. Due to the fact that air was used as a working gas for the torch, high concentration of N_2 (from 58 to 83 vol. %) can be seen. Produced gas is diluted by Ar as well, because Ar was added to the process and used as an internal standard for the calculation of the flow rate of produced gas.

Tab. 1. Experimental conditions and measured concentrations of main gas components (P of MW stands for the input power of the microwave plasma torch).

	mass rate kg/h	air slm	Ar slm	P of MW kW	CO	CO_2	Ar	O_2 vol. %	CH_4	H_2	N_2
PP	6	933	0	20	2.1	12.8	1.1	0.0	0.4	0.2	83.1
PP	15	1016	200	40	13.1	4.3	7.1	0.0	0.3	16.5	58.7
SHW	0	900	80	40	0.0	0.6	10.1	17.0	0.0	0.0	71.4
SHW	4.3	900	80	40	0.0	5.5	10.5	11.2	0.0	0.0	72.0
SHW	8.7	900	80	40	0.0	8.0	11.0	8.1	0.0	0.0	72.1
SHW	13.0	900	80	40	1.5	14.2	11.6	0.1	0.1	0.6	71.2
SHW	17.3	900	80	40	3.4	11.8	8.0	3.2	0.5	3.6	69.4
SHW	21.7	900	80	40	5.0	10.1	7.1	4.4	0.8	5.1	67.3
SRF	6.3	700	100	60	0.0	4.5	10.5	12.0	0.0	0.0	72.1
SRF	13	700	100	60	7.1	13.5	9.5	0.1	0.5	2.7	66.0
SRF	13.8	900	100	40	11.2	9.3	9.4	0.1	0.7	10.8	58.4
SRF	24.5	900	100	40	11.3	8.9	8.9	0.5	0.6	11.5	58.1

It can be seen that with the increasing mass rate of input material the concentrations of CO and H_2 increase as well. Maximum CO_2 concentrations are reached for medium input flow rates, when sufficient amount of O_2 in the reactor is provided, which is in good accordance with the theory. Lower concentrations of C_2H_2 and NOx were detected as well, but they are not presented in Tab. 1.

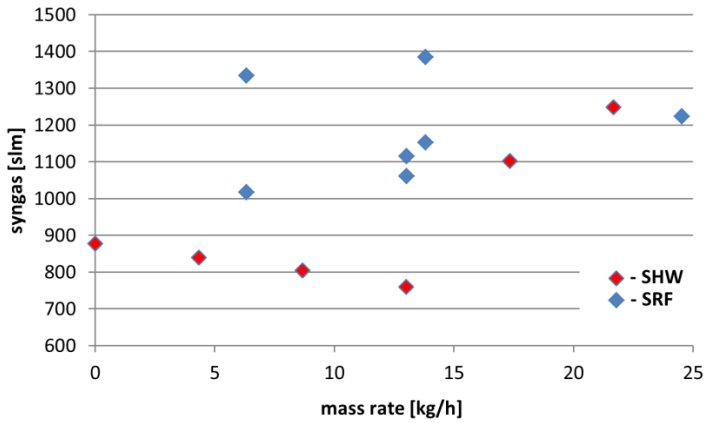

Fig. 1. The dependence of syngas flow rate on input material mass rate.

The dependence of syngas flow rate on the mass rate of treated material is insignificant due to the relatively low concentration of O_2 entering the gasification process. N_2 together with Ar form approximately 80 vol. % of the gas leaving the reactor. Next experiments should be performed with different working gases (H_2O vapour, O_2, CO_2 or their mixtures), what would lead to the production of synthetic gas with more advantageous composition [3].

5. Acknowledgement

The authors gratefully acknowledge the support of the Technology Agency of the Czech Republic [Projects TN02000069] and support of the Academy of Sciences of the Czech Republic [Strategy AV 21 – research program Sustainable Energy].

6. References

[1] Heberlein J and Murphy A B 2008 *J. Phys. D: Appl. Phys.* **41** 5.
[2] Tang Q, Hu Z B, Cui X X, Tao Z C and Tang J 2022 *Appl. Sci.* **12** 13.
[3] Shin D H, Hong Y, Lee S J, Sang J, Kim Y J, Ye J, Cho C H, Ma S H, Chun S M, Lee B J and Uhm H S 2013 *Surf. Coat. Technol.* **228** S520-S523.

TIME-OF-FLIGHT DIFFERENTIAL ELECTRON SCATTERING FROM MOLECULAR TARGETS: BENCHMARK CROSS SECTIONS

Mateusz Zawadzki[1] and Murtadha A. Khakoo[2]

[1]*Department of Electron Collision Physics, Institute of Physics and Applied Computer Science, Faculty of Applied Physics and Mathematics, Gdańsk University of Technology, 80-233 Gdańsk, Poland*
[2]*Department of Physics, California State University, Fullerton, California 92831, USA*

E-mail: mateusz.zawadzki@pg.edu.pl

We report time-of-flight differential cross section (DCS) measurements for the electron impact excitation transition in H_2. In this work, agreement between available theory and experiment is excellent overall, and marks a transition in electron molecule scattering where differential scattering of excitation is found to be in such precise agreement. We also prove that the newly built apparatus can be used for accurate measurement of the mass stopping power for low energy electrons for H_2 for which agreement between theory and experiment is found to be excellent.

1. Introduction

Collisions between electrons and molecules at low energy show unique quantum effects. Therefore electrons can be used as a powerful tool for testing quantum phenomena inside the matter. The scattering signal of electrons on different targets, in different range of incident energies, brings useful information about the quantum nature of processes occurring in electron-matter interaction. Our recent experimental work deals with the interactions of electrons with fundamental molecular targets. The simplest neutral molecule H_2 is the subject of investigation.

2. Differential scattering electron time-of-flight spectrometer

Accurate data for molecular hydrogen dissociation is of crucial importance [1-3]. The great advantage of a recently built time-of-flight (TOF) system is that it is not susceptible to transmission effects and can accurately give inelastic to elastic ratios for (in this case) electron excitation of H_2.

The electron beam was pulsed using an additional thin aperture lens placed between the filament and anode. The typical pulse duration was 2-5 ns. The TOF tube (see Fig. 1) was made compact, but long and able to rotate up to $\theta = 135^{\circ}$. It had an aluminum/titanium body which was coated with sprayed colloidal graphite, with an opening of 2 mm diameter. The TOF tube had four tandem thin molybdenum apertures, placed to subtend the same solid angle to the center of the collision region in an effort to reject secondary electrons. The TOF tube and the e-gun were heated by electrically shielded, biaxial, magnetically free heaters up to 150 $^{\circ}$C. The system was placed in a μ-metal lined chamber with a single vertical Helmholtz coil which was able to reduce the remnant *B* field of the Earth in the laboratory. More detailed description of the spectrometer can be found in [4,5].

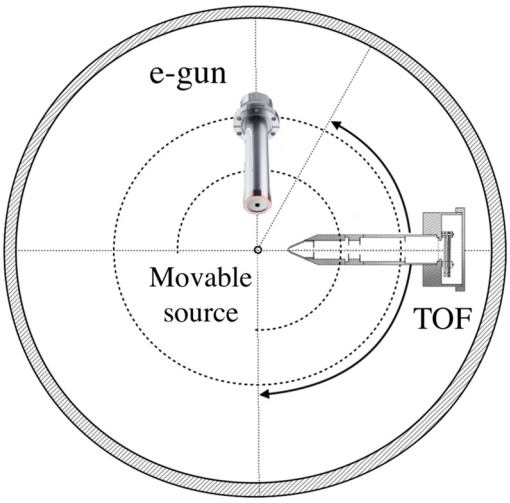

Fig. 1. Top view chamber diagram of the experimental setup. The electron beam is actuated by pulsing a lens placed between the filament and anode using a 0–40-V, 0.5–8-ns pulse generator. The TOF tube is ~24 cm long and 3.3 cm inner diameter) and able to detect electrons from $\theta = 20^{\circ}$ to 135°.

3. Results

The TOF spectrum was obtained by subtracting the background scattering with the gas beam collimator displaced away from the collision region from the signal plus background scattering with the gas beam collimator in place in the collision region. From such spectra we could determine accurate inelastic to elastic ratios (see Fig. 2). By normalizing the TOF spectrum of the $b^3\Sigma_u^+$ state of H_2 to the experimental elastic DCS of Muse *et al.* [6] we were able to determine the absolute differential cross section for this transition.

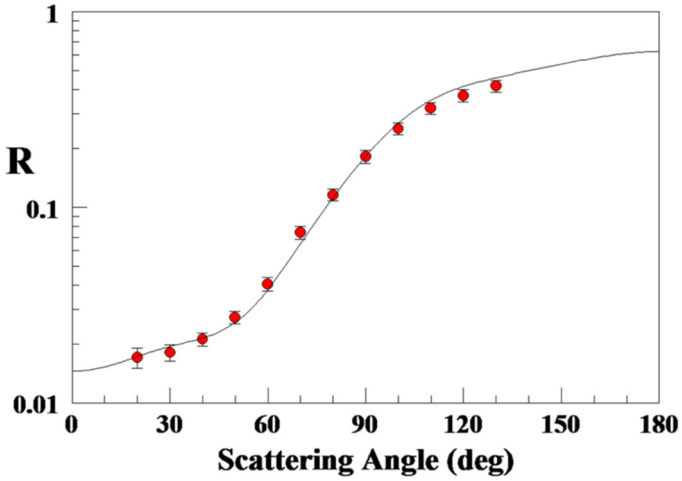

Fig. 2. Inelastic to elastic ratios R at 13.5 eV compared with the available convergent close-coupling (CCC) data (solid line).

The total inelastic DCSs which are obtained from our *R* values and the elastic scattering H_2 DCSs (Fig. 3).

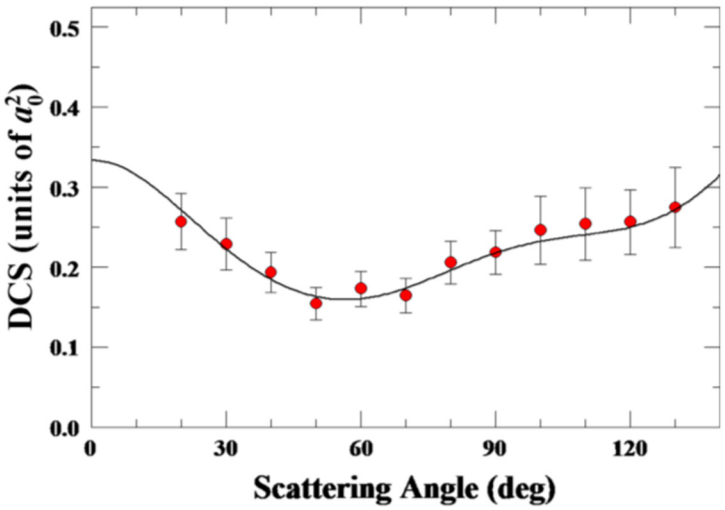

Fig. 3. Selected electron-impact total inelastic scattering (excitation plus ionization) differential cross section values (in atomic units) for H_2 at 14.5 eV.

4. Electron mass stopping power in H_2

The stopping power is of fundamental importance in biomedical dosimetry, radiation physics, chemistry, medicine and biology involving neutrons, protons, X-rays and electrons. Although, the mass stopping powers are widely used in many fields they are not easy to obtain experimentally.

The mass stopping power for low energy electrons traveling in gaseous H_2 is also the subject of the present work. Recent theoretical calculations have provided most of the mass stopping power estimates. The breakthrough CCC model of the Curtin University group [7] has provided accurate electron-H_2 cross sections, which were extended to the calculation of mass stopping powers for electrons on H_2 [8]. Using a TOF spectrometer we have measured electron scattering spectra and used them to provide experimental mass stopping powers of electrons in H_2 in the low electron energy range where there is no experimental data available [9].

5. References

[1] Boeuf J P, Hagelaar G J M, Sarrailh P, Fubiani G, Kohen N (2011) *Plasma Sources Sci. Technol.* **20**, 015002.
[2] Ju Y and Sun W(2015) Prog. Energy Combust. Sci. **48**, 21 .
[3] Yoshida N (2007) Astrophys. J. **663**, 687.
[4]Zawadzki M, Wright R, Dolmat G, Martin M F, Hargreaves L, Fursa D V, Zammit M C, Scarlett L H, Tapley J K, Savage J S, Bray I, Khakoo M A (2018) *Phys. Rev. A* **97**, 050702(R).
[5]Zawadzki M, Wright R, Dolmat G, Martin M F, Diaz B, Hargreaves L, Coleman D, Fursa D V, Zammit M C, Scarlett L H, Tapley J K, Savage J S, Bray I, Khakoo M A (2018) *Phys. Rev. A* **98**, 062704 .
[6] Muse J, Silva H, Lopes MCA, Khakoo M A (2008) *J. Phys. B: At., Mol. Opt. Phys.* **41**, 095203.
[7] Zammit M C, Savage J S, Fursa DV and Bray I (2016) *Phys. Rev. Lett.* **116**, 233201.
[8] Fursa D V, Zammit M C, Threlfall R L, Savage J S, Bray I (2017) *Phys Rev. A* **96**, 022709.
[9] Zawadzki M and Khakoo M A (2019) *Phys. Rev. A* **99**, 042703.

EFFECT OF ELECTRON BEAM REMELTING OF PLASMA SPRAYED NI-CR-RE COATINGS

Piotr ŚLIWIŃSKI[1], Marek Stanisław WĘGLOWSKI[1], Stanisław DYMEK[2], Izabela KALEMBA-REC[2], Mateusz KOPYŚCIAŃSKI[2], Adriana WRONA[3], Marcin LIS[3]

[1]Łukasiewicz – Institute of Welding, Błogosławionego Czesława 16-18 St., 44-100 Gliwice, Poland, EU

[2]AGH, Faculty of Metals Engineering and Industrial Computer Science, Czarnowiejska 66 St., 30-059 Kraków, Poland, EU

[3]Łukasiewicz - Institute of Non-Ferrous Metals, Generała Józefa Sowińskiego 5 St., 44-121 Gliwice, Poland, EU

E-mail: piotr.sliwinski@is.lukasiewicz.gov.pl

Atmospheric plasma spraying (APS) involves feeding a powdered input material into a plasma jet to melt and accelerate the particles and spray them onto a substrate. Unfortunately, very often coatings produced by thermal spraying technologies are characterized by the presence of pores and micro-cracks. To eliminate these defects, electron beam remelting can be used to improve the uniformity of plasma-sprayed coatings. In the present study, Ni-Cr coatings with Re addition, produced by plasma spraying on 316Ti stainless steel substrate were remelted by oscillating electron beam and the effects were studied. The structure and chemical composition of plasma-sprayed and electron-beam remelted coatings were analyzed by scanning electron microscopy (SEM) and energy dispersive spectroscopy (EDS). The results show that the electron beam melted coating is almost pore-free, and moreover, the chemical composition of the coatings becomes homogeneous.

1. INTRODUCTION

Due to its unique properties, rhenium has found use in industry as a refractory metal. It is often used as an alloying additive. Rhenium addition in nickel- or cobalt-based superalloys increases their creep strength. For this reason, it is also used to produce coatings or reinforced composites. Rhenium has very high tensile and creep strength over a wide range of temperatures. It has the third highest melting point and the second highest boiling point of all stable elements [1-4].

In order to obtain coatings with the desired chemical composition, a thermal spraying process such as atmospheric plasma spraying (APS) can be used. This technology makes it possible to produce layers of the desired thickness even on parts of complex shape. However, a significant disadvantage of plasma-sprayed layers is the lack of homogeneity and compactness in their structure, caused by the presence of pores and cracks. The porosity of these layers can be reduced by electron beam remelting [5-10].

This paper presents the effects of electron beam remelting processes for atmospheric plasma sprayed coatings with different rhenium content depending on different process parameters.

2. EXPERIMENTAL PROCEDURE

The coating materials used in this procedure were Ni20%Cr + 50%Re, Ni20%Cr + 40%Re, Ni20%Cr + 30%Re alloys. The procedure consisted of 3 stages. The first stage was the manufacturing of powders at the Łukasiewicz - Institute of Non-Ferrous Metals. The technique used for production of these powders consisted of a thermo-chemical treatment for producing metallic rhenium from NH4ReO4 (ammonium perrhenate) directly on the surface of modified commercial Ni20%Cr powders.

The second stage was the plasma spraying of powders with different rhenium content on an austenitic stainless steel (316Ti) substrate. The surface of the substrate was prepared by abrasive

blasting using corundum abrasive. The plasma spraying parameters were as following: arc voltage 69 V, current 530 A, plasma gas flow rate (H2) 9 l/min, shielding gas flow rate (Ar) 54 l/min, transport gas flow rate (Ar): 5 l/min, travelling speed 400 mm/s and spraying distance of 140 mm.

The last stage was the electron beam remelting that was carried out using a CVE EB756 Electron beam welding machine model XW150:30. 9 samples were made for each rhenium content with different process parameters (the parameters changed were the beam current and sample movement speed). Electron beam remelting parameters:

- 60 kV accelerating voltage,
- 300 mm working distance,
- 485 mA focusing lens current (focused beam),
- 500 Hz deflection frequency,
- 14 mm deflection amplitude (perpendicular to the direction of sample movement).

Other process parameters are given in Table 1.

Tab. 1. Variable electron beam remelting parameters.

Sample no.	Sample movement speed, mm/min	Beam current, mA	Beam Power, W
1	500	23	1380
2	500	25	1500
3	500	27	1620
4	1000	31	1860
5	1000	33	1980
6	1000	35	2100
7	1500	40	2400
8	1500	45	2700
9	1500	50	3000

The microstructures of the samples were investigated by light microscopy (Nikon MA200 Eclipse microscope) and scanning electron microscopy (FEI Nova NanoSEM 450) with energy dispersive spectroscopy (EDS). The SEM observations and EDS analysis were carried out with an acceleration voltage of 20 kV, at working distance of 7.5 mm.

3. RESULTS AND DISCUSSION

Metallographic studies of the coatings before and after remelting revealed that for most of the parameters used, it was possible to achieve metallurgical fusion with the base material and reduce defects such as porosity, as well as homogenize the microstructure. The cross-section SEM (BSED) images of the coatings before and after remelting are shown in Figure 1. Figure 1a shows photos of Ni20%Cr+30%Re plasma sprayed coating. It is characterized by high porosity (up to 6% according to analysis based on cross-sections analysis) and contain a lot of cracks and have typical plasma sprayed lamellar structure. On the contrary, Figure 1b illustrates the cross-section of the same coating after electron beam remelting. As it is visible in Figure 1b the remelting process effectively reduces the presence of pores (<0.2% according to analysis based on cross-sections analysis) and microcracks and changes the lamellar structure of the plasma sprayed coating to fine homogenous microstructure. The microstructure of all remelted coatings was characterized by a columnar or columnar-dendritic structure.

However, not all the parameters used made it possible to obtain coatings free of defects and characterized by a uniform chemical and phase distribution. Figure 2 shows a comparison of Ni20%Cr+40%Re samples of similar thickness remelted at 3 different speeds.

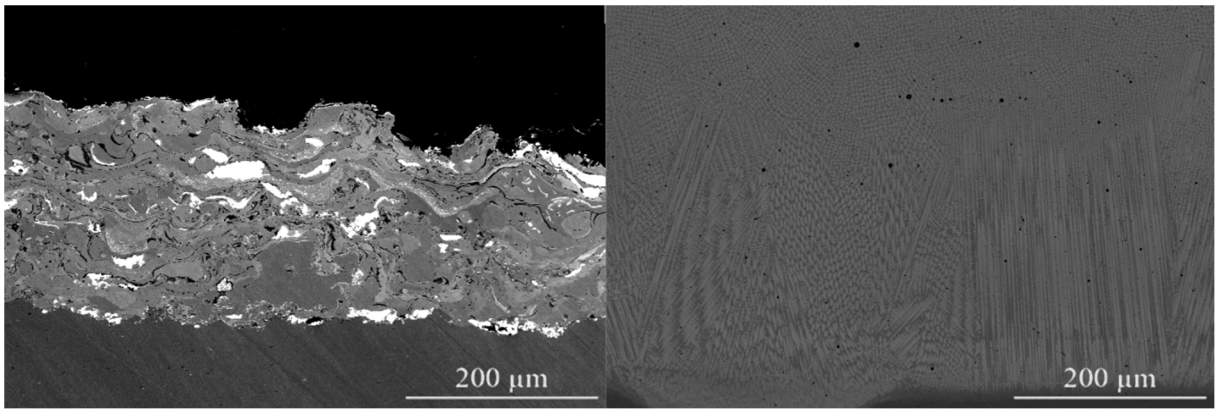

Fig. 1. The cross-section SEM (BSED) images of coatings: a) plasma-sprayed Ni20%Cr+30%Re coating; b) electron beam remelted Ni20%Cr+30%Re sample No. 3.

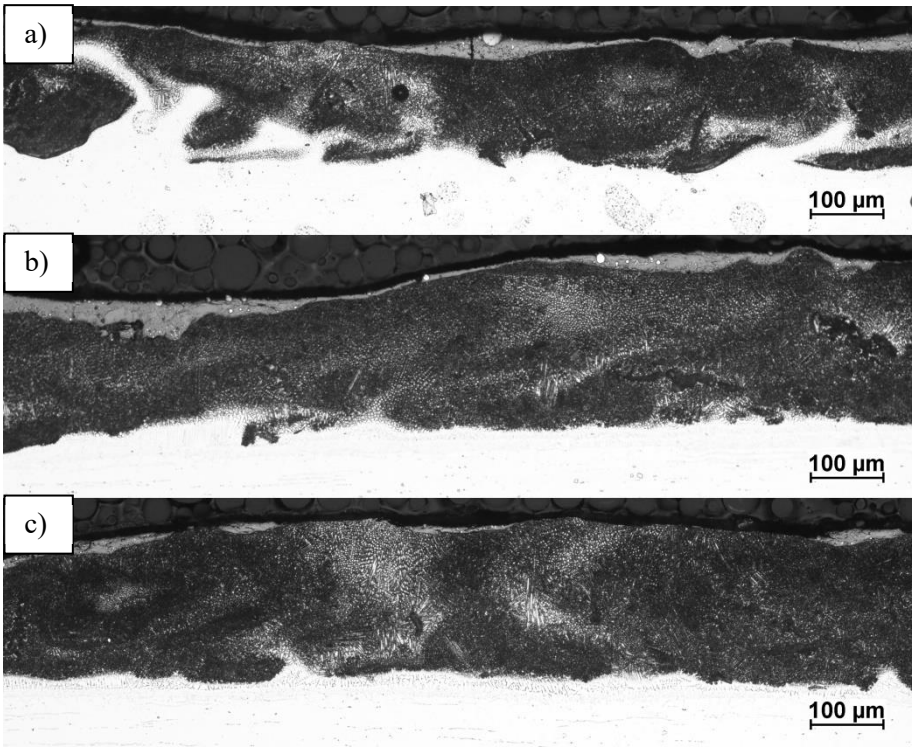

Fig. 2. Comparison of cross-sections of electron beam remelted Ni20%Cr+40%Re coatings of: a) sample No. 8 (1500 mm/min), b) sample No. 5 (1000 mm/min), c) sample No. 2 (500 mm/min).

As it is shown in figure 2, specimens remelted at 500 mm/min were characterized by the best remelted coating geometry, uniformity of structure and absence of defects. For all types of sprayed powders, samples remelted at 1500 mm/min were characterized by a highly uneven microstructure and occasional pores. In addition, for samples remelted at higher speeds, the thickness of the layers was very uneven and the fusion line was irregular. Samples sprayed with Ni20%Cr+50%Re powder at remelting speeds of 1000 mm/min and 1500 mm/min were most often characterized by the presence of irregularly shaped gas voids. In the case of samples sprayed with Ni20%Cr+30%Re powder remelted at 1500 mm/min, the occurrence of cracks was also observed. Figure 3 shows typical mictrostructure defects of samples remelted at higher speeds.

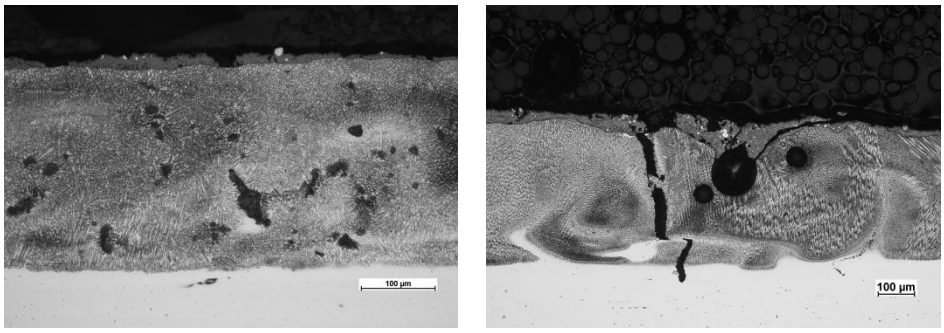

Fig. 3. Cross-section images of samples: a) Ni20%Cr+50%Re sample No. 5 (remelted with movement speed of 1000 mm/min) – visible large pores, b) Ni20%Cr+30%Re sample No. 9 (remelted with movement speed of 1500 mm/min) – visible cracks and large pores.

On the surface of all remelted samples, a layer with a different structure is visible, in which cracks were very often (regardless of the remelting speed). This layer is also very poorly bonded to the substrate, as for some of the samples it spontaneously fell off from the remelted layer during sample preparations.

In order to check the uniformity of the distribution of elements in the coatings, as well as to examine the elements present in the surface layer found on remelted coatings, all samples were subjected to EDS testing. Figure 4 shows the result of EDS analysis of the coating area sprayed with Ni20%Cr+40% Re powder and remelted with parameters for sample No. 2. While Figure 5 shows the result of EDS analysis of the coating area sprayed with Ni20%Cr+40% Re powder and remelted with parameters for sample No. 5

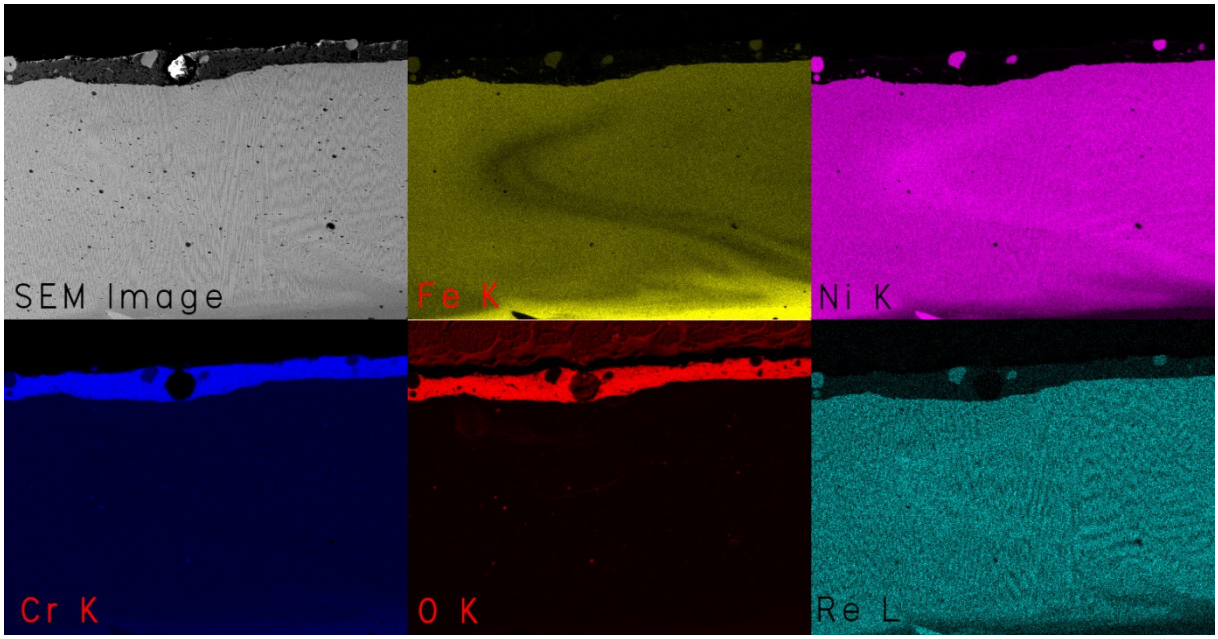

Fig. 4. EDS map scan results of the plasma-sprayed Ni20%Cr + 40%Re coating after electron beam remelting, sample No. 2 (500 mm/min).

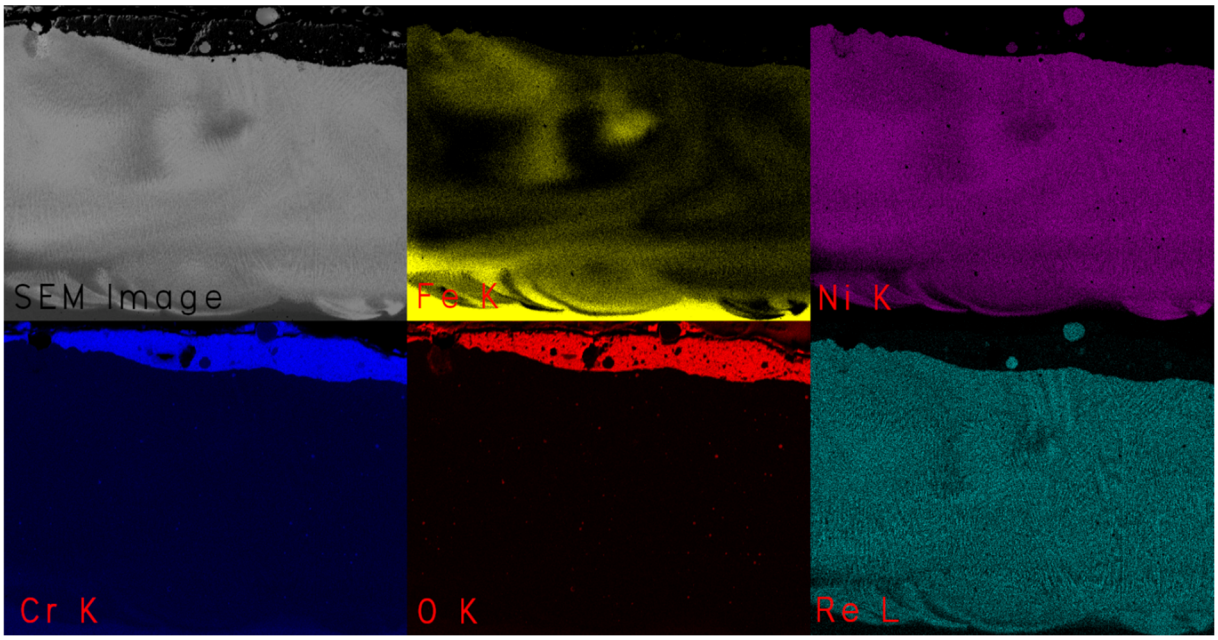

Fig. 5. EDS map scan results of the plasma-sprayed Ni20%Cr + 40%Re coating after electron beam remelting, sample No. 5 (1000 mm/min).

As can be seen in Figure 4, the distribution of elements in the structure of the coating remelted at low speed is uniform. Figure 5, on the other hand, shows clear unevenness in the elemental distribution of the sample remelted at 1000 mm/min. For both analyses, very high amounts of chromium and oxygen are present in the surface layer. Due to the fact that the electron beam remelting process is carried out in a high vacuum, the oxygen present in the coatings must come from the plasma spraying process. This is a negative phenomenon and leads to depletion of chromium in the coating. According to the fact that it is chromium element that provides good corrosion resistance properties, this phenomenon, therefore, can lead to a marked reduction in the corrosion resistance of the coatings obtained in this way (further research is needed to confirm).

Figure 6 and Table 2 show the results of EDS analysis with calculation of the chemical composition of the sample sprayed with Ni20%Cr+30% Re powder and remelted with parameters for sample No. 3. The result of the analysis shows that the chromium content of the remelted layer is lower than both the substrate material (16.5-18.5% Cr according to EN 10088-1) and the sprayed powder (14% Cr). Part of the chromium originally contained in the powder used for plasma spraying was oxidized during the process and was present in the top layer of the coating after remelting.

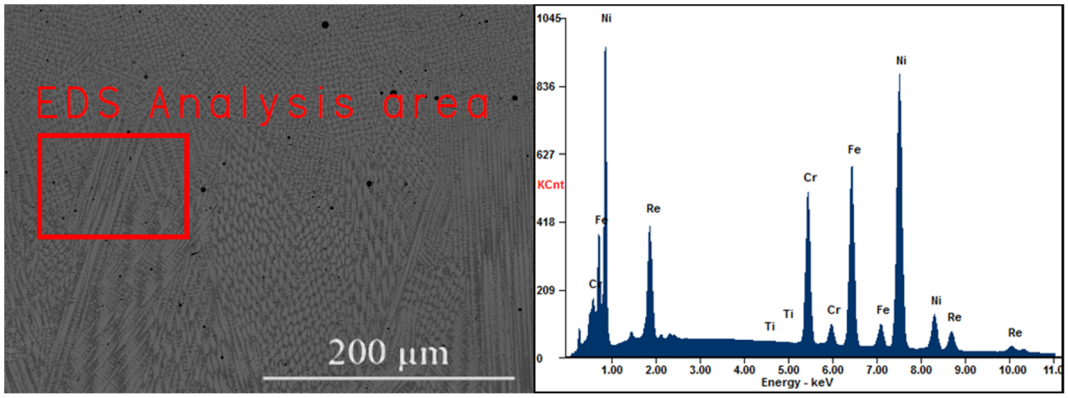

Fig. 6. The EDS analysis graph of electron beam remelted Ni20%Cr+30%Re sample No. 2.

Tab. 2. Ni20%Cr+30%Re sample No. 2 EDS analysis results (usunąć kolumnę At i wiersz Matrix)

Element	*Wt%*	*At%*
TiK	00.10	00.13
CrK	12.93	15.91
FeK	20.49	23.47
NiK	50.47	54.99
ReL	16.01	05.50
Matrix	Correction	ZAF

All remelted layers were also subjected to thickness measurements. The coatings thickness were measured by light microscopy examination of the cross-sections. The results of the measurements are presented in the graph shown in Figure 7. This graph shows the dependence of coating depth on beam power and remelting speed (for all sets of parameters from 1-9). Fusion was not achieved for samples No. 1 (for samples sprayed with Ni20%Cr+40%Re and Ni20%Cr+50%Re powders) and 7 (for all powders used).

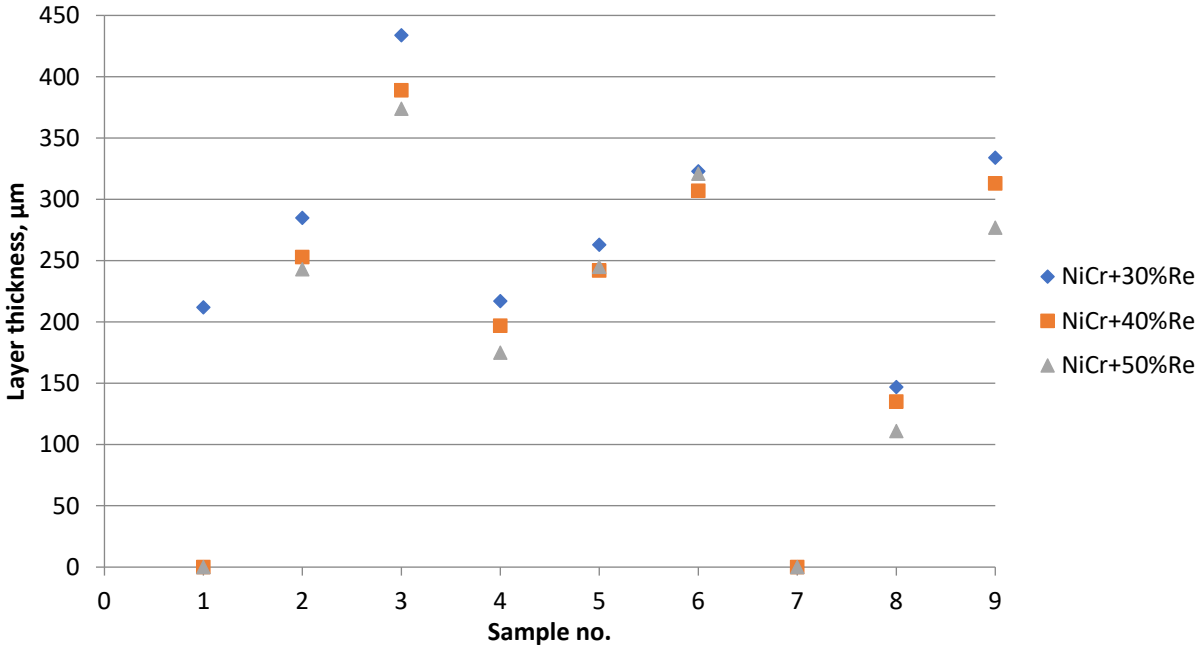

Fig. 7. Graph showing the thickness of the resulting coatings

Energy density (energy per unit area) is proportional to electron beam power, while it is inversely proportional to sample movement speed. From Figure 7, it is clear that an increase in electron beam power results in an increase in coating thickness (the distance between the top of the surface and the maximum depth of penetration in the substrate). If the sample movement speed increases, the penetration depth becomes smaller, and thus the total layer thickness decreases. Slight differences in fusion depths depending on rhenium content are also apparent. Samples with higher rhenium content generally have slightly lower thicknesses.

4. CONCLUSION

In this study, the effect of electron beam remelting on plasma-sprayed coatings was investigated. Ni-Cr-Re coatings with varying Re content were produced by plasma spraying and then remelted by electron beam. Plasma-sprayed coatings are characterized by high porosity and the presence of cracks. These coatings also exhibit the presence of a lamellar structure, resulting in a heterogeneous chemical composition.

After the electron beam remelting process, the coatings are bonded to the substrate through metallurgical bonding, rather than adhesively bonded as in the case of sprayed coatings. The electron

beam remelting process also reduces the presence of pores and micro-cracks. The structure and chemical composition become homogeneous. Coatings remelted at high speeds (1000 and 1500 mm/min) are characterized by the presence of gas voids and cracks. The occurrence of gas voids is particularly intense for samples sprayed with Ni20%Cr+50%Re powder. In addition, samples remelted at higher velocities were characterized by significantly lower homogeneity of chemical composition than samples remelted at 500 mm/min. Too high a remelting speed prevents effective degassing of the coating and thorough mixing of all components of the sprayed layer. The speed movement of the sample (remelting speed) has a significant impact on quality. Layers produced at lower beam travel speeds become more uniform and dense.

Metallographic studies showed the presence of an additional layer on the surface of remelted coatings. This layer is characterized by a different microstructure. EDS analyses showed an increased presence of chromium and oxygen atoms, suggesting intensive oxidation of powder components during the plasma spraying process (oxidation during electron beam treatment is impossible due to the process being conducted in a vacuum). This phenomenon causes chromium depletion of the remelted layers, which may lead to lower corrosion resistance. For further research, the degree of oxidation of the sprayed powder should be reduced.

In addition, coating thickness measurements have shown that the thickness of coatings usually increases with the power of the electron beam. In contrast, an increase in sample movement speed yields layers with smaller thicknesses. Too low a power results in failure to achieve fusion into the base material, failing to provide metallurgical bonding to the substrate.

Electron beam remelting using appropriate process parameters is a suitable method to improve the properties of plasma-sprayed layers. It allows metallurgical bonding of the coating to the substrate, reducing defects such as pores and microcracks, as well as homogenizing the chemical composition of the coating.

ACKNOWLEDGEMENTS
This work was performed with funding from National Science Centre in Poland within the frame of the research grant UMO-2018/29/B/ST8/01206 entitled: “Multi scale analysis of microstructural changes in wear resistant coatings produced by plasma spraying followed by remelting with an application of concentrated energy sources in view of the improvement of their mechanical properties”.

5. REFERENCES

[1] Snead L, Hoelzer D, Rieth M, Nemith A. 2019. *Refractory Alloys: Vanadium, Niobium, Molybdenum, Tungsten*.
[2] Zhang Y, Evans J R, Yang S. 2011. *J. of Chemical & Engineering Data* 56(2) 328-337
[3] Naor A, Eliaz N, et al. 2010 *The AMMTIAC Quarterly* **5(4)** 11-15
[4] Campbell I E, Rosenbaum D M, Gonser B W 1959 *J. of the Less Common Metals* 1(3) 185-191
[5] Pogrebnjak AD, Ruzimov SM, Alontseva DL, et al. 2007. *Vacuum.* 81 1243–1251.
[6] Wu YZ, Liao WB et al. 2018. *Journal of Alloys and Compounds.* 756 33–39.
[7] Węglowski MS, Jachym R, Krasnowski K, Kwieciński K, Pikuła J, Śliwiński P. 2021. *Bulletin of the Institute of Welding* 5 7-19
[8] Valkov S, Ormanova M, Petrov P. 2020. *Metals* 10(9), art. no. 9.
[9] Hamatani H, Miyazaki Y. 2002. *Surface and Coatings Technology* 154 176–183.
[10] Marginean G, Utu D. 2010. *Surface & Coatings Technology* 205 1985–1989.

RECOMBINATION OF COLD MOLECULAR IONS WITH ELECTRONS

Petr Dohnal[1], Liliia Uvarova[1], Miroslava Kassayová[1], Štěpán Roučka[1], Radek Plašil[1], Juraj Glosík[1]

[1]*Charles University, Faculty of Mathematics and Physics, V Holešovičkách 2, 180 00, Prague, Czech Republic*

E-mail: petr.dohnal@mff.cuni.cz

A Cryogenic Stationary Afterglow apparatus with Cavity Ring-Down Spectrometer and microwave diagnostics (Cryo-SA-CRDS) was utilized to probe the time evolutions of number densities of particular rovibrational levels of molecular ions and of electrons in afterglow plasma. The influence of internal excitation on measured recombination rate coefficient will be demonstrated on the case of N_2^+ ions.

1. Introduction

Recombination of positive ions with electrons is an important loss process for these ions in various environments ranging from interstellar gas clouds and planetary ionospheres to technical plasmas [1]. Many experimental techniques were utilized in past 70 years such as stationary or flowing afterglows, microwave diagnostics, Langmuir probe and absorption or emission spectroscopy [1]. Unfortunately, in many cases, most famously for H_3^+ ions [2], the results of various experiments varied by almost an order of magnitude or even more. It is evident that for reliable recombination rate coefficient determination in afterglow plasma, it is necessary to understand the underlying (and sometimes very complicated) chemistry leading to formation of studied ions. At low temperatures, that are of interest for interstellar chemistry, the decay of plasma in afterglow can be influenced by recombination processes assisted by third bodies (electrons, buffer gas particles) whose ternary recombination rate coefficients are largely unknown for molecular ions. The possible dependence of the recombination rate coefficient on internal excitation (rotational or vibrational) can also influence the measured recombination rate coefficients in some cases [3].

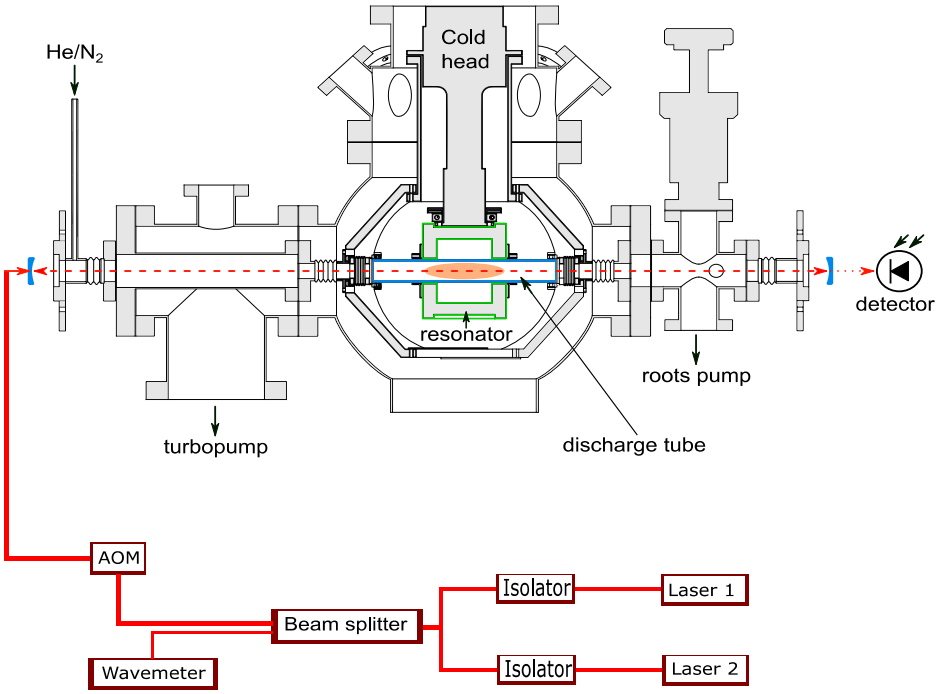

Fig. 1. A scheme of the Cryogenic Stationary Afterglow apparatus with Cavity Ring-Down Spectrometer (Cryo-SA-CRDS).

2. Experiment

A detailed description of the experimental setup, depicted in Fig. 1, can be found in ref. [4] so only short description will be given here. The discharge is ignited in a tube made of monocrystalline sapphire in a mixture of gases of desired composition (nitrogen gas in helium buffer gas, typically [He] ~ 10^{16} cm^{-3} and [N_2] ~ 10^{14} cm^{-3}). The microwave resonator is connected to the discharge tube via copper braids and attached to the cold head of the closed cycle helium refrigerator. The achievable temperature range is 30 – 300 K. On the axis of the discharge tube are positioned two plano-concave mirrors forming optical cavity of the CRDS. The laser is switched on and off by passing through an acousto-optic modulator (AOM) and then passes through mode matching optics (not in the figure) prior entering the cavity itself. The light leaking through the cavity is collected by an avalanche photodiode. Several laser diodes covering the transitions in the Meinel band of N_2^+ ($^2\Sigma_g^+$ - $^2\Pi_u$) originating in the ground and the first excited vibrational state of the ion were utilized in present study. The wavelength was measured absolutely by WA-1650 wavemeter. The electron number density was determined from the shift of the resonance frequency of the microwave resonator with respect to that of an empty resonator. In this way, the time evolutions of several rovibrational states and of electrons in afterglow plasma can be used for recombination rate coefficient determination.

3. Results and Conclusions

By probing the time evolutions of both electrons and ions we were able to determine the recombination rate coefficients for recombination of N_2^+ ions with electrons even at conditions where these ions were not dominant species in the afterglow plasma (for details on the data analysis see ref. [5]). The probed temperature range was 150 – 300 K. The lower temperature limit largely given by the formation of N_4^+ cluster ions. The obtained recombination rate coefficients are pertaining to the vibrational ground state of the N_2^+ ions. By comparison to data from previous experiments with vibrationally excited ions we estimated the recombination rate coefficient for v = 1 state of N_2^+. Details of these experiments will be presented at the conference.

4. References

[1] Larsson M and Orel A 2008 *Dissociative Recombination of Molecular Ions*, Cambridge University Press.
[2] Glosik J, Korolov I, Plasil R et al. 2008 *J. Phys. B-At. Mol. Opt. Phys.* **41** 191001.
[3] Novotny O, Wilhelm P, Paul D et al. 2019 *Science* **365** 6454.
[4] Plasil R, Dohnal P, Kalosi A et al. 2018 *Rev. Sci. Instrum.* **89** 063116.
[5] Shapko D, Dohnal P, Roucka S et al. 2021 *J Mol Spectrosc* **378** 111450.

COHERENCE TRANSFER SPECTROMETER FOR 2 *μm* RANGE

Peter Čermák[1], Ondřej Votava[2], Daniele Romanini[3], Hélène Fleurbaey[3], Didier Mondelain[3], Samir Kassi[3]

[1] *Department of Experimental Physics, Faculty of Mathematics, Physics and Informatics, Comenius University, Mlynská dolina, Bratislava 842 48, Slovakia*
[2] *J. Heyrovský Institute of Physical Chemistry, ASCR, Dolejškova 3, Prague 8, Czech Republic*
[3] *Université Grenoble Alpes, CNRS, LIPhy, F-38000 Grenoble, France*
E-mail: cermak@fmph.uniba.sk

High-Finesse optical Cavities (HFC) proved to be a very effective tool in both trace gas detection and reference absorption data acquisition. The achievement of ultimate sensitivity comes at a price of HFC's very-narrow frequency transmittance (typically around few kHz). For their effective integration into spectroscopic systems, laser with similar line-width and frequency stability are recommended solution. This constrain, on the other hand, makes it very difficult to produce spectrometer with both broad spectral coverage and fine (accurate and stable) frequency tuning.

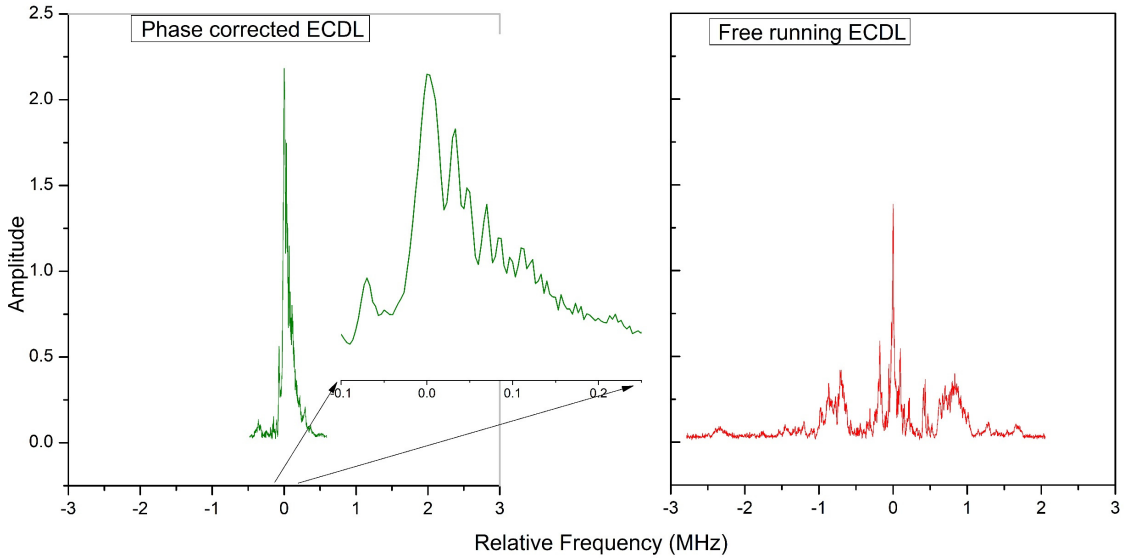

Fig. 1. Comparison of HFC transmittance for free running and phase corrected ECDL using the CCT technique

The present contribution aims to discuss the strategy of producing such spectrometer using the femto-second Comb Coherent Transfer (CCT) technique [1,2] applied to the Extended Cavity Diode Laser operating around 2 μm. Fig.1 shows the comparison of cavity transmittance using either free running ECLD or feed-forward phase corrected signal. The observed "ringing" pattern for the latter case, confirms the narrowing of the source to the mode width of the HFC, thus significantly improving the injection efficiency.

The second advantage of the spectrometer design is the capability of agile mode-hop-free frequency tuning. This is performed by controlling the radio-frequency (RF) offset which is mixed with the CCT signal before performing the ECDL emission correction. In this way, depending on the RF-chain bandwidth, the tuning range extends to 5-10 GHz with the step resolution below 1 kHz. Fig.2 shows an example of CO_2 absorption peak around 146.171 THz with a step size of 20 MHz.

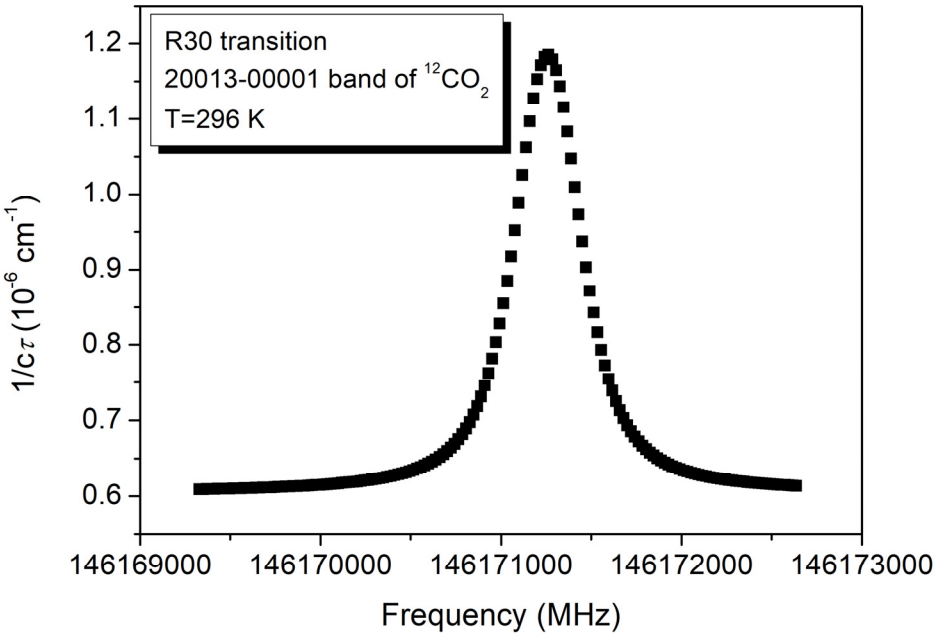

Fig. 2. An example of CCT-CRDS signal showing the CO_2 line around 146.171THz recorded with step of 20 MHz.

Further tuning of the spectrometer is performed by changing the "locked" frequency by tuning the ECDL. At the end the CCT spectrometer offers high-sensitivity on the whole tuning range of the ECDL (1975-2075 nm) with frequency resolution on the kHz scale.

Acknowledgments

This research was supported by the joint Slovak-Czech-French Danube Region project (DS-FR-19-0050), and by the Slovak Research and Development Agency (contract number APVV-19-0386). P.C. thanks CNRS for a one-month support at LIPhy-Grenoble.

1. References

[1] Gotti R. et al. 2018 *J. Chem. Phys*. **149** 154201.
[2] Votava O. et al. 2022 *Phys. Chem. Chem. Phys*. **24** 4157–4173.

A COMPUTATIONALLY ASSISTED TECHNIQUE TO MEASURE MATERIAL-SPECIFIC SURFACE COEFFICIENTS IN CAPACITIVELY COUPLED PLASMAS BASED ON CHARACTERISTICS OF THE ION FLUX-ENERGY DISTRIBUTION FUNCTION

Jan Benedikt[1,2], Christian Schulze[1], Zoltán Donkó[3]

[1]*Institute for Experimental and Applied Physics, Kiel University, Kiel, Germany*
[2]*Kiel Nano, Surface and Interface Science KiNSIS, Kiel University, 24118 Kiel, Germany*
[3]*Institute for Solid State Physics and Optics, Wigner Research Centre for Physics, Budapest, Hungary*
E-mail: benedikt@physik.uni-kiel.de

Secondary electron emission (SEE) is known to have a significant influence on plasma properties such as electron temperature and plasma density due to the injection of high-energy electrons into the plasma, which are generated when the emitted electrons are accelerated in the sheath potential. As the plasma properties and emitted electrons also have an impact on the sheath width and spatiotemporal potential distribution, the ion energy distribution function (IEDF) at the electrodes show signatures that depend indirectly on the emission coefficients. Here, the influence of SEE on the bimodal peak structure, which is formed by ions that traverse the sheath without collisions is analyzed in detail. In particular, (i) its position corresponding to the acceleration through the mean sheath potential and (ii) the peak separation in the bimodal structure, depend differently on the effective ion induced SEE yield (γ_{eff}) and the effective elastic electron reflection probability (r_{eff}). We present a technique that combines energy-resolved mass spectrometric measurements and 1d3v particle-in-cell/Monte Carlo collision simulations to determine both parameters simultaneously and independently in a symmetric rf capacitively coupled plasma in argon. The method is applied to stainless steel and aluminum oxide surfaces resulting in a good agreement with literature values. This technique allows for a straightforward and relatively fast estimation of the SEE coefficients for all materials that can be deposited on the plasma electrodes.

1. Introduction

Besides stochastic heating, secondary electron emission is the most important source of high-energy electrons: When ions, electrons, photons, metastable species or fast atoms hit the surface, the deposited energy can release secondary electrons from the surface, that are subsequently accelerated in the potential of the plasma sheath. These electrons enter the bulk plasma with high energies and can ionize the background gas in electron impact ionization collisions. Therefore, secondary electrons are capable of influencing the most important plasma parameters as plasma density and electron temperature and are important for the understanding of the plasma. We used this influence of the electron emission on plasma density to determine the effective ion induced secondary electron emission coefficient γ_{eff} and the effective elastic electron reflection probability r_{eff}.

2. Experimental setup and results

We designed a symmetric capacitively coupled plasma with an electrode distance of 25 mm as sketched in fig. (1). Two different electrode pairs were built out of stainless steel of which one was left uncoated (SS) and one was coated with a thin layer of aluminum oxide (Al_2O_3). We measured the emission profile through one of the slits in the cylinder wall and the ion flux-energy distribution of the Ar^+ ions with help of the Hiden Analytical PSM in the center of the discharge at an argon pressure of 5 Pa.

The emission profiles for the two different surface materials, see fig. (2), show a 20% higher peak emission for the Al_2O_3 surface and a lower sheath width which both indicate a higher plasma density

due to an increase in secondary electron emission. The ion flux-energy distribution in a rf discharge consists of a bimodal peak structure at high energies that is formed by ions crossing the plasma sheath without collisions and several broader maxima at lower energies that are formed by ion collisions with the background gas in the plasma sheath. The ion flux-energy distributions for the two different surface materials, see fig. (3), show significant differences in the number and positions of the collision peaks as well as the position and peak separation of the bimodal peak structure. Please note, that in our case the bimodal peak structure is influenced by collisions so that the high energy peak of the bimodal peak structure is distorted to a shoulder like structure. Nevertheless, we can estimate the peak positions from the high energy edge. We determined the position and peak separation of the bimodal peak structure, which correlate with the plasma sheath potential and the ion transit time. The ion transit time itself depends on the sheath width, which varies with the surface material as we have seen in the emission profiles in fig. (2).

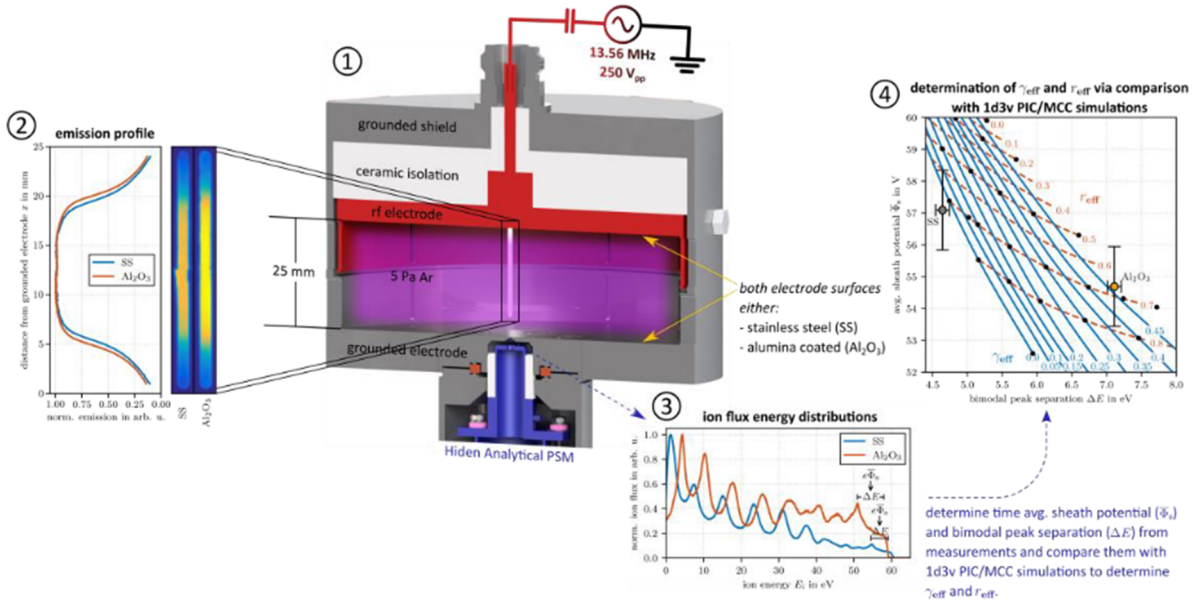

Figs. (1) Sketch of the symmetric electrode geometry and operation conditions. (2) Emission profile measurement through one of the slits in the cylinder wall. (3) Measurements of the ion flux energy distribution for stainless steel (SS) and aluminum oxide (Al2O3). (4) Comparison of the sheath potential and bimodal peak separation from the measurements and PIC/MCC simulations for the determination of the effective ion induced secondary electron emission coefficient γ_{eff} and the effective elastic electron reflection probability r_{eff}. Individual figures combined from reference [1].

Then, we compared the sheath potentials ($\bar{\Phi}_s$) and bimodal peak separations (ΔE) from the measurements with the same parameters as determined from the ion flux-energy distributions from 1d3v particle in cell/Monte Carlo collisions (PIC/MCC) simulations for different combinations of the effective ion induced secondary electron emission coefficient γ_{eff} and the effective elastic electron reflection probability r_{eff}. It turned out, that both parameters depend independently and differently on these two surface coefficients, which allows a determination of γ_{eff} and r_{eff}. The determined values are in good agreement with the literature, see [1] for details.

In the future, we plan to apply the method to different discharge conditions as gas pressure, electrode distance and other surface materials. Furthermore, including the positions of the collision peaks in the fitting routine might further improve the accuracy of the proposed technique.

3. References

[1] C. Schulze, Z. Donkó, J. Benedikt, *A computationally assisted technique to measure material-specific surface coefficients in capacitively coupled plasmas based on characteristics of the ion flux-energy distribution function*, Plasma Sources Sci. Technol. 31 (2022) 105017.

DECONTAMINATION OF RASPBERRIES INOCULATED WITH *ENTEROCOCCUS FAECIUM* BACTERIA USING PLASMA-ACTIVATED GASEOUS MEDIA

Vlasta Štěpánová[1], Felix Schottroff[2,3], Georg Rehbrunner[2], Alexandra Auer[2], Pavel Slavíček[1], Richard Krumpolec[1], Henry Jäger[2]

[1]*CEPLANT, Department of Physical Electronics, Faculty of Science, Masaryk University, Kotlářská 2, 611 37 Brno, Czech Republic*
[2]*Institute of Food Technology, Department of Food Science and Technology, Universität für Bodenkultur Wien (BOKU), Muthgasse 18, 1190 Wien, Austria*
[3]*BOKU Core Facility Food & Bio Processing, Universität für Bodenkultur Wien (BOKU), Muthgasse 18, 1190 Wien, Austria*

E-mail: vstepanova@mail.muni.cz

Multi-hollow surface dielectric barrier discharge (MSDBD) generating plasma-activated gaseous media was used to decontaminate fresh raspberries inoculated with *Enterococcus faecium* bacteria. The highest microbial inactivation of 2 $\log_{10}$ was achieved for the exposure time of 1 min, distance of 10 mm and flow rate of 15 L/min. No colour changes on raspberries were observed after the plasma decontamination process. Temperature monitoring of the raspberries' surface immediately after plasma treatment showed only a slight increase, therefore giving positive implications for the product quality.

1. Introduction and experimental

This study aimed to evaluate the decontamination effect of plasma-activated gaseous media on fresh food products. Food decontamination is an important topic that combines physical methods with microbiology to ensure that foods are safe to consume. Fresh raspberries were chosen as a raw material as they are very sensitive foods which hardly be washed or otherwise decontaminated as of now [1]. As a model microorganism, *Enterococcus faecium* was used for artificial contamination of raspberries and subsequent inactivation using plasma treatment. *Enterococcus faecium* is a Gram-positive bacterium typically coexisting in the gastrointestinal tract of humans and animals. It was used as a non-pathogenic surrogate for *Salmonella*. The evaluation of microbiological inactivation was carried out using the plate count method before and after plasma exposure. Inactivation was calculated based on counted colony forming units per gram of sample (CFU/g), as $\log_{10}(N/N_0)$, with N_0 and N referring to the CFU before and after the treatment, respectively.

Multi-hollow surface dielectric barrier discharge (MSDBD) working at atmospheric pressure was utilised for the experiments. This plasma source's geometry and electrical parameters are described elsewhere [2]. The dielectric plate of MSDBD contains many small holes, through which the working gas is flown, and thus this coplanar-type DBD plasma source is capable of generating plasma-activated gaseous media in volume [3]. The decontamination process of inoculated raspberries was carried out in a closed chamber. Some trials were performed in an open atmosphere for comparison. The apparatus enabled the variation of several treatment parameters, such as type (air, nitrogen) and flow rate (5-25 L/min) of the working gas, as well as the distance between the dielectric surface and the top of the sample (5-20 mm). The input power was set constant to 30 W, and exposure times in the range of 1-10 min were tested. As the temperature is an essential parameter for maintaining the quality of fresh fruit, the temperature of raspberries was measured immediately after the treatment using a contactless infrared thermometer.

The fresh raspberries were purchased every time from the same provider to minimise the natural inhomogeneities that could influence the results of the experiments. The halves of fresh raspberries (15 g) were surface inoculated with 50 µL of *Enterococcus faecium* working culture. Preparation of the working culture as well as the method for inoculation are described elsewhere [4]. Only the outer surface

of the berries was inoculated to simulate the natural contamination process in the field. After the plasma decontamination, microbiological analyses were carried out by mixing raspberries (15 g) with Ringer solution (135 ml) in a stomacher. Extracted liquid was serially diluted and plated on nutrient agar. Agar plates were incubated for 48 h at 37°C before colonies were counted and inactivation levels were calculated.

Moreover, colour analysis of samples before and after the plasma decontamination was carried out with an electronic visual analyser, ensuring reproducible light conditions.

2. Results and discussion

The effect of working gas type, its flow rate and the distance between the dielectric surface and the top of the sample on the microbiological inactivation were studied. The optimisation process aimed at a combination of treatment parameters leading to the highest reduction of microorganisms. The duration of the plasma decontamination process is a crucial parameter from an industrial point of view. The exposure time of 1 min led to a 2 $\log_{10}$ reduction of *E. faecium*. A further prolonged exposure time of up to 10 min did not result in a significantly higher effect. Similarly, the increased working gas flow rate up to 25 L/min did not result in a higher inactivation. The best results considering microbiological inactivation were achieved for the distance of 10 mm, flow rate of 15 L/min and exposure time of 1 min. The type of working gas (air, nitrogen) had only a minor effect on the microbial inactivation. The plasma decontamination proceeded in such a way that each half of the raspberry was treated separately. Finally, we decided to decontaminate all berries corresponding to one sample simultaneously. Surprisingly, the treatment of all raspberries (15 g) in one step resulted in similar results as the treatment of every single half of the berry. The main advantage of this finding is the decrease in treatment time needed to decontaminate a certain number of berries corresponding to one sample. Colour analysis of samples before and after plasma decontamination did not show any changes in colour. The temperature of treated raspberries measured immediately after treatment did not exceed the value of 40 °C, even for 10 min exposure time.

3. Conclusion

The MSDBD plasma decontamination under optimised conditions led to a reduction of *E. faecium* up to 2 $\log_{10}$, and there was no change in the colour of the raspberries at the same time. The highest microbial inactivation was achieved for the exposure time of 1 min. The temperature of the samples measured immediately after the treatment was only slightly higher than before plasma exposure, depending on the treatment parameters used, thus no thermal quality deterioriation took place. However, further optimisation of the plasma decontamination process leading to higher microbial inactivation is required in order to enable the implementation of the results in the food industry.

Acknowledgement

This research has been supported by the OeAD-GmbH – Austria's Agency for Education and Internationalisation, OeAD Aktion Austria-Czech Republic scholarship programme 2022/23 financed by the Federal Ministry of Education, Science and Research (BMBWF), Austria, and by the project LM2018097 funded by the Ministry of Education, Youth and Sports of the Czech Republic.

4. References

[1] A. Rajkovic, N. Smigic, I. Djekic, D. Popovic, N. Tomic, N. Krupezevic, M. Uyttendaele and L. Jacxsens 2017 *Food Control* Vol. **80**, pp. 151-161.
[2] T. Homola, R. Krumpolec, M. Zemánek, J. Kelar, P. Synek, T. Hoder and M. Černák 2017 *Plasma Chemistry Plasma Processing* Vol. **37(4)**, pp. 1149-1163.
[3] P. Dvořák, V. Procházka, R. Krumpolec and M. Zemánek 2020 *Plasma Process Polym.* Vol. **17**, pp. 1-7.
[4] W. Xu and Ch. Wu 2016 *Food Microbiology* Vol. **57**, pp. 135-143.

YOUNG SCIENTISTS' LECTURES

EFFECTS OF AIR PULSED STREAMER CORONA DISCHARGE ON SINGLE AND MIXED SPECIES BIOFILMS OF *S. AUREUS* AND *P. AERUGINOSA*

Aleksandra Lavrikova[1], Helena Bujdáková[2], Mario Janda[1], Karol Hensel[1]

[1]*Division of Environmental Physics, Faculty of Mathematics, Physics and Informatics*
[2]*Department of Microbiology and Virology, Faculty of Natural Sciences,*
Comenius University, Bratislava, Slovakia
E-mail: lavrikova6@uniba.sk

The pulsed streamer corona discharge generated in ambient air was applied to single- and mixed-species bacterial biofilms of different growth stages. Both types of biofilms underwent significant losses of biofilm biomass, suppression of metabolic activity, and removal from polystyrene or glass substrates. Despite the strong immediate effect on bacterial viability, the regrowth of biofilms on the next day showed a inadequacy of the used plasma treatment. Also, hydrated form of biofilms was found more resistant than dry-surface one. The gaseous species including O_3 and NO_x combined with the etching of biofilms are probably the main factors responsible for overall antibiofilm eradication induced by the pulsed streamer corona discharge plasma.

1. Introduction

The existence of microbial biofilms in various aspects of the human community causes severe economic and health-related issues. Cells in biofilms demonstrate enhanced resistance to stressful environmental conditions than planktonic bacteria and require higher concentrations of disinfectants to inactivate on surfaces. Biofilms with harmful effects can be eradicated by physical and chemical methods [1]. Cold plasma represents one of the alternative methods for biofilm infection control [2]. It is believed the plasma treatment combine both physical (ion bombardment, electroporation, electrostatic disruption) and chemical (oxidative and nitrosative stress) mechanisms. Besides damage to DNA, proteins, and cell membrane as main targets of reactive oxygen and nitrogen species (RONS), the etching effect and interference of quorum sensing have been reported among antibiofilm mechanisms of plasma treatment [3]. There is a number of challenges to biofilm destruction by cold plasma, such as heterogeneity in biofilm extracellular polymeric substances, its thickness, O_2 content, nutrient gradients, microbial species, persister cells, and location of the biofilm. The adequate treatment of such coordinated communities of bacteria is crucial to avoid the appearance of more adaptive biofilms, persister cells, or resistance to RONS generated by plasma. Yet, knowledge of complex network of interactions between bacteria in mixed-species biofilms as well as plasma-biofilm inactivation pathways is limited. The objective of this work was to investigate the effects of the pulsed streamer corona discharge plasma on single- and mixed-species biofilms of clinically relevant bacterial species *S. aureus* and *P. aeruginosa*.

2. Experimental setup

The pulsed streamer corona discharge was used for the treatment of biofilms (Fig.1). The discharge was generated in ambient atmospheric air between the tip of the needle electrode and the surface of the grounded electrode. The biofilms on the polystyrene or glass substrate were directly placed between the electrodes and treated by the discharge. The discharge was driven by a high voltage (HV) pulse generator (*FID Technology* FPG 20-10NM10) and its electrical characteristics are monitored by a HV probe (*Tektronix* P6015A) and Rogowski type current probe (*Pearson Electronics* 2877) connected to a digitizing oscilloscope (*Tektronix* TBS 2000). The applied voltage was set at 10 kV at 1 kHz.

The effects of plasma treatment were evaluated against models of 24-h / 48-h old single– and mixed–species biofilms of Gram-positive *S. aureus* and Gram-negative *P. aeruginosa*. Bacteria viability, biofilm biomass, metabolic activity, regrowth of biofilms after treatment, and intracellular ROS accumulation were analyzed. Standard microbiological, spectroscopic, and fluorescence technics were used. Additionally, the gas-phase chemistry of the discharge was evaluated by emission and absorption spectroscopy.

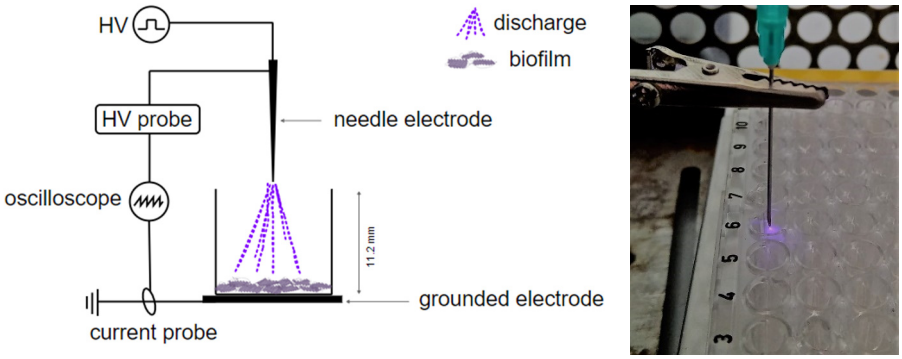

Fig. 1. Schematic diagram (left) and photograph (right) of the pulsed streamer corona discharge plasma.

3. Results and discussion

The pulsed streamer corona discharge plasma resulted in an effective biofilm inactivation (*P. aeruginosa* – complete inactivation, *S. aureus* ~ 4 log reduction). Both *S. aureus* and *P. aeruginosa* displayed higher resistance to plasma treatment in mixed-species biofilms compared to their single forms. A higher reduction in metabolic activity of bacteria was achieved for more mature 48-h biofilms. The fluorescence microscopy showed evident biofilm eradication from the glass substrate even at the shortest (30 s) treatment time. Interestingly, a significantly stronger inactivation was found for dry-surface biofilms compared with hydrated biofilms (Fig.2). Supposedly, plasma did not generate enough long-lived RONS in water responsible for bacterial lysis. Moreover, O_3 and NO_2 were dominant gaseous species generated by the discharge that seemingly contribute to the predominant etching mechanism of biofilm destruction.

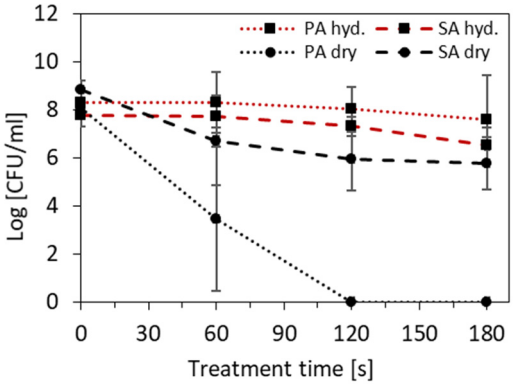

Fig. 2. Survival of 24-h old single species biofilms as a function of plasma treatment time.
(PA - *P. aeruginosa*, SA – *S. aureus*; hyd. – hydrated, dry – dry-surface biofilm).

4. Conclusion

Air streamer corona discharge has shown the ability to efficiently eradicate bacterial biofilms. The results showed the plasma did not lead to the complete inactivation of bacteria within biofilms since they regrew again the next day. A thorough fundamental understanding of cold plasma physicochemical properties and revealing of plasma-induced biological responses are required for the safe application of plasma in biomedicine.

5. Acknowledgments

This work was supported by Comenius University grant UK/206/2022 and Slovak Research and Development Agency grants APVV-17-0382 and APVV-20-0566.

6. References

[1] Yin W. et al., *Crit. Rev. Microbiol.*, **47** (1), 57-78, 2021.
[2] Abdo A., Schmitt-John T., and Richter K., *EMJ Microbiol. Infect. Dis.*, **2** (1), 38–39, 2021.
[3] Zhu Y. et al., *Trends Food Sci. Technol.*, **99**, 142–151, 2020.

NOVEL METHOD FOR THE SYNTHESIS OF CORE-SHELL NANOPARTICLES FOR FUNCTIONAL APPLICATIONS

Oguz Han Asnaz[1], Jonas Drewes[2], Marie Elis[3], Franko Greiner[1,4], Franz Faupel[2,4], Lorenz Kienle[3,4], Alexander Vahl[2,4], and Jan Benedikt[1,4]

[1]*Institute of Experimental and Applied Physics, Kiel University, 24098 Kiel, Germany*
[2]*Chair for Multicomponent Materials, Kiel University, 24143 Kiel, Germany*
[3]*Chair for Synthesis and Real Structure, Kiel University, 24143 Kiel, Germany*
[4]*Kiel Nano, Surface and Interface Science KiNSIS, Kiel University, 24118 Kiel, Germany*

E-mail: asnaz@physik.uni-kiel.de

A novel combination of a gas aggregation source and a secondary radio frequency discharge is used to generate, confine, and coat nanoparticles. The process is monitored using Fourier-transform infrared spectroscopy and localized surface plasmon resonance spectroscopy. It is demonstrated that Ag@SiO_2 nanoparticles can be synthesized with a well-defined surface coating.

Due to their size, noble metal nanoparticles have unique properties in comparison to their bulk counterparts. Applications range from photocatalysis, resistive switching, sensors, solar cells, to antibacterial coatings.
In this contribution, the Ag nanoparticles are created in a Haberland type gas aggregation source and then injected into a secondary radio frquency discharge for further confinement and treatment. This novel approach allows for treatments with much longer time scales than in traditional in-flight treatment setups and much finer control over the coating properties. The system is capable of holding particles over an hour without significant losses. The confined particles are measured using Fourier-transform infrared spectroscopy and localized surface plasmon resonance for monitoring of the on-going surface treatment. Ag nanoparticles between 5-60 nm have been coated with SiO_2 where a homogeneous coating was achieved after 10 min of treatment. For shorter coating times, island growth has been observed with a closing of the coating at around 5 min.
This method is very versatile and could be applied to many different particles ranging from different metal types, alloys to inorganic materials and even polymers. Furthermore different coatings can be applied and even the fabrication of a gradually changing coating is possible.

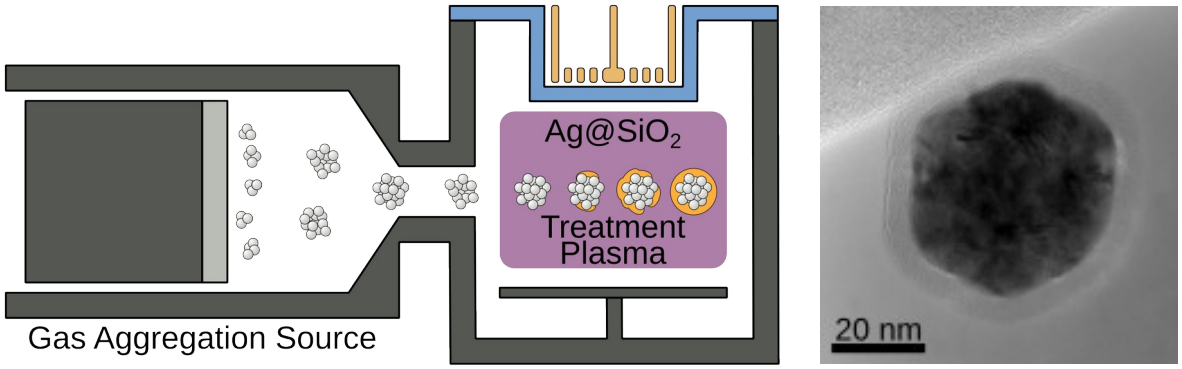

Fig. 1. Left: Sketch of the two-step fabrication process of Ag@SiO_2 nanoparticles. On the left, a Haberland type gas aggregation source is used to create Ag nanoparticles, which are then injected into the secondary radio frequency plasma for further confinement and treatment with SiH_4. Right: HRTEM micrograph of a Ag nanoparticle after 10 minutes of coating with SiH_4.

References

[1] O. Asnaz, J. Drewes, et al., submitted to Nanoscale Adv.

TIME RESOLVED SPECTROSCOPY OF DISCHARGES IN CONDUCTING LIQUIDS

Fayza Hassan,[1,2] Adrian Beattie,[1] Adam Murphy,[1] W.G. (Bill) Graham,[1] Thomas A. Field[1]

[1]*School of Mathematics and physics, Queen's University Belfast, Belfast BT7 1NNUK,*
[2]*Faculty of Engineering, Zagazig University, Sharkia 44519, Egypt*
E-mail: fhanafyhassan01@qub.ac.uk

Plasmas in liquids have many applications in areas such as material science and health care [1]. Recently the focus of the plasma-liquid interaction research has expanded to include various applications such as nanoparticles synthesis, material surface functionalization and water treatment [2,3,4]. With low voltage pulses and higher conductivity ionic solutions, the discharge normally follows the formation of a bubble or gas film around the electrode tip [5,6].

In this work, short HV pulses of ~7kV were applied to aqueous solutions. Typically pulse widths were < 10 μs and frequencies were ~ 1 Hz or lower. The frequency was kept low to minimise heating of the liquid. Two tungsten wire electrodes separated by a micro-gap of less than 1 mm were immersed in the solution. The production and evolution of plasma breakdown in saline (NaCl) and potassium bromide (KBr) solutions were investigated. An intensified charged-coupled device (iCCD) camera, iStar Andor, was used to take Images at various delays, enabling the creation of a sequence of frame-by-frame images to monitor the evolution of the vapour layer over time. The time evolution of emission spectra was also monitored with the iStar camera attached to an Oriel MS125 spectrometer. Hα, Hβ and OI emission lines are the most noticeable lines in the spectra. Fig. 1 shows the time resolved spectroscopy results for Hα emission at KBr solution at different delays with a fixed time width 0.5 μs. These results are being analysed to estimate electron densities.

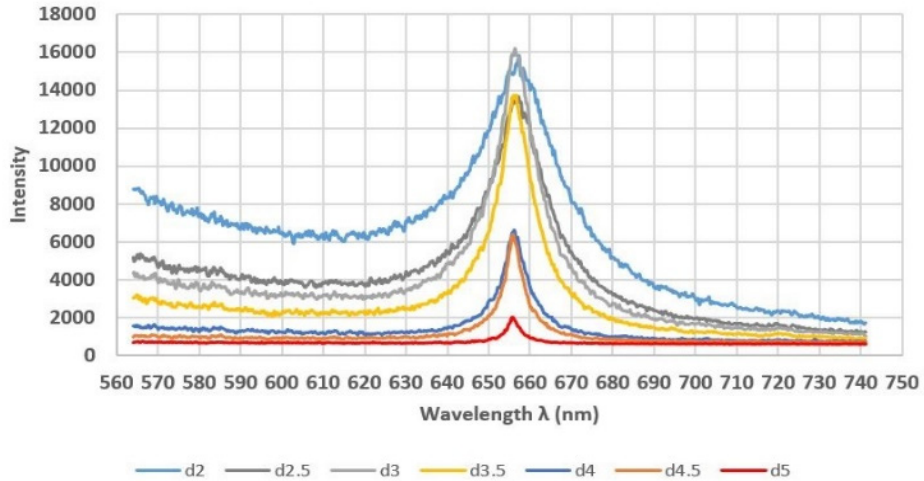

Fig. 1. Hα results for KBr solution at different delays; the labels dx refer to time windows of x to x+0.5 μs; e.g., d4 indicates a time window of 4.0 to 4.5 μs after the initiation of the discharge.

1. References

[1] Bruggeman, P. J., et al. "Plasma–liquid interactions: a review and roadmap." Plasma sources science and technology 25.5 (2016): 053002.

[2] Martin J C 1996 J.C. Martin on Pulsed Power (New York: Plenum)

[3] Webb M R and Hieftje G M 2009 Spectrochemical analysis by using discharge devices with solution electrodes Anal. Chem. 81 862–7

[4] Smoluch M, Mielczarek P and Silberring J 2016 Plasma-based ambient ionization mass spectrometry in bionanalytical sciences Mass Spectrom. Rev. 35 22–34

[5] Chang, Hung-wen, and Cheng-che Hsu. "Diagnostic studies of ac-driven plasmas in saline solutions: the effect of frequency on the plasma behavior." Plasma Sources Science and Technology 20.4 (2011): 045001.

[6] Asimakoulas, Leonidas, et al. "Fast framing imaging and modelling of vapour formation and discharge initiation in electrolyte solutions." Plasma Sources Science and Technology 29.3 (2020): 035013.

SILICON NANOCRYSTAL SYNTHESIS WITH THE ATMOSPHERIC PLASMA SOURCE HELIXJET

Maren Dworschak[1], Niklas Kohlmann[2], Filip Matějka[3], Pavel Galář[3], Lorenz Kienle[2], Jan Schäfer[4], Jan Benedikt[1,5]

[1]*Institute for Experimental and Applied Physics, Kiel University, Kiel, Germany*
[2]*Institute of Material Science, Kiel University Kiel, Germany*
[3]*Institute of Physics, Czech Academy of Science, Prague, Czech Republic*
[4]*Leibniz Institute for Plasma Science and Technology, Greifswald, Germany*
[5]*Kiel Nano, Surface and Interface Science KiNSIS, Kiel University, 24118 Kiel, Germany*
E-mail: dworschak@physik.uni-kiel.de

Atmospheric pressure plasmas open up a cost-efficient and modular way for the synthesis of nanocrystals with optical qualities. The improvements to the plasma source HelixJet result in a stable long-term operation which is needed for high particle yields. The jets parameters have been optimized for nanocrystal synthesis and the properties of the resulting particles have been analyzed with various methods.

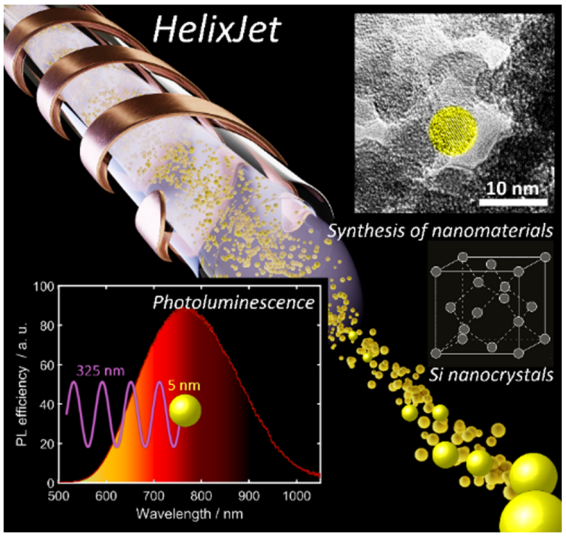

Fig. 1: The atmospheric plasma source HelixJet (top left) can be used to synthesize silicon nanocrystals (top right) that exhibit photoluminescence (bottom left).

Due to their opto-electrical properties semiconductor nanoparticles can be used for a wide range of applications including photovoltaic cells [1]. Cold atmospheric plasmas (CAP) are highly reactive systems that can be used for the generation of such nanoparticles. Compared to low pressure plasma systems [2] the production of crystalline particles is here more challenging, but also provides potential economic benefits. In this contribution we report on the HelixJet [3]. The HelixJet is a capacitively coupled RF-driven plasma source that is operating under atmospheric pressure. It consists of a dielectric in between two helix-shaped electrodes as seen in Figure 1. Two improvements in the form of an additional electrode and on-axis-gas-injection were made to the original jet design which make it suitable for long-term operation at low powers [4]. Using the reactive gas silane, silicon nanoparticles with a precise size control could be generated over a broad range of sizes. The particle size is determined with a 1 nm resolution scanning mobility particle sizer (SMPS). The synthesized particles have been analyzed in regard to their size, crystallinity, structure and photoluminescence. Distinct varieties of nanomaterials could be synthesized depending on the operation parameters of the HelixJet. In-flight annealing post synthesis allows the formation of large crystalline nanoparticles with diameters up to 200 nanometers. In addition, metals such as manganese could be incorporated into the nanocrystals creating silicides (e.g. manganese silicides).

References

[1] Y. H. Fu and A.I. Kuznetsov *et al*. 2013 Nature Communications **4**, 1527
[2] J. Schäfer and A. Quade *et al.* 2020 *Plasma Processes & Polymers* **17**, 1
[3] A. Bapat and C.R. Perrey *et al.* 2003 *Journal of Applied Physics*, **94**, 3
[4] M. Dworschak and N. Kohlmann *et al.* 2022 *Plasma Processes & Polymers*, **e2200129**

IMPACT OF CAPP ON THE YEAST *CANDIDA GLABRATA*

Kristína Trebulová[1], František Krčma[1], Petra Skoumalová[1], Zdenko Machala[2]

[1]*Brno University of Technology, Faculty of Chemistry, Purkyňova 118, 612 00 Brno, Czech Republic*
[2]*Comenius University, Faculty of mathematics, physics and informatics, Mlynská dolina, 84248 Bratislava, Slovakia*

E-mail: xctrebulovak@vutbr.cz.

This work focuses on a direct cold atmospheric-pressure plasma (CAPP) treatment of a model yeast example Candida glabrata. The main goal was to test the efficiency of chosen CAPP sources on the same microorganism and evaluate their antimycotic effects. The study also deals with the optimization of selected working parameters to meet the medical requirements and to choose the most suitable discharge for further studies focused on the treatment of superficial yeast-caused infections in animals and humans.

1. Introduction

Cold atmospheric-pressure plasma (CAPP) technology has become a very discussed topic in the past few decades, thanks to its wide range of applications in various fields of science. Compared to the well-known hot plasma technologies used in welding, plasma cutting or plasma spraying, the CAPP has much lower energy, and thus it can be used in fields like medicine, agriculture or food industry. This work is aiming to broaden the knowledge about antimicrobial effects of CAPP, mainly focusing on the antimycotic effects of different CAPP sources as a potential alternative method for yeast inactivation. In this study, 4 different cold plasma sources, namely: microwave discharges (unipolar and surface-wave) in the form of plasma jets, transient spark and corona discharge in the form of corona pen were tested. *C. glabrata* was chosen as a model yeast example as a representative of non-albicans species, in order to establish basic plasma set-up of chosen CAPP sources for further studies and experiments hopefully leading to clinical studies *in-vivo*.

C. glabrata

C. glabrata of the genus *Candida* is a natural part of human microflora and can be found mainly in the oral cavity, genitals and the digestive tract. From a phylogenetic point of view, *C glabrata* is genetically more similar to baker's yeast (*Saccharomyces cerevisiae)* than to its pathogenic sister *C. albicans,* to whom it is often compared to. This is because of its haploid genome, which also distinguishes it from other *Candida* species [1]. In the past few decades, it has been found that *C. glabrata* changed its lifestyle from a non-pathogenic yeast to an opportunistic pathogen, which means that when the host's immunity is weakened, it changes from a saprophytic yeast to a pathogenic yeast that can cause candidiasis (mycoses caused by the yeast *Candida*) affecting various parts of the body. Currently *C. glabrata* is considered to be the second most common cause of candidiasis in the world [2]. As in the case of the entire genus *Candida, C. glabrata* is a threat especially to the so-called at risk population groups: elderly people, small children, hospitalized patients, people with other serious diseases (HIV, cancer, etc.) and other vulnerable groups [3].

CAPP

CAPP treatment is a non-thermal process that uses plasma (ionized gas or gas mixture) as a source of electrons, ultraviolet radiation (UV), reactive oxygen species (ROS), such as hydroxyl radicals, ozone or hydrogen peroxide and reactive nitrogen species (RNS), such as nitric oxide and other NO_x [4]. In the case of direct application of the discharge to the treated subject, the electric field, which causes the so-called electroporation (opening of pores in cell membranes

due to a high electric field) occurs as well. All these effects synergistically cause various damage to microbial cell leading to apoptosis [5].
Numerous studies use low-temperature plasma in oncology [6] [7], dermatology [8], wound healing [9], but also disinfection and sterilization [10] [11] using plasma technologies are also very discussed topics. Some studies have already gone beyond the *in-vitro* experiments and are performed *in-vivo* and some have progressed to the phase of clinical trials in real patients.

2. Experimental part

The yeast strain *Candida glabrata* CCM 8270, supplied by the Czech Collection of Microorganisms in Brno [12]. Freshly prepared 24-hour inoculum was diluted to selected concentrations and inoculated onto the agar plates. These were immediately treated by the cold plasma under selected conditions. After treatment the samples were incubated in a thermostat at 37 °C and photographed after 24 h, 48 h. Results were then evaluated based on the size and stability of the inhibition zones. Detailed description of all the treatment conditions as well as description of chosen discharges can be found in: Studium interakce plazmatu s kvasinkami Candida glabrata [13]

3. Results and discussion

The aim of this work was to study the effects of chosen CAPP sources on the yeast *C. glabrata* in order to examine the effects of individual discharges on a selected microorganism and to find the most efficient way for its inhibition as well as to optimize the set-up for further measurements.
The overall comparison of the investigated discharges shows that the most effective discharge for yeast inactivation is the unipolar MW jet, followed by the surface-wave MW jet, then the transient spark discharge and the corona pen. These results are quite understandable given the power used in each discharge that strongly correlates with the concentration of active particles produced by the discharge. With bigger applied power more active species, that play a major role in microbial inhibition, are produced, thus resulting in greater inhibitory effects. In case of zone stability, the transient spark discharge created the most stable zones, followed by the corona pen and unipolar MW jet and lastly the surface-wave MW jet. This high stability of the zones created by the transient spart discharge could beneficially be used in indirect plasma treatment (production of plasma treated liquid) for the microbial inhibition.

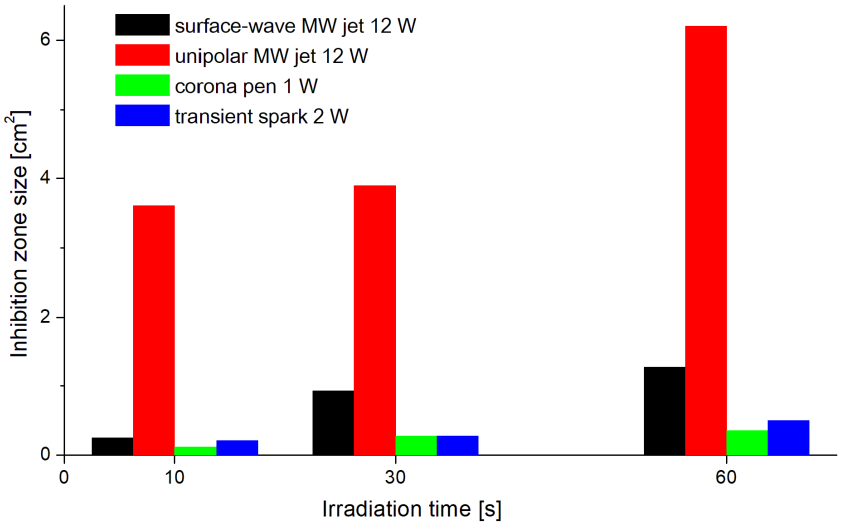

Fig 1: Comparison of efficiency in inhibition of *C. glabrata* for chosen CAPP sources

From previous experiments and studies, 3 basic parameters were selected: treatment time, power and initial concentration of cells, the effects of which have a major impact on the inhibitory effects. In all experiments, the general trend was confirmed: in the case of treatment time and power used, there is a directly proportional dependence of the inhibitory effects on these two factors. With longer treatment times and greater power, leading to more interactions of active particles with the microbial cells, better inhibitory effects can be achieved. On the other hand, the initial cell concentration shows an indirect dependency, and thus better inhibitory effects can be achieved with a smaller number of cells, which is mainly caused by greater susceptibility of planktonic cells compared to cells forming a compact layer or biofilm. The optimized parameters are listed below in Table 1 and will hopefully lead to further experiments with more complex inoculation substrates as well as to *in-vivo* tests.

Tab. 1. Table summarizing the optimized parameters for each discharge.

Optimized parameters	**Surface-wave MW jet**	**Unipolar MW jet**	**Corona pen**	**Transient spark**
Treatment time [s]	30 – 60	30 – 60	60 – 300	60 – x
Power [W]	9 – 12	9 – 12	1	2
Initial cell concentration [CFU/ml]	10^5, 10^6	10^5, 10^6	10^5, 10^6	10^4, 10^6, 10^8
Cultivation temperature [°C]	37			
Data gathering	24 h, 48 h, 7 days			

4. Conclusion

The main goal was to test the effects of different CAPP sources on the yeast C. glabrata and to optimize the plasma treatment to be applicable for the treatment of superficial candidias. From the measurements we can conclude that all tested CAPP sources have strong antimycotic effects, that are dependent on the treatment conditions. The unipolar MW jet was chosen as the most effective discharge for yeast inhibition and will therefore be used for further measurements.

5. References

[1] FIDEL, Paul L., Jose A. VAZQUEZ a Jack D. SOBEL. Candida glabrata: Review of Epidemiology, Pathogenesis, and Clinical Disease with Comparison to C. albicans. *Clinical Microbiology Reviews* [online]. 1999, **12**(1), 80-96 [cit. 2022-11-23]. ISSN 0893-8512. Dostupné z: doi:10.1128/CMR.12.1.80

[2] PFALLER, M. A. a D. J. DIEKEMA. Epidemiology of Invasive Candidiasis: a Persistent Public Health Problem. *Clinical Microbiology Reviews* [online]. 2007, **20**(1), 133-163 [cit. 2022-12-03]. ISSN 0893-8512. Dostupné z: doi:10.1128/CMR.00029-06

[3] SARDI, J. C. O., L. SCORZONI, T. BERNARDI, A. M. FUSCO-ALMEIDA a M. J. S. MENDES GIANNINI. Candida species: current epidemiology, pathogenicity, biofilm formation, natural antifungal products and new therapeutic options. *Journal of Medical Microbiology* [online]. 2013, **62**(1), 10-24 [cit. 2022-11-23]. ISSN 0022-2615. Dostupné z: doi:10.1099/jmm.0.045054-0

[4] BOECKMANN, Lars, Mirijam SCHÄFER, Thoralf BERNHARDT et al. Cold Atmospheric Pressure Plasma in Wound Healing and Cancer Treatment. *Applied Sciences* [online]. 2020, **10**(19) [cit. 2022-02-20]. ISSN 2076-3417. Dostupné z: doi:10.3390/app10196898

[5] NIEDŹWIEDŹ, IWONA, ADAM WAŚKO, JOANNA PAWŁAT a MAGDALENA POLAK-BERECKA. The State of Research on Antimicrobial Activity of Cold Plasma. *Polish Journal of Microbiology* [online]. 2019, **68**(2), 153-164 [cit. 2022-03-08]. ISSN 2544-4646. Dostupné z: doi:10.33073/pjm-2019-028

[6] SCHUSTER, Matthias, Rico RUTKOWSKI, Anna HAUSCHILD et al. Side effects in cold plasma treatment of advanced oral cancer—Clinical data and biological interpretation. *Clinical Plasma Medicine* [online]. 2018, **10**, 9-15 [cit. 2021-05-08]. ISSN 22128166. Dostupné z: doi:10.1016/j.cpme.2018.04.001

[7] SEMMLER, Marie Luise, Sander BEKESCHUS, Mirijam SCHÄFER et al. Molecular Mechanisms of the Efficacy of Cold Atmospheric Pressure Plasma (CAP) in Cancer Treatment. *Cancers* [online]. 2020, **12**(2) [cit. 2021-05-08]. ISSN 2072-6694. Dostupné z: doi:10.3390/cancers12020269

[8] KRČMA, František, Ivan TSONEV, Kateřina SMEJKALOVÁ et al. Microwave micro torch generated in argon based mixtures for biomedical applications. *Journal of Physics D: Applied Physics* [online]. 2018, **51**(41) [cit. 2021-05-08]. ISSN 0022-3727. Dostupné z: doi:10.1088/1361-6463/aad82b

[9] BOGDANOV, T., I. TSONEV a L. TRAIKOV. Microwave plasma torch for wound treatment. *Journal of Physics: Conference Series* [online]. 2020, **1598** [cit. 2021-05-08]. ISSN 1742-6588. Dostupné z: doi:10.1088/1742-6596/1598/1/012001

[10] SHALI, Parisa, Pegah ASADI, Mohammad Asna ASHARI a Babak SHOKRI. Cold atmospheric pressure plasma jet for tooth root canal disinfection. *2015 IEEE International Conference on Plasma Sciences (ICOPS)* [online]. IEEE, 2015, 1-1 [cit. 2022-02-20]. ISBN 978-1-4799-6974-6. Dostupné z: doi:10.1109/PLASMA.2015.7179714

[11] SAKUDO, Akikazu, Yoshihito YAGYU a Takashi ONODERA. Disinfection and Sterilization Using Plasma Technology: Fundamentals and Future Perspectives for Biological Applications. *International Journal of Molecular Sciences* [online]. 2019, **20**(20) [cit. 2021-05-08]. ISSN 1422-0067. Dostupné z: doi:10.3390/ijms20205216

[12] Katalog kultur: vláknité houby a kvasinky. In: *MUNI SCI: Ústav experimentální biologie Česká sbírka mikroorganismů* [online]. [cit. 2022-12-19]. Dostupné z: https://www.sci.muni.cz/ccm/houby/htmlh/T505.HTM

[13] TREBULOVÁ, Kristína. *Studium interakce plazmatu s kvasinkami Candida glabrata*. Brno, 2022. Diplomová práce. Vysoké učení technické, Fakulta chemická, Brno. Vedoucí práce Prof. RNDr. František Krčma, Ph.D.

PIC/MCC STUDIES OF LOW PRESSURE HELIUM CAPACITIVELY COUPLED RADIOFREQUENCY DISCHARGES WITH A STRUCTURED ELECTRODE

Ján Ďurian[1], Peter Hartmann[2], Štefan Matejčík[1], Andrew R. Gibson[3], Zoltán Donkó[2]

[1] *Department of Experimental Physics, Faculty of Mathematics, Physics and Informatics, Comenius University in Bratislava, Mlynská Dolina F2, 842 48 Bratislava, Slovak Republic*
[2] *Institute for Solid State Physics and Optics, Wigner Research Centre for Physics, 1121 Budapest, Konkoly Thege Miklós str. 29-33, Hungary*
[34] *Research Group for Biomedical Plasma Technology, Ruhr-Universität Bochum, Universitätsstraße 150, 44801 Bochum, Germany*

E-mail: durian5@uniba.sk

A low-pressure capacitively coupled radiofrequency (RF) helium discharge with structured electrodes is studied experimentally and numerically via kinetic simulations. In the experiment, Phase Resolved Optical Emission Spectroscopy (PROES) is used to obtain information on the electron-induced excitation dynamics with high spatial and nanosecond temporal resolution within the RF (13.56 MHz) period. The numerical simulations are carried out with a new 2d3v Particle-in-Cell/Monte Carlo Collisions (PIC/MCC) code accelerated by Graphics Processing Units (GPUs). The two approaches give consistent results for the excitation dynamics in and near a square indentation in the structured electrode. Lastly, the fluxes of vacuum ultraviolet (VUV) photons incident on the different surface parts of the electrode are studied. The results are discussed in relation to the relevant advanced surface processing and disinfection processes.

1. Introduction

Low pressure radiofrequency (RF) plasma sources are widely used in the field of surface treatment. This includes surface modification for textiles, plasma etching in the semiconductor industry, as well as coating deposition and surface sterilization in medical applications. These processes are primarily driven by ions, radicals and UV/VUV photons (known as active species) produced by excitation processes taking place in the RF discharges.

Radiofrequency plasma sources find wide utilization in the applications mentioned. RF plasmas showcase complex nanosecond time scale dynamics as the electrons react to the rapidly changing electric field thanks to their high mobility. These dynamics determine the overall properties of the plasma source, such as the electron energy distribution (EEDF) and the generation of active species, which in turn drives applications in the industry.

In most applications, a homogeneous treatment of the surface is desired, which means that fluxes of ions, radicals and UV/VUV photons should be constant along the entire surface that is being treated. The homogeneity of plasma, as well as the aforementioned fluxes, are greatly influenced by the plasma reactor design, the RF discharge parameters, as well as the shape of the electrodes and the material the electrodes are made of.

The aim of this work is to study the key parameters described in relation to the non-planar electrode structure via PIC/MCC simulations, and their implications on the application outcomes. We note that similar effects have already been studied in [1] experimentally and by an analytic model; the present work represents an advance as it provides a rigorous comparison between experimental data and results of kinetic particle simulations.

The results presented in this paper are published and explained in greater detail in [2].

2. Experimental setup

The discharge cell, situated inside a vacuum chamber, is composed of a top flat electrode and a bottom structured electrode 2.8 cm apart and 5 cm wide. Both electrodes are made of type 304 stainless steel, with the bottom electrode being modified with an indentation milled into it. The shape of the indentation is shown on Figure 1. The indentation is 1 cm deep, therefore the distance between the bottom of the indentation and the top electrode is 3.8 cm. The background gas is chosen to be helium at pressures from 40 Pa to 140 Pa.

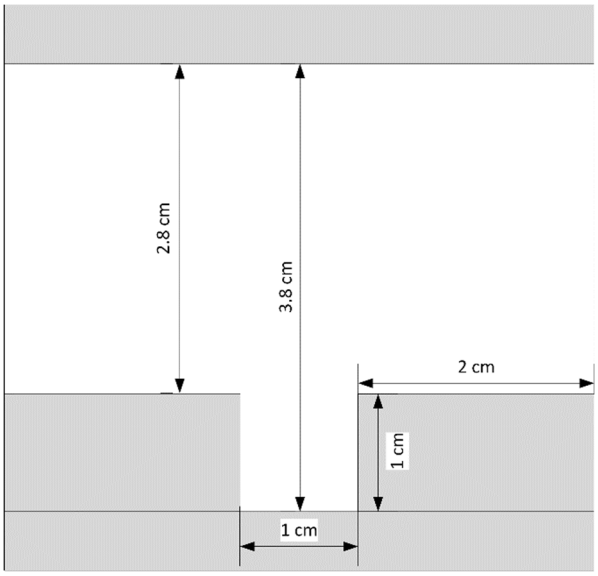

Figure 1 – Discharge chamber configuration with the structured electrode.

To validate our PIC/MCC model, the discharge is also studied experimentally using the PROES method [3]. The main diagnostic tool of the setup is a fast-gateable ICCD camera equipped with a telecentric lens centered on the axis of the indentation in the structured electrode. This diagnostic makes it possible to determine the spatio-temporal distribution of the excitation rate of a given atomic state of the working gas and this way it reveals information about the dynamics of high-energy electrons in the plasma.

3. PIC/MCC simulations and VUV photon tracing

A new Cartesian 2d3v GPU-accelerated PIC/MCC code was developed for modelling the discharge. The code is written in C/C++ and utilizes OpenMP of CPU-side computations while the GPU-side of the code was developed on top of the CUDA platform. The code is designed to handle arbitrary electrode shapes and boundary conditions (Dirichlet, periodic) that are definable by the user, allowing for a flexible means of modelling the discharges of our interest. The code uses numerical methods specifically tailored for execution on GPUs, namely the parallelized version of Successive Over-Relaxation (SOR) for solving the Poisson equation, and a massively parallelized Leapfrog scheme for integration of particle motion on a “one thread per particle” basis synchronized using atomic operations.

The code execution is split into the two parts: (i) the convergence stage during which only the particle counts are monitored, and (ii) the diagnostics stage during which detailed diagnostics data are collected. The convergence stage concludes once the particle counts reach overall constant levels, which requires simulating between 2000-3000 RF cycles of the discharge. The diagnostics data are not collected during the convergence stage to ensure maximum quality of the collected data.

The dimensions of the simulation domain defined by the model are 5 cm (laterally) and 3.8 cm (vertically). Periodic boundary conditions are applied at the left and right sides of the domain. The resolution of the computation grid is 256x192 points, which results in near-square grid cells given the

dimensions of the simulation domain. At the top boundary rests the flat, powered electrode, and at the bottom of the domain is the structured, grounded electrode.

In the collision model only electron-neutral and ion-neutral collisions are included. For electron-neutral collisions the "Biagi v8.92" [4] cross-section set is used. This set includes 51 collision types in total (elastic collisions, 49 excitation processes and ionization). For ion-neutral collisions only elastic collisions with neutral atoms are considered. A cross-section set proposed in [5-6] is used, and consists of an isotropic and a backwards scattering component to model this interaction.

Secondary electron emission and electron reflection are modelled at the electrode surfaces. Coefficients of $\gamma = 0.3$ and $\rho_e = 0.7$ are used for these two phenomena respectively, which are good estimates for the combination of the background helium gas and the stainless steel material used for the electrodes in the experimental setup [7-9].

The discharge is driven by a cosine waveform $\phi(t) = 0.5\,\phi_{pp} \cos(2\pi f t)$ with $\phi_{pp} = 340$ V. The simulations are executed for five different pressures: 40 Pa, 60 Pa, 80 Pa, 100 Pa and 140 Pa.

Computing of the fluxes of VUV photons is decoupled from the main PIC/MCC simulations. From the PIC/MCC simulations we obtain coordinates of excitation events to the state 2^1P, which is the one that leads to the emission of "primary" VUV photons of the resonance radiation. Subsequently, we can trace the propagation of these emitted photons, treating them as individual particles via Monte Carlo methods [10]. As these photons move through space, there is a probability P of them being absorbed into the background gas at every time-step

$$P = 1 - \exp(-n_0\,\sigma_{phabs}\,c\,\Delta t_{ph}) \quad (1)$$

where n_0 is the background gas density, σ_{phabs} is the photoabsorption cross section, c is the speed of light and Δt_{ph} is the time-step of the photon tracing simulation. The absorption of the photons is followed by re-emission and these processes repeat until the photons reach any of the boundary surfaces. This procedure makes it possible to compute the fluxes of the VUV photons at the various parts of the electrode surface.

4. Results

First, we present the comparison of experimental results with PIC/MCC simulations, as seen in Figure 2. The excitation rates to the 3s state of Helium (at 706 nm) at 40 Pa and 140 Pa pressures are presented, showing a very good agreement between the experiments and the simulations. Note that the experimental values are in arbitrary units, while the simulation results are in units of 10^{15} cm^{-3} s^{-1}. The bottom electrode is highlighted with a white contour.

The results show that at 40 Pa the plasma barely penetrates into the indentation in the structured electrode, while at 140 Pa very strong excitation is seen within the indentation. A crucial role in forming these excitation patterns is played by the potential, shown in Figure 3. The very high excitation rate at 140 Pa is caused by the potential penetrating into the indentation as seen in Figure 3(b1) where the potential closely follows the shape of the indentation. The sharp potential gradient creates an electric field sufficiently strong to form strong excitation within the indentation once the plasma sheath starts expanding, and the electrons are accelerated away from the walls of the indentation. This is not the case for lower pressures, 40 Pa, where the electric potential reaches into the indentation only very slightly. The potential above the indentation is about 125 V, which accelerates electrons away from the indentation towards the plasma bulk, leading to intense excitation not being observed within the indentation. Rather, the most intense excitation is observed right above the indentation.

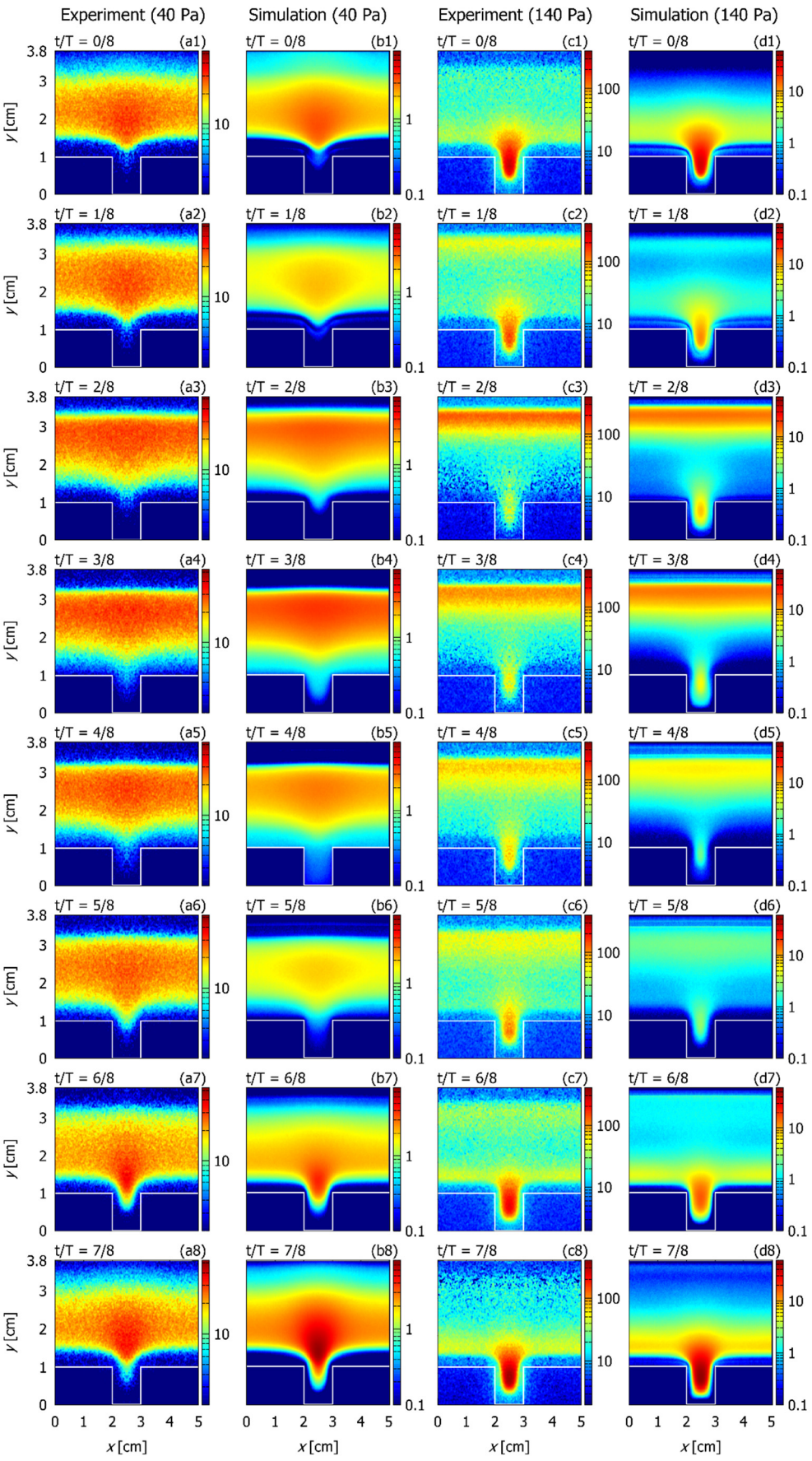

Figure 2 – Time evolution of the He 3s 706 nm excitation rate obtained from the experiments and PIC/MCC simulations [2].

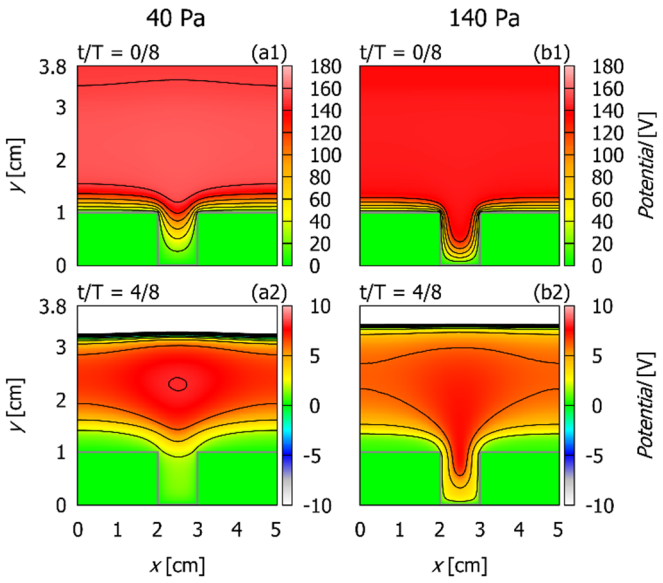

Figure 3 – Electric potential distributions for pressures 40 Pa and 140 Pa as computed by the PIC/MCC simulations [2].

The computed fluxes of ions and VUV (resonant) photons onto various parts of the structured electrode computed using the method described in section 3 as a function of pressure are shown in Figure 4. Like the PIC/MCC model, the photon tracing also uses periodic boundary conditions at the left and right sides of the simulation domain.

From the ion fluxes, only the ion flux on the top "face" part of the electrode shows a non-monotonic behavior, with its maximum at the pressure of 80 Pa. Since at higher pressures most of the excitation (and ionization) happens within the indentation of the electrode, the ion flux at the "face" of the electrode starts decreasing, and is eventually surpassed by the ion flux at the "side" walls of the structured electrode.

In all cases, the total flux of VUV photons increases with increasing pressure due to the excitation of the background helium atoms being more efficient. In this case, we observe a faster increase of VUV photon fluxes on the "side" and "bottom" parts of the electrode compared to the "face" part of the electrode. This indicates that at even higher pressures, the differences between the fluxes become insignificant, which means we can achieve high VUV photon fluxes inside the indentation of the electrode given the background gas pressure is high enough.

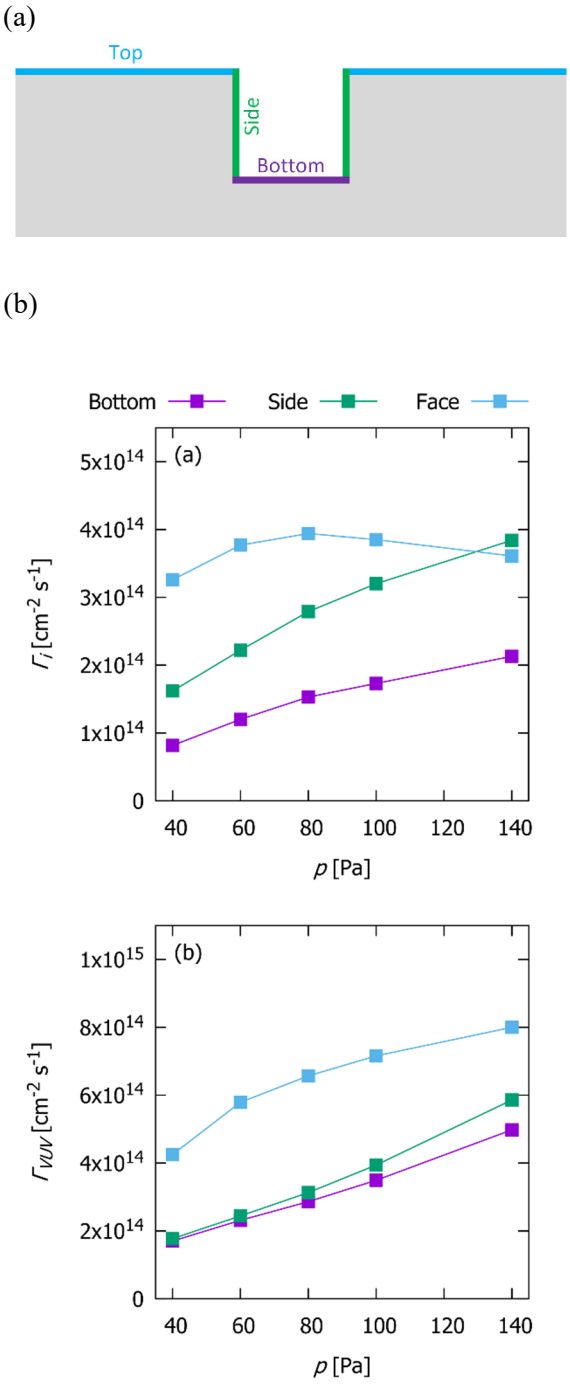

Figure 4 – Ion ((b) top) and VUV ((b) bottom) photon fluxes onto the different parts (shown in (a)) of the structured electrode [2].

5. Conclusion

A radio-frequency discharge with a structured electrode in helium gas at $f = 13.56$ MHz with peak-to-peak driving voltage of $\phi_{pp} = 340$ V was studied in the pressure range of 40 Pa to 140 Pa. A structured electrode with a 1 cm x 1 cm square indentation was used in the experimental and numerical studies.

The experiments relied on the Phase Resolved Optical Emission Spectroscopy (PROES) method, while the numerical simulations were carried out with the Particle-in-Cell/Monte Carlo Collisions (PIC/MCC) method. A new Cartesian 2d3v PIC/MCC GPU-accelerated code was developed to facilitate the numerical studies. The PROES measurements were performed on the

He-I 706 nm line and have revealed the 2D temporal dynamics of the excitation rate that is tightly related to the electron dynamics. The same excitation rates computed by the new PIC/MCC code showed a very good agreement with the experimental results.

Increasing the background gas pressure led to enhanced excitation within the indentation and around its entrance. At low pressures, no significant excitation was observed within the indentation, while at high pressures the excitation within the indentation was very strong.

This work studied key parameters relevant to charged particle dynamics and fluxes on surfaces in a well-defined two-dimensional system. In real application scenarios related to sterilization or coating deposition, more complex background gas mixtures and surface structures may be present. These differences will lead to quantitatively different results, however, some general application-relevant conclusion can still be drawn from the results of this work.

It was found that the background gas pressure has a very strong influence on the overall temporal dynamics of the primary species (electrons, ions) in the pressure range studied. As a result, the variation of the pressure can be utilized to control the electron dynamics in the discharge for the purpose of for instance enabling enhanced dissociation of molecules close to surfaces.

The ion fluxes were found to be the highest at the top “face” part of the structured electrode for most of the studied conditions, although the fluxes of ions at the “side” and “bottom” parts of the structured electrode were still significant.

Controlling the pressure also allows for influencing the homogeneity of VUV photon fluxes incident on different parts of the structured electrode, which is an important parameter in applications such as sterilization. We observed a 2 times lower VUV photon fluxes within the indentation of the structured electrode, which in practice would translate to a factor of 2 times longer sterilization time to ensure the indentation is effectively sterilized compared to a flat surface.

6. Acknowledgments

This work was supported by the Slovak Research and Development Agency Project No. APVV-19-0386, the Comenius University grant UK/205/2021 and the Hungarian Office for Research, Development and Innovation (NKFIH) grant K134462.

7. References

[1] Schmidt N, Schulze J, Schüngel E, Czarnetzki U 2013 Journal of Physics D: Applied Physics 46 505202

[2] Ďurian J, Hartmann P, Matejčík Š, Gibson A R and Donkó Z 2022 Plasma Sources Sci. Technol. 31 095001

[3] Ganz T, Schulz-von der Gathen V and Döbele H 2004 Plasma Physics 44 523

[4] Biagi S F, Fortran program MAGBOLTZ v8.92, www.lxcat.net, retrieved on October 22, 2021

[5] Phelps A V 1994 Journal of Applied Physics 76 747

[6] Compilation of Atomic and Molecular Data 2005; http://jila.colorado.edu/~avp/

[7] Doughty D, Den Hartog E and Lawler J 1987 Physical review letters 54 2668

[8] Den Hartog E, Doughty D and Lawler J 1988 Physical Review A 38 2471

[9] Schulenberg D A, Korolov I, Donkó Z, Derzsi A and Schulze J 2021 Plasma Sources Science and Technology 30 105003

[10] Fierro A, Moore C, Scheiner B, Yee B T and Hopkins M M 2017 Journal of Physics D: Applied Physics 50 063202

PLASMA ACTIVATED WATER: FROM THE SEED GERMINATION TO THE PLANT GROWTH

Ludmila Čechová, Kateřina Lišková, Tomáš Vozár, František Krčma, Zdenka Kozáková

Faculty of Chemistry, Brno University of Technology, Purkyňova 118/464, 612 00 Brno, Czech Republic

E-mail: ludmila.cechova@vut.cz

In this work, we investigated the effect of Plasma Activated Water (PAW) on seeds germination and subsequent plant growth. Plasma activated water was prepared by 3 different plasma systems and the content of reactive oxygen and nitrogen species was determined using colorimetric reagents and UV-VIS spectrometry. Distilled as well as tap water was used for preparation of PAW. A germination test was used to assess effects of PAW on germination and early growth of seedlings. It was found out that PAW can increase germination of seeds of *Zea maize* L. Pot experiments were conducted with the plant *Raphanus sativa* L. In pot experiments, however, PAW did not have any positive effect on the plant growth. The effect on the plant growth was determined by weighing of both underground part (bulb) and aboveground part (leaves) as well as by the content of the dry matter.

1. Introduction

The excessive use of pesticides in our agriculture can be potentially harmful to non-target organism such as aquatic organisms, birds, and animals. They can also have a negative impact on human health [1]. New field of plasma research, called plasma agriculture, is expanding. Plasma activated water (PAW) is prepared by the interaction of plasma with liquids. The chemistry of plasma activated water is like the gas plasma chemistry, with short-lived reactive oxygen and nitrogen species (RONS) such as NO·, ·OH or $\cdot O_2^-$. These short-lived species form long-lived RONS, such as hydrogen peroxide, nitrites, and nitrates, which stay present in water for days. Thanks to these RONS plasma activated water has its unique properties. Low pH of PAW causes antibacterial properties, NO_3^- can act as a source of nitrogen, which is a paramount plant nutrient, while H_2O_2 in very low concentrations can stimulate seed germination. These properties can make plasma activated water a new and environmentally friendly tool to increase and sustain agricultural production [2].

2. Experimental setup

Plasma activated water for seed gemination was prepared by 3 different plasma systems:

1. dielectric barrier discharge (DBD) with the liquid electrode generating plasma above the water surface [3];
2. a pin-hole electrode with the high frequency source generating plasma directly in liquids [4,5];
3. bubbling of gaseous products from dielectric barrier discharge into water.

Physical-chemical properties of PAW were analysed by measuring of pH, conductivity, and concentration of H_2O_2, NO_2^- and NO_3^-. H_2O_2 was analysed using titanium reagent and UV-VIS spectrometer, while NO_2^- and NO_3^- were analysed using commercial kit based on the Griess reaction.

The germination test is a standard test in botany. Seeds of *Zea maize* L. were placed on a Petri dish with a filter paper and 20 ml of PAW or control water. After 5 days, germinated seeds were counted, and length of root was measured. Germination G (in %) was calculated using the formula (1) where G_f is number of germinated seeds in 5 days and S is number of all seeds in experiment.

Pot experiments with *Raphanus sativa* L. were performed in growth chambers with controlled temperature and illumination. Pots were filled with approx. 1.5 kg of soil. First, seeds of *R. sativa* were germinated in the Petri dish either in distilled water (control group) or in PAW (PAW group). After 3 days, seeds were planted in pots with soil. After 40 days, experiment was finished. *R. sativa* was taken out of the pots, each plant was washed with water, and let dry. *R. sativa* was cut into 2 parts – the aboveground part (leaves) and the underground part (bulb) and all parts were weighted on scales. The amount of the dry matter was determined in 3 repetitions for each variant. The dry matter *DM* (in %) was based on the determination of the weight loss of the sample after its drying at temperature of 105 °C

to the constant weight, as calculated according to the formula (2), where M_1 is the weight of the fresh matter and M_2 is the weight of the dried matter.

$$G = \frac{G_f}{S} \cdot 100 \quad (1)$$

$$DM = \frac{M_2}{M_1} \cdot 100 \quad (2)$$

3. Results

Based on the plasma system used, the composition of PAW was different (Table 1). When using the pin-hole discharge, PAW contained mostly H_2O_2. With the DBDs (above water and with bubbling of products), NO_3^- was the dominant product. The pH of PAW was also changed based on the system, with the pin-hole discharge PAW from distilled water having the lowest pH 6. Based on this data, we can predict which PAW would be the most suitable for agricultural application. For germination tests, PAW made from all systems was tested. For pot experiments, PAW with NO_3^- as the dominant product was chosen, because nitrogen is the most important nutrient for the plant growth. The DBD with bubbling of products allowed PAW to be made in much higher quantities (in our case, 500 ml) than the DBD with the liquid electrode, which was the reactor that had the maximal volume of 75 ml, only.

Table 1 Properties of PAW prepared by different plasma systems in distilled and tap water. Time of plasma treatment for all PAWs was 2 minutes. Volume of water: DBD 75 ml; pin-hole 150 ml; bubbling 150 ml. (LOD = limit of detection)

Discharge	pH		G (μS·cm^{-1})		H_2O_2 (mg·l^{-1})		NO_2^- (mg·l^{-1})		NO_3^- (mg·l^{-1})	
	Distilled	Tap	Distilled	Tap	Distilled	Tap	Distilled	Tap	Distilled	Tap
Control	7.0	8.2	5	450	Under LOD	Under LOD	Under LOD	Under LOD	Under LOD	21.3±1.9
DBD	6.5	8.1	31	505	0.74±0.0	0.96±0.27	0.16±0.01	0.85±0.11	7.4±0.2	35.9±3.8
Pin-hole	6.0	7.9	37	520	6.97±0.01	2.1±0.3	1.55±0.01	0.01±0.01	1.0±0.1	28.6±3.4
Bubbling	6.9	8.1	20	500	0.79±0.09	0.84±0.11	0.02±0.01	0.11±0.06	4.5±0.2	27.6±1.9

Table 2 Properties of PAW used for pot experiments with *R. sativa*. The volume of water was 500 ml. (LOD = limit of detection)

Discharge	Time (min)	pH	G (μS·cm^{-1})	H_2O_2 (mg·l^{-1})	NO_2^- (mg·l^{-1})	NO_3^- (mg·l^{-1})
Control	0	7.0	5	Under LOD	Under LOD	Under LOD
Bubbling	40	5.0	200	0.57±0.09	0.0081±0.0008	30±3

Seeds of corn *Z. maize* were chosen for gemination tests. *Z. maize* seeds in control samples had germination of 50–55 %. Germination of seeds germinated in PAW had increased by 5–20 % based on the plasma reactor and type of water used for PAW. The best results were obtained when using PAW from the DBD with bubbling of products (Figure 1).

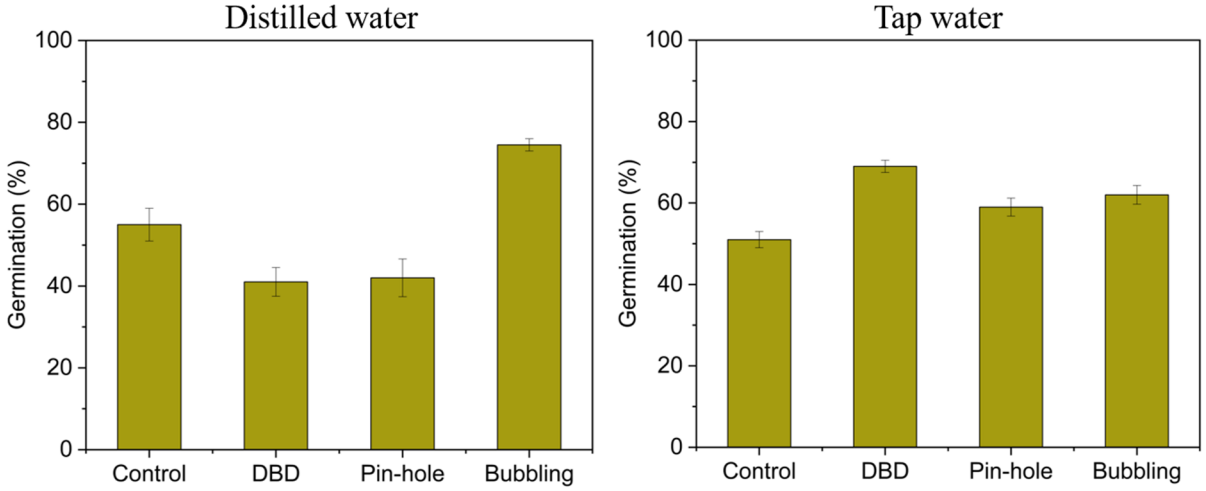

Figure 1 Graphical representation of results from germination test with *Z. maize* in PAW.

Based on results from germination tests, PAW made by the DBD with bubbling of products was chosen for pot experiments. The advantage of this system was that it allowed higher production of the PAW volume, which was necessary for the pot experiment. Another advantage of this system was that PAW can have different composition based on the volume of water and time of the discharge treatment. PAW was produced in 500 ml beaker with activation time of 40 minutes to ensure sufficient concentration of NO_3^-.

R. sativa was grown in 4 different variations: soil irrigation with distilled water (Control group), seeds germinated in PAW and then soil irrigated with distilled water (PAW group 1), foliar application of PAW with soil irrigation by distilled water (PAW group 2) and soil irrigation with PAW (PAW group 3). According to the results in Table 3, there was no significant increase of growth but rather a decrease in the case of seeds germinated in PAW and soil application of PAW. The results were processed using a two-population t-test, which confirmed that the difference in the weight of the underground part of PAW group 1 and PAW group 3 compared to the control is statistically significant at the level of significance $p = 0.01$. Bulb weights were decreased by the application of PAW. Only the variation with the foliar application of PAW did not influence the growth of *R. sativa* both negatively and positively. The data in Table 4 show that PAW increased the content of the dry matter of the underground part (by 1.2−2.3 %, only) and simultaneously, the content of dry matter of the aboveground part was decreased by up to 4.3 %. Overall, the effect of PAW on the growth of *R. sativa* was not significantly positive. The main issue here might be the pH 5.0 of the used PAW which decreased the growth of *R. sativa* in the soil irrigation group as well as in the germinated in PAW group. More research regarding to the PAW effect on the plant growth needs to be done to find a suitable composition and application of PAW which can help to induce the growth of plants.

Table 3 Mean weight of root and leaves of *R. sativa* at the end of pot experiments.

	Bulb weight (g)	Leaves weight (g)
Control group	30±13	16±9
PAW group 1	20±12	11±8
PAW group 2	29±18	16±11
PAW group 2	19±6	9±2

Table 4 Content of dry mass in *R. sativa* at the end of pot experiments.

	Dry mass bulb (%)	Dry mass leaves (%)
Control group	4.5±1.7	14.1±4.6
PAW group 1	6.4±0.8	10.4±2.0
PAW group 2	6.8±1.5	11.5±3.3
PAW group 3	5.7±1.2	9.8±0.8

4. Acknowledgements

This work was carried out within the frame of COST Action CA19110 (PlAgri).

5. References

[1] Mahmood I et al 2016 *Plant, soil and microbes* (Springer)
[2] Puač N, Gherardi M, Shiratani M 2018 *Plasma Processes and Polymers* **15** 1700174
[3] Škarpa, P et al. 2020 *Water* **12** 3545
[4] Krčma F et al 2018 *Plasma Sourc. Sci. and Technol.* **27** 065001
[5] Krčma F 2019 European Patent EP3122161B1.

CHALLENGES DURING THE DESIGN OF A DC MICROPLASMA CELL INTEDED FOR *IN SITU* TEM

Luka Hansen[1], Niklas Kohlmann[2], Lorenz Kienle[2], and Holger Kersten[1]

[1]*Institute of Experimental and Applied Physics, Kiel University, Kiel, Germany*
[2]*Institute for Material Science, Kiel University, Kiel, Germany*
E-mail: lhansen@physik.uni-kiel.de

A microplasma cell intended for *in situ* TEM studies of the plasma surface interaction is being designed. Several design challenges were already overcome and solutions for the remaining ones were apparently found. An overview of the designed microplasma discharge, as well as *ex situ* observed surface modifications induced by the microplasma and the recent progress regarding the *in situ* experiments is given.

The plasma surface interaction is still one of the most discussed topics in plasma technology due to its relevance to the production and modification of micro- or even nanostructured surfaces.
In situ observation of plasma surface modifications is possible if a microplasma is inserted into a TEM as shown by proof of principle experiments in 2013 [1]. Still, multiple challenges have to be overcome for the development of a microplasma cell suitable for TEM integration. The electrodes have to be electron beam transparent and are therefore restricted to tens of nanometers in thickness. With limited space available inside of the TEM, one is restricted to an atmospheric pressure microplasma, which has to be stable and can be operated without the risk of arcing or other instabilities, as they could break the thin electrodes. The microplasma itself has to be vacuum-proof encapsulated and high voltages for the plasma ignition have to be implemented into the TEM.
A DC microplasma was designed and intensively studied by current-voltage measurements and optical diagnostics to ensure its stable operation in the normal glow regime [2]. Further, passive thermal probes (PTPs) [3] have been used to measure the energy flux from the microplasma to the electrode surfaces. The energy flux is an important quantity to measure as it is responsible for plasma induced surface modifications [4,5].
Ex situ performed measurements proved the possibility to setup the electrodes thin enough for TEM imaging and study the surface modifications [6]. The observed surface modifications correlated with the measured energy fluxes. Larger energy fluxes resulted in stronger texturing and increased grain growths of the microplasma treated thin films. Further, not only the total amount of the energy flux is responsible for the surface modifications, also the composition and power transfer mechanisms influence the texture of the plasma treated thin film. Based on a simplified model, different power transfer mechanism of the plasma generated ions towards the surface were identified and correlated with the observed surface modifications [6].
Furthermore, the designed *in situ* microplasma cell was successfully introduced into the TEM and first images without plasma could be taken. Electrical isolation problems prevented plasma ignition inside of the TEM, but will be solved by rebuilding the vacuum-proof encapsulation from ceramic.
This contribution summarizes the already overcome challenges and updates about the recent steps towards *in situ* TEM imaging.

References

[1] K. Tai *et al.*, 2013 *Scientific Reports* **3** 1325
[2] L. Hansen *et al.,* 2022 *Plasma Sources Science and Technology* **31** 035013
[3] L. Rosenfeldt, L. Hansen and H. Kersten, 2021 *IEEE Transactions on Plasma Science* **49** 3325-3335
[4] H. Kersten *et al.* 2001 *Vacuum* **63** 385-431
[5] A. Anders, 2010 *Thin Solid Films* **518** 4087-4090
[6] L. Hansen *et al.,*2023 *Thin Solid Films* **765** 139633

ON THE IN-SITU DETERMINATION OF THE EFFECTIVE SECONDARY ELECTRON EMISSION COEFFICIENT IN LOW-PRESSURE CAPACITIVELY COUPLED RADIO FREQUENCY DISCHARGES

R.U. Masheyeva[1,2], P. Hartmann[1], J. Schulze[3,4], K.N. Dzhumagulova[2], M. Myrzaly[2], Z. Donkó[1]
E-mail: masheyeva.ranna@gmail.com

[1]*Wigner Research Centre for Physics, H1121 Budapest, Hungary*
[2]*IETP, Al-Farabi Kazakh National University, 71 Al-Farabi Ave., Almaty 050040, Kazakhstan*
[3]*Chair of Applied Electrodynamics and Plasma Technology, Department of Electrical Engineering and Information Science, Ruhr-University Bochum, D-44780 Bochum, Germany*
[4]*Key Laboratory of Materials Modification by Laser, Ion and Electron Beams, School of Physics, Dalian University of Technology, Dalian, China*

In most low-pressure plasma sources a considerable interaction exists between the plasma and the surrounding surfaces, including the electrodes. Most importantly, electron reflection and emission can influence the plasma density and the electron power absorption mechanisms. Data for the coefficients that characterize these processes are rather limited. Here, we propose a method for the determination of the effective secondary electron emission coefficient based on the DC self-bias voltage generation due to the Electrical Asymmetry Effect when the capacitively coupled radio frequency plasma is driven by two consecutive harmonics of a base radio frequency signal.

1. Introduction

Capacitively Coupled Plasma (CCP) sources have a wide range of applications for surface modification, layer deposition and etching, in, e.g., microelectronics [1,2]. Due to the use of radio frequency (RF) excitation in these systems the processing of non-conducting samples is also possible. For most efficient processing the knowledge-based optimization of these plasma sources is necessary, which requires well-defined laboratory experiments and high-fidelity modeling. For the latter, one needs to build discharge models which need a set of input data that describe the interaction of the charged species and radicals with the background gas / gas mixture as well as with the surfaces that surround the plasma. In order to obtain reliable modeling predictions for the plasma characteristics, accurate input data are necessary [3,4]. Among these data, the ones that describe the interaction of the plasma species with the surrounding surfaces are often not known to the desired accuracy. Most important examples of such data are the ion and electron-induced electron yields at the electrodes. When the energy of the charged species reaching the electrodes is limited, these processes can be approximated as (i) ion-induced electron emission via the potential mechanism and (ii) elastic reflection of impinging electrons.

In modeling studies, process (i) is often characterized by an effective electron yield, γ, which may also include contributions of species other than ions [5], while process (ii) is characterized by the effective reflection coefficient R. Ideally, these coefficients should be available to modelers for various gas/electrode material combinations. The situation is further complicated by the fact that these values may depend on the particle energy distribution functions and electrode surface conditions, which are influenced by the actual operating conditions of the discharge. Furthermore, the surface coefficient values available in the literature often originate from surface physics experiments conducted under ultrahigh vacuum conditions with heavily sputtered samples, which scenario differs strongly from those found in practical discharge physics experiments and applications.

Therefore, during the past years a number of studies applying various approaches have been carried out to determine the values of γ and R, in situ. These studies have all combined experimental recordings of some

plasma characteristics and computational studies in which the same characteristics have been derived as a function of the surface coefficients in CCPs. The determination of the latter was based on finding the best agreement between the measured and computed data. In [6], the spatio-temporal distribution of the electron-impact excitation rate was targeted to be matched in CCPs operated in argon gas. This approach utilized the changes of these excitation patterns as a function of the effective secondary yield, γ. In addition to these diagnostics, the electron density and the flux-energy distribution function of the positive ions was also used in [7] for finding the in-situ values of γ and R. Precise energy-resolved mass spectrometry measurements of the ion flux-energy distribution function that allowed revealing the details of the bimodal peak created by ions flying through the sheath without collisions [8] allowed the determination of the same pair of parameters for stainless steel and aluminum oxide surfaces. In a recent paper [9] we have also proposed an independent way to determine the surface coefficients discussed above. Our method is based on the measurements of the DC self-bias voltage that develops in a geometrically symmetrical CCP due to the Electrical Asymmetry Effect [10] when it is driven by a base RF harmonic and its second harmonic with a controllable phase angle. The method utilizes the dependence of this self-bias voltage on the surface coefficients.

2. Simulation method

Our numerical results are obtained from one-dimensional (1D3V) bounded electrostatic Particle in Cell / Monte Carlo Collisions (PIC/MCC) simulations. As this is a well-established method, the description of its details is omitted here, and only some details specific to the current study are outlined below. More information about the approach can be found in the literature, e.g. [11].

Our code considers electrons and Ar^+ ions and follows their motion in an electric field that is defined by the potentials of the electrodes and the presence of the charged particles in the electrode gap. For the $e - Ar$ collisions, we use a cross section set that includes elastic scattering, excitation, and ionization processes, while for $Ar^+ - Ar$ collisions, a set that includes elastic collisions with an isotropic and a backward scattering channel is used.

The plasma forms between two plane and parallel electrode; one of these situated at $x = 0$ is powered, while the other electrode at $x = L$ is grounded. The voltage waveform at the powered electrode is:

$$\phi(t) = V_1 cos(2\pi f_1 t) + V_2 cos(4\pi f_1 t + \theta) + \eta; \quad (1)$$

where V_1 and V_2 are the amplitudes of the two harmonic signals, θ is the phase angle between these, and the last term is the DC self-bias generated by the plasma.

The equation of motion of the charged particles is integrated using the leapfrog scheme, with a time step $\Delta t = T/3000$. The computational grid for the potential, the electric field, and the charged particle densities comprises 500 points. These parameters fulfill the relevant stability criteria of the PIC/MCC method. At the electrode surfaces, two processes are considered: (i) Ar^+ ions arriving at the surface induce the emission of a secondary electron with a probability that is expressed by the secondary electron yield, γ. (ii) Electrons reaching the electrodes undergo an elastic reflection event with a probability R. The DC self-bias voltage driven by *N=2* harmonics is determined in an iterative manner. At the initialization of the simulation, $\eta = 0$ V is set. After executing the simulation for a given number of RF cycles, the currents of the electrons and argon ions reaching each electrode are compared. Depending on the balance of these currents, the DC self-bias voltage is changed by a small quantity. This procedure is continued until η reaches a converged value and the time-averaged charged particle currents to each of the two electrodes balance.

3. Results

The simulations are carried out for Ar gas, for different values of pressure $p = 5$ Pa, 10 Pa, 40 Pa; electrode gap $L = 2.5$ cm; and base frequency $f_1 = 13.56$ MHz. Driving voltage waveforms specified by Eq. (1) are used with voltage amplitudes of $133.5\,V$ and $66.7\,V$, with phase angles $\theta = 90°$ (where η is

nearly minimized) and 180° (where η is nearly maximized). For the surface coefficients, we adopt the following values: the secondary electron yield γ is varied between 0 and 0.4 and the elastic reflection coefficient of the electrons ranges between R = 0 and 0.7.

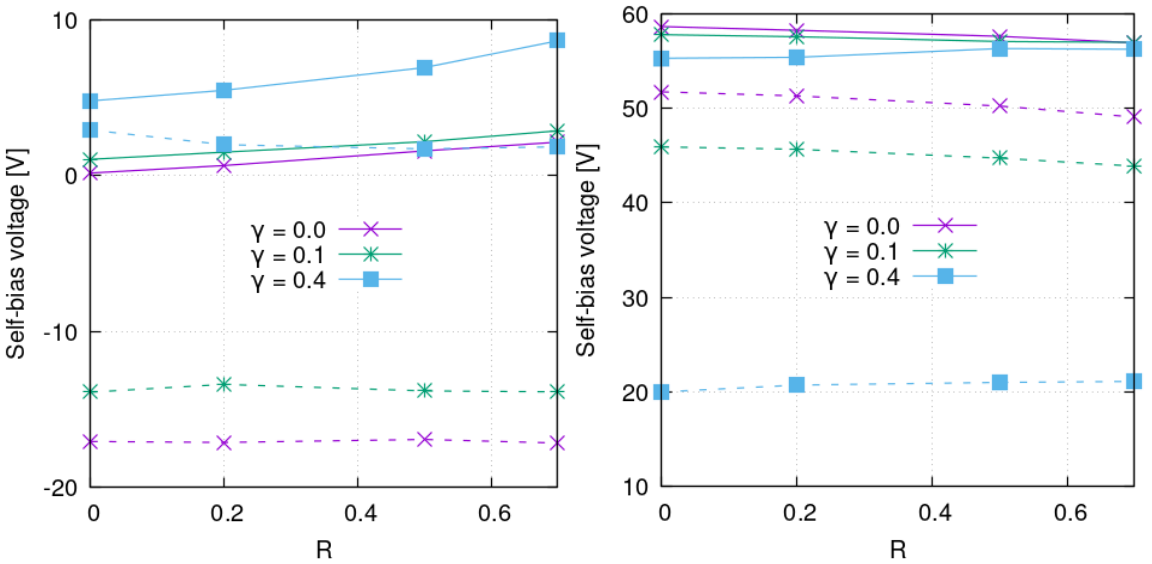

Fig. 1. Self-bias voltage as a function of the electron reflection coefficient R obtained from the PIC/MCC simulations for $\theta = 90°$ (left) and $\theta = 180°$ (right). Discharge conditions are as follows: Ar $p = 5$ Pa (solid lines), $p = 40$ Pa (dashed lines), $L = 2.5$ cm, $f_1 = 13.56$ MHz.

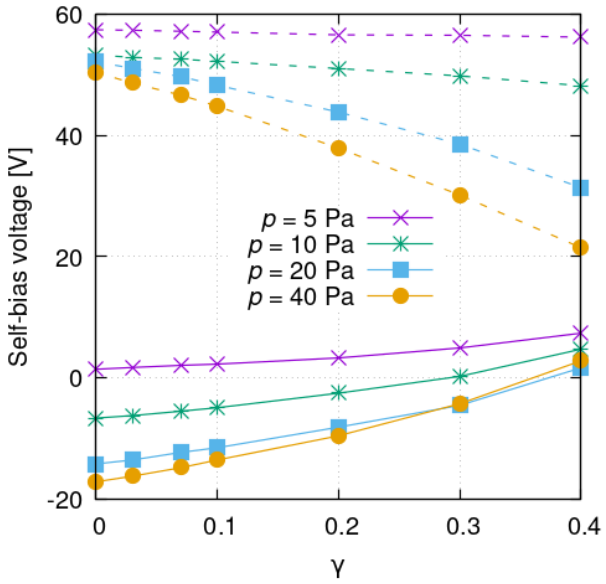

Fig.2. Self-bias voltage as a function of secondary electron yield (γ) obtained from the PIC/MCC simulations for $\theta = 90°$ (solid lines) and $\theta = 180°$ (dashed lines) for an electron reflection coefficient R is 0.5. Discharge conditions are as follows: $L = 2.5$ cm, $f_1 = 13.56$ MHz.

The values of the DC self-bias voltage (η) as a function of the surface coefficients, computed from the PIC/MCC simulations are shown in Figures 1 and 2. Figure 1 illustrates the dependence of the self-bias voltage on the reflection coefficient, computed at fixed values of gamma and the gas pressure, while Figure 2 displays the dependence of η on gamma, at fixed R and a sequence of pressures. These data

clearly indicate that the electron reflection has a weak effect on the self-bias voltage, especially at higher pressures, e.g., at 40 Pa, whereas at this pressure gamma appears to have a marked effect on η. These dependencies lead us to conclude that the method is not easily applicable for the determination of R, but has a good prospect for the measurement of gamma in CCPs.

Under the conditions of the specific excitation voltage waveform the charged particle dynamics generally differ at the two sides of the plasma. At very low pressures, however, the motion of electrons is highly non-local and this results in a softer dependence of η on gamma at e.g., 5 Pa pressure (see Figure 2). At higher pressures the effects related to secondary electrons taking place at the two sides of the plasma are more separated, and therefore, the best conditions for the determination of gamma in an experiment favor the relatively high pressures.

Laboratory experiments are currently conducted to provide a proof for this principle of in-situ determination of the effective ion-induced secondary electron yield in CCPs.

Acknowledgments

This work was supported by the National Office for Research, Development and Innovation (NKFIH) of Hungary (Grant No. K-134462), the German Research Foundation (Grant No. 428942393), and the Ministry of Education and Science of the Republic of Kazakhstan (Grant No. AP09058005).

4. References:

[1] Makabe T and Petrović Z L 2014 *Plasma Electronics: Applications in Microelectronic Device Fabrication* (London: Taylor and Francis) **26**.

[2] Chabert P and Braithwaite N 2011 *Physics of Radio-Frequency Plasmas* (Cambridge University Press).

[3] Bogaerts A and Gijbels R 2000 *Atomic and Molecular Data and Their Applications ed K A Berrington* (New York: American Institute of Physics) 49–66.

[4] Donkó Z et al 2018 *Plasma Phys. Control. Fusion* **60** 014010.

[5] Phelps A V and Petrović Z L 1999 *Plasma Sources Sci. Technol.* **8** R21.

[6] Daksha M, B Berger, E Schuengel, Korolov I , Derzsi A, Koepke M, Donkó Z and Schulze J 2016 *J. Phys. D Appl. Phys.* **49** 234001.

[7] Schulenberg D A, Korolov I, Donkó Z, Derzsi A and Schulze J 2021 *Plasma Sources Sci. Technol.* **30** 105003.

[8] Schulze C, Donkó Z, Benedikt J 2022 *Plasma Sources Sci. Technol.* **31** 105017.

[9] Masheyeva R U, Dzhumagulova K N, Myrzaly M, Schulze J and Donkó Z 2021 *AIP Advances* **11** 075024.

[10] Heil B G, Czarnetzki U, Brinkmann R P and Mussenbrock T 2008 *J. Phys. D: Appl. Phys.* **41** 165202.

[11] Donkó Z, Derzsi A, Vass M, Horvath B, Wilczek S, Hartmann B, Hartmann P 2021 *Plasma Sources Sci. Technol.* **30** 095017.

UTILIZING VUV/UV-RADIATION FROM AN ATMOSPHERIC PRESSURE PLASMA JET TO INITIATE PHOTO-CHEMISTRY IN ORGANOSILICON PRECURSORS

Tristan Winzer[1], Natascha Blosczyk[1], Jan Benedikt[1,2]

[1]*Institute of Experimental and Applied Physics, Kiel University, Kiel, Germany*
[2]*Kiel Nano, Surface and Interface Science KiNSIS, Kiel University, Kiel, Germany*
E-Mail: winzer@physik.uni-kiel.de

We will present a device for utilizing VUV/UV-radiation from an atmospheric pressure plasma to remotely initiate photo-chemistry in a precursor gas. This source was used to study the photo-chemistry of organosilicon precursors by ion mass spectrometry. Deposited films were analysed using Fourier-transform infrared (FTIR) spectrometry.

Atmospheric-pressure plasmas in pure helium or argon are efficient sources of vacuum-ultraviolet and ultraviolet radiation (VUV/UV) in a wavelength range between 60 nm and 150 nm [1]. The emission spectrum in this wavelength region is dominated by the excimer emission continua of helium (60 nm to 120 nm) and argon (105 nm to 145 nm). Excimers are efficiently produced in three-body-collisions due to the high collision rate at atmospheric pressure [2]. These highly energetic photons can be utilized to remotely initiate photo-chemistry in precursor gases like e.g. acetylene, hexamethyldisiloxane (HMDSO), tetramethylsilane (TMS) or hexamethyldisilane (HMDS) without direct contact to the plasma [3]. This enables film-deposition from precursor gases without several drawbacks from the interaction of the highly energetic electrons in the plasma with the precursor gas. These drawbacks include deposition inside the plasma source as well as particle formation due to negative ions from electron attachment processes [4].

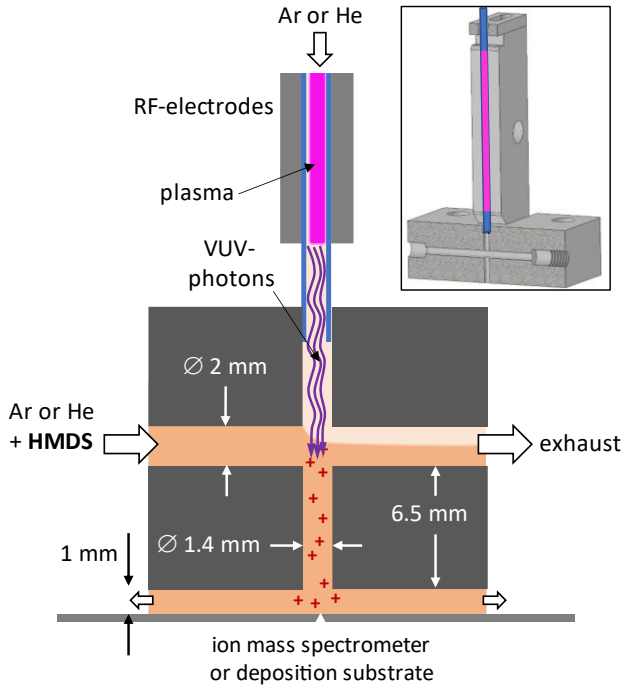

Figure 1: Schematic setup of the Crossflow-Capillary-Jet. The plasma feed gas is supplied from the top, while the precursor is admixed to a crossflow from the left side. The inset shows a 3D-cross-section of the real jet machined from stainless steel.

To study and optimize the photo-chemistry, a source that provides effective separation of plasma species and precursor gas flow as well as stable plasma operating conditions is necessary. The so-called Crossflow-Capillary-Jet is based on the UV-Jet introduced by Schneider et al. [5] and the Capillary-Jet [6]. The plasma is ignited inside a capillary acting as a dielectric in front of the electrodes by a sinusoidal RF-voltage with a frequency of 13.56 MHz. Due to the cross-field geometry, the plasma is closely confined between the electrodes. A sketch of the Crossflow-Capillary-Jet is shown in figure 1. The tip of the capillary is glued into a stainless-steel block housing the crossing gas channel. The distance between the plasma and the crossflow section is 10 mm. VUV/UV-photons produced in the plasma travel this distance through the noble gas atmosphere into the crossflow section. The crossing channel has approximately twice the cross-sectional area as the vertical channel, which is necessary for effective separation of plasma species and photo-chemistry products. Another requirement for this separation is the ratio of gas flows through both channels being 2-to-1 with the higher gas flow through the crossing channel.

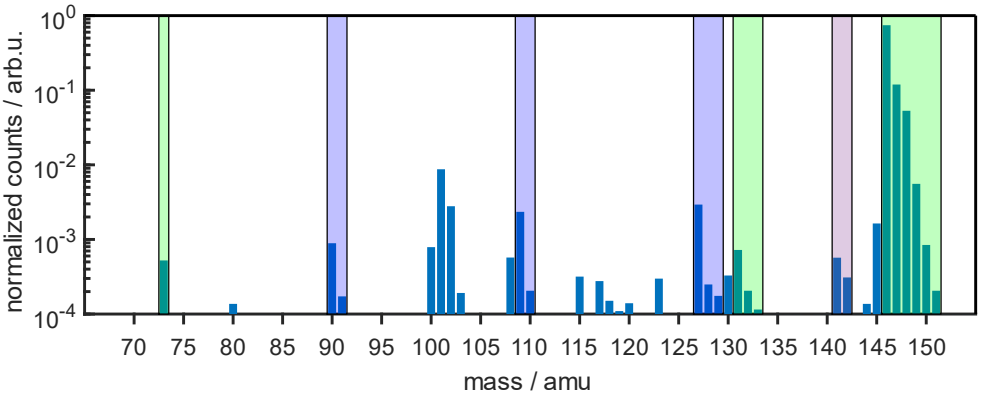

Figure 2: Ion mass spectrum of 500 ppm HMDS at 10 W generator power from 65 amu to 155 amu. The gas flow consisted of 400 sccm Ar through the plasma and 800 sccm Ar in the crossing gas flow.

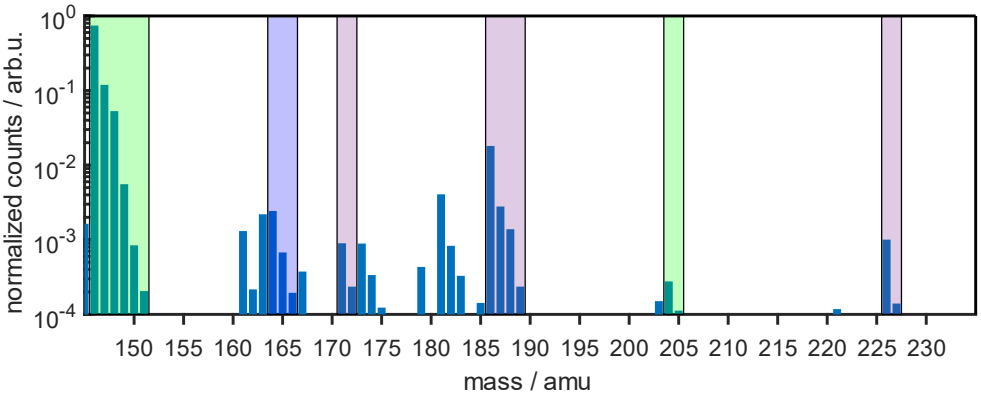

Figure 3: Ion mass spectrum of 500 ppm HMDS at 10 W generator power from 145 amu to 235 amu. The gas flow consisted of 400 sccm Ar through the plasma and 800 sccm Ar in the crossing gas flow.

Using the Crossflow-Capillary-Jet, we studied the photo-chemistry of organosilicon precursors like HMDS by positive ion mass spectrometry. The normalized mass spectra between 65 amu and 235 amu with 500 ppm HMDS in the crossing gas channel are shown in figures 2 and 3 with identfied species marked in green and peaks assinged to species produced via argon- and water-attachment as a artefact of the sampling technique marked in red and blue respectively. The monomer ion is the most abundant ion at a mass of 146 amu and the peaks from 147 amu to 151 amu are mainly attributed to its isotopes. Breaking of the Si-Si-bond is expected to be the dominant decomposition step, leading to two radicals with 73 amu. Breaking of the Si-C-bond also takes place and produces species with 131 amu and 15 amu (not shown). Follow-up reactions include the named radicals and will be presented in more detail in the talk, as well as results from deposited films obtained by FTIR spectroscopy.

[1] J. Golda, B. Biskup, V. Layes, T. Winzer, and J. Benedikt, *Plasma Process. Polym.* 17, 1900216 (2020)
[2] P. Kurunczi, J. Lopez, H. Shah, and K. Becker, *Int. J. Mass Spectrom.* 2001, 205, 277
[3] J. Z. Dávalos, T. Baer, *J. Phys. Chem. A* 2006, 110, 8572-8579
[4] F. Massines, C. Sarra-Bournet, F. Fanelli, N. Naudé, and N. Gherardi, *Plasma Process. Polym.* 2012, 9, 1041–1073
[5] S. Schneider, F. Jarzina, J.-W. Lackmann, J.Golda, V. Layes, V. Schulz-von der Gathen, J. E. Bandow, and J. Benedikt, *J. Phys. D: Appl. Phys.* 48, 444001 (2015)
[6] T. Winzer, D. Steuer, S. Schüttler, N. Blosczyk, J. Benedikt, and J. Golda, *J. Appl. Phys.* 132, 183301 (2022)

HIGH PRESSURE COAXIAL DIELECTRIC BARRIER DISCHARGE FOR CO_2 SPLITTING BY COMBINED ACTION OF PACKED BED

Rezvan Hosseini Rad[1], Milko Schiorlin [1], Volker Brüser [1], Ronny Brandenburg[1,2]

[1] *Leibniz Institute for Plasma Science and Technology, Felix-HausdorffStraße 2, 17489 Greifswald, Germany*

[2] *University of Rostock, Institute of Physics, Albert-Einstein-Str. 23-24, 18059 Rostock, Germany*

E-mail: brandenburg@inp-greifswald.de

CO_2 splitting in a coaxial Dielectric Barrier Discharges (DBDs) operated from 1 to 2 bar in CO_2/Ar gas mixtures is investigated. Electrical characteristics (discharge voltage, capacitances and transferred charge) are examined and correlated with plasma-chemical effects. The CO_2 conversion (from 3.4% to 12.7%) as well as the energy efficiency of CO formation (from 6% to 20%) enhances with pressure. A higher number of collisions between CO_2 molecules and active plasma species leading to dissociation explains such findings.

1. Introduction

Global environmental problems due to increasing CO_2 emissions have drawn much attention to the development of new, promising CO_2 capture and recycling processes [1,2]. However, the thermodynamic stability of the CO_2 molecule is high and its splitting requires high activation energy. Nonthermal plasmas are considered as a possible technology for the "on-demand" conversion of CO_2 at moderate gas temperatures, since electrons have sufficient energy for dissociation [3]. But, in DBDs the energy efficiency and products selectivity needs to be enhanced [4]. It is argued, that energy efficiency of DBDs can be improved by various parameters such as reactor geometry, combination with catalysts, gas flow rate, gas distribution and composition [1]. In this study, the effect of the process pressure as a parameter that has hardly been investigated so far is considered. This is done both in a classical coaxial DBD without and with a packed bed (glass beads); the effects of bed particles without and with a CeO_2 coating are compared. Furthermore, the admixture of Ar to CO_2 is used to reduce the breakdown voltage and enable full discharging of the gas at elevated pressures. The electrical and chemical properties of these DBDs are investigated and correlated with each other.

2. Experimental Section

Schemes of the coaxial DBD reactors are shown in Figure 1. The experimental set-up can be devided into three parts: 1) coaxial DBD reactor; 2) power supply and electerical analysis and; 3) gas supply system and gas analysis. The information of each part is given in Table 1.

Tab. 1. Information of experimental set up

DBD reactors	Power supply and electrical analysis	Gas supply and gas analysis
▪ Inner electrode: stainless steel tube ▪ Outer electrode (HV): foil, 5 cm wide, around dielectric tube ▪ Dielectric: quartz, 1.3 mm thick with OD: 18.5 mm ▪ Discharge gap: 2 mm ▪ With and w/o packed bed: glass beads, 1 mm diameter ▪ Pressure: 1-2 bar	▪ Power amplifier and HFHV output transformer ($\leq$ 23 kV_{pp}) ▪ Frequency: 4 kHz ▪ High voltage probe: 1:1,000 (P6015A) for *V(t)* ▪ Measuring capacitor: 21.4 nF for charge *Q(t)* ▪ Oscilloscopes: AFG 3101 (1GS/s) or DSO7032B (2 GS/s)	▪ 2 gas flow controllers for binary Ar:CO_2 mixtures (compared with pure Ar and pure CO_2) ▪ Total gas flow rate: 400 sccm ▪ µGC: 3000 Micro GC (Inficon)

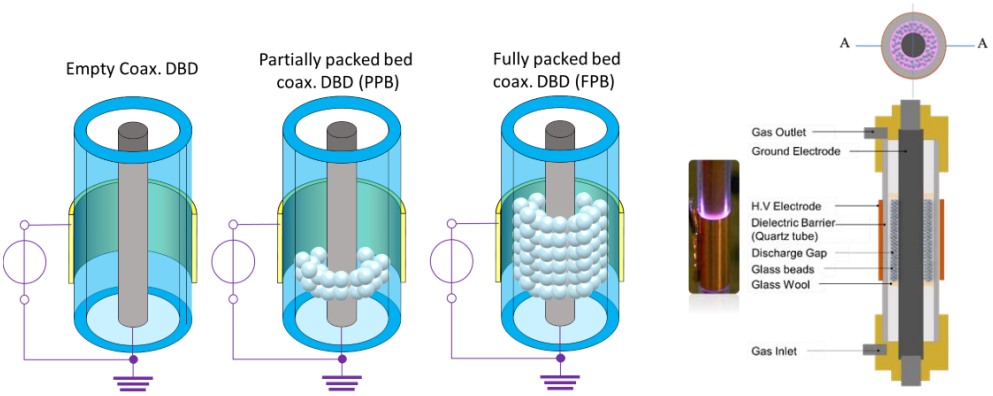

Fig. 1. Scheme of coaxial DBD, empty, partially (PPB) and fully (FPB) packed bed (left), and detailed sketch of the Reactor (right).

3. Results and Discussion

3.1- Electrical characterisation: Capacities, discharge voltage and transferred charge

Figure 2 shows a charge-voltage (Q-V) plots measured at atmospheric pressure for Ar:CO_2= 4:1 for the empty, PPB, and FPB reactor at an applied voltage amplitude of 12.5 kV_{pp}. Such Q-V plots are an established method for the determination of the discharge power. For all reactors in our study a parallelogram is obtained. For sufficient high voltage amplitudes, the lower slope characterises the capacity (C_{cell}+C_S). C_{cell} is the total capacity of the DBD arrangement (formed by the gas capacity C_g or the capacity of the packed bed C_{pb}, and the dielectric tube capacity C_{diel}) and C_S is a parallel parasitic or stray capacitance (independent from the DBD geometry). Figure 2 shows that C_{pd} is larger than C_g, leading to $C_{cell}^{pb} > C_{cell}^{em}$. However, the maximum of the larger slope of the active phase is the same for all three reactor assemblies and nearly matches with the value (C_{diel} + C_S). Obviously, in or PB reactor, the plasma operates between the inner wall of the dielectric tube and the inner electrode and not between the glass beads, as suggested in most of the literature about packed bed DBDs. The minimum sustaining voltage U_{min}, can also be investigated at the lower slopes of the Q-V plots. Its value increase with the addition of bed material, slightly for PPB and significantly for FPB. To obtain further insights in the voltage over the discharge and the charge transferred into the plasma the signals *V(t)* and *Q(t)* are further analysed, considering the capacities being obtained.

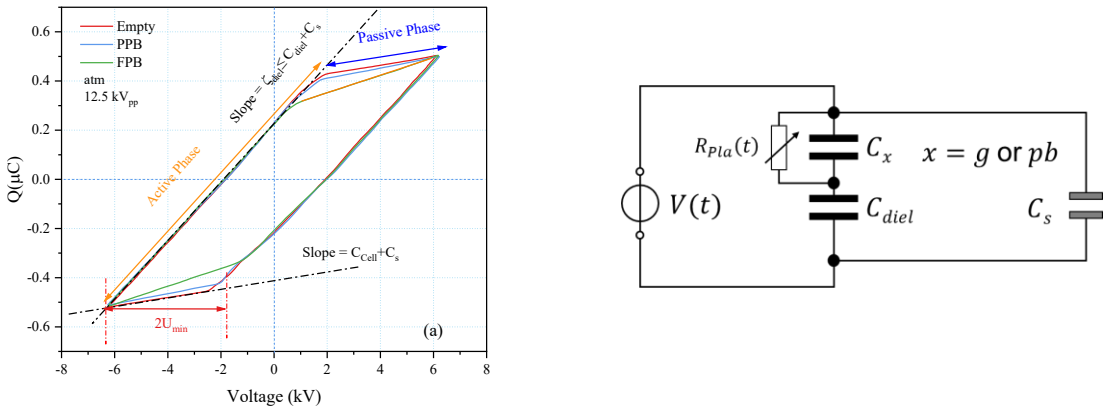

Fig. 2. Q-V plots measured at applied voltage amplitude of 12.5 kV_{pp} and frequency of 4 kHz in Ar:CO_2= 4:1 for different reactor assemblies (empty, PPT, and FPB), left and equivalent circuit, right.

Figure 3 shows the gap voltage U_g and the plasma charge Q_{Plas} calculated by equations (1) and (2) (red and blue solid lines) togehther with the measured sinusoidal applied voltage *V(t)* (red dashed line) and the total charge *Q(t)* (blue dashed line) for two pressures in the empty and FPB reactor, respectively.

The electrical measurements are an averarge over 512 cycles. Equations (1) and (2) consider the presence of C_S (few pF) in our set-up [5] and are valid for fully discharging of the DBD reactors (i.e. $\xi_{diel} \approx C_{diel}$, see [6] and [8] for further details).

$$U_g(t) = \left[1 + \frac{C_s}{C_{diel}}\right] V(t) - \frac{1}{C_{diel}} Q(t) \quad (1)$$

$$Q_{Plas} = \left(\frac{C_{diel}}{C_{diel} - C_{cell}}\right) [Q(t) - (C_{cell} + C_s) V(t)] \quad (2)$$

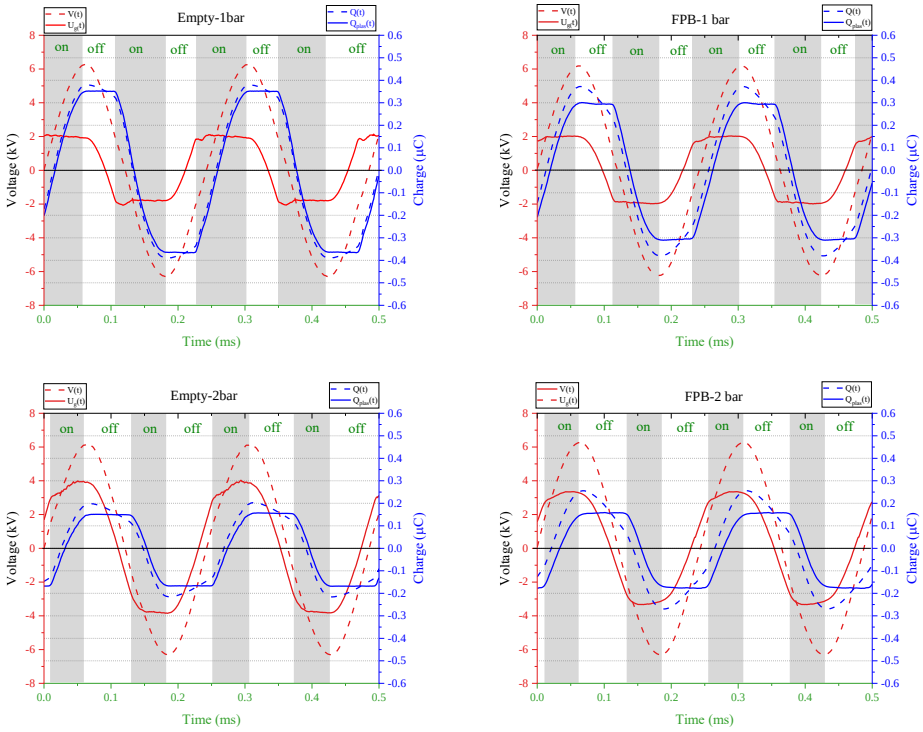

Fig. 3.Measured electrical signals and calculated gap voltage and plasma charge for empty and FPB reactor at 1 and 2 bar.

The gap voltage $U_g(t)$ is constant in the active phase („on“). These „plateau values“ (the so-called discharge voltage) increase with pressure, whether the gap is filled with glass beads or not. The increase with pressure is explained by Paschen's law. The filling has obviously no effect on this at atmospheric pressure. At 2 bar a decrease of the discharge voltage is obtained with the addition of glass beads. Maybe, the plasma is now also formed in the voids between beads, i.e. at smaller distances. The transferred plasma charge $Q_{Plas}(t)$ is constant during the passive phase („off“) and changes when the plasma is burning („on“). The amount of transfered charge is lower for the FPB at 1 bar, but shows no difference at 2 bar. Obviously, the plasma formation in the packed bed voids reduces the discharge current. This behaviour has direct consequences for the dissipated plasma power which must be related with the chemical performance described in the next section.

3.3- Plasma chemistry: CO_2 conversion and energy efficiency

Figure 4 (a) shows the absolute conversion (X_{abs}, equation (3)) and the specific energy input (*SEI*, equation (4)) as a fucntion of the pressure. The conversion increases with pressure in the empty and PPB reactor, while the trend is not clear for the FPB. As mentioned above and seen in the diagram, the different conditions lead to different *SEI* which must be considered further. Therefore, the energy efficiency (η, calculated by equation (5)) is given as a function of the effective conversion (equation (6)) in Figure 4 (b).

$$X_{abs}\,[\%] = \frac{[CO_2]_{in} - [CO_2]_{out}}{[CO_2]_{in}} \times 100\% \quad (3)$$

$$SEI[\mathrm{eV/particle}] = \frac{P[\mathrm{W}]}{Q_0[\mathrm{L_n/sec}]} \times \frac{\mathrm{L_n}}{2.69\ 10^{22}} \times \frac{1\ \mathrm{eV}}{1{,}609{\cdot}10^{-19}\mathrm{J}} \quad (4)$$

$$\eta[\%] = X_{eff} \times \frac{\Delta H_R}{SEI} \quad (5)$$

$$X_{eff}\,[\%] = X_{abs}[\%] \times r \quad (6)$$

ΔH_R = 2.9 (eV/particle) is the reaction enthalpy for the CO_2 splitting reaction ($CO_2 \rightarrow 0.5\ O_2 + CO$); r is the fraction of CO_2 in the gas mixture (0.2 in most cases), $[CO_2]_{in}$ and $[CO_2]_{out}$ are the molar concentrations of CO_2 in the gas mixture before and after plasma treatment. The *SEI* is determined by the discharge power P (in W) divided by the gas flow Q_0 (in L_n/sec), L_n are standard litres.

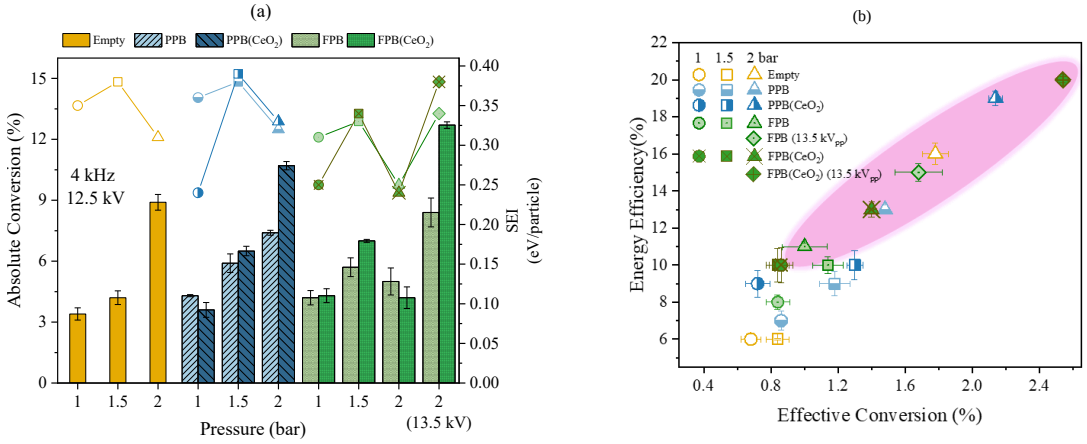

Fig. 4. Comparison of CO_2 Conversion and Energy efficiency in different reactor assemblies and different pressures, for details see [8].

The chemical performance is in a range typical for DBDs, i.e. conversion far below 40%, η below 20% [7], but at 2 bar (see the data marked with the pink ellipse in Figure 4 b) a significant enhancement in both, energy efficiency and effective conversion is obtained. CeO_2 coating on the glass beads supports the CO formation even further.

In DBDs the CO formation is mainly by electron collisions with the CO_2 molecules. Higher background gas density would lead to more collisions and thus, increase CO formation. However, in Ar/CO_2 gas mixtures the dissociative recombination of electron with CO_2^+-ions (see equation (13)) can play an important role [3]. The CO_2^+-ions are formed by charge transfer from Ar^+ and Ar_2^+ ions (11, 12), the latter being formed via excimer ionization (10). Excimer formation (9) and charge transfer are 3-body collisions, i.e. their rates and thus, the ion densities should increase with pressure. However, a dedicated numerical study is needed to explain the effect of pressure.

$e^- + Ar$	$\rightarrow 2e^- + Ar^+$	$E_{ion}^{Ar} = 15.8$ eV	(7)
$e^- + Ar$	$\rightarrow e^- + Ar^*$	$E_{exc}^{Ar} \geq 11.5$ eV	(8)
$Ar^* + 2Ar$	$\rightarrow Ar_2^* + Ar$		(9)
$e^- + Ar_2^*$	$\rightarrow 2e^- + Ar_2^+$	$E_{ion}^{Ar2} = 3.2;\ 4.7$ eV	(10)
$Ar^+ + CO_2$	$\rightarrow Ar + CO_2^+$		(11)
$Ar_2^+ + CO_2$	$\rightarrow 2Ar + CO_2^+$		(12)
$CO_2^+ + e^-$	$\rightarrow CO + O$		(13)

Another aspect is the back-reaction of CO with O to CO_2. CeO_2 might supress this because its oxygen storage and release properties. CeO_2 is noticed widely in CO_2 classical catalysis because of abundant oxygen vacancies, acid base bifunctionality, redox properties, and unique interaction between metal and support. The high oxygen vacancies can transfer between lattices. A possilbe interaction between CO_2

and the CeO_2 surface is CO_2 adsorption followed by carbonate formation, exchanging oxygen atoms and releasing CO [9].

4. Conclusion

Electrical characterization of coaxial DBD reactors operating at elevated pressure shows an increase of gap voltage with pressure, but also reduces the transfered charge. The additions of glass beads seems to support the plasma formation at elevated pressures, e.g. in the voids of the packed bed. The pressure increase leads to an enhancement of both, the CO_2 conversion and the energy efficiency, in the Ar/CO_2 gas mixture 4:1. Packed bed also increases the CO formation at 2 bar, and even more with CeO_2-coated packed bed particles. The suggestions to explain these effects are (1) a higher rate of collisions between electrons and gas molecules, (2) an enhancement of ion formation by 3-body processes and (3) the supression of back reactions at the CeO_2 surface.

5. References

[1] A. George et al. *Renewable and Sustainable Energy Reviews 135 (2021): 109702.*

[2] K. O. Yoro et al., In*: Advances in carbon capture, pp. 3-28. Woodhead Publishing, 2020.*

[3] M. Ramakers et al. *Plasma Process. Polym. 12(8) (2015) 755-763.*

[4] R. Aerts et al. *Chem. Sus. Chem. 8(4) (2015) 702-716.*

[5] F. Falkenstein and J.J. Cogan *J. Phys. D: Appl. Phys. 30 (1997) 817–825.*

[6] F.J.J. Peeters et al. *Plas. Sour. Scie. Technol. 24(1) (2014) 015016.*

[7] R. Snoeckx et al. *Chemical Society Reviews 46(19) (2017) 5805-5863.*

[8] R. Hosseini Rad et al. *Chem. Eng. J 456 (2023) 141072.*

[9] H. Chang et al. *ACS Catal., 10 (1) (2020) 613-631.*

ELECTRON INDUCED FLUORESCENCE OF NITROGEN

Ján Blaško, Barbora Stachová, Juraj Országh, Štefan Matejčík

Department of Experimental Physics, Faculty of Mathematic, Physics and Informatics, Comenius University in Bratislava, Mlynská dolina, 842 48 Bratislava, Slovakia
E-mail: jan.blasko@fmph.uniba.sk

Electron induced fluorescence of nitrogen was studied in the spectral range from 330 to 1030 nm and in the energy range from 6 to 100 eV. 2D spectral map of nitrogen was constructed. The map provides emission spectra and complete set of excitation-emission cross-sections data of individual transitions. The most intensive molecular emission bands of nitrogen were observed: First positive system N_2 ($B\ ^3\Pi_g^+$ - $A\ ^3\sum_g^+$), Second positive system N_2 ($C\ ^3\Pi_u$ – $B\ ^3\Pi_g$), First negative system N_2^+ ($B\ ^2\sum_u^+$ - $X\ ^2\sum_g^+$) and Meinel system N_2^+ ($A\ ^2\Pi_u$ – $X\ ^2\sum_g^+$) and several other transitions. Atomic lines of nitrogen N I and N II were also detected.

1. Introduction

Electron-induced fluorescence (EIF) is a series of physical processes that uses the principle of optical emission spectroscopy to analyse the emission of the products of electron – molecule collisions in the UV – VIS – IR spectral area. Using this technique electronic, vibrational, and rotational states of N_2 molecule were analysed. It is possible to measure optically forbidden states of molecules. A photon has quantized energy. Therefore, the photon must transfer all of its energy, while an electron transfers only a portion of its energy. Thanks to this, the electron is able to excite optically forbidden states. In addition to molecules and atoms interesting for astrophysics [1], emission spectrometry can study samples relevant for nanotechnology and electronics for the deposition of thin layers such as organometallic compounds. For these compounds, there are several works dedicated to UV absorption spectroscopy [2], or UV photodissociation [3]. Regarding the investigation of electron collisions with organometallic compounds, most works use mass spectroscopy as a detection method [4]. However, emission spectroscopy brings a unique possibility of detecting electrically neutral fragments, while the complex knowledge of fragmentation processes is critical for this application. Nitrogen and its electron induced excitation is observed in electrical discharges and is especially relevant for widely used atmospheric pressure discharges. Nitrogen is also often used as a working gas for lasers [5,6]. Nitrogen was used to determine vibrational and rotational temperatures of ions and neutrals in plasma discharges using electron induced processes [7,8]. A few articles on study of the nitrogen by electron induced excitation have been published. One of the most complex papers focused on electron – induced excitations of nitrogen was published by Mangina et al. [9]. Nitrogen was studied in the spectral range from 330 to 1100 nm at the energy of the interacting electrons 25 eV and 100 eV. They determined the value of emission cross-sections at the energy of 25 eV and 100 eV for most transitions. They also compared the experimental values with theoretical model and with other publications. Several other articles were also focused on the study of electron excitation of nitrogen [9-13]. The main goal was to obtain complete set of excitation-emission cross-section data on molecule N_2. Cross-sections have been published in articles only for selected transitions in the threshold region [13] or at selected energies [9] of interacting electrons. In our case, the 2D map provides complete information in the chosen spectral and energy range. This data is important for simulations or diagnostics in the field of optical emission spectroscopy, astrophysical environment, nanotechnologies, electrical discharges especially in atmospheric discharges, and other scientific fields where the electron collisions play an important role.

2. Experiment

The experimental device. for the research of electron-induced fluorescence is based on the principle of the collision of a molecular and electron beam at 90° angle (Fig. 1.). The experiment is carried out under binary collision conditions, which means that only one electron collides with one molecule. The measurement is performed in two standard modes. In the first mode, the spectrum is scanned at constant electron energy. and in the second mode the dependence of photon intensity at constant wavelength on electron energy is determined. The intensity of the photon signal is proportional to the emission effective

cross-section, by which in this case we mean the effective cross-section for the process of excitation by an electron impact and subsequent spontaneous deexcitation during which a photon is emitted.

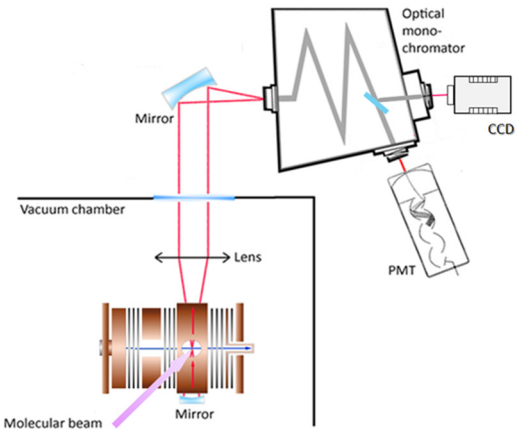

Fig. 1. The scheme of the electron induced fluorescence apparatus.

A trochoidal electron monochromator was used to generate the monoenergetic electron beam. The molecular beam is generated by effusive capillary with a diameter of 0.5 mm and a length of 5 mm, which is connected to an external gas inlet by a leak valve. Fluorescence radiation is collected by an optical system placed perpendicularly to the plane defined by electron and molecular beams. The optical system includes a plano-convex UV silicon lens placed in a vacuum, an MgF_2 window and a parabolic mirror that focuses the photons into the entrance slit of an optical monochromator (Oriel Cornerstone 260 Czerny – Turner) with a focal length of 0.25 m. The width of the slit of the optical monochromator is adjustable using micrometric screw in the range from 70 to 1000 µm, which also affects the spectral resolution reaching a maximum of 0.4 nm FWHM. After passing through the optical monochromator, the signal is detected by low-noise (0.5-2 cps) photomultiplier (Hamamatsu) sensitive in the range of 185- 710 nm or Andor iDUS 420 CCD camera (sensitive in 300-1100 nm range). Both detectors were thermoelectrically cooled using a Peltier cell to suppress thermal noise.

3. Results and discussion

In the Figure 2 we present the 2D spectral map of N_2 molecule. The 2D map was generated by measuring spectra with CCD detector in the range from 330 to 1030 nm at constant electron energy for each spectrum. The measurements were repeated in 1 eV steps in the range of 6 eV to 30 eV, 2eV steps in the range of 30 to 50 eV and 5 eV in the range of 50 to 100 eV. The higher step density in the range of 6 to 30 eV was chosen because most of the thresholds are in this range. The estimated error for the electron energy is ± 0.5 eV from 6 to 30 eV, ± 1 eV from 30 to 50 eV and ± 2.5 eV from 50 to 100 eV. The spectral lines were identified according to NIST database [14] and papers by Lofthus and Krupenie [10] and Mangina et al. [9]. The calibration of the electron energy was based on the cross-section measurement of the 0-0 transition in the Second positive system (2PS) which exhibits a sharp maximum at 14.1 eV [12]. The emission cross-section values were calibrated according to value of the 0-0 2PS transition given by Mangina et al. [9].

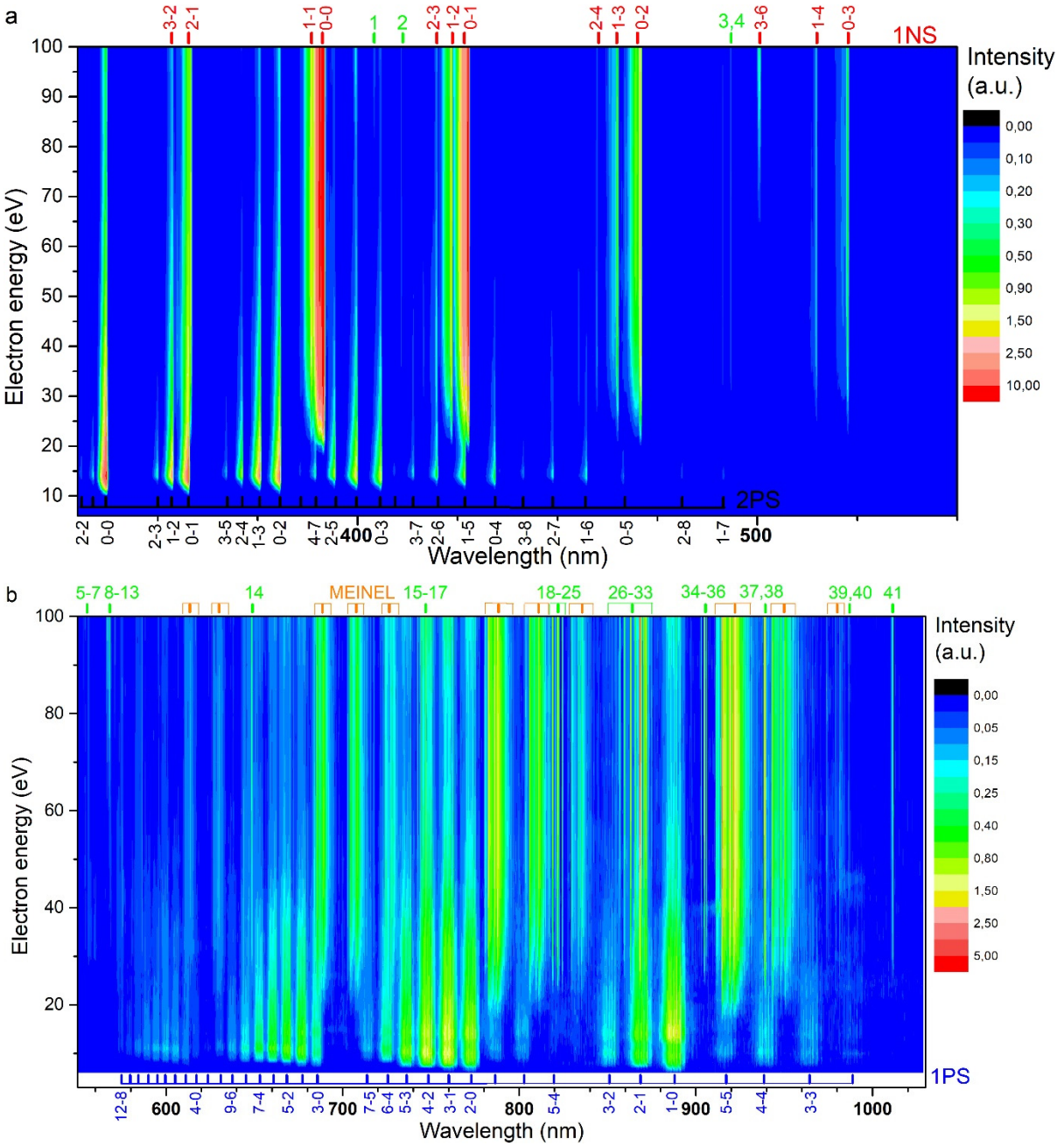

Fig. 2. 2D spectral map of nitrogen in the range a) 330 – 550 nm b) 550-1030 nm

In the 2D spectral map we can observe Second positive system (2PS) of N_2 ($C\ ^3\Pi_u$ – $B\ ^3\Pi_g$) (black marking), First negative system (1NS) of N_2^+ ($B\ ^2\Sigma_u^+$ - $X\ ^2\Sigma_g^+$) (red marking), First positive system (1PS) of N_2 ($B\ ^3\Pi_g^+$ - $A\ ^3\Sigma_g^+$) (blue marking), Meinel band system of N_2^+ ($A\ ^2\Pi_u$ – $X\ ^2\Sigma_g^+$) (orange marking) and atomic lines N I and N II (green marking). In the measured range the most intensive transition is 0 – 0 1NS at 391 nm. At some wavelengths, only one transition is present in the range from 6 to 100 eV, for example 0 – 0 transition of 2PS at 337.1 nm. However, at certain wavelengths, more than one transition can be present depending on the electron energy, for example 3 – 0 transition of 1PS at and Meinel band system 3 – 0 are present at the same wavelength (686 nm) and the contribution of each transition to the photon signal depends on electron energy. In the 2D spectral map we can observe ascending tendency of the thresholds of cross-sections of the 2PS and 1PS transitions. The transition 0 – X 2PS starts around the 10 eV, transition 2 – X 2PS starts around 11 eV around 3 – X 2PS starts around 11.5 eV. The ascending of the threshold value corresponds to the increase of the higher vibrational state, what corresponds to the former publications [11-13]. The 1PS has the lowest threshold approximately

7 eV. The second system with the lowest threshold is 2PS which starts at approximately 10 eV. Meinel band system has the thresholds around 17 eV and 1NS has thresholds around 18 eV.

Tab. 1. Transitions labelled in 2D spectral map.

Label	Particle	Wavelength (nm)	Transition	Label	Particle	Wavelength (nm)	Transition
1	N II	404.2	$3p\ ^1S - 3d\ ^3P^\circ$ /$3p\ ^1S - 3d\ ^3D^\circ$	22	N I	821.4	$2s^22p^2(^3P)3s - 2s^22p^2(^3P)3p\ ^4P–^4P^\circ$
2	N I	410.0,410.9	$2s^22p^2(^3P)3s - 2s^22p^2(^1D)3p\ ^2P–^2D^\circ$	23	N I	821.9	$2s^22p^2(^3P)3s - 2s^22p^2(^3P)3p\ ^4P–^4P^\circ$
3	N I	491.3	$2s^22p^2(^3P)3s - 2s^22p^2(^3P)4p\ ^2P–^2S^\circ$	24	N I	822.6	$2s^22p^2(^3P)3s - 2s^22p^2(^3P)3p\ ^4P–^4P^\circ$
4	N I	493.3	$2s^22p^2(^3P)3s - 2s^22p^2(^3P)4p\ ^2P–^2S^\circ$	25	N I	824.5	$2s^22p^2(^3P)3s - 2s^22p^2(^3P)3p\ ^4P–^4P^\circ$
5	N II	500.4, 500.7	$2s^22p(^2P^0)3p - 2s^22p(^2P^0)3d\ ^3D\text{-}^3F^0$	26	N I	857.0 859.7 863.2	$2s^22p^2(^3P)3s - 2s^22p^2(^3P)3p\ ^2P–^2P^\circ$
6	N II	553.4, 554.3	$2s2p^2(^4P)3s - 2s2p^2(^4P)3p\ ^5P–^5D^\circ$	27	N I	865.9 867.0	$2s^22p^2(^1D)3s - 2s^22p^2(^3P)5p\ ^2D–^2P^\circ$
7	N I	556.0	$2s^22p^2(^3P)3p - 2s^22p^2(^3P)5d\ ^4D^\circ–^4F$	28	N I	868.3	$2s^22p^2(^3P)3s– 2s^22p^2(^3P)3p\ ^4P–^4D^\circ$
8	N I	556.4	$2s^22p^2(^3P)3p - 2s^22p^2(^3P)5d\ ^4D^\circ–^4F$	29	N I	870.6	$2s^22p^2(^3P)3s– 2s^22p^2(^3P)3p\ ^4P–^4D^\circ$
9	N II	566.6	$2s^22p(^2P^\circ)3s - 2s^22p(^2P^\circ)3p\ ^3P^\circ–^3D$	30	N I	871.5	$2s^22p^2(^3P)3s– 2s^22p^2(^3P)3p\ ^4P–^4D^\circ$
10	N II	568.0	$2s^22p(^2P^\circ)3s - 2s^22p(^2P^\circ)3p\ ^3P^\circ–^3D$	31	N I	872.2	$2s^22p^2(^3P)3s– 2s^22p^2(^3P)3p\ ^4P–^4D^\circ$
11	N II	568.5	$2s^22p(^2P^\circ)3s - 2s^22p(^2P^\circ)3p\ ^3P^\circ–^3D$	32	N I	873.2	$2s^22p^2(^3P)3s– 2s^22p^2(^3P)3p\ ^4P–^4D^\circ$
12	N II	571.1	$2s^22p(^2P^\circ)3s - 2s^22p(^2P^\circ)3p\ ^3P^\circ–^3D$	33	N I	875.0	$2s^22p^2(^3P)3s– 2s^22p^2(^3P)3p\ ^4P–^4D^\circ$
13	N II	574.8	$2s^22p(^2P^\circ)3s - 2s^22p(^2P^\circ)3p\ ^1P^\circ–^3D$	34	N I	903.0	$2s^22p^2(^3P)3p – 2s^22p^2(^3P)3d\ ^2S^\circ–^2P$
14	N I N II	648.1-648.6 648.2	$2s^22p^2(^3P)3p– 2s^22p^2(^3P)4d\ ^4D^\circ–^4F$ $2s^22p3s - 2s^22p3p\ ^1P^\circ–^1P$	35	N I	904.7	$2s^22p^2(^1D)3s – 2s^22p^2(^1D)3p\ ^2D–^2F^\circ$
15	N I	742.5	$2s^22p^2(^3P)3s - 2s^22p^2(^3P)3p\ ^4P–^4S^\circ$	36	N I	906.2	$2s^22p^2(^3P)3p – 2s^22p^2(^3P)3d\ ^2S^\circ–^2P$
16	N I	744.3	$2s^22p^2(^3P)3s - 2s^22p^2(^3P)3p\ ^4P–^4S^\circ$	37	N I	938.9	$2s^22p^2(^3P)3s – 2s^22p^2(^3P)3p\ ^2P–^2D^\circ$
17	N I	746.9	$2s^22p^2(^3P)3s - 2s^22p^2(^3P)3p\ ^4P–^4S^\circ$	38	N I	939.5	$2s^22p^2(^3P)3s – 2s^22p^2(^3P)3p\ ^2P–^2D^\circ$
18	N I	817.0	$2s^22p^2(^1D)3s - 2s^22p^2(^3P)5p\ ^2D–^2D^\circ$	39	N I	982.6	$2s^22p^2(^3P)3p – 2s^22p^2(^3P)3d\ ^4D^\circ–^4D$
19	N I	818.9	$2s^22p^2(^3P)3s - 2s^22p^2(^3P)3p\ ^4P–^4P^\circ$	40	N I	986.6	$2s^22p^2(^3P)3p – 2s^22p^2(^3P)3d\ ^4D^\circ–^4D$
20	N I	819.1	$2s^22p^2(^3P)3s - 2s^22p^2(^3P)3p\ ^4P–^4P^\circ$	41	N I	1010.6-1011.7	$2s^22p^2(^3P)3p – 2s^22p^2(^3P)3d\ ^4D^\circ–^4F$
21	N I	820.4	$2s^22p^2(^3P)3s - 2s^22p^2(^3P)3p\ ^4P–^4P^\circ$				

4. Conclusion

The 2D spectral map of nitrogen was measured by electron induced fluorescence. It contains spectra in the range from 330 to 1030 nm at the energy range from 6 to 100 eV. The intensities of the spectra in the map were calibrated so the absolute values of the emission cross-sections can be determined by integrating the surface under the corresponding transition.

5. Acknowledgments

This research was partially supported by Slovak Research and Development Agency projects nr. APVV-19-0386, APVV-15-0580, Slovak grant agency VEGA projects nr. 1/0489/21 and 1/0553/22. Europlanet 2024 RI has received funding from the European Union's Horizon 2020 research and innovation programme under grant agreement No 871149.

6. References

[1] Bodewits D, Országh J, Noonan J, Ďurian M and Matejčík Š 2019 *Astrophys J* 885 167
[2] Lundquist R T and Cais M 1961 *J. Org. Chem.* 27 1167-1172
[3] Fujita Y and al. 1989 *J. Vac. Sci. Technol.* 276, doi: 10.1116/1.576111
[4] Constantine S P and al. 2000 *Rapid Commun. Mass Spectrom.* 14 329-334
[5] Fons J T, Schappe R S and Lin C C 1996 *Phys Rev A (Coll Park)* 53 2239
[6] Cartwright D C 1970 *Phys Rev A (Coll Park)* 2 1331
[7] Huang X J, Xin Y, Yang L, Yuan Q H and Ning Z Y 2008 *Phys Plasmas* 15 113504
[8] Linss V 2005 *Spectrochim Acta Part B At Spectrosc* 60 253
[9] Mangina R S, Ajello J M, West R A, Dziczek D 2011 *Astrophysical J., Supplement Series* 196
[10] Lofthus A, Krupenie P H 1977 *J. Phys. Chem. Ref. Data* 6 113
[11] Országh J and al. 2012 *Nuclear Instruments and Methods in Physics Research B* 279 76-79
[12] Zubek M 1994 *J. Phys. B: At. Mol. Opt. Phys*. 27
[13] Poparic G, Vicic M, Belic D S 1999 *Chem. Phys.* 240 283
[14] https://physics.nist.gov/cgi-bin/ASD/lines1.pl

POSTER PRESENTATIONS

ABSORPTION SPECTROSCOPY OF GASEOUS PRODUCTS GENERATED BY COPLANAR BARRIER DISCHARGE IN AIR AND N_2/O_2 MIXTURES

David Trunec[1], Zdeněk Navrátil[1], Věra Mazánková[2], Sandra Durčányová[3], Anna Záhoranová[3]

[1]*Department of Physical Electronics, Faculty of Science, Masaryk University, Kotlarska 2, 611 37 Brno, Czech Republic*

[2] *Department of Mathematics and Physics, Faculty of Military Technology, University of Defence in Brno, Kounicova 65, 662 10 Brno, Czech Republic*

[3] *Department of Experimental Physics, Faculty of Mathematics, Physics and Informatics, Comenius University, Mlynská dolina F1, 842 48 Bratislava, Slovakia*

E-mail: trunec@physics.muni.cz

Absolute densities of gaseous products generated by coplanar dielectric barrier discharge in N_2/O_2 mixtures and in ambient air were determined by absorption spectroscopy. Ozone (O_3) and nitrogen oxides (N_2O, NO_2 and N_2O_5) were identified as the stable products of the discharge. It was found that the actual product composition strongly depends on the gas temperature. At low input power with the low gas temperature, O_3 density was high and the NO_2 density was very low. At a specific input power (and the gas temperature) O_3 disappeared, while NO_2 density started to increase steeply.

1. Introduction

Low-temperature plasma (LTP) at atmospheric pressure is currently widely studied as a tool for plasma treatment of the surfaces of various materials. The reason for the wide interest is the potential of plasma applications associated with low costs and environmentally friendly technologies. Plasma interaction with the surfaces of materials depends on plasma composition. Therefore, plasma diagnostics plays the important role in the study of the effect of the plasma treatment.

Currently, there is increasing interest in the use of LTP generated by different types of dielectric barrier discharges, widely used are surface dielectric barrier discharges (SDBDs) of various electrode configurations. In our work, we focus on the diagnostics of coplanar surface barrier discharge plasma, which is often used in the surface treatment of various materials, in order to better elucidate the key components affecting the treated (for example biomaterial) surfaces.

2. Experimental

The coplanar dielectric barrier discharge (CBD) is a type of dielectric barrier discharge operated typically in air at atmospheric pressure. The coplanar electrode arrangement contains both electrodes on one side of the dielectric barrier. In the used set-up, 19 parallel electrode pairs, connected alternately in parallel, were deposited on 0.7 mm thick Al_2O_3 ceramics with dimensions 20 cm × 8 cm. The electrodes (1.5 mm wide with 1 mm gap) were immersed in oil and cooled by the oil cooling circuit. The electrode system was placed in a box with dimensions 16 cm × 30 cm × 8 cm made of plastics. The electrodes were supplied with AC high voltage (20 kV peak-to-peak, frequency 14 kHz). The input power to high voltage power supply was measured by FK Technics power meter. The ratio of the power delivered to the plasma and to the high voltage power supply input power is then 0.95. In this work, the CBD plasma source was operated in closed reactor as described above. The discharge was generated in an ambient air, oxygen, nitrogen and in mixtures of nitrogen and oxygen in ratio of 80:20, 60:40 and 40:60. The gas flow rate was kept at 3 l/min in all cases. The ambient air was first compressed to ensure the gas flow. The relative humidity of the air was approximately 50 %.

Optical absorption spectroscopy (OAS) of the discharge products in UV and VIS region was carried out using standard experimental set-up. The working gas flowed first through the plasma reactor chamber and then through a quartz cuvette (length 10 cm), located between deuterium halogen lamp

(Ocean Optics DT-Mini-2-GS) and grating spectrometer (Ocean Optics Red Tide USB 650UV). The light was transmitted into and from the cuvette by the optical fibers.
The OAS spectra were measured in the range 200 – 850 nm for various discharge parameters (discharge power and gas composition). The spectra were averaged over twenty samples. The ozone and NO_2 densities were determined using the absorption cross sections taken from Hitran database [1].

3. Results

The optical absorption spectroscopy provided a limited access to the discharge chemistry compared to the FTIR spectroscopy. Typical optical absorption spectra, measured at specific powers and in N_2:O_2 mixture 40:60 and in ambient air, are shown in Fig. 1.
For the 40:60 gas mixture and powers up to 200 W, the light in the 200 – 300 nm wavelength region was dominantly absorbed by the O_3 molecule, see the curve **a** in Fig. 1. Although the absorptions by N_2O_5 and N_2O molecules also fall in this region, they were not observed, as their densities (see the results of FTIR measurement in [2]) as well as their absorption cross sections were significantly lower than those of O_3.

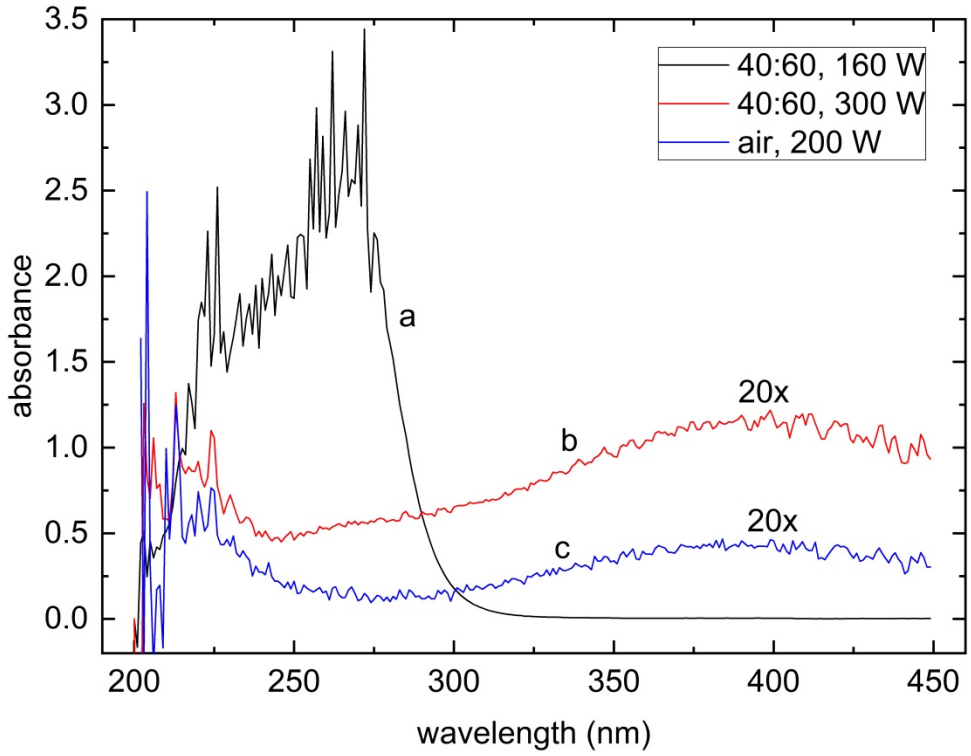

Fig. 1. The optical absorption spectra of gaseous plasma products for gas mixture 40:60 and air at various powers. Red and blue curves were multiplied by 20 in order to improve their readability.

Due to almost complete light extinction around O_3 absorption maximum (257 nm), the O_3 density was calculated from the 275 – 305 nm wavelength region.
At discharge powers above 233 W, the O_3 absorption peak was missing and the absorption peak of NO_2 spreads from 280 nm to 600 nm in the spectra, see curve **b** for 300 W in Fig. 1. The NO_2 density was calculated from 399 – 401 nm wavelength region. A small absorption band around 225 nm could be caused by N_2O or N_2O_5 molecules.
Similar absorption spectra were observed for the discharge burning in the air even at low discharge powers, see the curve **c** in Fig. 1. Besides N_2O_5 and N_2O molecules, HNO_3 with the pronounced part of the cross section within 180 – 240 nm can contribute to the UV light absorption in humid air plasma. Nevertheless, the similarity between curves **b** and **c** suggests that the nitric acid is not present at 200 W, in agreement with the FTIR measurement [2].

Power dependencies of the O_3 and NO_2 densities are along with the results of FTIR spectroscopy [2] shown in Fig. 2. In order to improve the image clarity, very low densities obtained by FTIR are not shown in the plot. Although the measured density values are slightly different, both OAS and FTIR spectroscopy provide a similar picture of the plasma chemistry development. As the FTIR and OAS spectra were not recorded in the same experiment, the deviations between the OAS and FTIR values were attributed to worse experiment repeatability, especially in the case of laboratory air. Generally, the OAS measurement had a lower sensitivity (at least due to the used instrumentation), and it also suffered more from the spectra overlap, compared to FTIR measurement.
The absence of the absorption peak in the spectrum could be used for the estimation of the upper-density limit. For example, no absorption was observed at 662 nm, where NO_3 absorption cross section has a maximum [3]. The NO_3 density was therefore below 2×10^{20} m^{-3}.
The uncertainty of the densities obtained by OAS was estimated to be about 10 %.

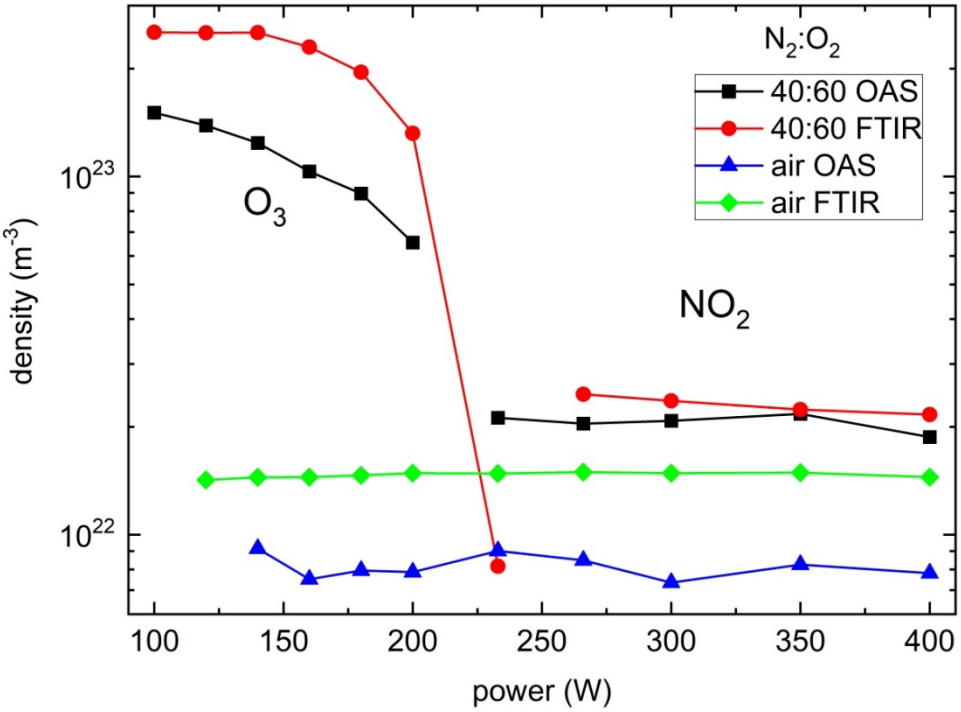

Fig. 2. Comparison of power dependencies of O_3 and NO_2 densities obtained using OAS and FTIR spectroscopy.

4. Conclusion

The absolute densities of stable gaseous products generated by coplanar dielectric barrier discharge in N_2/O_2 mixtures and in ambient air were determined by absorption spectroscopy. Ozone (O_3), nitrogen oxides (N_2O, NO_2 and N_2O_5) were identified as the stable products of the discharge in N_2/O_2 mixtures. The product densities were determined for a wide range of applied input powers (100 – 400 W). It was found that the actual product composition depends strongly on the gas temperature. At low input power, when the gas temperature is low, O_3 density is high and NO_2 densities are very low. At specific input power (and gas temperature) O_3 disappears, while NO_2 density rises steeply.

Acknowledgement
V.M. was supported by institutional support for the research organization development awarded by the Ministry of Defence of the Czech Republic.

5. References

[1] Kochanov R V et al. 2019 JQSRT **230** 172.
[2] Trunec D, Navrátil Z, Tomeková J, Mazánková V, Durčányová S and Zahoranová A 2022 *Plasma Sources Sci. Technol*. **31** 11501.
[3] Graham R A and Johnston H S 1978 *J. Phys. Chem.* **82** 254.

REACTORS FOR PLASMA-ASSISTED CATALYSIS AT ATMOSPHERIC PRESSURE

Kerstin Sgonina[1], Alexander Quack[1], and Jan Benedikt[1,2]

[1]*Institute of Experimental and Applied Physics, Kiel University, Kiel, Germany*
[2]*Kiel Nano, Surface and Interface Science KiNSIS, Kiel University, Kiel, Germany*

E-mail: sgonina@physik.uni-kiel.de

Different plasma reactors used for plasma-assisted catalysis for ammonia or methane synthesis are developed. The usage of dielectric barrier discharges operated with kHz- and radio-frequencies for effective catalysis reactions are studied. Different types of possible catalysts, like metal-organic-frameworks (MOFs) or inorganic catalyst based on cobalt, are tested for in- and post-plasma catalysis.

Nowadays, the energy efficient and decentralized performance of catalytic reactions, such as for the production of ammonia, has become even more important. Plasma-assisted catalysis can help to achieve these goals as it is available on demand and works without enormous external heating as for example needed for ammonia synthesis. Therefore, non-equilibrium atmospheric pressure plasmas are used to dissociate gaseous molecules, which can then react at the surface of the catalyst to form the desired products [1]. Plasma-assisted catalysis reactors at atmospheric pressure are often realized by packed bed reactors, in which the catalyst is packed into or deposited on millimeter-sized spheres [1-3]. However, these millimeter-sized spheres are not feasible for all types of possible catalysts.

Therefore, different plasma reactors for plasma-assisted catalysis were developed and tested with and without different catalysts for in-plasma catalysis, where the catalyst is in direct contact with plasma, and post-plasma catalysis, where only reactive species from the plasma are reaching the catalyst. Different types of possible catalysts are tested, like MOFs or inorganic catalyst based on cobalt. Dielectric barrier discharges operated at kHz- or radio-frequencies are used for ammonia synthesis using N_2 and H_2 as working gas as well as for methane formation experiments using CO_2 and H_2. With the use of mass spectrometry measurements, the obtained products are identified. Depending on the reactor-type and working gas, the gas temperature during plasma operation ranges from room temperature up to 200 °C. In order to compare the results of plasma-assisted catalysis with pure thermal catalysis, a setup was developed, that can be externally heated. It can be shown, that the observed products during plasma-assisted catalysis are not originating from the thermal catalysis.

Acknowledgements

The inorganic catalysts are synthesized by and chosen in cooperation with Jihao Wang, Sharif Najafishirtari, and Malte Behrens of the Institute of Inorganic Chemistry of the Kiel University. The metal-organic-frameworks are synthesized by and chosen in cooperation with Hauke Rohr and Norbert Stock of the Institute of Physical Chemistry of the Kiel University.

References

[1] Annemie Bogaerts *et al* 2020 *J. Phys. D: Appl. Phys.* **53** 443001.
[2] Jungmi Hong *et al* 2018 *ACS Sustainable Chemistry & Engineering* **6** (1), 15-31.
[3] Prateek Mehta *et al* 2019 *ACS Energy Letters* **4** (5), 1115-1133.

EXPERIMENTAL AND COMPUTATIONAL INVESTIGATION OF SURFACE PROCESSES IN RADIOFREQUENCY HELIUM DISCHARGES

Benedek Horváth[1,2], Ranna Masheyeva[1], Peter Hartmann[1], Zoltán Donkó[1], Aranka Derzsi[1]

[1]*Wigner Research Centre for Physics, Budapest, Hungary*
[2]*ELTE Eötvös Loránd University, Budapest, Hungary*
E-mail: horvath.benedek@wigner.hu

Phase Resolved Optical Emission Spectroscopy (PROES) measurements combined with Particle-in-Cell/Monte Carlo Collisions (PIC/MCC) simulations are used to study the effects of the electrode material on the discharge characteristics in low-pressure capacitively coupled plasmas (CCPs) in Helium. The plasma density is significantly affected by using different materials at the grounded electrode (stainless steel, copper and graphite), while using powered electrode made of stainless steel in a geometrically symmetric CCP reactor. The discharge symmetry is also influenced by using different electrode materials at the electrodes.

1. Introduction

Low-pressure CCPs are common tools for plasma-based material processing, such as etching, deposition and surface treatment in biomedicine [1–4]. In these applications, the interaction of the charged heavy particle species with the electrodes plays an important role. In order to optimize the flux and the energy of the particles colliding with the electrodes, a scientific approach is beneficial to understand the complex physics of the plasma. For example, understanding the electron power absorption dynamics [5] and the effects of surface processes on the plasma have become a central issue [6]. In the current work, these phenomena are studied in Helium discharges, by experiments and simulations: phase-resolved optical emission spectroscopy (PROES) measurements and Particle-in-Cell/Monte Carlo Collisions (PIC/MCC) simulations are performed at a low pressure and high voltages, which are ideal conditions for various surface processes due to the high particle energies. We use three different surface materials for the electrodes (stainless steel, copper, graphite) and compare some basic plasma parameters obtained from experiments and simulations.

2. Experimental setup and discharge conditions

The measurements are performed in a geometrically symmetric plasma reactor (our "Budapest v.3" cell, see figure 1): the electrodes are plain and parallel, with identical diameters of 14 cm and a gap of $L = 2.5$ cm between them, located within a quartz cylinder. One of the electrodes is driven by a sinusoidal RF waveform, while the other electrode is grounded. Both electrodes are made of stainless steel, although disks made of different materials can be placed on the grounded electrode. In the current work, stainless steel, copper and graphite disks (with diameters of 14 cm) are used at the grounded electrode. The PROES measurements are done with an ICCD camera with a temporal resolution of 1 ns and a spatial resolution of approximately 100 μm. The optical emission of the plasma is filtered for the He $3d_1$ atomic excited state with a threshold of 23.074 eV, providing the spatio-temporal distribution of the excitation rate of the selected state from the ground state [7]. The time frame of photocollection (the gatewidth) is set to 1.5 ns in the current study. The driving frequency is $f = 13.56$ MHz, the voltage amplitude is varied between $600\ \text{V} < V_0 < 1000\ \text{V}$, and the pressure is fixed at $p = 30$ Pa.

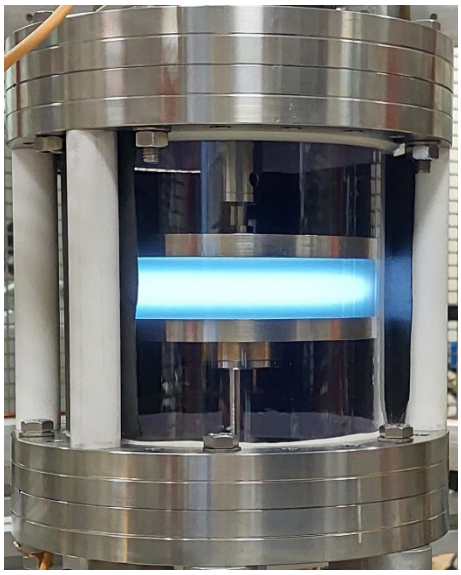

Fig. 1. Experimental setup. Picture of the "Budapest v.3" plasma reactor in our lab.

3. Simulation model

For the computational investigation of Helium CCPs, our 1d3v PIC/MCC simulation code is used. The cross sections for the gas phase collisions of electrons are taken from the Biagi-v8.97 database [8]. This set includes elastic reflection, 49 excitation processes and ionization. For the collision of He^+ ions with He atoms, isotropic and backward elastic scattering is considered [9]. The surface processes at the electrodes are treated based on a simple approach: electrons can be elastically reflected according to a constant probability η_e, and He^+ ions can cause secondary electron emission described by a constant γ coefficient. Note that these are estimated effective coefficients representing various other physical processes, e.g. electron-induced secondary electron emission, secondary electron emission caused by metastables, VUV photons etc. The emission probabilities via these elementary processes typically depend on the energy of the incident particles. In the current work, we estimate these energy-dependent processes with constant coefficients. The values of the elastic reflection coefficient of electrons and the secondary electron emission coefficient of ions are shown in table 1, for the three different surface material. They were chosen to reflect the experimental data available in the literature [10-13].

Tab. 1. Surface coefficients used for the various electrode materials at the grounded electrode in the PIC/MCC simulations.

	η_e	γ
Stainless steel	0.7	0.3
Copper	0.45	0.2
Graphite	0.35	0.15

4. Results

In figure 2, various discharge characteristics obtained from PIC/MCC simulations at a gas pressure of 30 Pa and driving voltage amplitude of 600 V are shown. The columns correspond to the three different grounded electrode materials: stainless steel, copper and graphite, respectively. From the PIC/MCC simulation results, the time-averaged charged particle density profiles, the spatio-temporal distribution of the electric field, the electron power absorption rate, the ionization rate and the He $3d_1$ excitation rates are shown in the different rows. The He $3d_1$ excitation rates obtained from PROES measurement for the different grounded electrode materials are also shown in the last row.

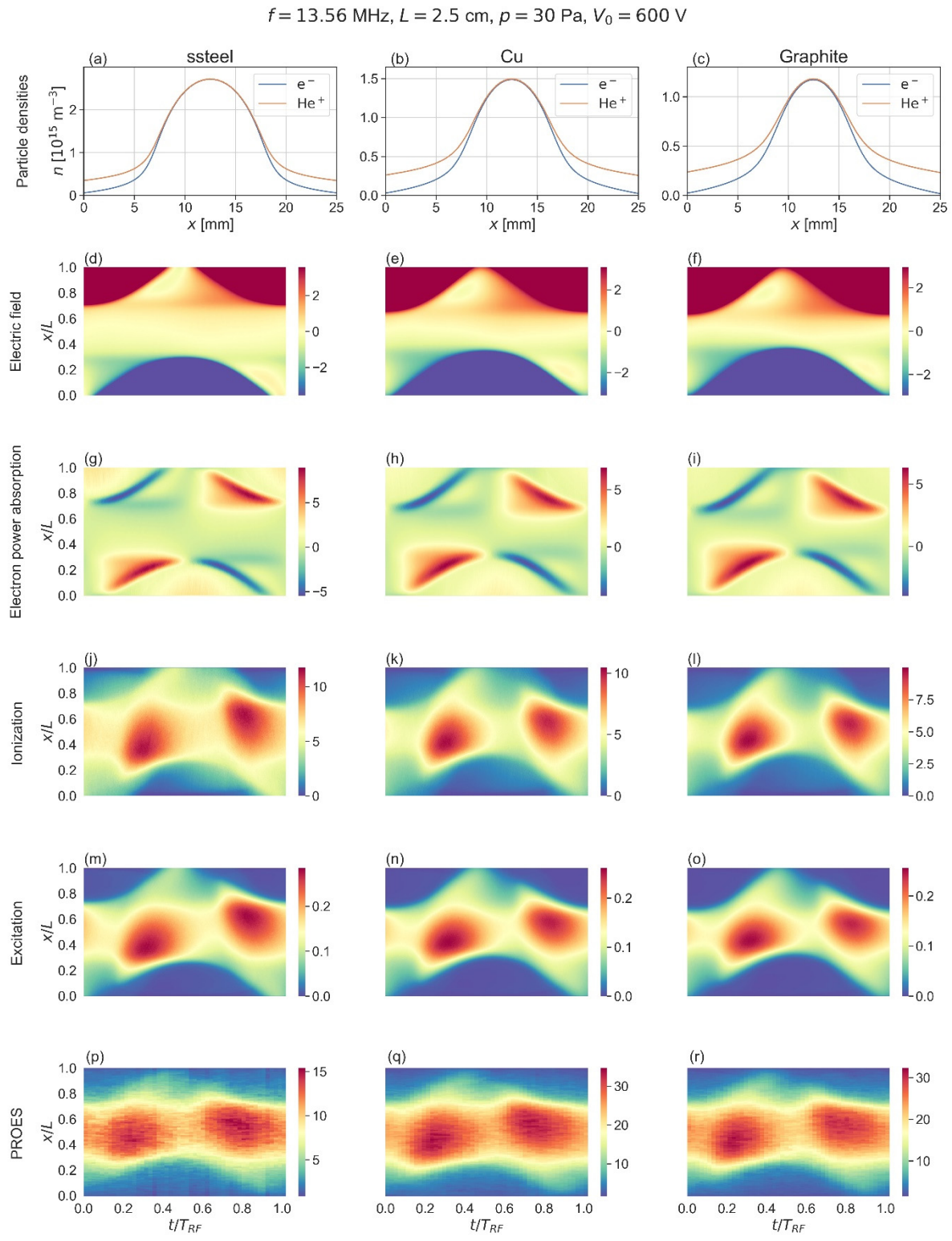

Fig. 2. Time-averaged charged particle density profiles (a-c), and spatio-temporal distributions of the electric field [10^3 Vm^{-1}] (d-f), the electron power absorption [10^4 Wm^{-3}] (g-i), the ionization rate [10^{20} $m^{-3}s^{-1}$] (j-l), and the He $3d_1$ excitation rate [10^{20} $m^{-3}s^{-1}$] (m-o) obtained from the simulation at a pressure of 30 Pa and a driving voltage amplitude of 600 V. The last row shows the He $3d_1$ excitation rates [a.u.] measured by PROES (p-r). The columns correspond to the three different grounded electrode surface materials. In panels (d-r), the horizontal axis corresponds to one RF period ($T_{\mathrm{RF}} = 1/f$). The powered electrode is located at $x/L = 0$, and the grounded electrode is at $x/L = 1$.

When the grounded electrode is made of stainless steel, i.e. it is identical to the powered electrode (first column), the particle density profiles are symmetric (panel (a)). The electric fields periodically develop at one electrode to accelerate the electrons away from the electrode, forming a depleted sheath region (panel (d)). In accordance with that, there are peaks in the spatio-temporal distribution of the electron power absorption at the edges of the expanding sheaths (panel (g)). The electrons gaining energy at these phases are able to cause ionization and excitation, forming localized peaks in the spatio-temporal distribution of the ionization and the excitation rates as well (panels (j) and (m), respectively). This is called α-mode discharge operation, which is typical in electropositive CCPs. Similar excitation patterns can be observed in the experimental results (panel (p)): a good qualitative agreement is obtained between the results from PROES and the PIC/MCC simulation.
The second column of figure 2 corresponds to the case when copper disk is used at the grounded electrode, while the powered one is made of stainless steel. The most important difference compared to the previous case (stainless steel electrodes at both electrodes) can be seen by comparing the central charge densities: instead of $2.35 \times 10^{15}\mathrm{m}^{-3}$, it takes a value of $1.5 \times 10^{15}\mathrm{m}^{-3}$, which is a decrease by 36%. The spatio-temporal distributions of the other plasma parameters are qualitatively similar to the previous case, and the simulated excitation rate corresponds to the PROES measurement as well. By using copper electrode instead of stainless steel as ground, the sheaths become slightly wider. The reasons of the decreased plasma density and the wider sheaths are the lower values of the electron reflection and the secondary electron emission coefficients (η_e and γ, see table 1) used in the simulations.
When the grounded electrode is made of graphite (third column in figure 2), the discharge still operates in α-mode, and the qualitative picture is similar to the other two cases with stainless steel and copper electrodes at grounded position. However, the central charge density decreases to $1.2 \times 10^{15}\mathrm{m}^{-3}$, which is 80% of the density obtained with copper grounded electrode and approximately half of the density obtained with stainless steel electrode.

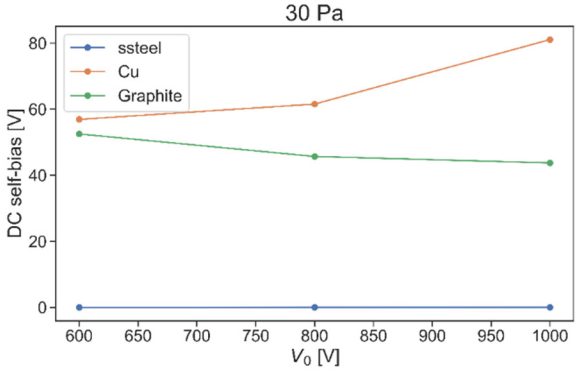

Fig. 3. The DC self-bias forming between the two electrodes as a function of the driving voltage amplitude, obtained from PIC/MCC simulation, for various surface materials used for the grounded electrode.

When the two electrodes are made of different materials, electrical asymmetry can develop even in case of a geometrically symmetric electrode configuration. The reason is the different interaction of plasma particles with the electrodes, i.e. different particle yields and sticking ratios for different electrode materials. This effect is illustrated in figure 3 based on PIC/MCC simulations: the DC self-bias developing between the two electrodes is shown for the different grounded electrode materials for different voltage amplitudes at 30 Pa. As it is expected, the self-bias is technically zero when both electrodes are made of stainless steel. However, when the grounded electrode is replaced by copper or graphite, a self-bias develops with a value between 40-80 V, which is 7-13% of the driving voltage amplitude. Nevertheless this self-bias is still not significant and does not cause a noticeable asymmetry in the particle density profiles and the spatio-temporal distributions of various plasma parameters (shown in figure 2) under the studied discharge conditions.

5. Acknowledgements

This work was supported by the Hungarian National Research, Development and Innovation Office via Grants K-134462 and FK-128924 and by the the ÚNKP-21-3 New National Excellence Program of the Ministry for Innovation and Technology from the source of the National Research, Development and Innovation Fund.

6. References

[1] Liebermann M A and Lichtenberg A J 2005 *Principles of Plasma Discharges and Materials Processing* 2nd ed (New York: Wiley)
[2] Makabe T and Petrovic Z 2006 *Plasma Electronics: Applications in Microelectronic Device Fabrication* (London: Taylor and Francis)
[3] Chabert P and Braithwaite N 2011 *Physics of Radio-Frequency Plasmas* (Cambridge: Cambridge University Press)
[4] Makabe T 2019 *Jpn. J. Appl. Phys.* **58** 110101
[5] Belenguer P and Boeuf J P 1990 *Phys. Rev.* A **41** 4447–59
[6] Donkó Z 2001 *Phys. Rev.* E **64** 026401
[7] Schulze J, Schüngel E, Donkó Z, Luggenhölscher D and Czarnetzki U 2010 *J. Phys. D: Appl. Phys.* **43** 124016
[8] Biagi S F 2010 Fortran Program, MAGBOLTZ v8.97, www.lxcat.net (accessed 4 November 2022)
[9] Phelps A V ftp://jila.colorado.edu/collision_data/ unpublished, retrieved on August 22, 2005
[10] Doughty D A, Den Hartog E A and Lawler J E 1987 *Phys. Rev. Lett.* **58** 2668
[11] Den Hartog E A, Doughty D A and Lawler J E 1988 *Phys. Rev.* A **38** 2471
[12] Schulenberg D A, Korolov I, Donkó Z, Derzsi A and Schulze J 2021 *Plasma Sources Sci. Technol.* **30** 105003
[13] Larciprete R, Grosso D R, Di Trolio A, Cimino R 2015 *Appl. Surface Sci.* **328** 356

ELECTRON EXCITATION DYNAMICS IN LOW-PRESSURE CAPACITIVELY COUPLED ARGON-OXYGEN PLASMAS

A. Derzsi[1], M. Vass[1,2], R. Masheyeva[1], B. Horváth[1], Z. Donkó[1], P. Hartmann[1]

[1]*Wigner Research Centre for Physics, Budapest, Hungary*
[2]*Ruhr University Bochum, Bochum, Germany*

E-mail: derzsi.aranka@wigner.hu

Phase Resolved Optical Emission Spectroscopy measurements combined with Particle-in-Cell/Monte Carlo Collisions simulations are used to study the electron excitation dynamics in capacitively coupled plasmas in argon-oxygen mixtures. The measurements and the simulations show good qualitative agreement in a wide parameter range. Various emission/excitation patterns develop at different pressures and different mixing ratios of the two gases. The mechanisms behind the formation of these patterns are revealed based on the simulation results.

1. Introduction

In low-pressure capacitively coupled plasmas (CCPs), experimental observation of the space and time-resolved plasma emission based on Phase Resolved Optical Emission Spectroscopy (PROES) provides information on the electron power absorption and excitation dynamics. The spatio-temporal distribution of the electron-impact excitation rate from the ground state into the selected excited atomic/molecular state is generally considered to probe the ionization dynamics (which determines the discharge operation mode) as well. In this work, we study the electron power absorption and excitation/ionization dynamics in CCPs operated in mixtures of argon and oxygen. Such systems, i.e. low-pressure CCPs operated in gas mixtures containing oxygen are highly relevant in plasma-based material processing. The study is performed for a geometrically symmetric CCP reactor by combining PROES measurements with Particle-in-Cell/Monte Carlo Collisions (PIC/MCC) simulations in a wide parameter range.

2. Methods

A geometrically symmetric plasma reactor (our "Budapest v.3" cell) is used for the measurements. In this discharge cell, the plain parallel electrodes, made of stainless steel, with identical diameters of 14 cm, are situated within a quartz cylinder. One electrode is driven by radiofrequency voltage, while the other electrode is grounded. The electrode gap is 2.5 cm. The PROES measurements are performed by using a fast-gateable ICCD camera. In argon-oxygen mixtures, the optical emission from the Ar 2p1 state with a wavelength of 750.4 nm is measured. Detailed description of the experimental setup is given in [1].

The simulations are based on our one dimensional in space and three dimensional in velocity space (1d3v) PIC/MCC simulation code. This code (named PICit!) is suitable to model geometrically symmetric CCPs in various mixtures of electropositive/electronegative gases. The particles traced in the simulations of argon-oxygen gas mixture plasmas are electrons, Ar^+ ions, fast Ar atoms (Ar^f), O_2^+ ions, O^- ions and fast O_2 molecules (O_2^f). In total, 61 collision processes are included in the argon-oxygen discharge model: the collision processes used previously for simulation studies of CCPs operated in pure argon and oxygen, complemented with "cross processes" between oxygen and argon species and collision processes for fast neutrals. The cross sections are taken from [2]. As surface processes, secondary electron emission due to ions, elastic reflection of electrons and surface quenching of $O_2(a^1\Delta_g)$ metastable molecules are considered and constant surface coefficients are used for these processes. The density of the $O_2(a^1\Delta_g)$ metastable species is determined self-consistently in the simulations. The heating of the background gas due to elastic collisions of fast neutrals and ions with background atoms/molecules, as well as the heating of the electrodes due to inelastic collisions of plasma particles reaching the electrodes are also considered in the model [1].

3. Results

The study is performed at a driving frequency of 10 MHz and a peak-to-peak voltage of 350 V. The pressure of the gas mixture is varied between 15 Pa and 400 Pa, while the argon/oxygen concentration

is tuned between 10% and 90%. For the whole parameter range covered in this study, the spatio-temporal distributions of the electron-impact excitation rate measured by PROES and obtained from PIC/MCC simulations show good qualitative agreement. This is illustrated in Fig. 1, in which PROES results and PIC/MCC results are presented for 10% O_2 – 90 % Ar mixture and 90% O_2 – 10 % Ar mixture at p = 240 Pa.

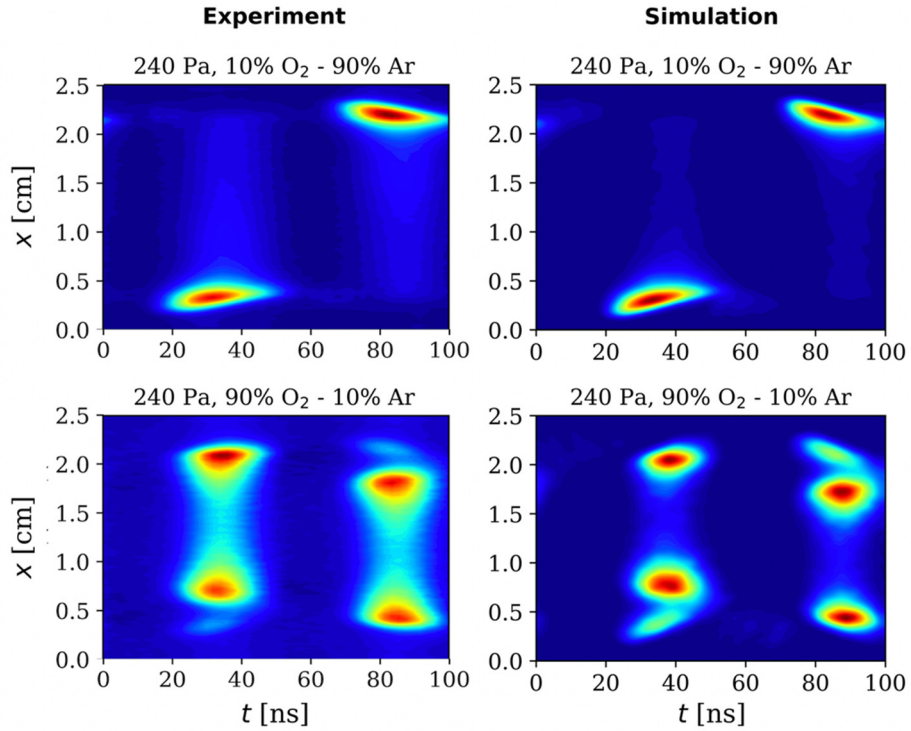

Fig. 1. Spatio-temporally resolved electron impact excitation rate from the ground state into the Ar2p1 state [a.u.] obtained from experiment by PROES (first column) and from PIC/MCC simulation (second column) for 10% O2 – 90% Ar (first row) and for 90% O2 – 10% Ar (second row) mixtures at p = 240 Pa, f = 10 MHz, V_{pp} = 350 V peak-to-peak voltage, L = 2.5 cm discharge gap.

Based on the measured and calculated excitation patterns, multiple discharge operation regimes are identified. The simulations provide information about the mechanisms behind the formation of these patterns. At the lowest pressure, a weak α-peak at the expanding sheath edge, a strong ambipolar peak, and a weak drift feature in the bulk region are found in the excitation rates. With increasing pressure, the α-peak and the drift feature are found to be enhanced, while the ambipolar peak is reduced. At intermediate pressures, the α-peak is found to be the dominant excitation pattern in all mixtures. Further increase of the pressure results in the formation of two distinct excitation peaks at the edges of the bulk region (caused by local maxima in the electronegativity), which dominate the excitation at high O_2 concentrations (see panels in the bottom row of Fig. 1).

Acknowledgement: This work was supported by the Hungarian National Research, Development and Innovation Office via grants K-134462 and FK-128924, and by the ÚNKP-22-3 New National Excellence Program of the Ministry for Culture and Innovation from the source of the National Research, Development and Innovation Fund.

4. References

[1] A Derzsi *et al*, *Plasma Sources Sci. Technol.* **31** 085009 (2022).

[2] Hayashi database, Biagi-v8.9 database, www.lxcat.net; Vahedi V and Surendra M 1995 *Comput. Phys. Commun.* **87** 179; Gudmundsson J T *et al*, *Plasma Sources Sci. Techno*l. **22** 035011 (2013); Phelps A V, *J. Appl. Phys*. **76** 747 (1994); Flesch G D, Nourbakhsh S, Ng C Y, *The Journal of Chemical Physics* **92** 3590 (1990); Langevin P, Une formule fondamentale de theorie cinetique (1905); Bronold F *et al*, *J. Phys D: Applied Physics* **40** 6583 (2007).

TIME-RESOLVED SPECTROSCOPY OF DISCHARGES IN CsCl SOLUTIONS

Kamila Shojaa[1], Fayza Hassan[1], David McCartney,[1] Tom A Field,[1]

[1]*Centre for Light Matter Interactions, School of Maths and Physics, Queen's University Belfast, BT71NN, Northern Ireland, U.K.*
E-mail: kshojaa01@qub.ac.uk

Time resolved optical spectra have been recorded of discharges in aqueous CsCl solutions. The strongest atomic lines observed are from the hydrogen Balmer series, but there are also broader features in the spectrum. There are significant changes in the intensity and shape of these features in the spectra with time.

Plasma discharges have been generated in caesium chloride (CsCl) solution between two tungsten pin electrodes. Time resolved optical spectra have been recorded with an ICCD iStar Andor camera and a small broad band UV-visible spectrometer. Approximately 320 nm of the UV-visible spectrum can be recorded with the camera and a 300 line/mm diffraction grating in the specgtrometer with a optical resolution of approximately 1 nm and time resolution of better than 10 ns. In reality time windows for spectra are generally significantly wider than 10ns. The Balmer Hα, Hβ, and Hγ are being analysed to try to determine electron densities as a function of time.

CHARACTERIZATION OF MICROGAP VACUUM BREAKDOWNS GENERATED BY PULSED ELECTRIC FIELD

Mária Maťašová[1], Matej Klas[1], Peter Čermák[1], Marija Radmilović-Radjenović[2], Leonid Satrapinskyy[1], Štefan Matejčík[1]

[1]*Department of Experimental Physics, Faculty of Mathematics, Physics and Informatics, Comenius University, Mlynská dolina, 842 48 Bratislava, Slovakia*

[2]*Institute of Physics, University of Belgrade, Pregrevica 118, 11080 Belgrade, Serbia*

E-mail: maria.cibikova@fmph.uniba.sk

The main objective of this work is to investigate the microgap vacuum breakdowns between palladium electrodes set in the sphere-plane geometry and to characterize the emission current generated in the pre-breakdown stages. The conditioning of electrodes and saturated breakdown voltages were measured for different gap distances from 1 μm up to 10 μm. The microdischarges were generated by a pulsed electric signal with a voltage ramp speed of 10^7 kV/s.

1. Introduction

The first attempts to characterize microdischarges were performed in the fifties of the last century by Boyle, Germer, Kysliuk, and others [1,2,3]. They investigated the question of the origin of microgap discharge breakdown and field emission (FE) phenomena mostly from the fundamental point of view. In 1996, Schoenbach has shown a stable discharge generated in the microdischarge cavity at high pressure with several potential applications [4,5]. Now, the microdischarges are used mostly in the various plasma sources due to their high current densities caused by high electric field intensity.

However, there is still an unknown process behind the initiation of discharge due to field emission. Due to the fast ionization processes ongoing in the discharge region, it is difficult to measure the pure field emission at high pressure. For this reason, it is beneficial to provide the measurements in a vacuum where the impact of gas on the electric breakdown can be neglected. In our previous study [6] we focused on the characterization of FE from stainless-steel electrodes. The main objective of this work is to follow our previous research and to investigate the phenomena occurring in the breakdown and pre-breakdown stages for electrodes made from palladium. Thereafter, based on the Fowler-Nordheim theory, the measured data can be used for the determination of other important parameters for the general characterization of microdischarge such as emission current density, emission area, and factor of a locally enhanced electric field.

Palladium belongs to the group of noble metals characterized by corrosion resistance and high thermal conductivity [7]. It is mostly used in catalytic converters or multi-layer ceramic capacitors, but also in spark plugs for enhancement discharge properties [8,9]. However, there are no available data about the conditioning processes of noble metals or investigation of field emission phenomena which are important for their complex characterization. For this purpose, we decided to use palladium metal to represent the noble metal group and investigate its vacuum breakdown phenomena for a better understanding of processes occurring in the discharge region.

2. Experimental apparatus

A Schematic of the experimental apparatus is shown in Fig. 1. The vacuum system consisted of a vacuum chamber and pumping system which included a turbomolecular pump with pre-vacuum secured by a dry forepump. The background pressure in the vacuum chamber was achieved at 2.10^{-4} Pa. The palladium electrodes were set in sphere-plane geometry in the vacuum chamber. The sphere represented the cathode with a diameter of approx. 5 mm. The plane anode was connected via a series of resistors to the pulsed signal generated by a high-voltage power supply and switch controlled by a function generator. The voltage ramp speed of the signal was ~ 10^7 kV/s. The size of the gap was set from 1 up to 10 μm using a micrometer head. The 0 μm separation was established by measurement of electrical contact between electrodes by using an ohmmeter.

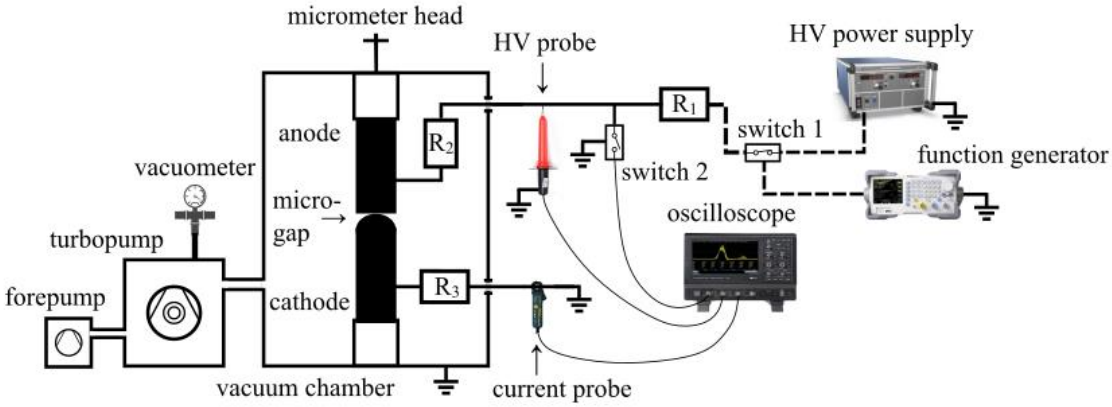

Fig. 1: The scheme of the experimental apparatus for generation and measuring microdischarges.

3. Experimental results

Before measurement, the conditioning (cleaning of electrode surface from impurities by successive breakdowns) is the key process for the subsequent investigation of field emission phenomena. The conditioning is usually measured for one selected microgap ~ 10 μm. Fig. 2 represents the evolution of breakdown voltage during the conditioning.

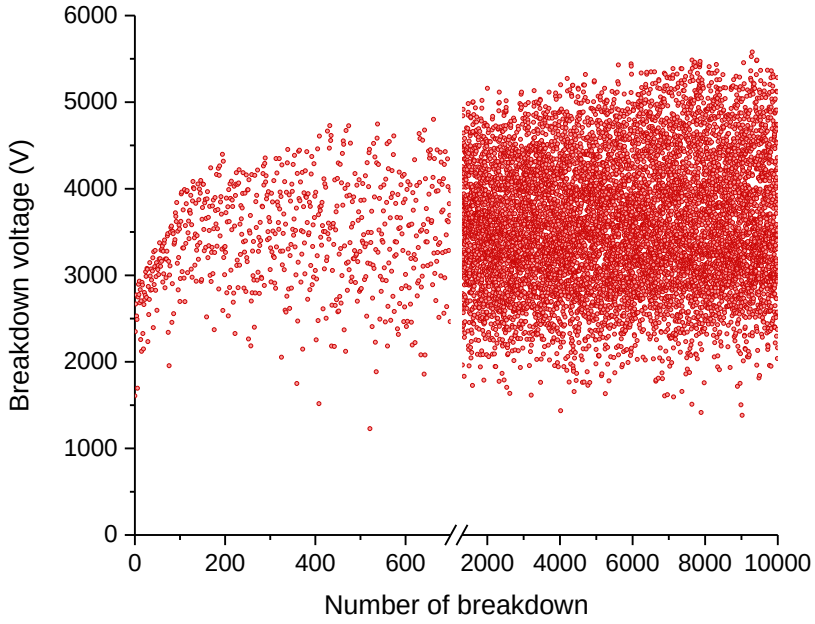

Fig. 2: Evolution of breakdown voltage during conditioning (10^7 kV/s, 10 μm).

As shown in Fig. 2, during the conditioning of electrodes the average value breakdown voltage increased. This augmentation was referred to as an unsaturated state. When the average breakdown voltage had become saturated (stable), the electrodes were considered to be conditioned. However, the fluctuation of breakdown voltage after full conditioning is still present. This is due to the formation of protrusions and pinholes occurring on the electrode surface after each successful breakdown. An interesting point is the finding that two successive breakdowns are not accidental. It is shown in Fig. 3 which represents the correlation of the difference between two consecutive breakdown voltages $V_{B(n+1)} - V_{B(n)}$ versus the earlier one $V_{B(n)}$ determined for different gap sizes measured in the saturated voltage region. The correlations represent the atypical graphs showing some trends which manifest non-randomness of consecutively generated breakdowns.

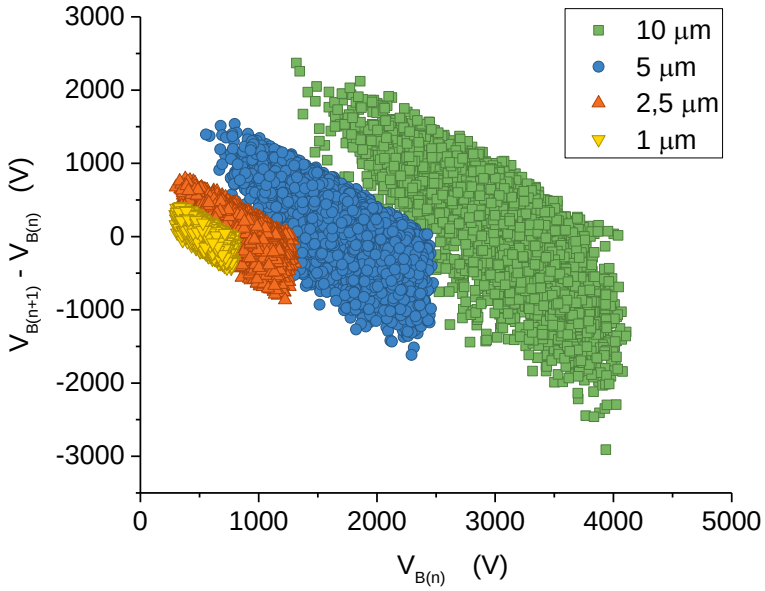

Fig. 3: Correlation between $V_{B(n+1)} - V_{B(n)}$ versus $V_{B(n)}$ breakdowns.

In the saturated state was also measured the maximum field emission current before breakdown for different distances of microgap. Fig. 4 shows the field emission current and corresponding breakdown voltages for different gap distances. The maximum field emission current was obtained for 5 μm and decreased on both sides for higher or lower electrode distances. This is in good agreement with the work of Tsuruta [10] who proposed this current behavior if anode breakdown is dominant.

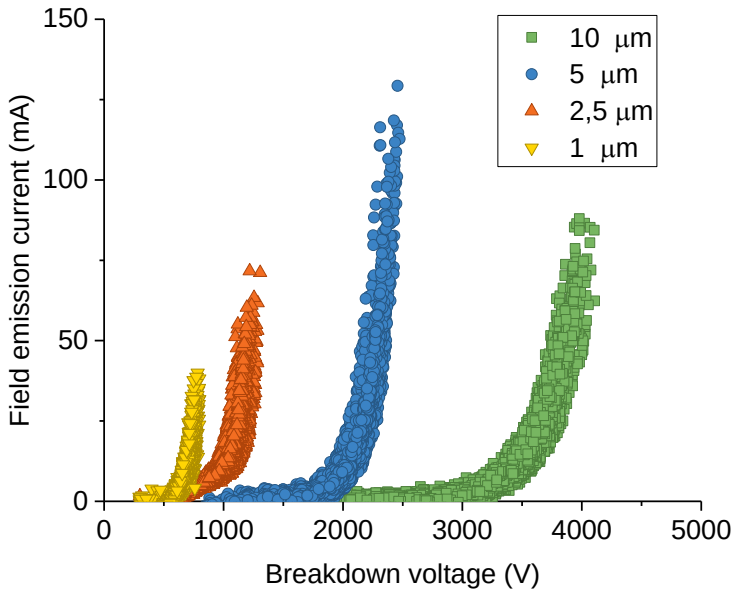

Fig. 4: Field emission current measured for different sizes of microgap.

Acknowledgments

The authors acknowledge partial support from Slovak Grant Agency for Science VEGA Nr. 1/0489/21, Slovak Research and Development Agency under project Nr. APVV-19-0386 and SK-SRB-21-0004.

4. References

[1] Dyke, W. P., & Trolan, J. K. (1953). Field emission: Large current densities, space charge, and the vacuum arc. Physical Review, 89(4), 799.

[2] Utsumi, T. (1967). Cathode-and Anode-Induced Electrical Breakdown in Vacuum. Journal of applied physics, 38(7), 2989-2997.

[3] W.S. Boyle, P. Kisliuk, L.H. Germer, Electrical breakdown in high vacuum, J. Appl. Phys. 26 (6) (1955) 720–725.

[4] Schoenbach, K. H., Verhappen, R., Tessnow, T., Peterkin, F. E., & Byszewski, W. W. (1996). Microhollow cathode discharges. Applied Physics Letters, 68(1), 13-15.

[5] Schoenbach, K. H., & Zhu, W. (2012). High-pressure microdischarges: Sources of ultraviolet radiation. IEEE Journal of Quantum Electronics, 48(6), 768-782.

[6] Klas, M., Čermák, P., Borkhari, A. F., Satrapinskyy, L., Matejčík, Š., Radjenović, B., & Radmilović-Radjenović, M. (2021). Vacuum breakdown in microgaps between stainless-steel electrodes powered by direct-current and pulsed electric field. Vacuum, 110327.

[7] Beamish, F. E. (2013). The analytical chemistry of the noble metals. Elsevier.

[8] Zogbi, D. (2003). Shifting Supply and Demand for Palladium in MLCCs. TTI, Inc. http://www. ttiinc. com/object/ME_Zogbi_20030203. html.

[9] Seymour, R. J., O'Farrelly, J. I., & Potter, L. C. (2012). Platinum‐Group Metals. Kirk‐Othmer Encyclopedia of Chemical Technology.

[10] Tsuruta, K. (1983). Prebreakdown field emission current and breakdown mechanism of a small vacuum gap. IEEE Transactions on Electrical Insulation, (3), 204-208.

FIELD EMISSION PARAMETERS OF LARGE AREA PALLADIUM ELECTRODES IN A VACUUM

Matej Klas[1], Mária Maťašová[1], Peter Čermák[1], Marija Radmilović-Radjenović, Štefan Matejčík[1]

[1]*Department of Experimental Physics, Faculty of Mathematics, Physics and Informatics, Comenius University, Mlynská dolina, 842 48 Bratislava, Slovakia*

[2]*Institute of Physics, University of Belgrade, Pregrevica 118, 11080 Belgrade, Serbia*

E-mail: matej.klas@uniba.sk

The presented study is focused on the investigation of emission current from the large surface area palladium electrodes with a sphere to plane geometry. The measurements were performed at the electrode distances in the range of 500nm up to 10 μm at the pulsed electric field rate of 10^{10}V/s. The breakdown voltages were measured depending on the pulse rise time and the electrode separation. The emission current was analyzed using the field emission theory described by the Fowler-Nordheim equation. The enhancement factor, the radius of the emitting area, and current density were subsequently determined.

1. Introduction

The key parameter of utilizations of field emission microdischarges (FEM) in industry is the electrode resistance to the corrosive atmosphere at high current densities. Our previous research [1] of FEM was focused on the characterization of the electrode with stainless steel (SS). The maximum current drawn from the SS electrodes before the breakdown occurs was approximately 1mA @ (10^5V/s; 5μm). At slower pulses was even lower with the strong influence of tip heating. Moreover, the oxidative environments rapidly erode the electrode surface [2]. This leads to the search for a new reliable metal for FEM electrodes. One of the possibilities is the use of precious metals due to their unique properties as high electrical and thermal conductivity, high melting point, and resistance to oxidative atmospheres. For this purpose, we focused in this study on the field emission properties of palladium electrodes.

2. Experimental setup

The schematic of the apparatus used in this experiment is shown in Fig. 1. The palladium electrodes were situated in a vacuum chamber (p ~1.10^{-4}Pa) in sphere to plane geometry, ensuring a quasi-uniform electric field. The sphere electrode represents the cathode with a diameter of approximately 5 mm. The electrode surfaces were mechanically polished with the diamond pastes (down to 0,25 μm grain size) and afterward ultrasonic cleaned with isopropyl and distilled water. The voltage pulse was generated by switching (Behlke) high voltage through the limiting resistor R1(20k**W)**.

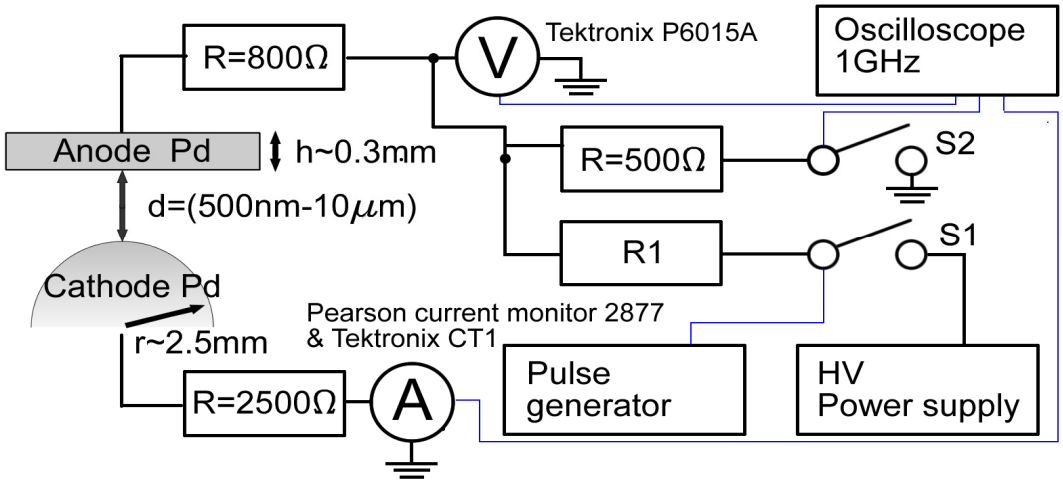

Fig. 1 Schematic of the apparatus with electrical circuit generating HV pulse

3. Results and discussion

The field emission parameters -enhancement factor β, emitter area A and the current density J, were extracted from the measured current–voltage waveforms $I(U)$ following the standard approach as defined by Forbes et al. [3]. Fig. 2 shown calculated enhancement factor β prior to breakdown as function of voltage. The average β starts from ~22 at 10µm down to ~8 for 0.5µm. This is almost 3 times lower than for similar measurements for large area copper electrodes [4]. Maximum FE current drawn from the electrode was observed at the peak of 5µm with a current of more than 200mA while decreasing to 70mA for 10 µm and 2.5µm. Based on the surface morphology and the current behavior at different electrode spacing [5], we assumed the anode dominant breakdown occurs in all electrode distances and the field emission current is primarily limited by the anode melting point heated by the electron beam from the whisker.

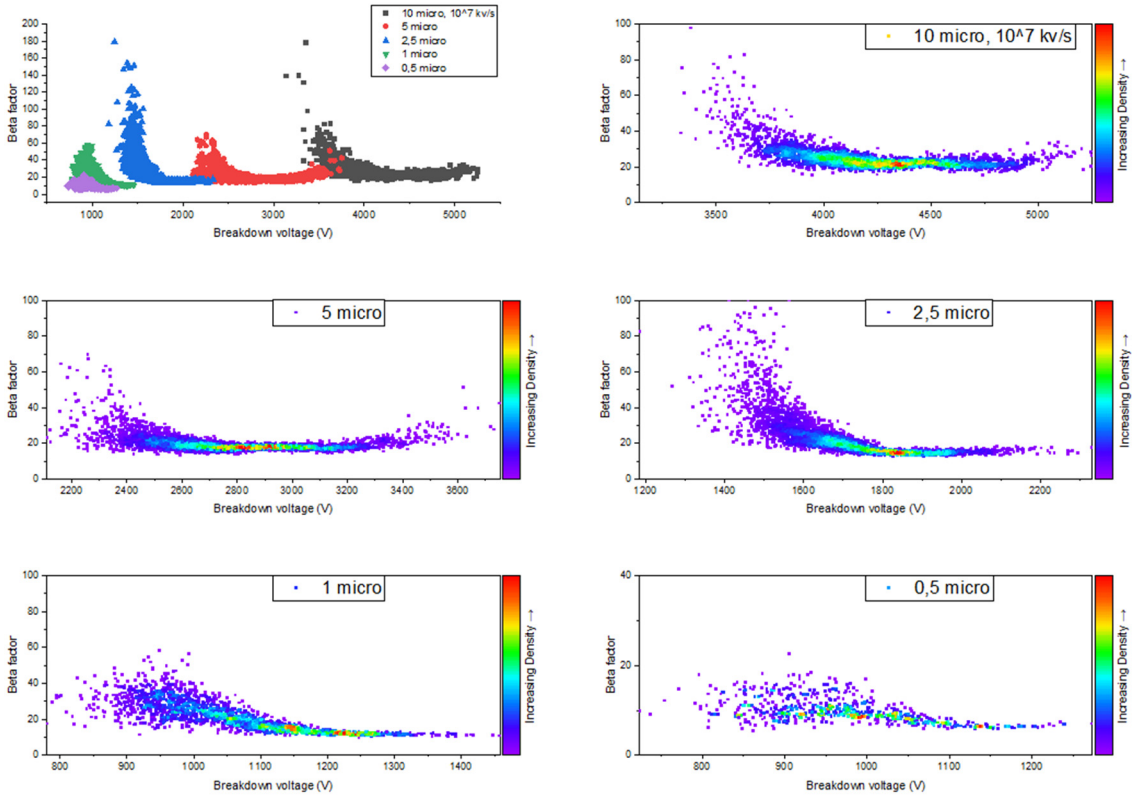

Fig. 2 Scatter density graph of enhancement factor β at different electrode distances

Acknowledgements

The authors acknowledge partial support from Slovak Grant Agency for Science VEGA Nr. 1/0489/21, Slovak Research and Development Agency under project Nr. APVV-19-0386 and SK-SRB-21-0004.

4. References

[1] Klas, M., Čermák, P., Borkhari, A. F., Satrapinskyy, L., Matejčík, Š., Radjenović, B., & Radmilović-Radjenović, M. (2021). Vacuum breakdown in microgaps between stainless-steel electrodes powered by direct-current and pulsed electric field. Vacuum, 110327.

[2] M Klas, L Moravsky, Š Matejčik, M Zahoran, V Martišovitš, B Radjenović, M. Radmilović

(2018) The breakdown voltage characteristics of compressed ambient air microdischarges from direct current to 10.2 MHz Plasma Sources Science and Technology 26 (5), 055023
[3] R.G. Forbes, J.H.B. Deane, (2007) Reformulation of the standard theory of fowler–nordheim tunnelling and cold field electron emission, Proc. R. Soc. A: Math. Phys. Eng. Sci. 463 (2087) 2907–2927
[4] Tsuruta, K. (1983). Prebreakdown field emission current and breakdown mechanism of a small vacuum gap. IEEE Transactions on Electrical Insulation, (3), 204-208
[5] Utsumi, T. (1967). Cathode-and Anode-Induced Electrical Breakdown in Vacuum. Journal of applied physics, 38(7), 2989-2997.

ANALYSIS OF THE NUMBER AND LENGTH OF GLIDING ARCS FOR DIFFERENT COMPOSITIONS AND FLOW RATES OF THE WORKING GAS

Piotr Terebun[1], Michał Kwiatkowski[1], Joanna Pawłat[1],
Mario Janda[2], Karol Hensel[2], Zdenko Machala[2]

[1]*Institute of Electrical Engineering and Electrotechnologies, Lublin University of Technology*
[2]*Faculty of Mathematics, Physics and Informatics, Comenius University*
E-mail: p.terebun@pollub.pl

One of the advantages of gliding-arc plasma reactors is the ability to operate in a wide range of composition and flow rate of working gas. Due to the significant influence of gas-dynamic forces, the gas parameters directly affect the shape of the discharge and thus the efficiency of plasma treatment and the requirements for the system geometry. The study presents the results from imaging of discharges in a miniature, two-electrode gliding-arc reactor for applications in environmental engineering and food technology using the high-speed camera (Photron FASTCAM SAZ 2100K). On the basis of the obtained images, the position and speed of the arc were analyzed for two values of the working gas flow rate, which was air, nitrogen or oxygen.

A comparison of the results shows the significant influence of the gas-dynamic forces resulting from the forced gas flow. At the higher flow rate, the discharges lasted for a shorter time, but the arc was much longer. In addition, it was possible to observe the appearance of a main, longest discharge followed by successive, shorter ones. Adding up the duration of all the discharges per period of the voltage signal, the discharges thus lasted as long as individual discharges at a lower flow rate. Combined with the significantly longer length of the arc itself, represented by the positions of the discharges, the obtained results allow to indicate one of the possible reasons for the higher generation of reactive oxygen and nitrogen species for the higher flow rate. Differences between the different working gas compositions were negligible, where slightly higher arc positions were observed for oxygen as the working gas.

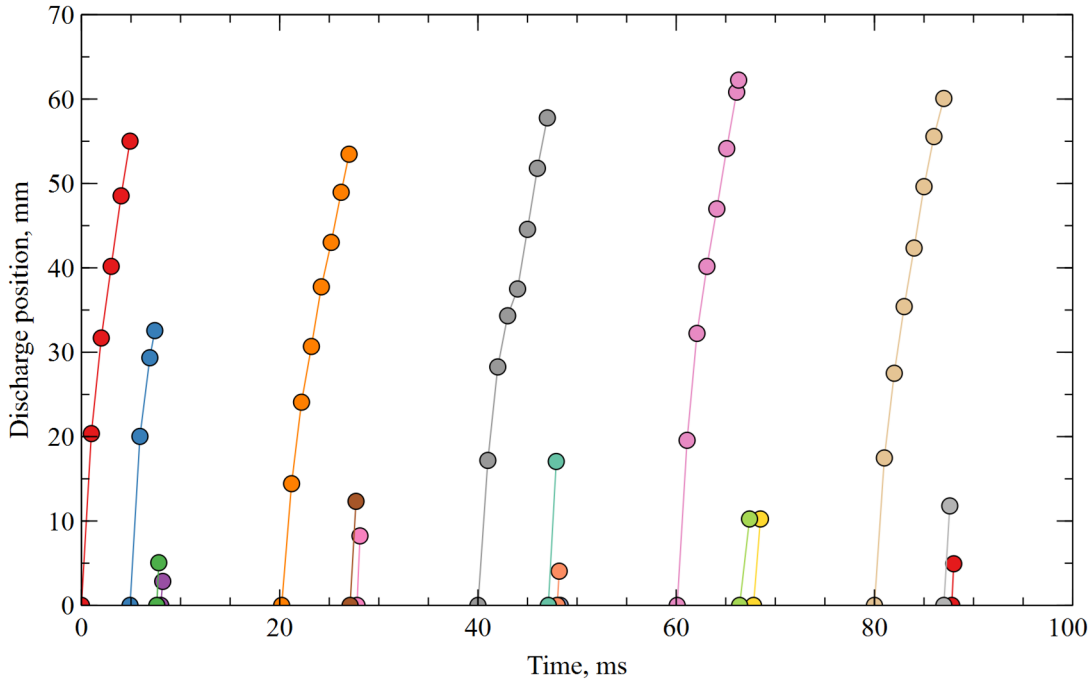

Fig. 1. Position of individual discharges as a function of time (oxygen, 440 l/h).

MOLECULAR HYDROGEN MASS STOPPING POWERS FOR LOW-ENERGY ELECTRONS

Mateusz Zawadzki[1] and Murtadha A. Khakoo[2]

[1]*Department of Electron Collision Physics, Institute of Physics and Applied Computer Science, Faculty of Applied Physics and Mathematics, Gdańsk University of Technology, 80-233 Gdańsk, Poland*
[2]*Department of Physics, California State University, Fullerton, California 92831, USA*

E-mail: mateusz.zawadzki@pg.edu.pl

We present experimental mass stopping powers of electrons in gaseous H2 obtained with a newly developed electron time-of-flight spectrometer, for the incident electron energy range of 10 eV to 25 eV. In our procedure the average energy loss is derived from our conversion of electron time-of-flight spectra into equivalent electron energy loss spectra so as to obtain the values of mass stopping power using energy loss as the parameter for electron scattering.

1. Introduction

The mass stopping power (MSP) - a useful parameter obtained from collision studies - is of fundamental importance in biomedical dosimetry, radiation physics, chemistry, medicine and biology involving neutrons, protons, X-rays and electrons [1]. Although, MSPs are widely used in many fields they are rarely obtained experimentally. This is because in these measurements the complete electron energy loss spectrum should be measured, and the spectrum should be corrected for instrumental transmission effects.

The mass stopping power is defined by the well-known formula:

$$\mathrm{MSP} = \frac{1}{\rho}\frac{dE}{dx} = \frac{N_\mathrm{a}}{M}\langle E_\mathrm{L}\rangle\,\sigma_\mathrm{inel} \tag{1}$$

where *N*a is Avogadro's number, *M* is the molar mass of the molecule, $\langle E_L \rangle$ is the mean inelastic energy loss, and is the mean inelastic energy loss, and σ_{inel} is the integral inelastic cross section in a.u. and ρ, is the density of gaseous H_2 .

2. Experiment

Our measurements were obtained from a recently constructed time-of-flight (TOF) spectrometer, consisting of an intense energy unselected pulsed electron gun and a TOF analyser [2,3]. In our studies we collide low-energy electrons with target H_2 gas molecules in a crossed beam configuration, and we measure transmission-free TOF electron scattering spectra. We used these TOF spectra provide experimental MSP of electrons in H_2 in the low electron energy range [4].

3. Results

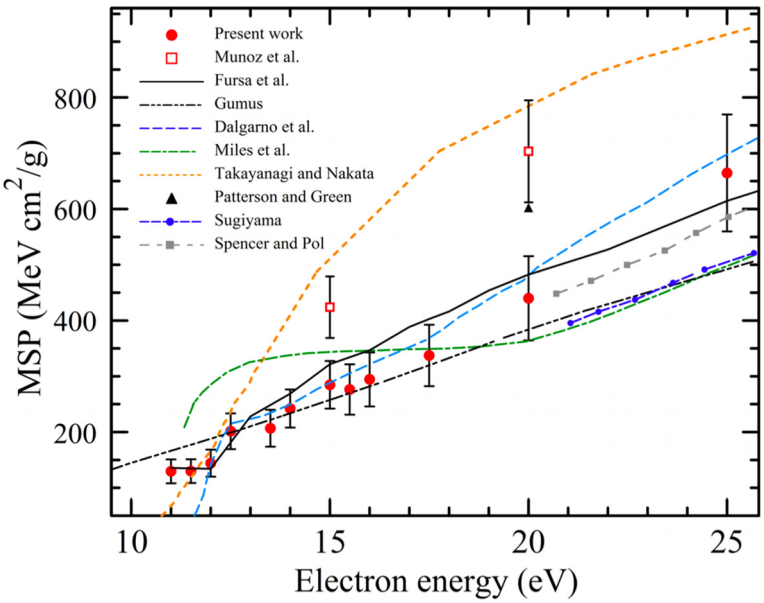

Fig. 1. MSP for electron scattering from the ground state of H2. Experiment: Munoz et al. [5]; Theory, Fursa et al. [6], Gumus [7], Dalgarno et al. [8], Miles et al. [9], Takayanagi and Nakata [10], Peterson and Green [11], Sugiyama [12] and Spencer and Pol [13].

4. References

[1] Mayles P, Nahum A, Rosenwald J C, *Handbook of Radiotherapy Physics: Theory and Practice* (CRC Press, Boca Raton, 2007).
[2] Zawadzki M, et al. (2018) *Phys. Rev. A* **97**, 050702.
[3] Zawadzki et al. (2018) *Phys. Rev. A* **98**, 062704.
[4] Zawadzki M, Khakoo M A (2019) *Phys. Rev. A* **99**, 042703.
[5] Munoz M et al. (2007) *Chem.Phys.Lett.* **433**, 253.
[6] Fursa D V et al. (2017) *Phys Rev. A* **96**, 022709.
[7] Gumus H (2005) *Radiat. Phys. Chem*. **72**, 7 .
[8] Dalgarno A et al. (1999) *Astrophys. J. Suppl*. **125**, 237.
[9] Miles W T, Thompson R, Green A E S (1972) *J. Appl. Phys.* **43**, 678.
[10] Takayanagi K and Nakata K (1970) *Bull. Inst. Space Aeronaut. Sci.* **6**, 849.
[11] Peterson L R and Green A E S (1968) *Proc. Phys. Soc., Series* **2**, 1, 1131.
[12] Sugiyama H (1985) *Phys. Med. Biol.* **30**, 331 .
[13] Spencer L V and Pol R (1978) *National Bureau of Standards, Report NBSIR 78-1523.*

PLASMA TREATMENT FOR CONDITIONING OF JUICE

Dawid Zarzeczny[1], Piotr Terebun[1], Michał Kwiatkowski[1], Joanna Pawłat[1], Agnieszka Starek-Wójcicka[2], Barbara Chudzik[2], Zdenko Machala[3], Karol Hensel[3]

[1]*Institute of Electrical Engineering and Electrotechnologies, Lublin University of Technology, Nadbystrzycka 38a, 20-618 Lublin, Poland*

[2]*Department of Biological Bases of Food and Feed Technologies, University of Life Sciences in Lublin, Głęboka 28, 20-612 Lublin, Poland*

[3]*Department of Environmental Physics, Comenius University, Mlynská dolina F2, 842 48 Bratislava, Slovakia*

E-mail: d.zarzeczny@pollub.pl

The aim of the research was to investigate the effect of Cold Atmospheric Plasmas (CAP) treatment on various parameters of freshly pressed NFC (Not From Concentrate) apple juice, including on microbiological quality, physicochemical and structural properties. In addition, the conducted research will be used to assess the usefulness of CAP in extending the shelf life of fresh apple juice with minimized loss of valuable nutrients.

1. Research topics

At present, not-from-concentrate juices (NFC) also referred to as one-day or fresh juices are premium products on the food market. They are produced by pressing fruit pulp or mechanical mashing raw materials. Many scientific studies confirm that cloudy juices (vs. clear juices) contain several-fold higher amounts of beneficial bioactive compounds, which exhibit strong anti-cancer, anti-inflammatory, and anti-aging activities.

Currently conducted research, described by many authors, confirms the rightness of using CAP in order to eliminate unwanted bacteria and fungi from food products. However, there is little evidence of the effectiveness of the disinfection of fruit and vegetable juices. The most frequently performed experiments are based on the analysis of the effect of CAP on specific microorganisms in pasteurized juices. An interesting area, due to the prevailing trends related to healthy eating, is the possibility of extending the shelf life of unpasteurized juices [1-6].

Using a modified GildArc (GAD) reactor connected to a flow system, the potential use of low-temperature plasma technology to condition unpasteurized apple juice was investigated. The conducted experiments were aimed at determining the optimal conditions of food processing with the use of CAP.

2. References

[1] Liao, X. et al. Application of a Dielectric Barrier Discharge Atmospheric Cold Plasma (Dbd-Acp) for Eshcerichia Coli Inactivation in Apple Juice. Journal of Food Science 83, 401–408 (2018).

[2] Dasan, B. G. & Boyaci, I. H. Effect of Cold Atmospheric Plasma on Inactivation of Escherichia coli and Physicochemical Properties of Apple, Orange, Tomato Juices, and Sour Cherry Nectar. Food Bioprocess Technol 11, 334–343 (2018).

[3] Xu, L., Garner, A. L., Tao, B. & Keener, K. M. Microbial Inactivation and Quality Changes in Orange Juice Treated by High Voltage Atmospheric Cold Plasma. Food Bioprocess Technol 10, 1778–1791 (2017).

[4] Surowsky, B., Fröhling, A., Gottschalk, N., Schlüter, O. & Knorr, D. Impact of cold plasma on Citrobacter freundii in apple juice: Inactivation kinetics and mechanisms. International Journal of Food Microbiology 174, 63–71 (2014).

[5] Pankaj, S. K., Wan, Z., Colonna, W. & Keener, K. M. Effect of high voltage atmospheric cold plasma on white grape juice quality. Journal of the Science of Food and Agriculture 97, 4016–4021 (2017).

[6] Starek A., Pawłat J., Chudzik B., Kwiatkowski M., Terebun P., Sagan A. & Andrejko D., Evaluation of selected microbial and physicochemical parameters of fresh tomato juice after cold atmospheric pressure plasma treatment during refrigerated storage. Scientific Reports 9:8407, 1–11 (2019).

EXCITATION OF ACETONE INDUCED BY ELECTRON IMPACT

Juraj Országh[1], Barbora Stachová[1], Ján Blaško[1], Bartosz Michalczuk[2], Štefan Matejčík[1]

[1]*Department of Experimental Physics, Comenius University in Bratislava, Slovakia*
[2]*Institute of Chemistry, Faculty of Sciences, Siedlce University of Natural Sciences and Humanities, Siedlce, Poland*
E-mail: juraj.orszagh@uniba.sk

Electron induced fluorescence of acetone was studied by optical emission spectroscopy. Acetone is the simplest ketone and it is an abundant compound of the interstellar medium. The emission spectrum following electron impact on acetone is studied in a crossed-beam experiment. The spectrum is measured at several electron energies in range from 10 to 100 eV within the wavelengths of 280 - 950 nm. The emission bands of CH (A-X), CH (B-X) and CH (C-X) along with emission lines of hydrogen's Balmer series are detected. Relative emission cross sections of several emission lines and bands are measured as well and their threshold energies and dissociative excitation channels are estimated.

1. Introduction

Dissociation electron impact excitation processes can provide a remote diagnostic method of neutral gases and chemical and physical properties of the environment in atmospheres around planets and small bodies in our solar system [1]. Due to specific distribution of electron, vibrational and rotational energy levels each compound has its own spectral fingerprint in IR, VIS and UV. The efficiency of the excitation process strongly depends on collision energy [2]. In other words, the emission cross section strongly depends on the kinetic energy of colliding electron. The shape of the spectrum is given by population of individual energy levels of the molecule which depends on the process producing the excited particle. In the figure 1 comparison of three spectra of OH(A-X) is shown. From the shape of the spectrum the process leading to emission can be derived. Sufficiently rich database of the emission spectra induced by different processes can be a strong tool for remote diagnostics of the planetary environment [3]. Acetone itself has been found in various types of environments where electron induced processes play a significant role. It was detected in gases surrounding young star by ALMA [4], in interstellar space [5], it is the most abundant volatile organic compound in the Earth atmosphere which has a significant impact on atmospheric chemistry [6].

2. Experiment

The experimental apparatus used in this work is based on a crossed electron and molecular beams method and is further described in a previous publication [3]. Trochoidal electron monochromator located in a vacuum chamber generates a monochromatic electron beam. The electron beam interacts with a perpendicular molecular beam formed by an effusive capillary. The background pressure of the vacuum chamber is $\sim 10^{-8}$ mbar and the pressure of the molecular beam is set to sustain binary interactions – one electron with one molecule. One of the products of electron-molecule interactions are excited species. These are unstable and emit radiation as they de-excite. The emitted radiation is collected by a UV fused silica lens and guided out of the vacuum chamber to a parabolic mirror, which focuses this radiation to the entrance slit of a Czerny-Turner optical monochromator. To maximise the detected signal, a spherical mirror is placed opposite to the collecting lens with its focus at the centre of collision. To acquire signal from the emitted radiation, either a Hamamatsu photomultiplier R4220P (PMT) or an Andor iDUS 420 CCD camera can be used. The photomultiplier is sensitive to wavelengths of 185 – 700 nm and collects the signal at one wavelength at a time. The CCD camera is sensitive to 300 – 1100 nm wavelength range and can obtain signal from an approximately 85 nm interval of wavelengths which makes the CCD camera more efficient for measuring spectra. The scheme of the experimental apparatus is shown in Figure 1.

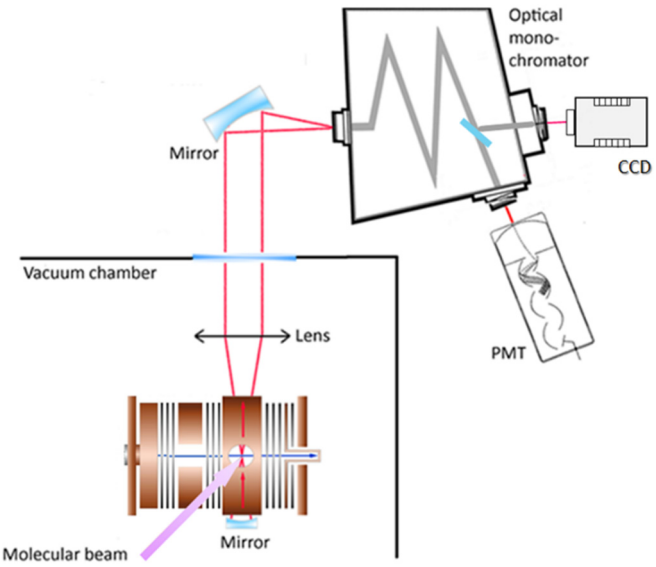

Fig. 1. Simple scheme of the experimental system.

The emission spectrum of acetone was measured in the wavelength range of 280 – 950 nm at 50 eV electron energy and corrected for apparatus sensitivity. There were no detected transitions in the region of 300 – 380 nm. The wavelength region of 445 – 900 nm consists of the lines of hydrogen's Balmer series H_α at 656.3 nm and H_β at 486 nm, and the Swan system of C_2 ($d^3\Pi_g$–$a^3\Pi_u$) within 460 – 472 nm. The emission spectrum within the wavelengths of 380 - 445 nm is depicted in Figure 2. The emission band in the range of 415 – 445 nm corresponds to the radiation of CH ($A^2\Delta$–$X^2\Pi$) (v,v) fragment. Less intensive radiation of CH ($B^2\Sigma^-$–$X^2\Pi$) (0,0) fragment was identified within 386 – 402 nm. Several emission lines of hydrogen's Balmer series H_γ – H_η were detected throughout the spectrum as well. Individual rotational transitions from P, Q, R branches of both CH fragments are resolved in the Fig. 2.

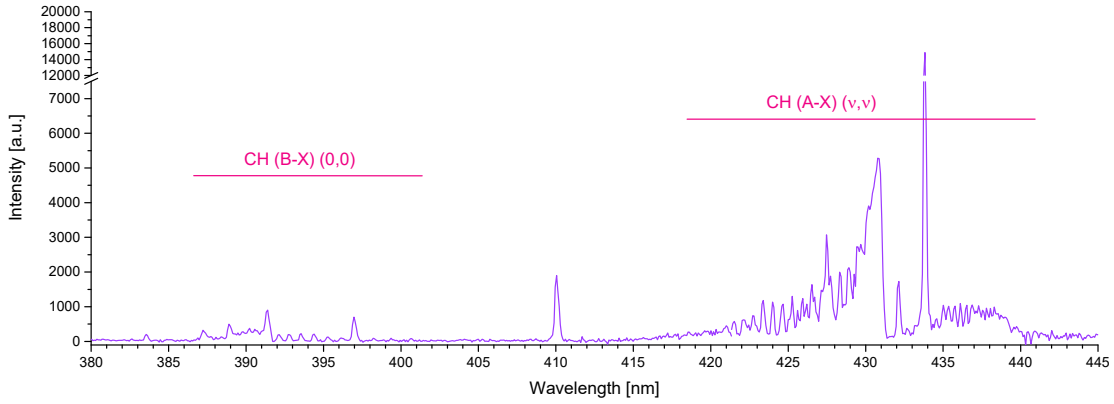

Fig. 2. The main detected molecular bands CH (A-X) and CH (B-X).

3. Conclusions

Electron induced fluorescence of acetone was studied in a crossed-beam experiment. The emission spectrum of neutral fragments of acetone was measured, analysed and compared with simulated spectra from LIFBASE. Experimental threshold energies were determined from the relative emission cross sections of selected transitions (H_β, H_γ, CH ($A^2\Delta$–$X^2\Pi$)). Theoretical values were calculated from enthalpy of formation and excitation energies and compared to experimental results. The comparison was used as a basis for suggesting dissociative excitation channels for selected transitions. Further

research will be focused on less intensive and other possible transitions in the spectrum and threshold energies of all identified transitions. Individual dissociative excitation channels will be distinguished as well.

Acknowledgments. The presented research was partially supported by Slovak grant agency VEGA within the projects nr. 1/0489/21, 1/0553/22, by Slovak Research and Development Agency within projects nr. APVV-19-0386, APVV-15-0580. This research has received funding from the European Union's Horizon 2020 research and innovation programme under grant agreement No 871149.

4. References

[1] Galand M and Chakrabarti S 2002 *GMS* **130** 55.
[2] Itikawa Y and Mason N J 2005 *JPCRD* **34** 1.
[3] Bodewits D, Országh J, Noonan, J et al. 2019 *ApJ* **885** 167.
[4] Lykke J M, Coutens A, Jorgensen J K et al. 2017 *A&A* **597** A53.
[5] Combes F, Gerin M, Wootten A et al. 1987 *A&A* **180** L13.
[6] Franco B, Clarisse L, Stavrakou T et al. 2019 *GRL* **46** 2884.

ELECTRON IMPACT EXCITATION OF CARBON MONOXIDE

Barbora Stachová[1], Ján Blaško[1], Juraj Országh[1], Steven Bromley[2], Dennis Bodewits[2], Štefan Matejčík[1]

[1]*Department of Experimental Physics, Faculty of Mathematics, Physics and Informatics, Comenius University in Bratislava, Slovak Republic*
[2]*Department of Physics, Auburn University, Alabama, USA*
E-mail: barbora.stachova@fmph.uniba.sk

Optical emission spectroscopy was used to study electron induced fluorescence of carbon monoxide [CO]. CO is one of the dominant carbon bearing molecules in extra-terrestrial bodies such as comets or centaurs. It is also present in interstellar gas clouds which are the precursors of star formation. The emission spectrum following electron impact on CO molecule was studied in a crossed-beam experiment. The spectrum was measured at several electron energies in range from 2.5 to 100 eV within the wavelengths of 275 - 510 nm. The emission bands of CO and CO^+ dominate this spectral region. Excitation-emission functions of several emission lines and bands were measured as well and their threshold energies were estimated.

1. Introduction

Electron-molecule interactions play an important role in various environments, whether it is the Earth's atmosphere or extra-terrestrial objects. Electron induced fluorescence (EIF) is one of the phenomena that occur during the inelastic interaction of molecules with low energy electrons. It results in excitation and subsequent emission of radiation as excited particles de-excite. Studying EIF provides information on these radiative processes, which is needed to produce reference data for the analysis of astronomic spectra, theoretical modelling of complex systems such as atmospheric processes, electric discharges and other research or industrial applications. EIF can be studied by optical emission spectroscopy, which is of particular importance for astrophysical research that is focused on plasma-chemical processes such as excitations, ionizations and dissociative reactions. Emission spectroscopy is one of the few methods enabling remote analysis of a chosen object and therefore it is vital for studying these extra-terrestrial bodies. The examples are the observations of the atmosphere of Jupiter's moon Ganymede [1] or the spectroscopic data obtained by the Rosetta mission, which was the first ever to orbit a comet's nucleus - 67P/Churyumov Gerasimenko [2]. These data show that electron induced processes in comas and planetary atmospheres play a significantly more important role than it used to be anticipated.

Carbon monoxide is a relatively abundant molecule in the Universe and it is an essential life-forming molecule. It is one of the dominant carbon bearing molecules in extra-terrestrial bodies such as comets or centaurs. Especially the $A^2\Pi - X^2\Sigma^+$ transition of CO^+ is prominent in emission spectra of the comet tails and is referred to as the Comet Tail system. The diagnostic of these cometary volatiles is a necessity for solar system formation models [3]. CO molecule is also present in interstellar gas clouds which are the precursors of star formation. It is commonly used as a tracer of H_2 in the interstellar medium, which is difficult to observe on its own as it lacks a permanent dipole moment [4]. It is also an important compound of planetary atmospheres, such as Mars or Venus. Tracking atmospheric CO on Mars is an effective method for exploring the oxidizing capacity of the Martian atmosphere [5].

There are several papers on electron impact excitation of the CO molecule. Many are focused on the Comet Tail system of CO^+ such as [6]. [7] studied the emission cross-sections of CO in within 126 – 500 nm for the Fourth Positive system and the Cameron system of CO, and the First Negative system and the Comet Tail system of CO^+. A comprehensive review of the literature on the band spectrum of CO was compiled by [8]. It consists of critically evaluated numerical data on band positions, molecular constants, energy levels and potential energy curves. The aim of this experiment is to extend already existing collection of the emission cross-sections to be sufficient for the study and theoretical modelling of the processes that occur on numerous extra-terrestrial bodies.

2. Experimental apparatus

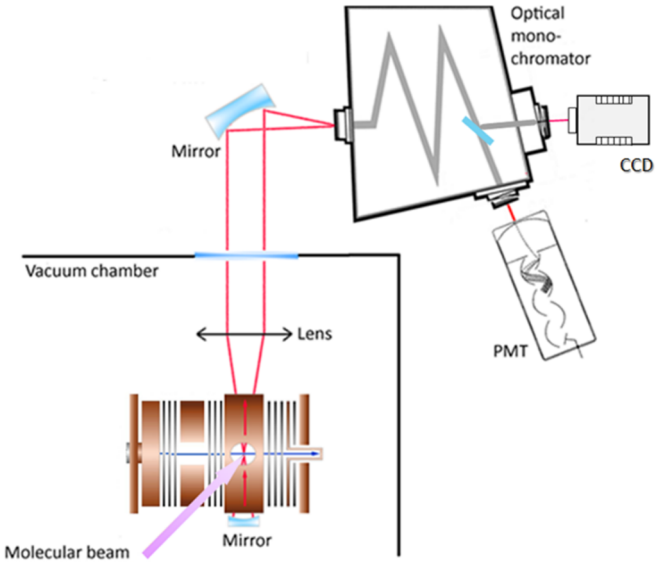

Fig. 1. The scheme of the experimental setup used to study electron induced fluorescence. *Blue* - electron beam, *red* - fluorescence signal, *violet* - molecular beam.

The experimental apparatus used in this work is based on a crossed electron and molecular beams method and is further described in a previous publication [9]. A trochoidal electron monochromator located in a vacuum chamber generates a monochromatic electron beam. The electron beam interacts with a perpendicular molecular beam formed by an effusive capillary. The background pressure of the vacuum chamber is ~10^{-8} mbar and the pressure of the molecular beam is set to sustain binary interactions – one electron with one molecule. One of the products of electron-molecule interactions are excited species. These are unstable and emit radiation as they de-excite. The emitted radiation is collected by a UV fused silica lens and guided out of the vacuum chamber to a parabolic mirror, which focuses this radiation to the entrance slit of a Czerny-Turner optical monochromator. To maximise the detected signal, a spherical mirror is placed opposite to the collecting lens with its focus at the centre of collision. To acquire signal from the emitted radiation, either a Hammamatsu photomultiplier R4220P (PMT) or an Andor iDUS 420 CCD camera can be used. The photomultiplier is sensitive to wavelengths of 185 – 700 nm and collects the signal at one wavelength at a time. The CCD camera is sensitive to 300 – 1100 nm wavelength range and can obtain signal from an approximately 85 nm interval of wavelengths at once which makes the CCD camera more efficient for measuring spectra. The scheme of the experimental apparatus is shown in Fig. 1.

The experimental apparatus operates in two regimes – measuring the intensity of the radiation as a function of wavelength (emission spectra), which gives information on the transitions that occur during the process of de-excitation of species. The second regime measures the dependency of photon intensity on the electron energy (excitation-emission function) corresponding to a specific transition. These provide information on the probability of the given transition occurrence and its threshold energy.

3. Experimental results and discussion

The emission spectrum of CO was measured in the wavelength range of 300 – 510 nm at 50 eV electron energy and is depicted in Fig. 2. This spectral region is dominated by the Comet Tail system of CO^+ ($A^2\Pi - X^2\Sigma^+$) and its vibrational transitions that were identified according to [7,8]. There are also few emission bands of the Baldet – Johnson system of CO^+ ($B^2\Sigma - A^2\Pi^+$) but their relative intensity is considerably weaker than of the Comet Tail system. Along with the emission bands of ionized CO^+, we have identified several emission bands of neutral CO. These bands spread along the whole spectral region, but they are also much weaker than the Comet Tail system, so they cannot be identified in the 50 eV spectrum.

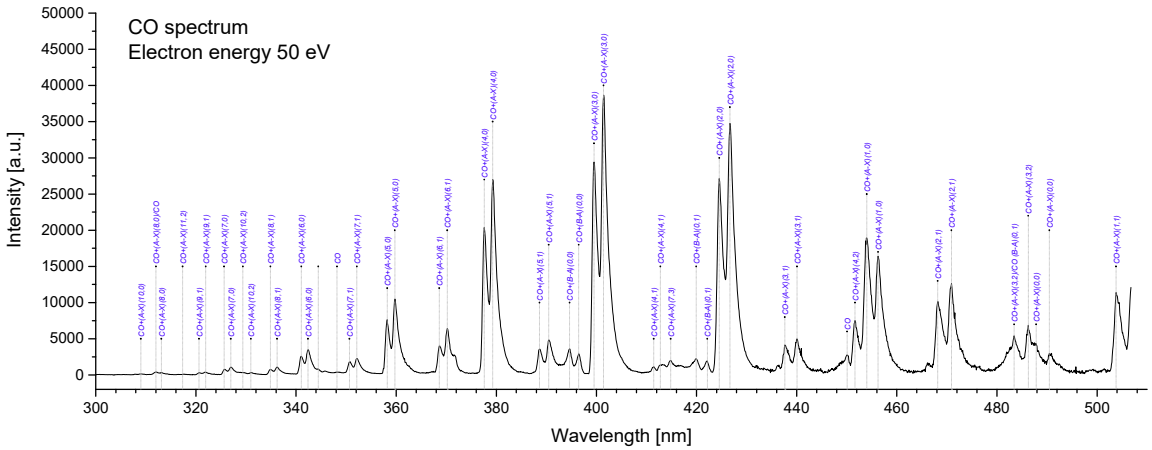

Fig. 2. The emission spectrum of CO measured by CCD camera at 50 eV.

The emission spectrum of CO within the wavelengths of 275 – 510 nm was measured at several electron energies ranging from 2.5 eV to 100 eV with steps closely together in the threshold region and with lower density above 50 eV. The spectra form a surface corresponding to excitation-emission functions for transitions within the selected spectral range which can be calibrated to absolute scale to determine emission cross-sections in the measured spectral and energy range. Thanks to spectral resolution high enough to distinguish vibrational transitions it is possible to determine excitation-emission functions for individual vibrational levels by selecting appropriate cut along the Y axis. The 3D graph of CO spectra is shown in Fig. 3. The 3D graph shows that there are features that do not correspond to the CO^+ emission bands at lower electron energies. Spectra below 17.5 eV are dominated solely by the emission bands of neutral CO.

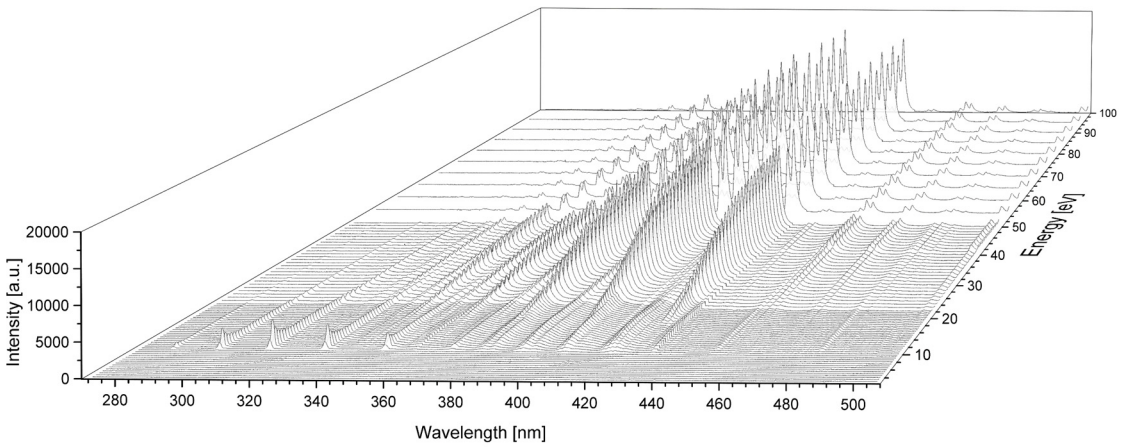

Fig. 3. The 3D spectral graph of the emission spectrum of CO measured at multiple electron energies.

Excitation-emission functions of selected transitions were measured at electron energy range within 2.5 – 100 eV. The excitation-emission function measured at 377.6 nm is depicted in Fig. 4. It is a mixture of signal from two different transitions, which are characterized by two threshold energies. Threshold energy of a transition is the minimum possible energy for a given process to occur. The first threshold at 9.5 eV is of the emission of neutral CO. The second one at 17.5 eV corresponds to the emission of CO^+ ($A^2\Pi - X^2\Sigma^+$) (4,0).

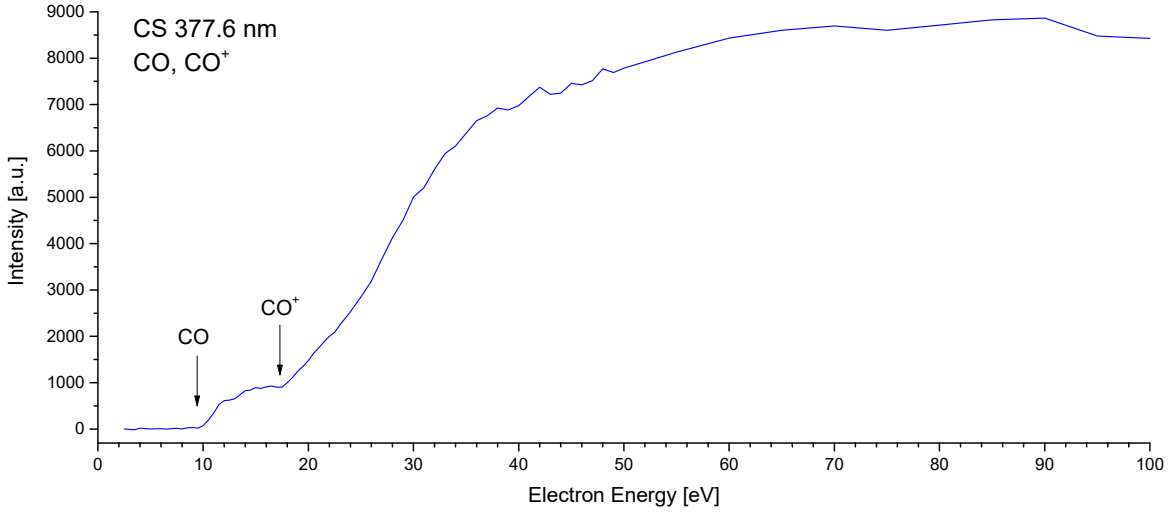

Fig. 4. Excitation-emission function of a mixture of CO and CO^+ emission at 377.6 nm.

4. Conclusions

Electron induced fluorescence of CO was studied in a crossed-beam experiment. The emission spectrum composed of neutral CO and CO^+ emission bands was measured at several electron energies ranging from 2.5 to 10 eV. Excitation-emission functions were measured as well as the 3D graph of CO spectra was constructed. Further research will be focused on the identification of CO emission bands at energies lower than 17.5 eV. These energies are not sufficient for the ionization and excitation of CO. We will also determine threshold energies of all identified transitions and compare them to theoretical values. A comprehensive study on electron impact excitation of CO will be published in a peer reviewed journal.

Acknowledgments. The presented research was partially supported by Slovak grant agency VEGA within the projects nr. 1/0489/21, 1/0553/22, by Slovak Research and Development Agency within projects nr. APVV-19-0386, APVV-15-0580, by CU Grants 2022 within project nr. UK/307/2022 and by NASA ROSES project nr. NNH18ZDA001N-RDAP. This research has received funding from the European Union's Horizon 2020 research and innovation programme under grant agreement No 871149.

5. References

[1] Roth L et al. 2021 *Nature Astronomy.* **5** 1043–1051.
[2] Bodewits D et al. 2016 *The Astronomical Journal.* **152** 130.
[3] Fortenberry R C, Bodewits D, Pierce D M 2021 *The Astrophysical Journal Supplement Series.* **256:6** (8pp).
[4] Jarugula S et al. 2021 *The Astrophysical Journal.* **921:97** (26pp).
[5] Olsen K S et al. 2021 *Nature Geoscience.* **14** 67-71.
[6] Holland R F and Maier II W B 1972 *The Journal of Chemical Physics.* **56** 11.
[7] Ajello J M 1971 *The Journal of Chemical Physics.* **55** 7.
[8] Krupenie P H 1966 *The Band Spectrum of Carbon Monoxide. National Standard Reference Data Series. **3**.*
[9] Országh, J, Danko M, Čechvala P, Matejčík Š 2017 *The Astrophysical Journal. **841*:17** (10pp).

LOW ENERGY ELECTRON ATTACHMENT TO CARBON TETRACHLORIDE CLUSTERS

Dušan Mészáros, Peter Papp, Štefan Matejčík

Department of Experimental Physics, Faculty of Mathematics, Physics and Informatics, Comenius University in Bratislava, Mlynská dolina, 842 48 Bratislava, Slovakia
E-mail: dusan.meszaros@fmph.uniba.sk

We present low energy electron (0-12 eV) interaction studies of CCl_4 clusters formed in supersonic expansion. Negatively charged products of this interaction were analysed by mass spectrometry. We have observed the following negative ions: Cl^-; Cl_2^-; CCl_2^-; CCl_3^-; as well as cluster ions: $[(CCl_4)_nCl]^-$ $(1 \leq n \leq 3)$; $[(CCl_4)_nCl_2]^-$; $[(CCl_4)_nCCl_3]^-$. Moreover, the parent anion CCl_4^- and its clusters $[(CCl_4)_n]^-$ $(1 \leq n \leq 3)$ were also observed. In this study, we include ion yields for production of all products.

1. Introduction

Interaction of low energy electrons with molecules and molecular clusters is one of the elemental processes in plasma and plasma technologies. At the Comenius University in Bratislava we are focusing on electron attachment (EA) and dissociative electron attachment (DEA) studies, in this work on carbon tetrachloride clusters $(CCl_4)_n$. Carbon tetrachloride is widely known for its large cross section for thermal electron attachment [1].

The CLUSTER-ILN experiment [2] (Fig. 1) was used to measure the electron molecular and cluster interactions. It is equipped with a trochoidal electron monochromator (TEM) and quadrupole mass analyser used for identifying the charged products of electron impact, both are in a perpendicular orientation. The ratio 1:150 of CCl_4:Ar was expanded via 80 μm nozzle into the high vacuum (expansion chamber, background pressure ~10^{-5} Pa); this supersonic expansion is sufficient for gas cooling to produce a beam of molecular clusters which is then separated with the skimmer (0.8 mm) into the reaction chamber (background pressure ~10^{-6} Pa). Clusters interact with the electrons produced in TEM with a well-defined kinetic energy (electron energy resolution ~200 meV in this work). The relevant EA reactions to CCl_4 molecules (1a), $(CCl_4)_nAr_m$ clusters (2a) and (3a); and the corresponding DEA reactions to molecules (1b) and clusters (2b), (2c), (3b), (3c), (3d), (3e) measured with the CLUSTER-ILN experiment are summarized below.

$$e^- + AB \rightarrow AB^{-*} \quad (1a)$$
$$AB^{-*} \rightarrow A^{\cdot} + B^- \quad (1b)$$
$$e^- + (M)_n \rightarrow (M)_n^- \quad (2a)$$
$$\rightarrow X^- + R(M)_{n-1} \quad (2b)$$
$$\rightarrow X^-(M)_{n-1} + R \quad (2c)$$
$$e^- + M_mN_n \rightarrow (M_mN_n)^- \quad (3a)$$
$$\rightarrow X^- + R(M_{m-1}N_n) \quad (3b)$$
$$\rightarrow X^-(M_{m-1}N_n) + R \quad (3c)$$
$$\rightarrow A^- + B(M_mN_{n-1}) \quad (3d)$$
$$\rightarrow A^-(M_mN_{n-1}) + B \quad (3e)$$

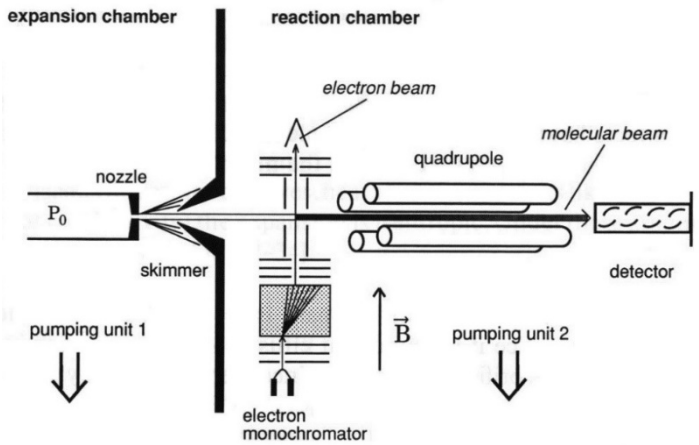

Fig. 1. The schema of CLUSTER-ILN experiment at the Comenius University in Bratislava (built at the Freie Universität Berlin [2]). P_0 is the sample pressure at the nozzle, typically 150-300 kPa.

2. Dissociative electron attachment to CCl_4 clusters

During our study of DEA to $(CCl_4)_nAr_m$ clusters we observed the well-known products from previous studies: fragments of molecule Cl^-, Cl_2^-, CCl_2^-, CCl_3^- from gas phase studies [3,4] and the cluster ions of $[(CCl_4)_{n+1}]^-$ $1 \leq n \leq 9$ and its fragments $[(CCl_4)_n+Cl]^-$, $[(CCl_4)_n+Cl_2]^-$, $[(CCl_4)_n+CCl_3]^-$, as well as the parent anion [5]. In this study we measured the electron energy ion yields (in Figure 2) for the following cluster fragments $[CCl_4+Cl]^-$, $[CCl_4+Cl_2]^-$, $[CCl_4+CCl_3]^-$, parent anion CCl_4^- and its clusters $[(CCl_4)_2]^-$, $[(CCl_4)_3]^-$. The gas phase measurement ion yields for Cl^-, Cl_2^-, CCl_2^- and CCl_3^- from previous studies [3,4] agree well with the recent measurements (upper panel of graphs and the third from top in the middle in Figure 1). For these fragments the recent electron-cluster measurements confirmed all resonances reported in the gas phase studies except 1.8 eV resonance for CCl_2^-, which is however also very week in [3,4]. On the other hand, additional resonance was observed at 3.5 eV for the Cl^-; and at 0 eV for Cl_2^-, CCl_2^- and CCl_3^-. The high energy resonances in the ion yield of Cl_2^- at 6 eV and 8 eV are more intense in comparison to the 1.1 eV resonance as in the gas phase study of Scheunemann et al. [3]; or Ragesh et al. [4] who reported only one higher energy resonance at 8 eV. On the other hand, for CCl_3^- we observed resonances at 5.5 eV and 8 eV; which were not seen by Scheunemann et al. [3] and Ragesh et al. [4] did observe resonance only at 6.1 eV.

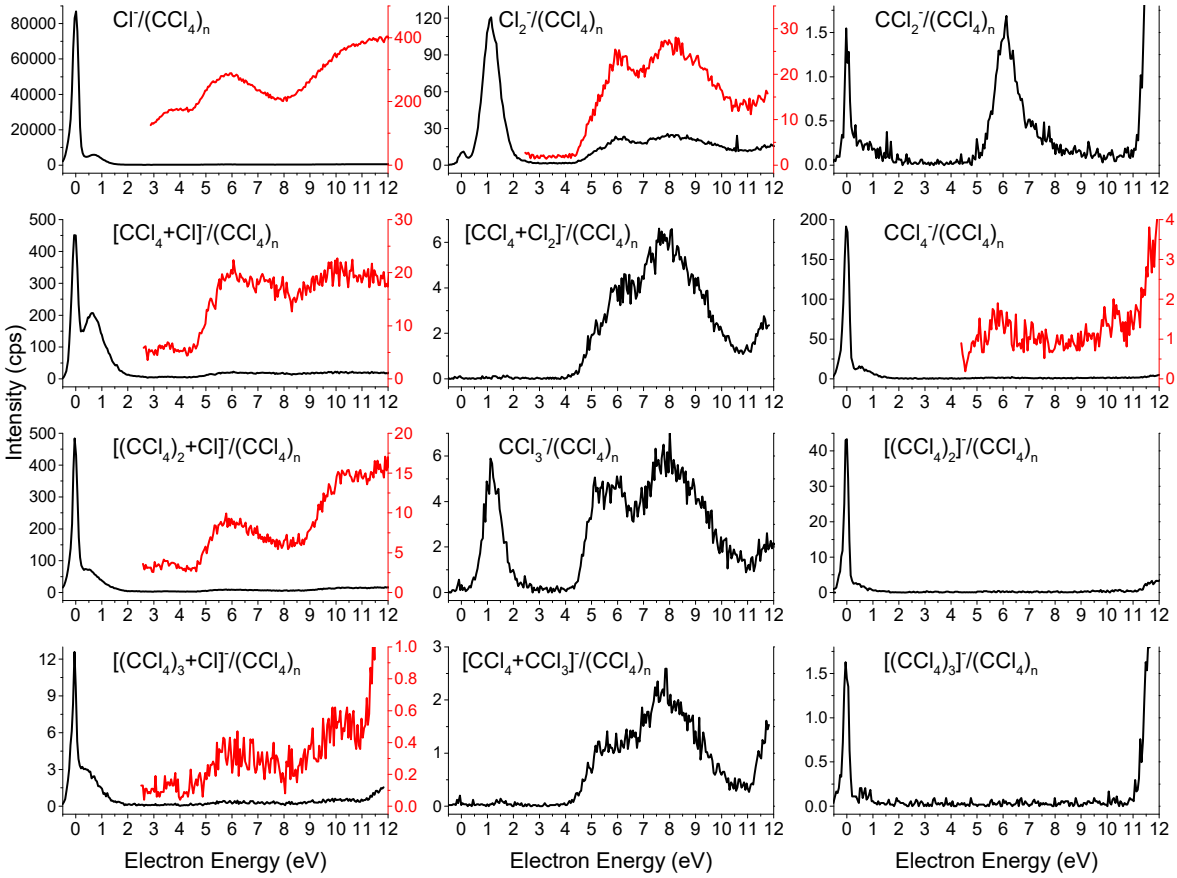

Fig. 2. Negative ion yield for production of all observed products from interaction $e^- + (CCl_4)_n$

For $[(CCl_4)_n+Cl]^-$ cluster ions with $1 \leq n \leq 3$ we observed almost identical shape of ion yields as for the isolated Cl^- fragment, they differed only in the relative ratio of the low energy resonances to high energy resonances and with relatively more intensive 10 eV resonance. The ion cluster $[CCl_4+Cl_2]^-$ exhibits a decrease in intensity of the 6 eV resonances compared to the 8 eV and the complete absence resonance at 0 eV in comparison with our Cl_2^- fragment. We observed similar behaviour for the resonances at 5.5 eV and 8 eV of $[CCl_4+CCl_3]^-$ cluster ion compared to our CCl_3^- fragment measurement.

Contrary to previous studies [3,4] we have recorded the ion yield of the parent ion CCl_4^-, which is a stable product only for electron-cluster interactions contrary to electron-molecular gas phase interactions. Formation of CCl_4^- ion was observed with ion-pair studies of potassium with CCl_4 [6]. Generally, after

electron attachment to CCl_4 at 0 eV an energy could be released, according to Ragesh et al. [4] the calculated threshold energy for the Cl^- DEA channel is exothermic; -0.71 eV (CCSD(T)) or -1.03 eV (DFT/B2PLYP). This means that the electron attachment to CCl_4 will almost always lead to dissociation into $Cl^- + CCl_3$ when there is no possibility to release the excess energy. If there is an environment around the excited anion CCl_4^{-*} as in clusters, excess energy can be dissipated to it and the molecular anion can be stabilised. The ion yield of CCl_4^- is similar to Cl^-, dominant resonance is at 0 eV, 0.5 eV, and a weaker resonance at 6 eV. For the $[(CCl_4)_2]^-$, $[(CCl_4)_3]^-$ clusters we have recorded only the low energy resonances.

In Figure 2 an increase of the signal for electron energies above 11 eV is obvious, which arises from energetic secondary electrons produced via deexcitation of metastable $Ar^{\#}$ atoms (produced at 11.548 eV [7]) when hitting the deflection plates of quadrupole mass analyser.

3. Conclusion

The electron attachment and dissociative electron attachment to CCl_4 clusters was performed at this study. We have found a good agreement with previous CCl_4 gas phase studies [3,4], we reported new resonances at 3.5 eV for Cl^-, 5.5 eV and 8 eV resonance for CCl_3^- and 0 eV resonance for Cl_2^-, CCl_2^- and CCl_3^-. We observed the same cluster fragments $[(CCl_4)_n+Cl]^-$ $1 \leq n \leq 3$, $[CCl_4+Cl_2]^-$, $[CCl_4+CCl_3]^-$, parent anion CCl_4^- and $[(CCl_4)_2]^-$, $[(CCl_4)_3]^-$ as in [5], but additionally we measured the ion yields for these products. Parent ion CCl_4^- was observed with resonances at 0 eV, 0.5 eV and 6 eV. This ion has very short lifetime in the gas phase and dissociates to $Cl^- + CCl_3$. However, in clusters the excess energy can be distributed to the medium and this leads to stabilisation of the ion CCl_4^-. Its dimer $[(CCl_4)_2]^-$ and trimer $[(CCl_4)_3]^-$ have resonances only at 0 eV and 0.5 eV. The $[(CCl_4)_n+Cl]^-$ $(1 \leq n \leq 3)$ clusters have similar resonances as Cl^- with more intensive 10 eV resonance, $[CCl_4+Cl_2]^-$ and $[CCl_4+CCl_3]^-$ have resonances only at higher energies ~6 eV and 8 eV.

4. Acknowledgments

This work was supported by the Slovak Research and Development Agency contract no. APVV-19-0386, SK-PL-21-0025 and the Slovak Grant Agency for Science contract no. VEGA 1/0552/22.

5. References

[1] Chutjian A and Alajajian S H 1985 *Phys Rev A (Coll Park)* **31** 2885–92.
[2] Ingólfsson O, Weik F and Illenberger E 1996 *Int J Mass Spectrom Ion Process* **155** 1–68.
[3] Scheunemann H-U, Illenberger E and Baumgärtel H 1980 *Ber. Bunsenges. Phys. Chem.* **84** 580–5.
[4] Ragesh R K, Brynjarsson B, Ómarsson B, Hoshino M, Tanaka H, Limão-Vieira P, Jones D B, Brunger M J and Ingólfsson O 2018 *Int J Mass Spectrom* **426** 12–28.
[5] Mitsuke K, Tada H, Misaizu F, Kondow T and Kuchitsu K 1988 *Chem Phys Lett* **143** 6–12.
[6] Lacmann K, Maneira M J P, Moutinho A M C and Weigmann U 1983 *J Chem Phys* **78** 1767–76.
[7] Kramida A, Ralchenko Yu, Reader J and NIST ASD Team (2022). NIST Atomic Spectra Database (ver. 5.10), [Online]. Available: https://physics.nist.gov/asd [2023, January 14]. National Institute of Standards and Technology, Gaithersburg, MD.

ELECTRON-INDUCED DEPROTONATION OF ACETIC ACID CH_3COOH CLUSTERS EMBEDDED IN ARGON AND OLIGOMERS FORMATIONS

René Cartaya[1], Dušan Mészáros[2], Peter Papp[2], Štefan Matejčík[2]

[1]*Institute for Applied and Physical Chemistry, Faculty 2 (Chemistry/Biology), University of Bremen, Leobener Straße 5, 28334 Bremen, Germany*
[2]*Department of Experimental Physics, Faculty of Mathematics, Physics and Informatics, Comenius University in Bratislava, Mlynska dolina F2, 84248 Bratislava, Slovakia*
E-mail: rene.cartaya@uni-bremen.de

The present work studies the electron-induced deprotonation in acetic acid CH_3COOH carried by argon as aggregation gas in clusters-phase and the formation of oligomers. The CH_3COOH is aimed to get insight into electron-induced deprotonation in the carboxylic acids present in the top layer of HKUST-1 SurMOF, as responsible for electron-induced activation for nanofabrication purposes. The studies include mass and energy spectrums performed collecting ion signals in combination with channeltron to analyse negative ions. The anions were produced under Dissociative Electron Attachment (DEA) regime for CH_3COOH clusters and studied under single collision conditions in a cross-beam setup.

1. Introduction

Understanding the electron-induced process has gained maximum relevance since the disruption of semiconductors beyond the 10 nm node. This resolution can only be achieved either with extremely short wavelength light sources such as Extreme Ultraviolet (EUV) and X-rays or electrons and ion sources [1]. In the current study, a cross-beam device is used to study electron-induced processes with high control over the electron energy but also guarantee that the driven processes are triggered by a single electron collision [2], which brings a more detailed insight into the process. In the current experimental study, processes induced by low-energy electrons in single collision conditions are studied over CH_3COOH molecules embedded in argon clusters. Previously, it has been demonstrated how low-energy electrons induce deprotonation in carboxylic groups via DEA [3], [4], and [5].

2. Experimental setup

The cross-beam experiments were performed in the CLUSTER-ILN detailed previously [6] and more recently by [7]. For the present studies, the CH_3COOH precursors were held externally in liquid form in a sample reservoir at room temperature. The precursor reservoir allows the generation of vapours that were conducted to the mixing reservoir at controlled pressures. The precursor vapours were mixed with specific argon (Ar) pressures generating a mixture that acted as an effusion source with controlled pressure via a reducing valve. The mixture of CH_3COOH carried by Ar was then injected into the expansion chamber through a nozzle with a diameter of 80 micrometre. The injection of the mixture into the vacuum chamber is induced by pressure difference. The mixture vapours with a pressure ranging 1.0-1.5 atm were injected into the expansion chamber with a working pressure of $1.0\times10{-}4$ mbars. The injected gas expands in the chamber, generating a cluster beam. The cluster beam formed in the expansion chamber passes a skimmer narrowing the cluster beam travelling to the monochromator. Thereafter the cluster beam is crossed with an electron beam produced by the trochoidal electron monochromator (TEM). After the electron-molecule/cluster collision, charged products are analysed by quadrupole mass analysers and detected by channeltron.

3. Results and discussion

Mass spectrums were recorded using monochromatic electrons according to the possible position of the resonances identified. The mass scans were measured at 1.36 eV over the CH_3COOH clusters embedded

in argon. The spectrums recorded show how electrons at specified energies can lead to the production of deprotonated species alongside oligomers.

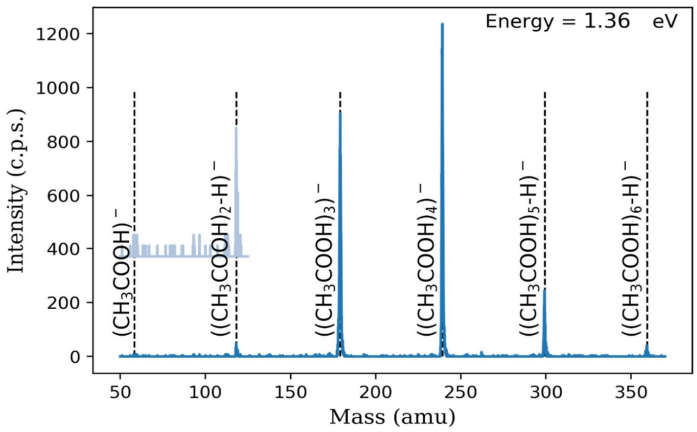

Fig. 1. Mass spectrum of anions formed via DEA of CH_3COOH.

The acid trimer $(CH_3COOH)_3$ and tetramer $(CH_3COOH)_4$ are the dominant products, as can be seen in the mass spectrum in Fig. 1. Presence of water molecules in the context of HKUST-1 is considered coordinated with the copper nodes, according to the current study, such molecules could have a role in the electron-induced process. This water should not be considered pollution from the chamber, since the ability of CH3COOH to attach water molecules has been previously demonstrated [3].

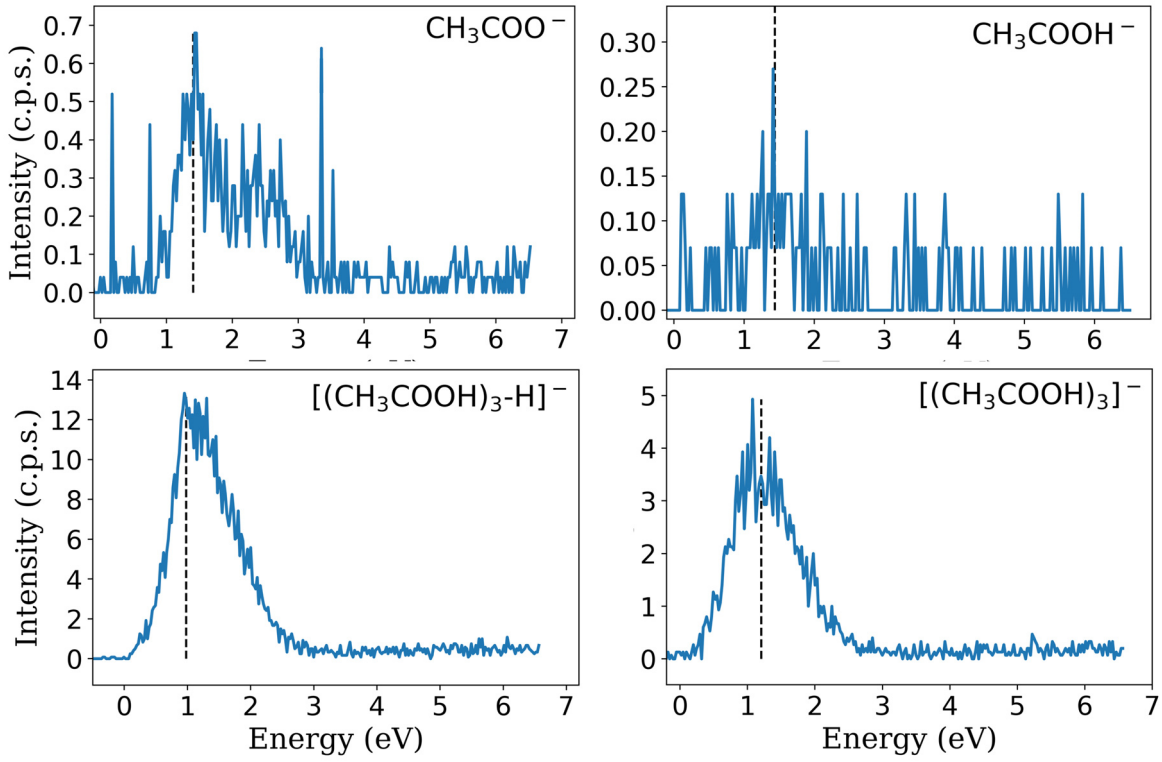

Fig. 2. Comparison of ion yielding of anions and their deprotonated version formed under DEA of CH_3COOH clusters as a function of the incident electron energy.

DEA in acetic acid monomer in the gas phase has been previously reported [5]. The anion CH_3COO^-, as a deprotonated species of the parent acid precursor, is identified in the study's spectrums. Deprotonated species could be considered the trigger of more complex products, as will be detailed in

upcoming works. The results show clear evidence of DEA's ability to favour the aggregation via the deprotonation of the CH_3COOH. When we compare the monomer's energy scan with its deprotonated version in Fig. 2, there we can see how deprotonated oligomers require less energy for their desorption from the neutral cluster. This could explain why deprotonated species have higher abundances, as is evidenced in Fig. 2 where the abundance of CH_3COO^- is at least twice as much as CH_3COOH^-, while $[(CH_3COOH)_3\text{-}H]^-$ is almost three times more abundant than $[(CH_3COOH)_3]^-$.

4. Conclusions

The mass spectrums recorded for CH_3COOH in cluster regime evidence the electron's ability to produce negative fragments and clusters for the precursor. In this context, it is evidenced also by the higher yielding in the production of deprotonated products in comparison with the parent precursors. Deprotonation of CH_3COOH in cluster regime under electron capture of low energy electrons has been evidenced only for the acetic acid monomer and dimer.

5. Acknowledgement

The research was conducted with the financial support of EU Horizon 2020 Marie Curie-Sklodowska Innovative Training Network "ELENA", grant agreement no 722149. This work was supported by the Slovak Research and Development Agency contracts no. APVV-19-0386, APVV-15-0580, and the Slovak Grant Agency for Science contract no. VEGA 1/0552/22.

6. References

[1] Lawson R and Robinson A 2016. *Frontiers of Nanoscience*.
[2] Illenberger E 1992 *Chemical reviews* **92** 1589.
[3] da Silva F, Jaksch S, Martins G, Dang H, Dampc M, Denifl S, Märk T, Limao-Vieira P, Liu J, Yang S, and Ellis A 2009 *Physical Chemistry Chemical Physics* **11** 11631.
[4] Martin I, Skalicky T, Langer J, Abdoul-Carime H, Karwasz G, Illenberger E, Stano M, and Matejcik S 2005 *Physical Chemistry Chemical Physics* **7** 2212.
[5] Sailer W, Pelc A, Probst M, Limtrakul J, Scheier P, Illenberger E, and Märk T 2003 *Chemical Physics Letters* **378** 250.
[6] Ingólfsson O, Weik F, and Illenberger E 1996 *International Journal of Mass Spectrometry and Ion Processes* **155** 1.
[7] Mészáros D, Papp P, and Matejčík S 2021 *Proc. Symposium on Application of Plasma Processes 49*.

EFFECT OF GAS TEMPERATURE ON THE ELECTRON DYNAMICS IN AN ATMOSPHERIC PRESSURE RF PLASMA JET BASED ON A HYBRID MODEL

Máté Vass[1,2], David Schulenberg[1], Zoltán Donkó[2], Maximilian Klich[3], Peter Hartmann[2], Ihor Korolov[1], Nikita Bibinov[1], Julian Schulze[1], Thomas Mussenbrock[1]

[1]*Chair of Applied Electrodynamics and Plasma Technology, Ruhr-University Bochum, 44780 Bochum, Germany*
[2]*Institute for Solid State Physics and Optics, Wigner Research Centre for Physics, 1121, Budapest, Hungary*
[3]*Chair of Theoretical Electrical Engineering, Ruhr-University Bochum, 44780 Bochum, Germany*
E-mail: vass@aept.rub.de

A 1D hybrid (fluid+kinetic) simulation is applied to investigate the effect of the background gas temperature on the electron dynamics in a radiofrequency microplasma jet operated in a He-N_2 mixture (with a ratio of 1000:1) at atmospheric pressure, excited by a single frequency waveform with V=600 V amplitude and f=13.56 MHz frequency. The results show good agreement with experimental results, based on Phase Resolved Optical Emission Spectroscopy (PROES). It is shown, that by increasing the gas temperature the plasma undergoes a power absorption mode transition from the Omega-mode to the Penning mode. The temperature increase is observed along the discharge channel from the gas inlet towards the nozzle in the experiment.

1. Introduction

Radiofrequency (RF) driven micro-atmospheric pressure plasma jets have numerous applications, such as surface manufacturing (sterilization, surface functionalization) and plasma medicine (wound healing, cancer treatment), mainly due to the high generation rate of certain reactive radicals [1-3]. For an effective generation of such species, the electron dynamics have to be thoroughly understood, since reactive species are mostly created through electron impact processes. In this work we investigate how the variation of the gas temperature can affect the electron dynamics in the COST reference microplasma jet [4, 5]. By comparing the experimentally measured Phase Resolved Optical Emission Spectroscopy (PROES) results for the electron impact excitation rate, with those obtained from a one dimensional hybrid simulation, it is inferred that the gas temperature increases along the gas flow direction in the discharge channel between the inlet and the nozzle. Furthermore, we show, that this temperature increase leads to an electron power absorption mode transition, from the Omega-mode (where bulk electrons are accelerated by the high Ohmic electric field due to the atmospheric pressure) to the Penning-mode (where electrons created by Penning ionization as well as secondary electrons determine the electron dynamics) [4].

2. Experimental technique and computational method

The COST reference microplasma jet consists of two plane-parallel stainless-steel electrodes covered by quartz plates, confining the discharge domain of 30 mm x 1 mm x 1 mm. The electrode gap is 1 mm. The sketch of the experimental setup is shown in fig. 1. The source is driven at a frequency of f=13.56 MHz by a power generator (Coaxial Power Systems RFG 150-13) through a matching network with an amplitude of V=600 V. Helium and nitrogen of 5.0 purity are used. Their flow rates (along the 30 mm length) are set to 1 slm and 1 sccm, respectively. The nozzle is located at z=0. Phase Resolved Optical Emission Spectroscopy (PROES) with an interference filter at 700 nm and 15 nm of full width at half maximum is used to monitor the helium emission line at 706.5 nm [5]. The spatio-temporally resolved emission is recorded by an ICCD camera of 1 ns gate width.

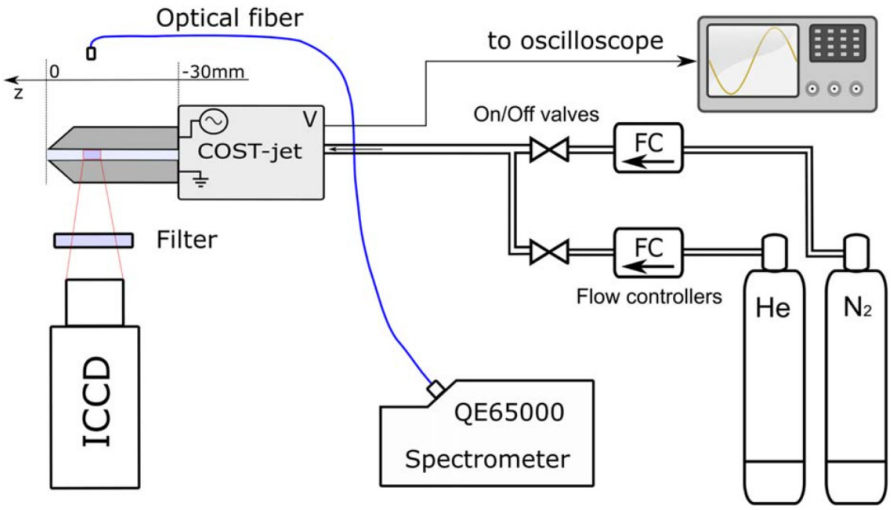

Fig. 1. Sketch of the experimental setup [5].

The simulations are based on a hybrid scheme, where charged particles as well as neutrals are described by a fluid model, by solving the continuity equation based on the drift-diffusion approximation, as well as Poisson's equation. In order to capture kinetic effects, a separate Monte Carlo Collision (MCC) module is used for the electrons, which are accelerated by the electric field calculated from the fluid module. As a result, rates for various electron impact processes are calculated, which serve as sources and losses for the continuity equation of the respective species in the fluid model. The two modules are run in an iterative way until convergence in the species densities is achieved. Results obtained based on this scheme are within a 10% agreement with PIC/MCC results in the atmospheric pressure regime, while the runtime of the hybrid model is significantly shorter compared to the fully kinetic PIC/MCC model.

The charged species considered in the simulation are electrons, He^+ ions, He_2^+ ions, N_2^+ ions and N_4^+ ions. The electron impact processes include elastic collisions, triplet and singlet excitation and ionizing collisions with helium, while with nitrogen there is an elastic channel, one rotational excitation, eight vibrational excitations, twelve electronic excitations, one dissociation and ionization. References for the corresponding cross section data and additional information can be found in [5]. One active neutral species is considered, the (metastable) excited state of helium, which is defined as an effective state comprising both the triplet and singlet excited states. Reactions between the heavy charged particles and with neutrals are taken into account in the fluid module based on reaction rates. These include ion conversion for the generation of He_2^+ ions and N_4^+ ions, and Penning ionization between the helium metastables and nitrogen.

The COST jet is assumed to have plane-parallel electrodes with an electrode gap of L=1 mm, where the powered electrode is excited by a single frequency waveform with V=600 V amplitude and f=13.56 MHz frequency. The gas temperature is varied between 200 K and 500 K. An elastic reflection of 50% for electrons is used, while the secondary electron emission coefficient is set to 0.2 for He^+ ions, to 0.12 for He_2^+ ions, and to 0.07 for both N_2^+ and N_4^+ ions. In order to keep the collision probability below 5% in the MCC module, the number of timesteps is set to $2.7 \cdot 10^6$, while this value is set to 400 in the fluid module. The number of grid points is 200 in both modules.

3. Results

Figure 2 shows the measured spatio-temporal distribution of the electron impact excitation rate from the ground state of helium atoms into the He–I 1s3s $^3S_1$ level obtained from measurements of the 706.5 nm He line emission at different spatial positions along the flow channel. The positions marked in the

respective panels correspond to the distance from the end of the nozzle (cf. fig. 1), i.e. the first panel is closest to the nozzle, while data shown in subsequent panels are measured at further positions. The intensity in each panel is normalized to its respective maximum value. In the panel closest to the inlet (at the position z=-28.25 mm) the discharge is in the Omega-mode, since the maximum value of the Omega-peak (at approximately 40 ns, which is a result of the "sheath expansion") is large compared to the respective Penning-peak (at e.g. 50 ns, corresponding to electrons created by Penning ionization, reflected electrons and secondary electron emission).

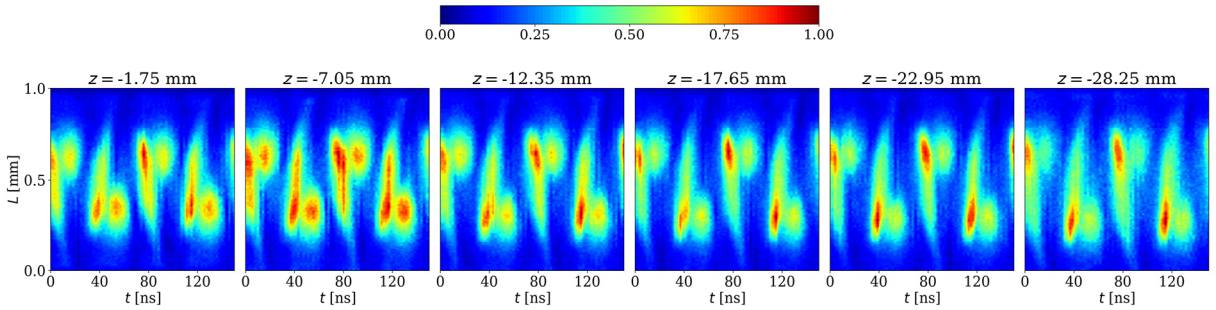

Fig. 2. Experimental results for the normalized electron impact excitation rate from the ground state of helium atoms into the He–I 1s3s $^3S_1$ level at different positions of the COST-jet along the flow direction. The positions in the panel titles correspond to the distance from the nozzle (cf. fig. 1).

The excitation patterns change along the flow: the closer the position of the nozzle (z=0 mm) the more pronounced the Penning-peak gets, being slightly larger than the corresponding Omega-peak at the position closest to the nozzle (first panel). This means, that along the flow channel, the electrons undergo a power absorption mode transition, from the Omega-mode near the inlet to a mixed Omega-Penning-mode. One possible explanation for this behaviour is presented by the increased gas temperature along the gas flow direction. In order to investigate this effect, 1D hybrid simulations have been conducted at various gas temperatures. Figure 3 shows the normalized excitation rates obtained from simulations, corresponding to the He line recorded in the experiments, for a gas temperature range between 200 K and 450 K over 2 RF cycles. This temperature interval has been chosen such that a transition from purely Omega-mode to the mixed Omega-Penning-mode is visible.

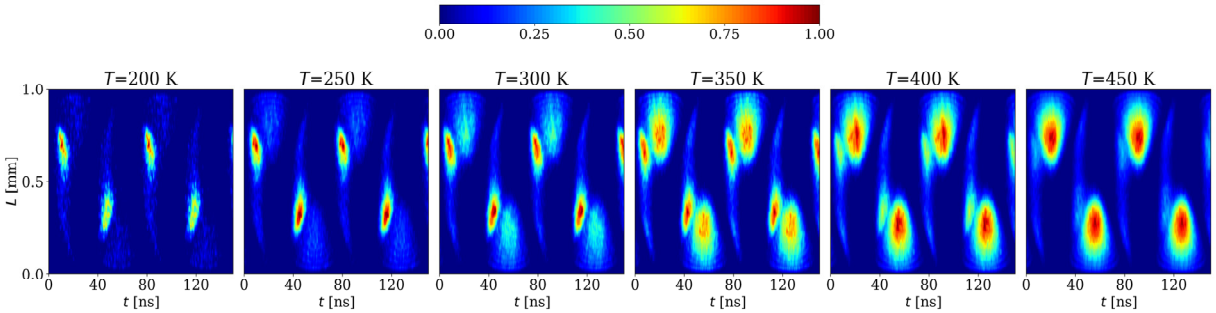

Fig. 3. Simulation results for the normalized electron impact excitation rate from the ground state of helium atoms into the He–I 1s3s $^3S_1$ level for different gas temperatures.

The electron power absorption mode transition is clearly visible as the temperature is increased: while in case of 200 K a pure Omega-mode is observed, the Penning-peak increases as the temperature gets higher, and becomes dominant when the gas temperature reaches the value of 400 K. Based on this, and comparing figs. 2 and 3, one can draw the conclusion, that the gas temperature increases along the gas flow, possibly between 300 K and 400 K. This is verified by Optical Emission Spectroscopy measurements for the gas temperature, which show an approximately 80 K increase in temperature

between the inlet and the nozzle. The temperature was obtained from measuring the emission spectrum of the 0-1 band of the 2nd positive system of nitrogen and fitting the signal to simulation results using a wavelength range from 354 nm to 358 nm. The observed electron power absorption mode transition can be understood based on the hybrid simulation as follows: by increasing the gas temperature the background gas density decreases (since the pressure is kept constant), and thus the electron mean free path increases so that Penning electrons can gain more energy over one mean free path due to their acceleration by the strong sheath electric field. The increased ionization leads to an increase in the electron density, a shorter sheath width, and thus a higher electric field. This results in an increase of the excitation caused by Penning electrons relative to the maximum, caused by the Ohmic electric field inside the bulk. The increased mean free path and average energy also lead to a higher metastable density inside the sheaths, which in turn leads to even more Penning ionization. This mechanism stops when the source and loss term for the metastables, i.e. electron excitation and Penning ionization, balance each other.

Acknowledgements

Funding by the German Research Foundation (DFG), in the framework of the CRC 1316 (ID 327886311), projects A4 and A8 is gratefully acknowledged.

References

[1] Adamovich I et *al.* 2022 *J. Phys. D: Appl. Phys.* **55** 373001
[2] Bruggeman P and Brandenburg R 2013 *J. Phys. D: Appl. Phys.* **46** 464001
[3] Laroussi M et *al.* 2022 *IEEE TRPMS* **6** 127–157
[4] J Golda et *al* 2016 *J. Phys. D: Appl. Phys.* **49** 084003
[5] L Bischoff et *al.* 2018 *Plasma Sources Sci. Technol.* **27** 125009

PRODUCTION MECHANISM OF HYDROGEN PEROXIDE IN TRANSIENT SPARK DISCHARGE AND ELECTROSPRAY SYSTEM

Pankaj Pareek[1], Saeed Kooshki[1], Peter Tóth[1], Mário Janda[1]

[1]*Faculty of Mathematics, Physics, and Informatics, Comenius University Bratislava, Slovakia*

E-mail: pareek1@uniba.sk

Transient spark (TS) is a dc driven self-pulsing discharge with typical repetition frequency 1-10 kHz. The main advantage of TS is its ability of simultaneous generation of the plasma and the formation of microdroplets by electrospray (ES) of water directly inside the discharge zone. In this study, the production mechanism of hydrogen peroxide (H_2O_2) was analyzed with oxygen as input gas in TS and ES system. These results are important for optimization and tuning of plasma activated water generation process.

1. Introduction

Generation of plasma activated water (PAW) has become an important research topic in recent years due to many potential applications in medicine, agriculture, and food industries [1]. PAW may contain various reactive oxygen and nitrogen species (RONS), generated either by transfer of reactive species from plasma, or by secondary chemical reactions in water. Hydrogen peroxide (H_2O_2), ozone (O_3), nitrites (NO_2^-) and nitrates (NO_3^-) belong to the important long-lived species in the PAW. Exact composition of PAW depends on many parameters, e.g., plasma source, inlet gas or plasma/water interface characteristics. In previous research in our group, it was found that the increase of gas/water interface by electrospray (ES) of water to microdroplets enable higher transport rate of RONS from gas to liquid phase in comparison to bulk water [2]. In this study, we employed TS with water ES in a one stage system (1SS) in dry oxygen (O_2) gas and TS operated in dry or humid O_2 followed by water ES in a two-stage system (2SS). The aim was to show the significance of direct plasma-liquid interaction in 1SS for the generation of high concentrations of reactive species in PAW. TS was operated in RC (R=4.6 MΩ, C=50 pF) driven circuit with DC power supply in closed reactor. A needle of 0.6 mm diameter was used as high voltage electrode, which was kept at a gap of 0.8 cm with the ground electrode. The needle electrode also served for deionized water inlet (flow rates 0.4-1 mL/min), pumped by syringe pump. Oxygen gas was supplied into the system at constant gas flow 1L/min.

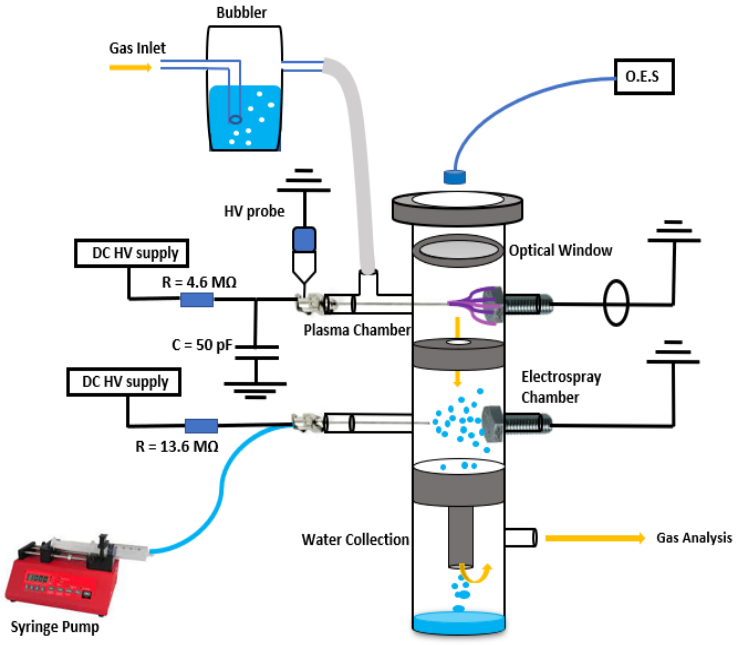

Fig. 1. Schematic of two stage system (2SS) with seperated TS and ES sections.

The concentrations H_2O_2 in water were detected using colorimetric methods. The gas phase concentrations of RONS were monitored using UV-Vis and FTIR absorption spectroscopy techniques. The time integrated optical emission spectroscopy (OES) was used to identify excited species in generated plasma.

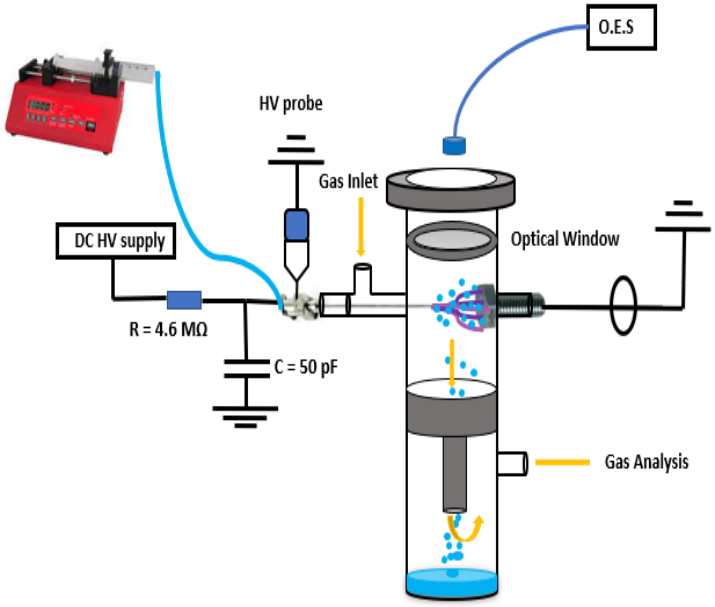

Fig. 1. Schematic of one stage system (1SS) with TS and ES cogenerated by the same pair of electrodes.

2. Results and Discussion

To study the production mechanism of H_2O_2 in TS and ES system, we performed the experiments with pure O_2 to minimize the interaction of H_2O_2 in the gas phase and water phase with other RONS. In pure oxygen we detected no NO_2^- and NO_3^- in PAW. There are significant differences in the concentrations of H_2O_2 in 1SS and 2SS in PAW. In 1SS, where TS and ES are in direct contact has higher amount of H_2O_2 production. In 2SS with humidified O_2 as input gas, much less H_2O_2 is found (Fig.: 3). Optimum conditions for H_2O_2 production are depicted in the contour plot Fig:4. Maximum concentration of H_2O_2 was observed at lower flow rate and high input energy density. At higher water flow rate in 1SS, TS discharge is less stable, which can affect the H_2O_2 generation in water.

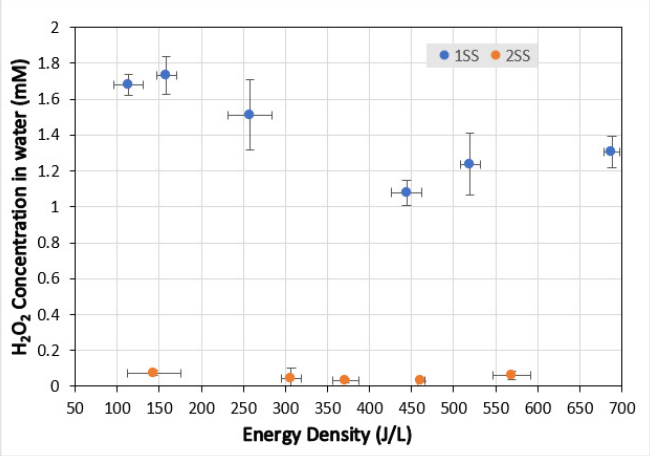

Fig. 3.H_2O_2 concentration in 1SS (TS+ES) and 2SS (TS and ES, with humid O_2).

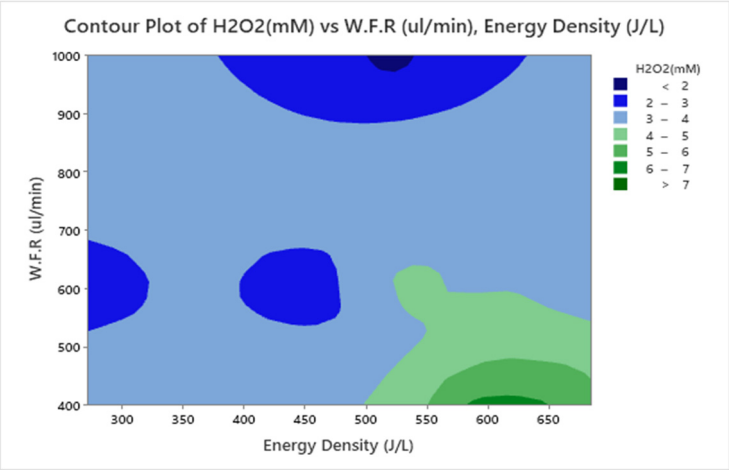

Fig. 4. Contour plot of H_2O_2 concentration in 1SS with different water flow rate (W.F.R) and energy density.

To get in depth views of plasma liquid interaction we performed optical emission spectroscopy test in dry or humid O_2 and with ES. There are hundreds of lines of O II (O+), Fe I, Fe II (Fe+), and even O III (O++). The synthetic spectra were calculated for excitation temperature 30 kK, and 10 kK. Here, the goal was just the identification of lines, not exact calculation of the excitation temperature. Fig.6 shows comparison of emission spectra in range 225-500 nm from experiments in dry O_2, humidified O_2 and dry O_2 with ES (water flow rate 300 mL/min). All spectra are normalized to intensity of O II line at around 410 nm. There is only a negligible difference between spectra measured in dry or humid O_2.

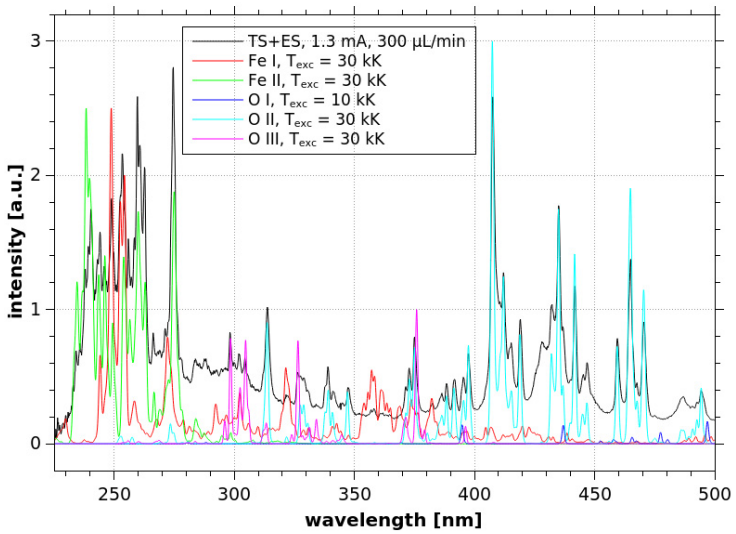

Fig. 5. Comparison of synthetic emission spectra of O, O^+, O^{++}, Fe and Fe^+ species in the range 225-500 nm with experimental emission spectrum of TS with ES; in 1SS, with dry O_2 at inlet, mean discharge current 1.3 mA, water flow rate 300 µl/min.

There is very significant increase of relative intensity of Fe I and Fe II lines in spectra of TS with electrospray microdroplets (Fig. 5). This indicates enhanced sputtering of electrodes due to presence of water flowing through the needle electrode. The emission spectrum is much simpler in the region 500-1000 nm with only lines of O I, and Hα line at 656 nm. Fig:.6 shows comparison of VIS-NIR emission spectra from experiments in dry O_2, humidified O_2 and dry O_2 with ES (water flow rate 300 mL/min). All spectra are normalized to intensity of O I line at around 777 nm. The only difference is the intensity of Hα line at 656 nm.

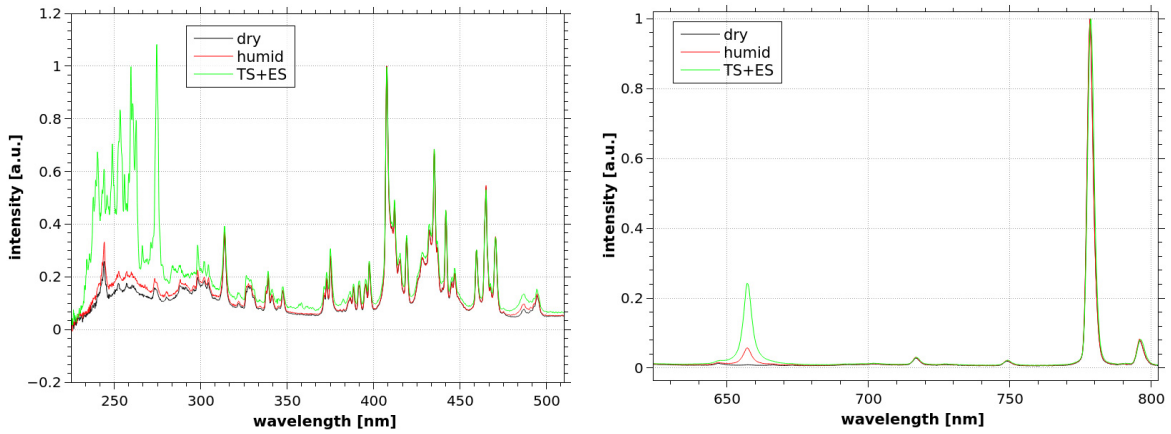

Fig. 6. Comparison of optical emission spectra of TS generated in dry O_2, humid O_2, and in dry O_2 with ES.

This line is absent in dry O_2, and present in humid O_2 and in ES measurements. In case of ES spectra, the H line is much stronger than in humid O_2. It can be explained by higher absolute H_2O density in discharge zone, where the temperature is elevated compared to the room temperature. The higher Hα is indication that more H_2O molecules are dissociated to H and OH radicals in comparison to humidified O_2.

3. Conclusion

TS discharge operated in dry and humid synthetic air can produce NO_2, HNO_2, NO in the gas phase which can then be transported to ES microdroplets to produce PAW in 1SS and 2SS both. To limit the interactions of nitrites (NO_2^-) with H_2O_2, pure O_2 was used as input gas. We observed that unlike NO_2 and HNO_2, no significant amount of H_2O_2 is produced in gas phase. It is probable that OH radicals which are transported from plasma to water combines to generate H_2O_2 in liquid phase. For this reason, the concentration of H_2O_2 was much higher in 1SS (TS+ES) than in 2SS (TS and ES separated) because direct contact between plasma and liquid water is possible only in 1SS. Optimum conditions for H_2O_2 generation in TS+ES system were found. These results are beneficial for understanding the mass transport from gas phase to water and for the tuning of plasma activated water for various potential applications.

4. References

[1]Z Machala et al 2019 J. Phys. D: Appl. Phys. 52 034002
[2] EL Hassan et al Water **2021**, 13, 182. https://doi.org/10.3390/w13020182

CHARACTERIZATION OF PLASMA ACTIVATED WATER FOR BIO-APPLICATIONS

Kateřina Šindelková[1], Zdenka Kozáková[1], František Krčma[1]

[1]*Faculty of Chemistry, Brno University of Technology, Purkyňova 118/464, 612 00 Brno, Czech Republic*

E-mail: Katerina.Sindelkova1@vut.cz

Plasma activated water was prepared using three different systems providing plasma-liquid interactions above, inside or via bubbling of the discharge gas products into the liquid. Concentration of reactive species produced in PAW was determined spectrophotometrically and compared. Time stability as well as pH and conductivity were measured, too. The antimicrobial activity of PAW on selected microorganisms *E. coli* and *C. glabrata* was also investigated.

1. Introduction

Plasma activated water is created by the interaction of non-thermal plasma with water. Thanks to this interaction, reactive species with different lifetimes are formed. Short lifetime species include hydroxyl, oxygen and hydrogen radicals, excited electrons, etc. while long lifetime species include hydrogen peroxide, nitrates, nitrites, peroxynitrite, ozone, etc. [1]. PAW has antimicrobial effects thanks to the high oxidation potential caused by oxygen and nitrogen species (RONS). The composition of plasma activated water depends on different environment in which the plasma is created, the concentration of reactive species and other physical and chemical properties changes [2]. Therefore, it is important to choose the right plasma system for the chosen application in order to achieve the optimal composition. Thanks to its unique properties, PAW has a wide range of applications, both in biomedicine and in agriculture [3].

2. Experimental setup

In this work, three different plasma systems were used for the preparation of PAW (Fig. 1). The first system generating plasma above the water surface was based on a dielectric barrier discharge with a liquid electrode [3]. In the second system, the plasma is generated directly in the liquid by a high-frequency voltage applied to the pin-hole based main electrode [4]. The plasma reactor consisted of two electrodes – the main high voltage electrode and the second (counter) electrode. The main electrode was constructed from a tungsten wire inserted into a ceramic head and an outer glass tube serving as a holder. The second (counter) electrode was a flat aluminum plate. In the third system, the plasma was not in a direct contact with the liquid. Gaseous products from an ozonizer operating in synthetic air were bubbled into the liquid. The activation time of 2 minutes was the same for all plasma systems. Experimental parameters such as applied power and treated volume are presented for individual systems in Table 1.
Physical and chemical changes (pH, conductivity, and RONS) were characterized in PAW. For the detection of hydrogen peroxide, nitrates and nitrites formed in PAW produced from distilled water, colorimetric methods combined with the UV-VIS spectrometry were employed.

Tab. 1. Comparison of applied powers and treated volumes in used plasma systems.

Plasma system	Power (W)	Volume (ml)	Time (min)
DBD	36	75	2
AC pin-hole	65	150	2
O_3 bubbling	30	150	2

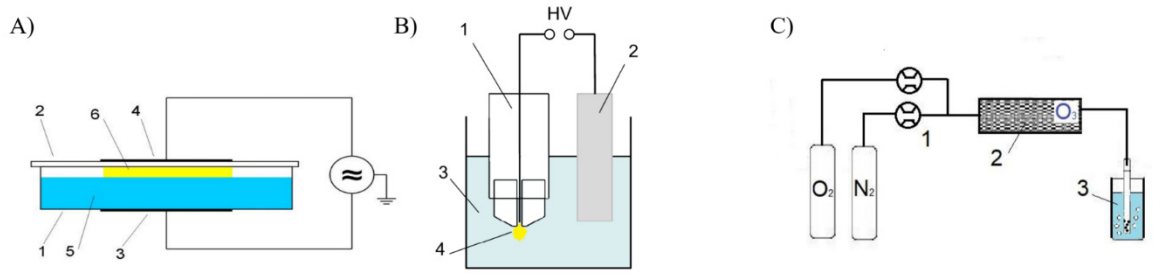

Fig. 1. Plasma systems: A) DBD with the liquid electrode: 1 – Petri dish, 2 – ceramic cover, 3 – graphite electrode, 4 – silver electrode, 5 – distilled water, 6 – plasma; B) AC pin-hole: 1 – HV electrode, 2 – aluminium plate electrode, 3 – distilled water, 4 – plasma; C) O_3 bubbling: 1 – mass flow controllers, 2 – ozonizer (DBD plasma), 3 – distilled water.

3. Results

For each plasma system, the composition of the reactive species was different, therefore the concentrations of hydrogen peroxide, nitrate and nitrite are plotted in Fig. 2. As the experimental parameters of each system slightly differed, production efficiency in $kJ \cdot dm^{-3}$ was calculated and compared in Table 2. The highest concentration of generated particles was determined for the AC pin-hole discharge. However, sufficiently low energetic efficiency of nitrates was also achieved in the DBD and O_3 bubbling systems.

PAW prepared in all systems was also applied in microbial tests, namely on yeast *Candida glabrata* and bacteria *Escherichia coli*. We had expected that PAW prepared in AC pin-hole system would have higher antimicrobial effect due to the high concentration of hydrogen peroxide and nitrites. However, only mild antimicrobial effects up to 5.5 % were observed in case of PAW prepared in the DBD plasma system (Tab. 3).

For individual types of PAW, their stability over time was also monitored at two storage conditions: at room temperature as well as in the fridge, both in dark. In general, the PAW prepared in the DBD plasma system (Fig. 3) was more stable than the AC pin-hole or O_3 bubbling systems. Only a slight decrease of hydrogen peroxide concentration connected with the reduction of nitrates to increase concentration of nitrites was observed within four hours. In the AC pin-hole system, amount of nitrates drops more rapidly to form nitrites due to the high concentration of hydrogen peroxide. In case of O_3 bubbling, delayed formation of hydrogen peroxide was observed at room temperature, only.

Tab. 2. Production efficiency of RONS in PAW prepared in used plasma systems.

Plasma system	E_{spec} ($kJ \cdot dm^{-3}$)	Production efficiency ($kJ \cdot mg^{-1}$)		
		H_2O_2	NO_3^-	NO_2^-
DBD	58	73	11	94
AC pin-hole	52	4	6	26
O_3 bubbling	24	67	8	0

Tab. 3. Antimicrobial effects of PAW prepared in used plasma systems (+ 0–2.5 %; ++ 2.5–5.5 %).

Plasma system	*Candida glabrata*	*Escherichia coli*
DBD	++	++
AC pin-hole	+	+
O_3 bubbling	++	+

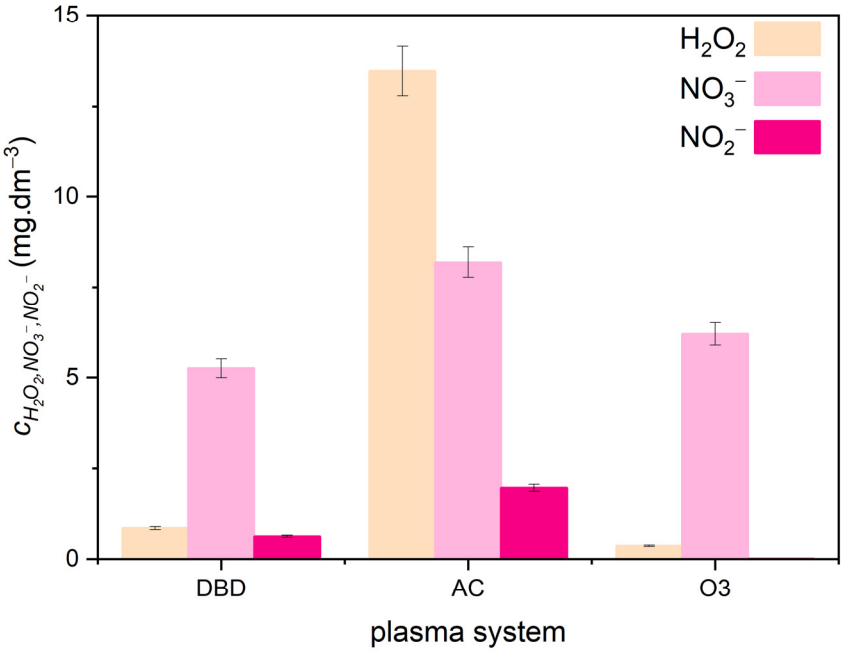

Fig. 2. Comparison of concentration of reactive particles in used plasma systems.

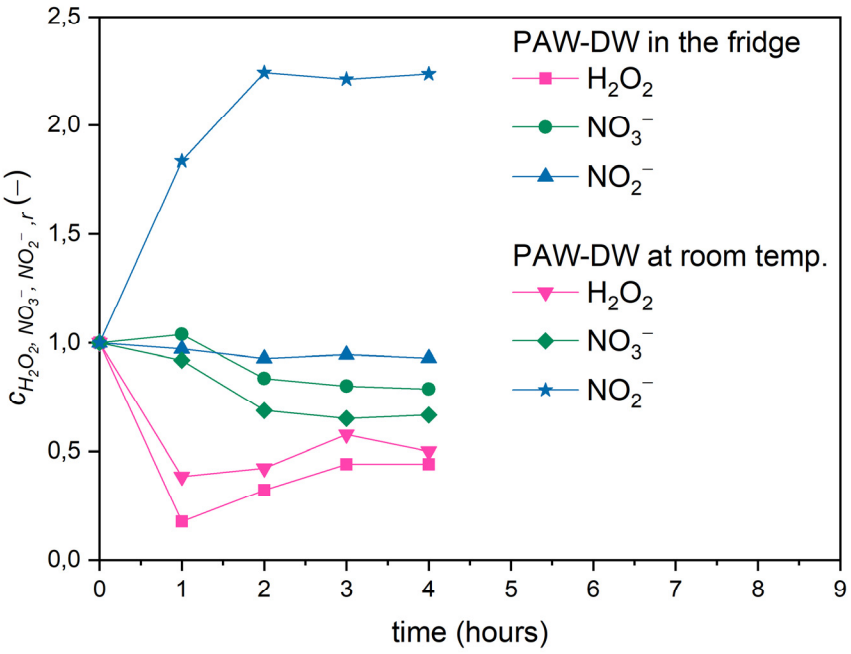

Fig. 3. Time stability of PAW prepared in the DBD plasma system with the liquid electrode.

4. References

[1] Bruggeman P J et al. 2016 *Plasma Sources Sci. Technol.* **25** 053002.
[2] Kozáková Z et al. 2022 *Proc. of CESPC-9* 121.
[3] Šimečková J et al. 2020 *Water* **12** 2357.
[4] Krčma F et al. 2018 *Plasma Sources Sci. Technol.* **27** 065001.

PLASMA POLYMERIZATION OF ANTIBACTERIAL THIN FILMS FROM PROPANE-BUTANE MIXTURE IN ATMOSPHERIC PRESSURE DISCHARGE

Věra Mazánková[1], Daniela Podzemná[2], Erika Podzemná[2], Pavel Sťahel[3], Lubomír Prokeš[3], Marián Lehocký[4], David Trunec[3]

[1]*Department of Mathematics and Physics, Faculty of Military Technology, University of Defence in Brno, Kounicova 65, 662 10 Brno, Czech Republic*
[2]*Institute of Physical and Applied Chemistry, Faculty of Chemistry, Brno University of Technology, Purkyňova 118, 612 00 Brno, Czech Republic*
[3]*Department of Physical Electronics, Faculty of Science, Masaryk University, Kotlářská 2, 611 37 Brno, Czech Republic*
[4]*Faculty of Technology, Tomas Bata University in Zlín, Vavreckova 275, 760 01 Zlín, Czech Republic*
E-mail: vera.mazankova@unob.cz

Polymeric thin coatings were deposited on teflon substrates using atmospheric pressure plasma polymerization from propane-butane (PB) mixture. The plasma polymerization was performed in surface barrier discharge burning in nitrogen at atmospheric pressure. The chemical composition of PB films was studied by EDX. The film surface properties were studied by surface energy measurement. The thin film deposited samples were highly active against both *Staphylococcus aureus* and *Escherichia coli* strains in general.

1. Introduction

Plasma polymerization is the process of creating a highly-branched polymer by plasma-initiated polymerization of the gas precursor. Typically, plasma polymer is created as a thin layer consisting of short chains with random organization and a high degree of crosslinking. The formation of thin layers and coatings on the surface of a material makes it possible to significantly change its properties without affecting the volume, or to combine the properties of two or more materials. Thin films are widely used as functional, reinforcing, reflective, conductive and dielectric materials in the formation of contacts, the production of printed circuit boards, integrated circuit elements in microelectronics, the creation of light filters and the basic elements of optoelectronics. Intensive experimental and theoretical research and development of thin film technology lead to significant progress in recent years [1–3]. Based on the set conditions, the properties of the selected substrate and the selected configuration of the electrodes, it is possible to deposit either hydrophobic or hydrophilic layers [1]. Several hydrophilic polymers were employed as candidates to develop hydrophilic anti-biofouling coatings. Among them, poly(ethylene glycol) (PEG), zwitterion-containing polymers and their derivatives were widely investigated [4]. Poly(2-oxazoline) (POx) thin films are an example of antifouling coatings [5], which could replace PEG coatings. In our previous studies, POx thin coatings were deposited using plasma polymerization with 2-methyl-2-oxazoline or 2-ethyl-2-oxazoline vapour as a monomer [6,7]. In this contribution, we present preparation and diagnostic of thin polymer films prepared by plasma polymerisation from propane-butane (PB) mixture. The films were deposited on polytetrafluoroethylene (teflon) substrates. It was already shown that thin films deposited from PB mixture in nitrogen atmospheric pressure discharge are highly hydrophilic [8]. Now, it is also shown that such thin films have also strong antibacterial properties.

2. Experimental set-up

The experimental setup was described in detail in [9]. Deposition apparatus consists of a custom build reactor with surface dielectric barrier discharge (SDBD) using high voltage AC generator (Lifetech, Brno, Czech Republic) with a frequency of 30 kHz. The electrode system consists of 11 upper revolving cylindrical surface electrodes made of brass with a length of 10.4 cm and a diameter of 1 cm, between which there are gaps with a width of 2 mm. Lower flat electrode with dimensions 13.6 cm × 10 cm is placed below cylindrical electrodes and is covered by mica dielectrics with 1 mm thickness. Nitrogen as working gas was supplied between the upper electrodes with a flow rate of 6.5 slm. The

PB mixture was added to this nitrogen flow with flow rates from 20 sccm to 80 sccm, so the PB concentration was 0.31-1.23 %. The deposition time was 6.5 s.
The total surface free energy of films was determined by measuring the static contact angle using the sessile drop method. Sessile drop of a volume of 1 μl was dropped onto the measured surface and analyzed using See System (Advex Instruments, Brno, Czech Republic). The contact angles of three standard liquids (deionized water, diiodomethane and ethylenglykol) were measured and the surface free energy was calculated by the Owens, Wendt, Rabel and Kaelble (OWRK) model [8].
The deposited films were imaged with scanning electron microscope (SEM) MIRA3 (TESCAN, Brno, Czech Republic) with Schottky field emission electron gun equipped with secondary electron and back-scattered electron detectors as well as with characteristic X-ray detector (EDX) analyzer (Oxford Instruments, High Wycombe, UK), which was used to determine film elemental composition.
Two bacterial strains, gram-negative *Escherichia coli* (CCM 4517) and gram-positive *Staphylococcus aureus* (CCM 4516), were used for the antibacterial tests. The antibacterial testing was performed according to ISO 22196 with modifications. Bacterial suspensions (*Escherichia coli* 2.7×10^5 CFU mL^{-1}; *Staphylococcus aureus* 5.4×10^4 CFU mL^{-1}) were prepared in 1/500 Nutrient broth (HiMedia laboratories, India). The bacterial suspension was dispensed on the sample surface (dimensions 25 mm × 25 mm) in the volume 100 mL and the sample was covered with the polypropylene foil (dimensions 20 mm × 20 mm). Samples with foils were cultivated at 35 °C and 100% relative humidity for 24 hours. After the incubation time, polypropylene foil was removed and each sample was completely washed by SCDLP broth (HiMedia laboratories, India), which was subsequently collected. The viable bacteria count was determined by the pour plate culture method (PCA, HiMedia laboratories, India).

3. Results and discussion

The contact angles between the test liquids and PB films were measured using the sessile drop technique in order to determine the total surface free energy and its components. Three test liquids (distilled water, glycerol and diiodomethane (CH_2I_2)) were used. The acid-base theory with multiple regression [10] was used to calculate the total surface free energy and its components – the Lifshitz–van der Walls (LW) interaction component and the acid–base (AB) interaction component. The surface free energy and its above mentioned components of PB films are given in Table 1. The deposited films were hydrophilic with the water contact angle in range 13°-23° and surface free energy in range 58-61 mJ/m^2.

Tab. 1. The contact angles for different liquids and surface free energy and its components of PB films deposited at different monomer flow rates. Teflon marks bare substrate.

flow rate (sccm)	**contact angle (°)**			**surface free energy (mJ/m^2)**		
	water	CH_2I_2	glycerol	total	LW	AB
teflon	83.5 ± 1.2	63.2 ± 1.3	74.7 ± 1.3	30.3 ± 1.0	26.7 ± 0.8	3.5 ± 0.8
20	12.7 ± 1.6	32.8 ± 1.7	58.1 ± 1.7	61.2 ± 3.6	43.0 ± 1.2	18.2 ± 2.5
35	16.2 ± 1.2	37.8 ± 0.8	60.0 ± 4.0	58.8 ± 4.9	40.7 ± 0.4	18.2 ± 4.5
50	21.0 ± 1.3	38.2 ± 1.0	60.9 ± 3.0	58.6 ± 5.4	40.2 ± 0.6	18.7 ± 4.8
65	20.9 ± 1.5	29.4 ± 5.0	62.8 ± 1.0	61.0 ± 2.2	40.1 ± 0.4	20.8 ± 1.8
80	22.8 ± 1.2	38.3 ± 1.1	62.9 ± 3.6	60.8 ± 3.9	40.5 ± 0.5	20.4 ± 3.4

The elemental composition of PB films deposited at different monomer flow rates determined by EDX is shown in Table 2.
Tab. 2. The elemental composition of films deposited at different monomer flow rates. The elemental composition is given in atomic %.

flow rate (sccm)	**C**	**N**	**O**
20	31.1	48.9	20.0
35	40.2	43.0	16.8
50	47.9	37.5	14.6
65	55.2	31.8	13.0
80	53.8	33.0	12.6

The carbon content in films increases with increasing PB flow rate, the nitrogen content decreases with increasing PB flow rate. Because the deposition setup is not closed in a vacuum chamber, ambient air can diffuse in the discharge and therefore the oxygen is also present in films. The elemental composition of PB films is close to the elemental composition of POx films [6,7].
The results of the number of viable bacteria per cm^2 of sample (CFU/cm^2) and the values of antibacterial activity (R) against the growth of *Staphylococcus aureus* CCM 4516 and *Escherichia coli* CCM 4517 are given in Table 3. The calculation of antibacterial activity values was performed according to ISO 22196: 2011.

Tab. 3. Resulting numbers of surviving colonies (CFU/cm2) on the PB films deposited at different monomer flow rates. Teflon marks bare substrate.

flow rate (sccm)	***S. aureus* CCM 2022 (CFU/cm^2)**	***E. coli* CCM 4517 (CFU/cm^2)**
teflon	6.2×10^4	9.1×10^5
20	< 1	< 1
35	< 1	< 1
50	< 1	< 1
65	< 1	< 1
80	4.5×10^3	< 1

The samples had a very strong effect against both Gram-negative and Gram-positive test strains, the values of antibacterial activity (R) are ≥ 4.8 for *S. aureus* and ≥ 5.9 for *E. coli*. Such values of antibacterial activity represent strong antibacterial properties according to ISO 20743: 2014. The only exception is the sample deposited at the flow rate of 80 sccm. Only weak antibacterial activity against *S. aureus* was measured for this sample. The strong antibacterial activity may be caused by the presence of amines.

4. Conclusion

A fast and cheap method for the deposition of antibacterial coatings on teflon surface was developed. The deposition time was 6.5 s only, so the deposition can be done online. The coatings deposited at all monomer flows used were hydrophilic. The coatings deposited with PB flow rate up to 65 sccm had a very strong antibacterial activity against *S. aureus* and *E. coli*. The antibacterial activity of PB films can be caused by their hydrophilicity and the presence of amines. Due to similar elemental composition with POx films it can be concluded that the PB films can also have antibiofouling properties.

Acknowledgement
V.M. was supported by institutional support for the research organization development awarded by the Ministry of Defence of the Czech Republic.

5. References

[1] Levchenko I et al. 2021 *Plasma and polymers: Recent progress and trends. Molecules,* 26(13).
[2] Danilaev M P et al. 2020 *Single-stage plasma-chemical synthesis and characterization of carbon nanoparticle-polymer suspensions. Plasma Processes and Polymers*, 17(4).
[3] Vesel A and Mozetic M 2008 *Modification of pet surface by nitrogen plasma treatment. Journal of Physics: Conference Series*, 100(1).
[4] Leng C et al.2015 *Probing the Surface Hydration of Nonfouling Zwitterionic and PEG Materials in Contact with Proteins. ACS Appl. Mater. Interfaces*, 7, 16881–16888.
[5] Maan A M C; Hofman A H; de Vos W M; Kamperman M 2020 *Recent Developments and Practical Feasibility of Polymer-Base Antifouling Coatings. Adv. Funct. Mater.* 30.
[6] Stahel P et al. 2019 *Atmospheric Pressure Plasma Polymerized Oxazoline-Based Thin Films-Antibacterial Properties and Cytocompatibili Performance. Polymers* 11.
[7] Mazankova V et al. 2020 *Atmospheric Pressure Plasma Polymerized 2-Ethyl-2-oxazoline Based Thin Films for Biomedical Purposes. Polymers* 12. https://doi.org/10.3390/polym12112679.

[8] Dvorakova H et al. 2019 *Fast Surface Hydrophilization via Atmospheric Pressure Plasma Polymerization for Biological and Technical Applications. Polymers*, 11.
[9] Horňák, R. Bachelor's thesis. https://is.muni.cz/th/rda5f/?lang=en.
[10] Navratil Z et al. 2004 *On the analysis of surface free energy of DLC coatings deposited in low pressure RF discharge. Czech. J. Phys.* 54, C877-C882.

USE OF DIRECT APPLICATION OF PLASMA FOR THERAPEUTIC PURPOSES

Zuzana Měšťánková, František Krčma

Faculty of Chemistry, Brno University of Technology, Purkyňova 118/464, 612 00 Brno

E-mail: Zuzana.Mestankova@vut.cz

Staphylococcus epidermidis and *Escherichia coli* are nosoclonal pathogens and our aim is to investigate the effect of plasma on these bacteria, for which we want to achieve growth inhibition. Fresh pig skin simulating human skin was used to culture the bacteria. Pig skins treated with plasma showed a visible reduction in bacterial growth after culture compared to control (untreated) skins. The number of colonies decreased after plasma treatment and the colony size was significantly reduced.

1. Introduction

Inhibition of bacteria by plasma is a non-selective process that does not build up resistance, which is a major problem nowadays. Plasma is characterized by antimicrobial effects due to generation of active particles, ultraviolet radiation in the UV-C region, pH reduction, heat generation and electromagnetic waves [1].

Staphylococcus epidermidis

Staphylococcus epidermidis belongs to the genus *Staphylococcus* and is a gram-positive cocci that is immobile, does not form spores or a case. They are facultatively anaerobic bacteria. *Staphylococci* can be arranged singly, in pairs, tetrads, short chains, but mostly in irregular clusters in a grape shape. The bacterium is one of the most widespread species found on human skin and mucous membranes. *Staphylococcus epidermidis* is classified as a member of the coagulase-negative *Staphylococci* (CoNS) group. It is generally considered a commensal organism and is less invasive and virulent than coagulase-positive *Staphylococci*. *Staphylococcus epidermidis* has become a common nosoclonal pathogen in recent years, mostly in patients with poor defense mechanisms. Many strains of *S. epidermidis* are able to form biofilms and easily colonize implanted medical devices [2, 3].

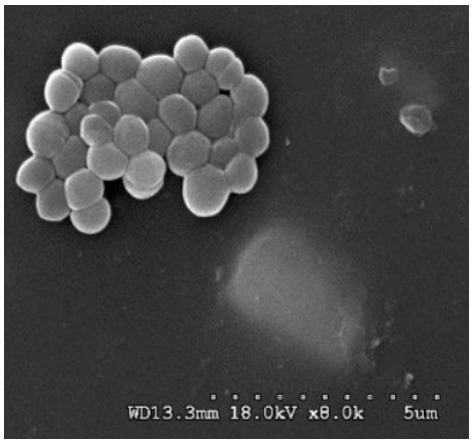

Figure 1: SEM photograph of Staphylococcus epidermidis [4]

Escherichia coli

Escherichia coli is a facultatively anaerobic Gram-negative bacterium belonging to the *Enterobacteriaceae* family. The bacterium is commonly found as a commensal in the normal intestinal

flora of humans and warm-blooded animals, and the evolution of the microorganism has resulted in pathogenic strains that cause serious extraintestinal infections in humans and animals. Pathogenic

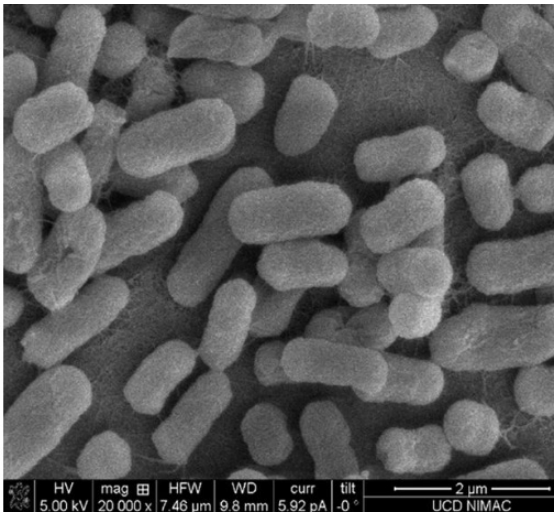

Figure 2: SEM photograph of Escherichia coli [6]

E. coli are mainly divided into two groups according to the site of disease: extraintestinal pathogenic *E. coli* (ExPEC) and intestinal pathogenic *E. coli* (InPEC) [5, 6].

2. Experimental setup

Microwave torch with direct gas supply

Microwave torch was generated in Argon direct flow of 5 Sl/min at frequency of 2.5 GHz and discharge power of 12 W according to the scheme shown in Figure 3. The active unipolar like discharge was blown out of the cavity in the form of torch. Bacteria were plated on sterilized fresh pig skin. Then the skin was treated with a plasma beam that was 5 mm away from the sample. Plasma was applied for 30 and 60 seconds (Figure 4) [7].

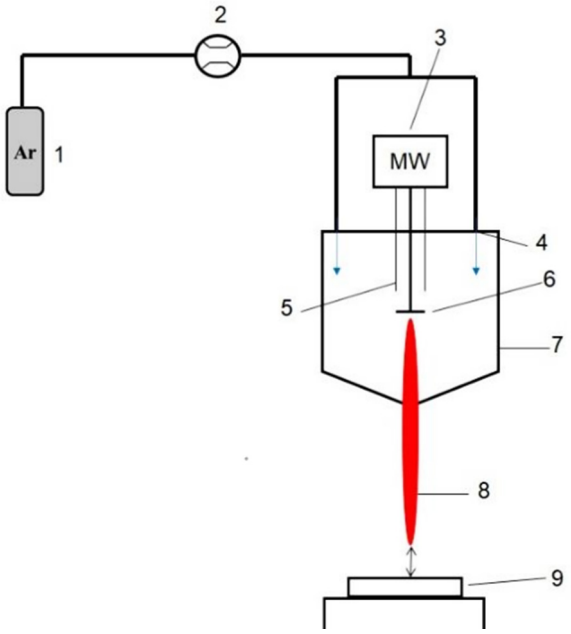

Figure 3: Scheme of the experimental connection of the torch discharge with direct gas flow:1 – argon source; 2 – mass flow controller; 3 – MW source; 4 – direct supply of argon; 5 – MW-coaxial cable; 6 – MW antenna; 7 – discharge cavity, 8 – plasma beam; 9 – Petri dish; 10 – Petri dish holder [7]

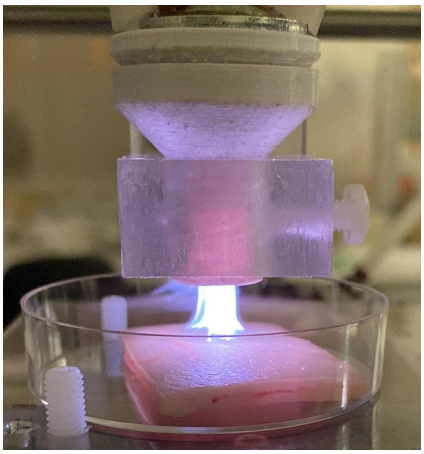

Figure 4: Pig skin treated with a plasma beam

3. Results

10 and 20 µl of *S. epidermidis* and *E. coli* cultures were applied to the pig skin and then plasma was applied to the prepared sample for 30 and 60 s. The process was carried out in a Petri dish without or with a lid (in a closed area). In the Figure 5 it can be observed that the samples in which plasma was applied with the lid showed a higher inhibition of bacterial growth than the samples without the lid. The number of colonies decreased and their size was significantly reduced after the plasma exposure.

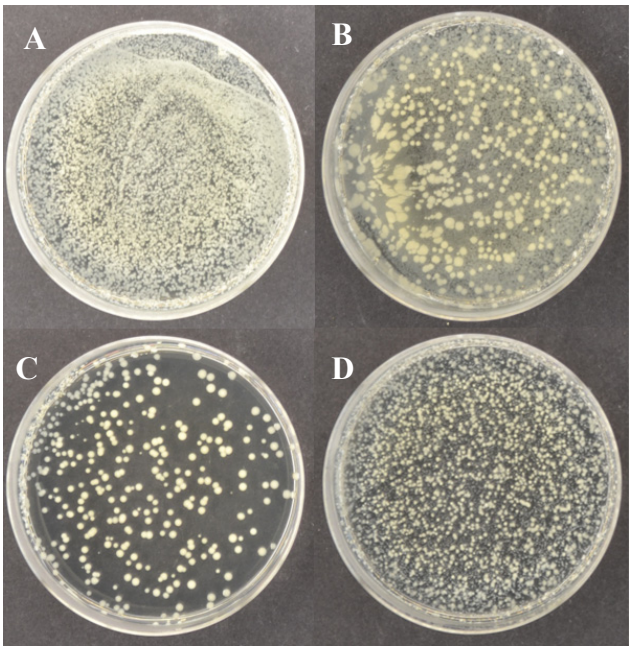

Figure 5: Demonstration effect of plasma: Staphylococcus epidermidis 30 s plasma treatment, power 12 W: A - culture concentration 10 µl without lid, B - culture concentration 20 µl without lid, C - culture concentration 10 µl with lid, D - culture concentration 20 µl with lid

4. References

[1] Niedźwiedź I 2019 *Polish Journal of Microbiology* **68**
[2] Naylor S 2005 *International Journal of Medical Microbiology* **419-441**
[3] Paradis S 2005 *International Journal of Systematic and Evolutionary Microbiology* **55**
[4] Yujie L 2021 *Annals of Translational Medicine* **6**
[5] Foster T 1996 *Staphylococcus: Medical Microbiology* Chapter **12**
[6] Boehm D 2016 *Applied and Environmental Microbiology* **455**
[7] Trebulová K 2022 *Diploma thesis Study of plasma interaction with yeast Candida glabrata* **32**

PREPARATION OF PROTECTIVE HYDROPHOBIC LAYERS ON ALUMINUM USING PLASMA POLYMERIZATION AT ATMOSPHERIC PRESSURE

Sandra Ďurčányová[1], Michal Stano[1], Pavol Ďurina[1], Miroslav Zahoran[1], Anna Zahoranová[1], Monika Stupavská[2], Dušan Kováčik[1,2]

[1]*Comenius University in Bratislava, Faculty of Mathematics, Physics and Informatics, Department of Experimental Physics, Mlynská dolina, 842 48 Bratislava, Slovakia*
[2]*Department of Physical Electronics, Faculty of Science, Masaryk University, Kotlářská 2, 611 37 Brno, Czech Republic*
E-mail: sandra.durcanyova@fmph.uniba.sk

This contribution deals with the plasma polymerization of hexamethyldisiloxane as a method of preparing protective hydrophobic layers on aluminum. The plasma-polymerized layers were characterized using ATR-FTIR, XPS, SEM and WCA measurements. A new and optimized experimental apparatus has been designed and constructed.

1. Introduction

The preparation of hydrophobic layers, and polymerization in general, is conventionally realized by the means of chemical processing. Plasma polymerization (PP) is an alternative method, by which polymer-like layers are created using a plasma source. Highly reactive particles of the plasma activate the monomer present in the working gas and initiate the PP process without the need of additional solvents or catalysts [1]. Plasma-polymerized layers have the potential to be mechanically and chemically resistant, insoluble, thermally stable and homogeneous due to their high degree of monomer cross-linking, and adhere well to different types of surfaces [2]. Further advantages of PP include generally lower costs than conventional polymerization methods and the ability to precisely control multiple parameters of the PP process (input power, exposure time, electrode system configuration, etc.) to create layers of a desired thickness and functionality (protective, hydrophobic, anti-corrosion, anti-icing etc.). Therefore, plasma polymerization can be considered a promising and environmentally friendly method of hydrophobic-layer preparation.

Many works on the topic of hydrophobic-layer PP deal with the polymerization of hexamethyldisiloxane (HMDSO). The presented work builds on our promising research in this field related to PP of HMDSO on aluminum [3] and glass substrates [4]. In the previous PP-related research conducted at our department, PP was carried out using a DCSBD-based plasma reactor. However, this reactor had certain shortcomings (e.g. large volume of the working chamber; imprecise positioning of the sample above the DCSBD surface; working gas enriched with the monomer was supplied far from the sample; movement of the sample during PP was realized on an unnecessarily long path, etc.), which needed to be eliminated. In order to advance in our PP research, we set two main objectives for this work: creating pp-HMDSO layers on aluminum by using this reactor while studying the PP process itself; and designing and constructing an improved version of this reactor for future experiments.

2. Experiment

The main component of our experimental apparatus is the special DCSBD reactor where PP takes place. A preliminary set of experiments was conducted with this reactor to study the PP process, while also assessing its limitations and finding how to improve the design and the operating process of the new reactor.

The input power of the DCSBD plasma source was 300 W. Different exposure times were studied (30, 60, 120 s). Post-treatment, i.e. plasma treatment of already deposited pp-HMDSO layers without supplying the monomer to the working gas, was also studied, as it poses a way to further refine the layers and achieve even better anti-corrosion properties or durability [5]. The working gas was prepared in the following way: nitrogen flowed into a bubbler filled with HMDSO, and the HMDSO-enriched nitrogen was then mixed with pure nitrogen in the desired ratio through two mass flow controllers. The relative

flow was 15.8 (8 slm of nitrogen + 1.5 slm of HMDSO-enriched nitrogen). The pp-HMDSO layers were characterized using ATR-FTIR, XPS, SEM and WCA measurements.

3. Results and discussion

WCA measurements showed that keeping a precisely defined distance between the sample and the DCSBD surface is one of the crucial parameters of an effective PP process. They also indicated that after 30 s of PP, the aluminum surface is already completely covered with pp-HMDSO, as there appears to be no additional effect of exposure times longer than 30 seconds on the hydrophobicity of the layers. This was confirmed by the XPS analysis since no traces of the Al substrate were left in the spectra after 30 s of PP. Similarly, there were no significant differences in the chemical composition caused by longer exposure times. The post-treated sample showed a significant increase in oxygen on the surface, which is typical for a plasma treatment without an added monomer in the working gas. An additional increase in silicon in the post-treated sample shows that the post-treatment utilizes HMDSO molecules that have not yet been polymerized in the first step of the treatment, as was found in previous works [5].
The ATR-FTIR spectra of plasma-polymerized samples exhibited gradually growing absorption peaks attributed to bonds of different parts of the HMDSO molecule. This showed the increasing thickness of the layers as well as the radical fragmentation of the HMDSO monomer in the plasma, which leads to cross-linking in the pp-HMDSO layer [6].

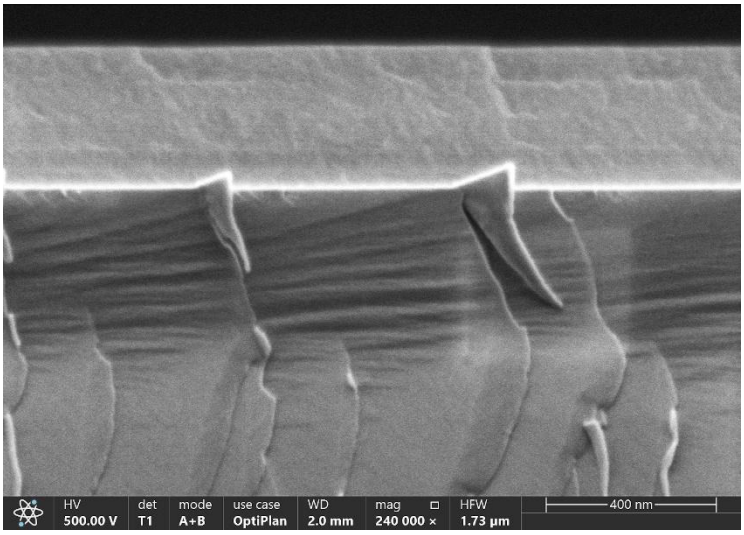

Fig. 1. SEM image: a cross-section of the pp-HMDSO layer deposited on a silicon wafer, PP time 120 s.

SEM analysis of the pp-HMDSO layer deposited on a silicon wafer showed that the layer is homogeneous and its surface is smooth and without defects (Fig. 1). The thickness of the layer after 120 s of PP was 334 nm, from which we can roughly estimate the deposition rate as 167 nm/min.
Our main objective was to design and construct the new and optimized PP reactor, which we successfully accomplished. The volume of the new reactor is 3 l, whereas the volume of the old one was 18 l. Therefore, we achieved a six-fold reduction in the time needed to fill the reactor chamber with working gas. The distance between the sample and the DCSBD surface is kept constant at 0.34 mm. The movement of the sample is now completely automatized, which helps to firmly define one of the parameters of the PP process and presents a more user-friendly operation.

4. Conclusions

The obtained preliminary results confirm the applicability of the DCSBD plasma source for creating hydrophobic pp-HMDSO layers on the aluminum substrate. The pp-HMDSO layers have been visualized with SEM, and their thickness and deposition rate were estimated. The effect of various exposure times and post-treatment was studied with WCA, ATR-FTIR and XPS analyses.

Based on our observations, a new and optimized PP rector has been designed and constructed, successfully eliminating the limitations of its predecessor and enabling more advanced PP experiments for future research.
Our upcoming work involves focusing on the durability and anti-corrosion properties of the pp-HMDSO layers with ageing tests and salt tests, as well as more precise measurements of their thickness and deposition rate with SEM and profilometry.

This work was financially supported by the Slovak Grant Agency for Science VEGA (No. 1/0811/21).

5. References

[1] Friedrich J 2012 *The Plasma Chemistry of Polymer Surfaces: Advanced Techniques for Surface Design*, Wiley-VCH, Weinheim
[2] Yasuda H 1981 *Journal of Polymer Science: Macromolecular Reviews* **16** 199
[3] Bónová L 2012 *Chem. Listy* **106** 1431
[4] Krumpolec R 2012 *WDS'12 Proceedings of Contributed Papers* 24
[5] Bour J 2008 *Plasma Processes and Polymers* **5**(8) 788
[6] Krumpolec R 2012 *Chem. Listy* **106** 1450

PROPERTIES OF LOW-PRESSURE RF DISCHARGES SUITABLE FOR TREATMENT OF ABSORBANTS

A. Derzsi[1], B. Horváth[1], K. Kutasi[1], K. Spasic[2], M. Puač[2], N. Puač[2] and N. Škoro[2]

[1]*Wigner Research Centre for Physics, Budapest, Hungary*
[2]*Institute of Physics, Belgrade, Serbia*

E-mail: derzsi.aranka@wigner.hu

Particle-in-Cell/Monte Carlo Collisions simulations are performed to provide a detailed characterization of low-pressure capacitively coupled radiofrequency gas discharge plasmas suitable for treatment of absorbants. Based on the simulations, discharge characteristics such as particle densities, and particle flux and energy distributions at the surfaces relevant for treatment of Zeolite are determined.

Zeolite has long been recognized as a mineral with excellent absorptive properties. This material, made up of arrays of aluminum, silica, and oxygen, has been recently introduced as a novel microporous material suitable for application in water decontamination. Since it is a porous material, the absorption process results in not only capturing particles between grains, but also insertion of the particles into its pores. Due to its high effective surface area, desorption is typically performed using suitable solutions. However, this way of Zeolite regeneration proved to be ineffective for some adsorbed pharmaceuticals. Experimental investigations performed so far showed that in this case regeneration can be efficiently performed by plasma treatment which also represents an efficient and ecologically responsible procedure. These procedures are based on the interaction of adsorbed particles and chemically active species created in the plasma. However, the desirable effects can be achieved only for a narrow range of treatment conditions. For the reliable, knowledge-based optimization of the applications, a detailed characterization of the plasma reactor used for surface treatment is required, including information on the plasma properties and surface processes. In this work, one-dimensional in space and three dimensional in velocity space (1d3v) Particle-in-Cell/Monte Carlo Collisions (PIC/MCC) simulations are performed in low-pressure capacitively coupled plasmas in Argon, under conditions corresponding to the experiments for treatment of Zeolite (4.5 cm electrode gap, driving frequency of 13.56 MHz, pressures < 600 mTorr, voltage amplitudes < 450 V). For these conditions, the voltage-current characteristics, as well as the power and emission spectrum for the discharge are available from the experiments. In the simulations, electrons, Ar^+ ions, and fast Ar atoms are traced. As surface processes, secondary electron emission due to heavy particles and elastic reflection of electrons are considered. The PIC/MCC simulations provide information on many plasma parameters and distributions of interest, such as densities of the traced particles and their flux and energy distribution at the surfaces, the spatiotemporal distribution of the electric field, the power absorption and energy of particles, as well as the ionization and excitation dynamics in the discharge.

Acknowledgement: This work was supported by the grant 2019-2.1.11-TÉT-2020-00162 “Characterization of radiofrequency gas discharges applied for surface treatment” of the Hungarian National Research, Development and Innovation Office and bilateral project Hungary-Serbia (2021-2023).

MODIFICATION OF MICROPOROUS POLYPROPYLENE MEMBRANES BY PLASMA-INITIATED GRAFTING OF ACRYLIC ACID

Martin Kuťka[1], Michal Stano[1]

[1]*Department of Experimental Physics, Faculty of Mathematics, Physics and Informatics, Comenius University, Mlynska Dolina F2, 842 48, Bratislava, Slovakia*
E-mail: martin.kutka@fmph.uniba.sk

This work deals with the hydrophilic surface modification of microporous polypropylene membranes by plasma-initiated grafting of acrylic acid. The membranes were activated in low-pressure radiofrequency discharge in argon or oxygen. The long-term stability of grafted membranes was studied in deionized water and in 30 wt.% KOH aqueous electrolyte. The results revealed that membranes activated in argon plasma exhibit considerably higher stability than membranes activated in oxygen plasma.

1. Introduction

In order to reduce the amount of greenhouse gas emissions, an increase in the share of electricity production from wind and solar photovoltaic energy is expected in the near future. The disadvantage of these energy sources is that they do not allow continuous production of electricity. Therefore, it is necessary to store energy when it is possible to produce more energy than is demanded. Nowadays, approximately 99 % of the energy produced from wind and solar energy sources is stored using pumped storage hydropower plants [1]. However, it is difficult to choose a suitable location, and therefore the development of energy storage in the form of hydrogen is expected in the future. In this case, electrical energy is converted into hydrogen using water electrolysis. During the electrolysis of water, the passage of an electric current through the aqueous electrolyte between the electrodes breaks down the water molecules into gaseous hydrogen and oxygen. To effectively separate the produced gases and prevent their subsequent mixing, a separator is inserted between the electrodes. There are several types of electrolysis cells, the two main types being PEM (proton exchange membrane) electrolysers and alkaline electrolysers. PEM electrolysers, compared to the alkaline electrolysers, have a higher investment cost and a shorter lifetime [2]. In alkaline electrolysers, separators are made of porous and electrically non-conductive materials. The transfer of ions between the electrodes is made possible by a liquid electrolyte (usually a 30 wt.% aqueous solution of KOH), which fills the pores of the separator. Therefore, the conductivity depends not only on the conductivity of the electrolyte, but also on the properties of the separator [3]. High conductivity, or low resistance of the membrane is important for the efficiency of the electrolysis cell. Hydrophilicity is also an important property of the separator. In the case of insufficient wetting of the separator with electrolyte, precipitation and trapping of gas bubbles inside the separator occurs, which causes an increase in resistance and promotes gas mixing [4]. In the past, chrysotile asbestos was used to produce separators, but this was abandoned after asbestos was classified as a carcinogen. Nowadays, porous polymer membranes are most often used as separators. Among the polymers that are sufficiently chemically resistant in an alkaline electrolyte environment are polypropylene, polysulfone, polyphenylene sulfide and polytetrafluoroethylene [5], [6]. Although these polymers are mechanically strong and tough, they lack wettability by aqueous electrolytes [7]. Therefore, inorganic additives are used to increase hydrophilicity. An example of such membrane is a composite of polysulfone and ZrO_2, also known as Zirfon® Perl [8]. The influence of the mass fraction of ZrO_2 on the properties of the membrane was studied in the work [9], which shows that increasing mass fraction of ZrO_2 leads to deterioration of the mechanical strength of the membranes.

Another approach to achieve hydrophilic surface modification is treatment by low-temperature plasma. Various reactions with active plasma particles (electrons, ions) and UV radiation undergoes on the surface of the polymer, the result of which, depending on the gas used, is the formation of a wide spectrum of functional groups on the surface of the polymer. In addition to functional groups, radicals

also form on the surface of the polymer (activation of the surface). When these radicals come into contact with another monomer, we can achieve covalent binding and subsequent polymerization of this monomer, resulting in a copolymer. This process is called grafting [10]. Radicals required for grafting can be created on the surface of the membrane using an inert gas plasma or through the creation of hydroperoxide groups with oxygen plasma, which create radical when heated. A suitable monomer for achieving hydrophilicity is acrylic acid (CH_2=CH–COOH), the grafting of which creates a polyacrylic acid copolymer containing a large number of carboxyl groups on the surface of the membrane [11], [12]. Modification of microporous polypropylene membranes by graft polymerization of acrylic acid was previously investigated for their application as separators in alkaline rechargeable batteries [11] and alkaline water electrolysers [13]. It was found that grafting of acrylic acid strongly improves electric conductivity of membranes in alkaline electrolytes. Moreover, grafting of acrylic acid also reduces permeation of gases dissolved in electrolyte and thus improves purity of hydrogen and oxygen produced in water electrolyser. The main drawback of this type of separators is limited lifetime in alkaline environment. A long-term aging test of the grafted membranes in 30 wt.% KOH aqueous electrolyte was conducted in the work [13], which revealed that although the high wettability was retained for almost one year, the membranes continuously lost most of the grafted material during this period. The objective of this work is to optimize the process of graft polymerization for improved durability of the modified membranes in alkaline electrolytes with focus on comparing membranes produced by two methods differing by composition of plasma used for membrane activation.

2. Experiment

Microporous polypropylene membranes (Merck) with nominal pore size of 1.2 μm, diameter of 47 mm and thickness of 150 μm were used as substrates. The membranes were activated in a low-pressure capacitively-coupled radiofrequency (RF) discharge in argon or oxygen. Schematic of the experimental apparatus is shown in Fig. 1. The membrane was placed in plasma reactor on a polypropylene holder. Prior to activation, the reactor was evacuated to 1 Pa by a rotary vane pump. Afterwards, argon or oxygen was introduced into the reactor and pump was used to maintain pressure during the activation. To generate the plasma in the reactor, two electrodes located on the outer wall of the reactor were used. We used the electrodes to generate a RF discharge powered by RF power generator with a frequency of 13.56 MHz. Pressure maintained in the reactor during activation, power delivered to plasma and activation time are given in Tab. 1.

Tab. 1. Parameters during plasma activation of membranes.

Working gas	Pressure	Plasma power	Activation time
Argon	100 Pa	6 W	1 min
Oxygen	50 Pa	3 W	2 min

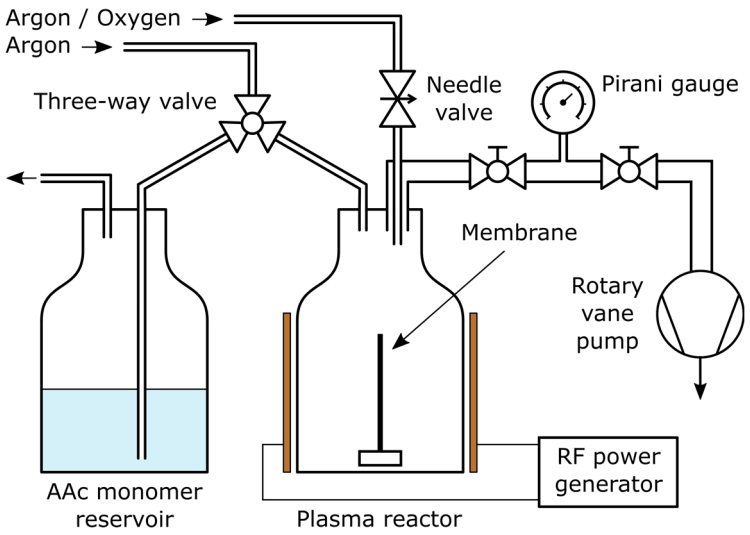

Fig. 1. Experimental apparatus used for modification of microporous membranes.

Grafting procedure was conducted immediately after plasma activation. Acrylic acid (AAc, Sigma-Aldrich) was purified by vacuum distillation and dissolved in deionized water to obtain a solution with concentration of 10 vol.%. Prior to grafting, the AAc monomer solution was deaerated with argon for at least 1 hour. After activation of membrane, approximately 40 ml of this solution was poured into the reactor via three-way valve. Activated membrane was immersed in grafting solution and sealed in the reactor under argon atmosphere. Afterwards, the reactor was detached from the rest of the apparatus and put into heated shaking bath to maintain grafting temperature. The grafted membranes were washed in deionized water immediately after grafting, dried and characterized by grafting degree (*GD*). *GD* was determined gravimetrically and represents the ratio of the weight of the polymer of polyacrylic acid, which was formed on the surface of the membrane, to the weight of the membrane before grafting. *GD* was calculated from the measured weight of the membrane before activation m_0 and after grafting m_G according to

$$GD = \frac{m_G - m_0}{m_0} \times 100 \quad [wt.\%] \tag{1}$$

Grafting time, grafting temperature and resulting *GD* of each membrane are given in Tab. 2.

Tab. 2. Grafting of membranes.

Membranes activated in argon plasma			Membranes activated in oxygen plasma		
Grafting time	Grafting temperature	*GD*	Grafting time	Grafting temperature	*GD*
1 h 31 min	70 °C	13.0 wt.%	29 min	70 °C	16.7 wt.%
1 h 33 min	70 °C	12.1 wt.%	30 min	70 °C	14.9 wt.%
2 h 14 min	60 °C	18.9 wt.%	30 min	70 °C	17.3 wt.%
1 h 50 min	60 °C	12.5 wt.%	30 min	70 °C	15.1 wt.%

To compare the long-term stability of grafted membranes activated by argon and oxygen plasmas, aging tests in deionized water and 30 wt.% KOH aqueous electrolyte were conducted. Each membrane was put into small bottle filled with deionized water or 30 wt.% KOH. During the aging tests, one half of membranes was kept at laboratory temperature, while the other half was put into oven to maintain temperature of 60 °C. The stability of grafted membranes was studied by measuring their weight and calculating *GD* during several weeks. Before each measurement, each membrane was taken out of the bottle, washed in deionized water and dried in oven. After the measurement, each membrane was put into its bottle to continue the aging test.

3. Results

The results of the aging test in deionized water are shown in Fig. 2. The decrease in *GD* at both temperatures is significantly faster for membranes activated in oxygen plasma (O_2) in comparison with membranes activated in argon plasma (Ar). The decrease in *GD* for Ar membranes is not only slower, but also more linear. On the other hand, O_2 membranes had faster decrease in *GD* during the first 5 weeks than during the rest of the aging test. The results of the aging test in 30 wt.% KOH are shown in Fig. 3. The decrease in *GD* is again faster for O_2 membranes. Moreover, the decrease in GD is clearly faster for membranes kept at 60 °C than at laboratory temperature, regardless of the plasma activation gas.

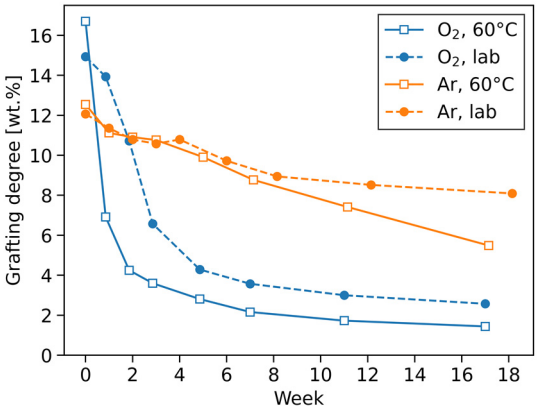

Fig. 2. Aging test in deionized water.

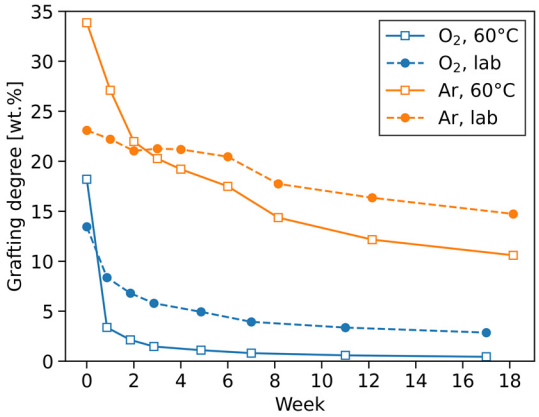

Fig. 3. Aging test in 30 wt.% KOH.

4. Conclusions

The results show that membranes grafted after argon plasma activation exhibit better stability than membranes grafted after oxygen plasma activation. The rate of aging of argon plasma activated membranes in caustic electrolyte does not significantly exceed the rate of aging in deionized water. This indicates that caustic environment is not significant contributing factor to aging rate of argon plasma activated membranes and that argon plasma activated and acrylic acid grafted microporous membranes are promising candidates for separators in alkaline water electrolysers.

Acknowledgement

This work was supported by the Slovak grant agency VEGA, project 1/0811/21.

References

[1] F. Geth, T. Brijs, J. Kathan, J. Driesen, and R. Belmans, 'An overview of large-scale stationary electricity storage plants in Europe: Current status and new developments', *Renewable and Sustainable Energy Reviews*, vol. 52, pp. 1212–1227, Dec. 2015, doi: 10.1016/j.rser.2015.07.145.

[2] A. Ursua, L. M. Gandia, and P. Sanchis, 'Hydrogen Production From Water Electrolysis: Current Status and Future Trends', *Proc. IEEE*, vol. 100, no. 2, pp. 410–426, Feb. 2012, doi: 10.1109/JPROC.2011.2156750.

[3] A. Godula-Jopek, *Hydrogen Production by Electrolysis*. Weinheim, Germany: Wiley-VCH Verlag GmbH & Co. KGaA, 2015.

[4] M. Schalenbach, W. Lueke, and D. Stolten, 'Hydrogen Diffusivity and Electrolyte Permeability of the Zirfon PERL Separator for Alkaline Water Electrolysis', *J. Electrochem. Soc.*, vol. 163, no. 14, pp. F1480–F1488, 2016, doi: 10.1149/2.1251613jes.

[5] R. Renaud and R. Leroy, 'Separator materials for use in alkaline water electrolysers☆', *International Journal of Hydrogen Energy*, vol. 7, no. 2, pp. 155–166, 1982, doi: 10.1016/0360-3199(82)90142-2.

[6] V. Rosa, 'New materials for water electrolysis diaphragms', *International Journal of Hydrogen Energy*, vol. 20, no. 9, pp. 697–700, Sep. 1995, doi: 10.1016/0360-3199(94)00119-K.

[7] V. Buršíková, J. Buršík, and J. Jan, *Surface Energy Evaluation of Plasma Treated Materials by Contact Angle Measurement*. Brno: Masaryk University, 2004.

[8] P. Vermeiren, W. Adriansens, J. P. Moreels, and R. Leysen, 'Evaluation of the Zirfon® separator for use in alkaline water electrolysis and Ni-H2 batteries', *Int. J. Hydrogen Energy*, vol. 23, no. 5, pp. 321–324, 1998.

[9] L. Xu, Y. Yu, W. Li, Y. You, W. Xu, and S. Zhang, 'The influence of manufacturing parameters and adding support layer on the properties of Zirfon® separators', *Front. Chem. Sci. Eng.*, vol. 8, no. 3, pp. 295–305, Sep. 2014, doi: 10.1007/s11705-014-1433-y.

[10] J. Friedrich, *The Plasma Chemistry of Polymer Surfaces: Advanced Techniques for Surface Design*. Weinheim, Germany: Wiley-VCH Verlag GmbH & Co. KGaA, 2012. doi: 10.1002/9783527648009.
[11] A. Ciszewski, I. Gancarz, J. Kunicki, and M. Bryjak, 'Plasma-modified polypropylene membranes as separators in high-power alkaline batteries', *Surface and Coatings Technology*, vol. 201, no. 6, pp. 3676–3684, Dec. 2006, doi: 10.1016/j.surfcoat.2006.08.146.
[12] S. Saxena, A. R. Ray, and B. Gupta, 'Graft polymerization of acrylic acid onto polypropylene monofilament by RF plasma', *J. Appl. Polym. Sci.*, p. NA-NA, 2010, doi: 10.1002/app.31823.
[13] Ľ. Staňo, M. Stano, and P. Ďurina, 'Separators for alkaline water electrolysis prepared by plasma-initiated grafting of acrylic acid on microporous polypropylene membranes', *International Journal of Hydrogen Energy*, vol. 45, no. 1, pp. 80–93, Jan. 2020, doi: 10.1016/j.ijhydene.2019.10.233.

SURFACE CLEANING OF ARCHEOLOGIC LEAD BY LOW PRESSURE PLASMA

František Krčma, Kateřina Bubnová

Faculty of Chemistry, Brno University of Technology, Purkyňova 118, 612 00 Brno, Czech Republic
E-mail: krcma@fch.vut.cz

The low-pressure hydrogen and argon-hydrogen plasmas application on corrosion products removal from metallic archeologic objects was used for the surface cleaning of silver and iron since 80's of the last century [1]. More recently, proper procedures for lower melting point materials such bronze were successfully developed [2, 3]. The presented contribution gives the first results obtained during the treatment of lead that is the most temperature sensitive metallic material used in human history.
To be able to observe influence of different treatment parameters, the model corrosion layers on lead surface were prepared with dual composition were prepared. The technical purity lead samples were put to desiccator with sand and organic acid. The samples corroded in environment of acetic acid or formic acid with the aim of creating the corrosion, which would be at least partially simulated with corrosion on the original artefacts. The corrosion process lasted for eleven months. After that, the samples were dried out under reduced pressure, put to the protecting foil with humid and oxygen absorbers. The low pressure RF plasma operating in continuous as well as pulsed regimes was created in pure hydrogen or hydrogen-argon mixture of different composition. Sample temperature was continuously monitored by special thermometer mounted on the sample surface; the optical data transfer was used to obtain related temperatures in RF electromagnetic field [3]. The plasma chemical treatment efficiency, i.e. removal of oxygen form the corrosion layers, was monitored by optical emission spectrometry of OH radical [3].
The samples surface was analysed by SEM, EDX, XRD methods to check the corrosion layers removal efficiency. Based on the obtained results, the optimal treatment conditions were proposed and successfully tested at treatment of original lead artefacts (recently excavated bullets from the battle at Hradec Králové in 1866).

References

[1] Vepřek S, Patscheider J and Elmer J Th 1985 *Plasma Chemistry and Plasma Processing* **5** 201.
[2] Fojtíková P, Řádková L, Janová D and Krčma F 2015 *Open Chemistry* **13** 362.
[3] Tiňo R, Vizárová K, Krčma F, Reháková M, Jančovičová V and Kozáková Z 2021 *Plasma Technology in the Preservation and Cleaning of Cultural Heritage Objects* CRC Press.

COLD ATMOSPHERIC PLASMA FOR PRESERVATION OF BREAD

Joanna Pawłat[1], Michał Kwiatkowski[1], Piotr Terebun1, Dawid Zarzeczny[1]
Agnieszka Starek[2]

[1]Instituite of Electrical Engineering and Electro technologies, Lublin University of Technology, Nadbystrzycka 38a, 20-618 Lublin, Poland
[2]Department of Biological Bases of Food and Feed Technologies of University of Life Sciences in Lublin, Głęboka 28, 20-612 Lublin, Poland
E-mail: askmik@hotmail.com

Cold atmospheric plasma was used for bakery products treatment. The aim of the work was to investigate the effect of the use of gliding arc discharge on the on basic physico-chemical properties and bread texture were determined during storage by 0, 3 and 6 days. Studies have been conducted for gluten-free and mixed wheat-rye bread treated by 2 and 10 minutes of CAP. A decrease in the moisture content of the bread accompanied by a significant increase in hardness and a slight springiness of the bread. was observed.

1. Experimental set-up

Two electrode, gliding arc discharge (GAD) reactor operated at atmospheric pressure was applied for the treatment of the bread samples [1,2]. Bread samples were cut in the cubes with dimensions of 15x15x15 mm and placed in the shallow open-batch glass container located under the GAD reactor's gas outlet in the vertical distance of 1 cm between the sample surface and electrode's tip. The photo and schema of the set up are presented in the Fig. 1.

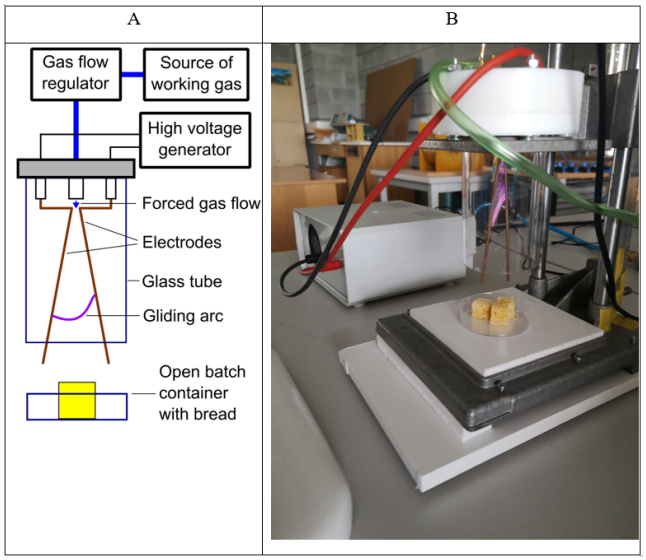

Figure 1. Experimental set-up (A-schema, B-photo)

After 2 min and 10 min plasma exposition the temperature of samples was measured using a DT-847U temperature meter with Type K thermocouple. All physicochemical analyses of bread were performed after 0, 3 and 6 days of storage. The protein content was determined using a Kjeltec apparatus and ASN 3100 software. Total fat was determined with the method on Soxtec apparatus. The moisture content of bread was determined according to the method of ICC (1996). The textural parameters of the bread crumb texture were determined by TPA test, with a double compressing a bread sample. During the measurements, the hardness and springiness were evaluated.

2. Results and conclusions

The treatment of both gluten-free and mixed wheat-rye bread with CAP has gradually reduced the moisture content, however, there were no significant differences in the moisture content of bread during storage of 0, 3 and 6 days stored in closed foil bags. The longer the plasma application time, the greater the increase in bread hardness. The use of plasma for 2 min resulted in a significant increase in bread hardness after three days of storage, but only by about 12%, while the use of plasma for 10 min increased the hardness of gluten-free bread by 28%. Much greater changes in hardness were observed in the case of mixed wheat-rye bread. The springiness of both the gluten-free bread and the mixed wheat-rye bread also increased.

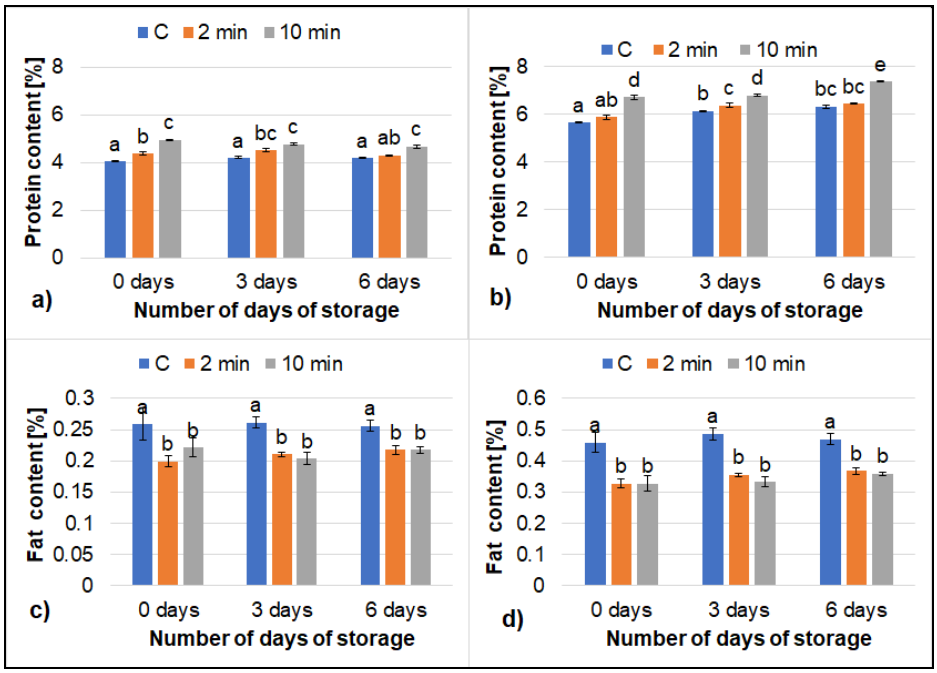

Figure 2. Protein (a-b) and fat (c-d) content of bread, a), c) gluten-free bread, b), d) mixed wheat-rye bread, mean values in the same figure marked with different letters are significantly (α=0.05) different

The use of plasma increased the percentage of protein in the bread (Fig.2.). For gluten-free bread, this value increased by about 8% after a 2-minute plasma application and by 23% after a 10-minute plasma application. In our study CAP treatment of bread reduced the fat content of the bread after just a 2 minute treatment time. There were no significant differences after 2 or 10 min of plasma treatment.

3. References

[1] Pawłat J, Terebun P, Kwiatkowski M Tarabová B, Kovaľová Z, Kučerová K, Machala Z, Janda M and Hensel K 2019 Plasma Chem Plasma Process **39** 627–642
[2] Starek A, Sagan A, Andrejko D, Chudzik B, Kobus Z, Kwiatkowski M, Terebun P, Pawłat J *Scientific Reports* **10(1)** 20959

Acknowledgement

We acknowledge fruitful discussions and scientific cooperation with members of CEEPUS CIII-AT-0063, COST Action PlAgri CA19110 and COST Action PlasTHER.

INFLUENCE OF PAW APPLICATION ON WATER AGGREGATE STABILITY OF SOIL – CONTAINER EXPERIMENT

Jana Šimečková[1], Jan Jedlička[1,] Fabián Voldán, Zdenka Kozáková[2], František Krčma[2]

[1]*Faculty of AgriSciences, Mendel University in Brno, Zemědělská 1, 613 00 Brno, Czech Republic*
[2]*Faculty of Chemistry, Brno University of Technology, Purkyňova 118, 612 00 Brno, Czech Republic*
E-mail: xsimecko@mendelu.cz

Plasma-activated water (PAW) has the potential to be used in a wide range of human activities. One of them is as fertilizer and protection of crops. However, sufficient knowledge about the potential impact of PAW application in agricultural practice on the environment is necessary. The paper presents a container experiment focused on the effect of PAW application on the water stability of soil aggregates.

1. Application of plasma-activated water in agriculture practice

Agriculture is currently filed of rapid changes caused by population pressure, which is based on reducing the impact on the environment or reacting to changes in climate conditions. This results in a change in sowing methods, a change in the cultivation system (e.g., introduction of no-till, cultivation of catch crops). There is also pressure to reduce inputs of mineral fertilizers as well as various hazardous chemicals and search for new means of plant protection that would be more environmentally friendly. Contemporary knowledge and recently published results indicate that plasma-activated water (PAW) could become a suitable alternative to replace mineral fertilizers (nitrate content) and additionally to reduce the input of plant protection agents (with bactericidal or fungicidal effects) [1, 2, 3].

However, it is necessary to appeal for an extensive and detailed investigation of the PAW direct application effect in the landscape on other components of the environment. One of them is the soil that PAW will land on when applied to plants. Although it will be a small amount, it can have a cumulative effect that can lead to permanent modify or even damage the soil properties. Recently, the narrow cooperation between the University of Technology in Brno and the Mendel University in Brno was established also in the field of the monitoring of PAW effect on various soil properties (pH value, conductivity, water sorption and retention, [4]). One among the monitored properties is the stability of soil aggregates. Aggregates are the particles of the soil attached together in clusters. They have various shapes (see Fig. 1.). Soil structure (basic unit aggregate of mm up to cm sizes) is extremely important property of any soil because determines pore space, content and transmission of air and water in soil, germination, seedling emergence, root growth, tillage, overland traffic, and erosion. In addition to the shape, the aggregates are evaluated according to their water resistance, which shows the resistance of the aggregates to the washing effect of water (low water resistance leads to higher manifestations of erosion). [5]

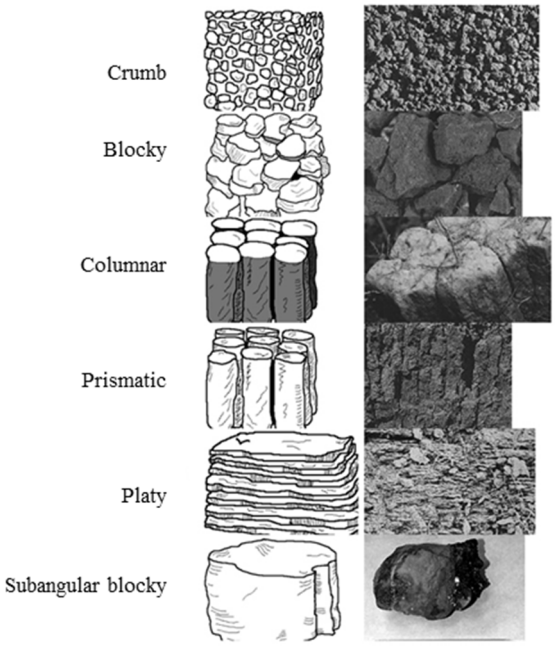

Fig. 1. Forms of soil aggregates. [6]

2. Effect of PAW application on water stability of soil aggregates

It is hypothesized that due to its composition, PAW could disrupt the stability of soil aggregates and thus contributes to the erosion increase.

Two PAWs with different composition (see Tab. 1.) were prepared and immediately applied on the soil. The first PAW was prepared using DBD discharge with liquid electrode according to procedure described in detail in [4]. Briefly, 75 ml of distilled water were treated by DBD plasma 8 times for 15 seconds. The second PAW was prepared by audio frequency (10 kHz) discharge generated directly in distilled water using our special electrode configuration [7, 8]. 500 ml of distilled water was treated for 5 minutes in this case.

Tab. 1. Characteristic of used treatment. [9]

Variant	cH_2O_2 ($mmol.l^{-1}$)	cNO_3^- ($mg.l^{-1}$)	cNO_2 ($mg.l^{-1}$)	pH	G ($\mu S.cm^{-1}$)
distilled water					2
PAW-AC	0,44	7,21	1,58	5,4	25
PAW-DBD	0,02	3,65	0,50	5,3	21

The laboratory experiment was carried out in pots (diameter 11 cm, height 9 cm) with a volume of 630 cm^3, in which dry natural chernozem (750 g, sieved by 10 mm) excavated at Polkovice (CZ, 49.3951167N, 17.2462244E) was placed. The individual pots were watered with distilled water/PAW-AC/PAW-DBD. The first dose was applied on the soil free surface in a volume of 300 ml (6times per 50 ml) in order to moisten the entire volume of the pot. Subsequently, a dose of 75 ml (3times per 25 ml) was applied on the soil free surface in steps of 3–4 days up to the end of experiment. The pots were placed in a closed dark room to avoid fast water evaporation. Every 14-days three pots of each variant were selected, and soil samples was taken from the upper third of the volume of each pot. It was assumed that the greatest influence of the applied liquid on the soil properties will be at the pot top part. Soil samples were dried by ambient air and sieved using 2 and 1 mm sieves. Thus, water resistance was determined using particles with size of 1–2 mm. Tab. 2. shows the total dose of the solutions (distilled water/PAW-AC/PAW-DBD) in individual sampling dates. Each treatment option and collection date was represented by 3 pots, as is written above.

Tab. 2. Dose of applied liquid (distilled water/PAW-AC/PAW-DBD) in sampling dates.

Date of sampling	Total dose of liquid (ml)
1.	525
2.	825
3.	1 125
4.	1 425
5.	1 725

Water resistance was determined by washing in distilled water (42 strokes/minute, [10]) in 4 repetitions for each pot. Therefore, 12 values were obtained from each measurement for each variant.
Fig. 2. presents the results of water resistance depending on the applied liquid for individual sampling dates. It can be seen a gradual decrease in the water resistance of soil aggregates in all variants with the duration of liquids application. The highest aggregates water resistance over time was shown for the variant treated with PAW-DBD, although the initial value (measured after 14 days) was the lowest of all the variants used. This variant had the highest water resistance of the soil aggregates at the end of the experiment (i.e., after a dose of 1 725 ml of the chemical). The remaining variants in this term had similar values. For all variants, it is possible to observe uneven changes in the water resistance of the aggregates about the amount of applied substance. For example, for samples watered with distilled water and PAW-AC, it is possible to observe an increase in the value in the 4th sampling compared to the 3rd sampling, but for the variant treated with PAW-DBD, the values remained the same.

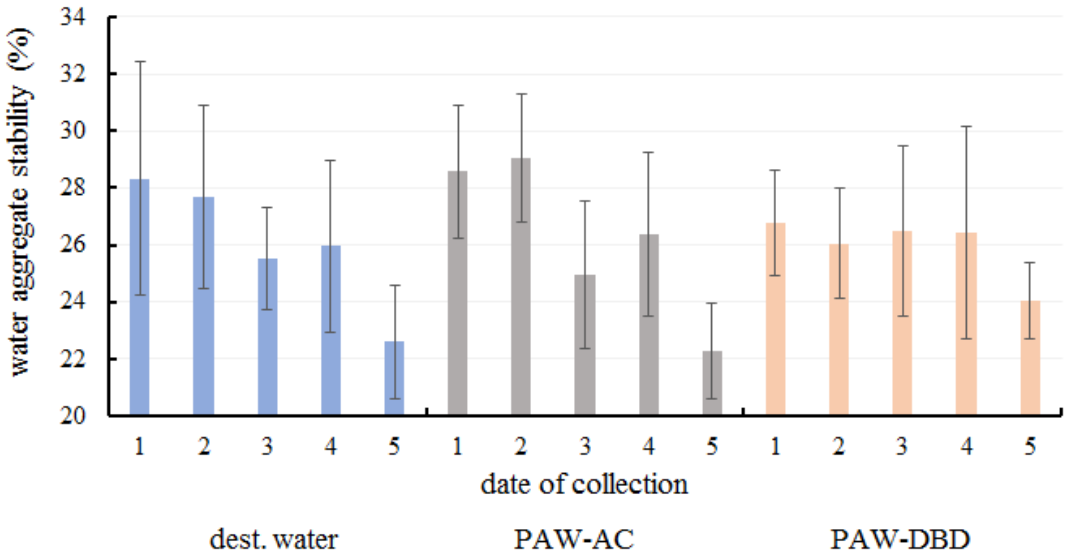

Fig. 2. Water aggregate stability after application of liquid (distillate water, PAW-AC, PAW-DBD) in different doses.

3. Conclusion

In this experiment, a high dose of PAW prepared by different plasma-liquid systems was deliberately applied to determine the possible effect on the soil environment, specifically the water resistance of soil aggregates. The results show that the huge application of PAW-AC and PAW-DBD should not have a negative effect on this soil property because they showed the same or even better water resistance values of soil aggregates than soil samples treated with distilled water (as control), which can simulate water in the form of rain.

Acknowledgement
This work was caused within COST Action CA19110.

4. References

[1] Hensel K, Kučerová K, Tarabová B, Janda M, Machala Z, Sano K, Mihai C T, Ciorpac M, Gorgan L D and Jijie R 2015 Effects of air transient spark discharge and helium plasma jet on water, bacteria, cells, and biomolecules. *Biointerphases* **10** 029515.
[2] Xu Z, Shen J, Zhang Z, Ma J, Ma R, Zhao Y, Sun Q, Qian S, Zhang H and Ding L 2015 Inactivation effects of non-thermal atmospheric-pressure helium plasma jet on Staphylococcus aureus biofilms. *Plasma Process. Polym*. **12** 827–835.
[3] Puac N, Gherardi M and Shiratani M 2018. Plasma agriculture: A rapidly emerging field. *Plasma Process. Polym.* **15**, e1700174.
[4] Šimečková J, Krčma F, Klofáč D, Dostál L a Kozáková Z 2020 Influence of Plasma-Activated Water on Physical and Physical-Chemical Soil Properties. Water **12** 2357-1-2357-13.
[5] Hillel D 2008 Soil in the Environment, crucible of Terrestiral Life. *Academic Press*, United Kingdom ISBN 978-0-12-348536-6
[6] General Structure types occurring in soils [online]. © 2022 [cit. 2023-01-19]. Available at: https://sagrainmag.co.za/2019/03/06/soil-the-producers-most-important-asset-oil-the-producers-most-important-asset-part-5-2-physical-properties-of-soil-structure/
[7] Krčma F 2019 *Method for plasma generation in liquids using jet system* patent EP3122161B1.
[8] Krčma F, Kozáková Z, Mazánková V, Horák J, Dostál L, Obradovic B, Nikiforov A, and Belmonte T 2018 Characterization of novel pin-hole based plasma source for generation of discharge in liquids supplied by DC non-pulsing voltage. *Plasma Sourc. Sci. Technol.* **27** 065001.
[9] Šindelková K 2022 *Characterization of plasma activated water for biomedical aaplications*, Master Thesis, Brno University of Technology, in Czech, p. 45.
[10] Kandeler E 1996: Aggregate stability. In: Schiner et al. (Eds.): *Methods in Soil Biology*. Berlin, Springer-Verlag, 426 pp.

PLASMA MODIFICATION OF METAL OXIDE NANOWIRES FOR ZN-AIR BATTERIES

Martin Müller[1,2], He Li[1], Christian Schulze[1], Sadekh Askari[1], Jan Benedikt[1]

[1] *Institute of Experimental and Applied Physics, Kiel University, Germany*
[2] *Institute of Physics, Czech Academy of Sciences, Prague, Czech Republic*
E-mail: mullerm@fzu.cz

Plasma treatment of substrates depends on the ion flux and energy. The vacuum chamber with inverted geometry, where the driven electrode has a significantly higher area than the grounded electrode/substrate holder, enables to measure of the energy and flux of ions coming to the substrate by a mass spectrometer.

The synthesis of modern nanostructured materials for electronic and photonic devices and sensors often requires plasma treatment of interfaces to modify or enhance their properties. Radio-frequency (RF) plasmas that are widely used for film synthesis or treatment can be used as a versatile source of ions with energies that can be tuned exactly to reach the activation energy of desired processes (e.g. doping or creating active sites on the surface) and keep the material otherwise unharmed.
We use the combination of a capacitively coupled RF plasma (CCP) with an inductively coupled plasma (ICP) to tune the energy of nitrogen ions in the range of units to tens of electronvolts to modify the catalytic substrates for batteries such as hydrothermally grown films with $NiCo_2O_4$ nanowires. This substrate is being used as an electrode in Zn-air batteries. Nitrogen doping is being considered to improve the electric conductivity of metal oxide nanostructures and therefore should lead to better electrocatalytic activity. Unlike the wet chemical treatment with nitrogen-containing precursors, the plasma treatment does not require high-temperature annealing and avoids chemical contamination.
We study the nitrogen ion flux and energy for various settings of ICP and CCP plasma source, as shown in Figure 1, and the effect of such a nitrogen plasma treatment on the cycling performance of a Zn-air battery with a $NiCo_2O_4$ electrode using cyclic voltammetry, oxygen evolution reaction (OER) and oxygen reduction reaction (ORR). After treatment with a nitrogen plasma, the electrodes show better OER and ORR performance, a faster reaction rate constant, and a higher double-layer capacitance indicating the increase of the active surface area.

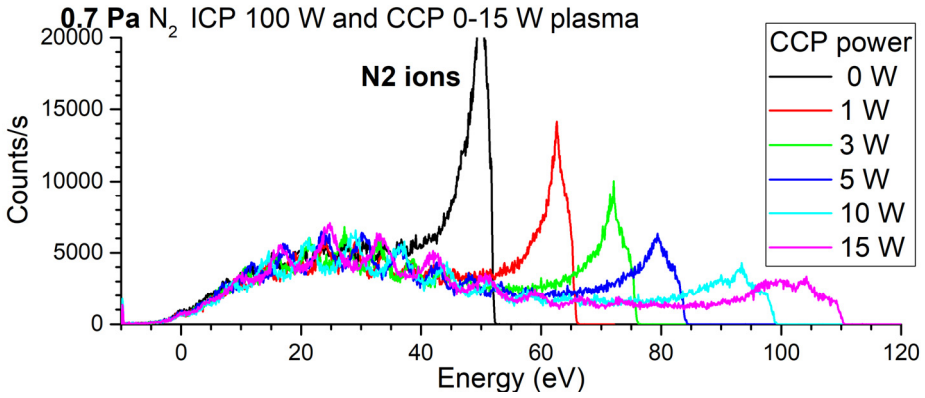

Fig. 1. The energy distribution of N_2 ions in an ICP plasma measured for various biases of substrate electrode provided by tuning of CCP power.

References

[1] Schulze, C.; Li, H.; Mohn, L.; Müller, M.; Benedikt, J. Plasma 2022, 5, 295-305. https://doi.org/10.3390/plasma5030023
[2] Wild, C.; Koidl, P. Appl. Phys. Lett. 1989, 54, 505–507. https://doi.org/10.1063/1.100913
[3] L. Xu, Q.Q. Jiang, Z.H. Xiao, X.Y. Li, J. Hao, S.Y. Wang, L.M. Dai, Angew. Chem. Int. Edit., 2016, 55, 5277-5281. https://doi.org/10.1002/ange.201600687

COMPARISON OF CONTINUOUS AND PULSED LOW POWER DC SPUTTERED TI THIN FILMS

Anna Maria Reider[1], Ariane Kronthaler[1], Felix Laimer[1], Fabio Zappa[1], Masoomeh Mahmoodi-Darian[1,2] , Paul Scheier[1]

[1]*Institute of Ionphysics and Applied Physics, University of Innsbruck, Technikerstr. 25/3, 6020 Innsbruck, Austria*

[2]*Department of Physics, Karaj Branch, Islamic Azad University, Karaj, Iran*

E-mail: anna-maria.reider@uibk.ac.at; masoomeh.mahmoodi@uibk.ac.at

In this work, titanium thin films with thicknesses up to 105 nm were deposited on borosilicate glass implementing low power continuous (25 W) and pulsed (85 W) DC magnetron sputtering. The characteristics of the resulting films were studied via atomic force microscopy (AFM), X-Ray Photoelectron Spectroscopy (XPS), VIS spectroscopy and four-point-probe measurements. For both the continuous and pulsed sputtering, the films exhibit a comparably low surface roughness with no visible column-and-void structure. Additionally, the films show overall high reflectivity and constant transmission and reflectance for wavelengths in the visible range of the spectrum. The electric resistivity could be measured even for film thicknesses down to the single nanometer range and approaches the bulk value for higher film thicknesses. The low power regime of magnetron sputter deposition does not only offer the possibility of studying the development of physical characteristics during the growth of ultra-thin films but also provides the advantage of extremely low heat development and no mechanical force on the substrate during the coating process. This concept may hence be utilized in temperature-sensitive coating processes, such as the fabrication of conductive coatings on flexible antennas.

MASS SPECTROMETRY OF LARGE ASYMETRICAL CCP OXYGEN DISCHARGE

Nevena Puač[1], Kosta Spasić[1], Nikola Škoro[1], Gordana Malović[1] and Zoran Lj. Petrović[2]

[1]*Institute of Physics, University of Belgrade, Pregrevica 118, 11080 Belgrade, Serbia*
[2]*Serbian Academy of Sciences and Arts, Knez Mihailova 35, 11000 Belgrade, Serbia*
E-mail: nevena@ipb.ac.rs

We present the results of mass spectrometry of large asymmetrical CCP discharge. The discharge operated at 13.56 MHz with oxygen as working gas at the pressures of 300 mTorr, 450 mTorr and 600 mTorr. Threshold Ionization Mass Spectrometry (TIMS) was used to detect excited and metastable oxygen molecules and oxygen atoms.

1. Introduction

Motivation for research of non-thermal low pressure plasmas stems from wide range of possible applications. Due to the possibility of fine tuning of the discharge conditions and ability of the reactive species from the discharge to modify and activate surfaces, low pressure plasmas are being exploited for a long time for applications in fabrication of microelectronic devices, in textile industry, sterilization of medical equipment, cleaning of archaeological samples, nitriding of metals etc. Lately this lists has expanded in the field of plasma agriculture for treatment of seed to increase germination, plant yield or to remove pathogens. In order to satisfy various demands in many different applications in which plasma is used various types of plasma reactors had to be developed.

It is already known that reactive oxygen species (ROS) play important role in metabolism of plants with most of them being also the signalling molecules. [1, 2]. Since ROS are easily created in oxygen containing discharges the effects of these plasmas on plants metabolism is increasingly being studied for discharges in both atmospheric and low pressures [2, 3]. In order to make the first steps towards identifying the mechanisms responsible for triggering of signalling pathways in the treated seeds it is important to determine chemistry produced in the plasma. Here we will present results of mass spectrometry of the oxygen low pressure discharge in the large asymmetric CCP chamber.

2. Experimental setup and results

A cylindrically shaped reactor chamber was made of stainless steel. The length of the chamber was 2.5 m with the diameter of 1.17 m. Axially placed aluminium rod served as a powered electrode while the chamber wall was used as a grounded electrode. The power supply unit operated at 13.56 MHz and it was equipped with Variomatch matching network for reducing reflected power. In all measurements the reflected power was kept below 1 % of the forwarded power. Vacuum was achieved by mechanical Pfeiffer Vacuum rotary vane pump. We have used mixture of 99% of O_2 with 1% of Argon added. Flow meters were used to control flow of each gas, in appropriate proportion, so that pressure could be set to selected values of 300, 450 and 600 mTorr. Mass energy HIDEN Analytical EQP analyser was used for mass and energy measurements of plasma species. It was introduced into the chamber side-on, perpendicular to the powered electrode, with its orifice positioned at fixed distance of 31.5 cm from powered electrode. For the detection of neutral species we have used RGA (residual gas analysis) mode. The mass spectra of neutral species was recorded for the range 1 amu to up to 50 amu. In order to determine the amount of oxygen excited and metastable species created in the discharge we have also performed Threshold Ionization Mass Spectrometry (TIMS). We have done this type of measurements for oxygen molecules and atoms with electron energy varied from 4 to 25 eV with resolution of 0.1 eV. In Figure 1(a). Distribution of O_2^+ as a function of the electron energy emitted from the ionising source of the mass spectrometer is shown. We can see that for lower powers there are no excited and metastable species detected by the mass spectrometer.

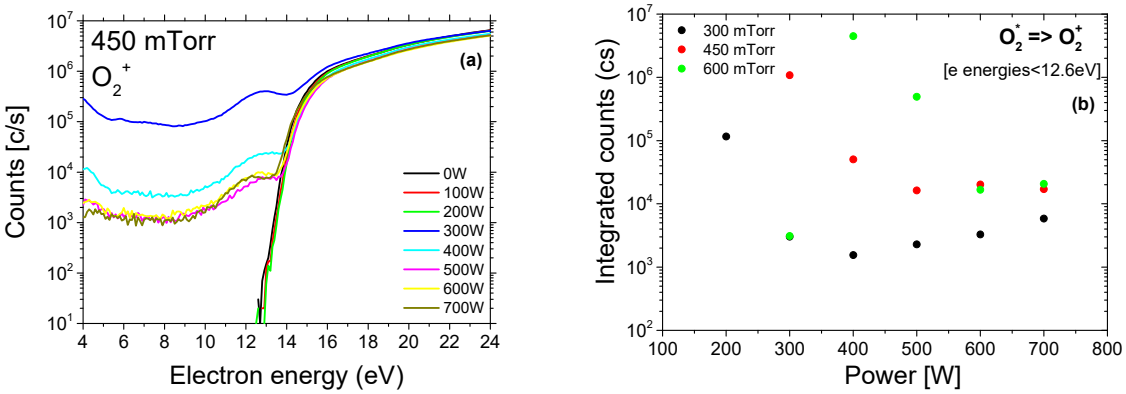

Figure 1. (a) Distribution of O_2^+ molecule detected by mass spectrometer as a function of energies of electrons emitted by analyser's ionising source. (b) Number of excited and metastable O_2 species detected by mass spectrometry as a function of power given by RF power supply.

In Figure 1(b) we present integrated counts obtained by ionizing excited and metastable oxygen molecule coming for the discharge. The integration of the mass spectrometer signals (shown in Figure 1(a)) was performed from 4 eV to 12.5 eV. We have used this range of energies in order to be below the ionization threshold for the neutral oxygen molecule. The maximum of detected excited and metastable oxygen molecules moves towards higher powers given by the RF power supply with the increase of the working pressure. This can be explained by the decrease in the mean free path of the species and the position of the mass spectrometer orifice. Also, with the increase of the power plasma expands towards the wall of the chamber.

3. Conclusion

We have presented the mass spectrometry results obtained in a large asymmetric CCP low pressure oxygen discharge. The mass spectrometry was used to detect reactive oxygen species with the emphasis on the excited and metastable species. We have used TIMS to determine the behaviour and abundance of metastable and excited oxygen molecule and oxygen atoms.

Acknowledgement: This work was supported by MSTDI Republic of Serbia grant number 451-03-68/2022-14/200024 and NOWELTIES project - EU H2020 MSCA ITN No. 812880.

4. References

[1] Bailly C 2004 *Seed science research* **14** 93-107.
[2] Graves D B 2012 *J. Phys. D: Appl. Phys.* **45** 263001 (42pp).
[3] Puač N, Škoro N, Spasić K, Živković S, Milutinović M, Malović G and Petrović ZLj 2018 *Plasma Processes and Polymers* **15** 1700082.

ATMOSPHERIC PRESSURE CHEMICAL IONIZATION STUDY OF SULPHUR-CONTAINING COMPOUNDS BY ION MOBILITY SPECTROMETRY AND MASS-SPECTROMETRY

Ladislav Moravský[1,2], Arian Fateh Borkhari[1], Štefan Matejčík[1,2], Alexey Yu. Adamov[2], Alexey A. Sysoev[2]

[1]*Department of Experimental Physics, Comenius University in Bratislava, 84248 Bratislava, Slovakia*
[2]*Molecular Physics Department, National Research Nuclear University, Moscow Engineering Physics Institute, 115409 Moscow, Russia*
E-mail: ladislav.moravsky@fmph.uniba.sk

To study the atmospheric pressure chemical ionization of selected sulphur-containing hydrocarbons (Thiophene C_4H_4S, 2-Methyl thiophene C_5H_6S, 2,5-Dimethyl thiophene C_6H_8S, Benzothiophene C_8H_6S and 2-Methyl benzothiophene C_9H_8S) in positive polarity the ion mobility spectrometry (IMS) and IMS combined with time-of-flight mass spectrometer (IMS-TOF MS) techniques were used in the dry air at 373 K drift gas temperature. The dominant ionization reaction was the direct proton transfer while the ionization was performed using the $H_3O^+(H_2O)_{3,4}$ reactant ions (RIs). The ionization resulted in the appearance of $M.H^+$ ions for all substances except for Thiophene which forms M^+ and $M.NO^+$ ions. The limit of detection for all studied compounds was calculated.

1. Introduction

One of the affordable and reliable energy resources which are currently considered are petroleum oils from fossil-based materials [1]. The molecular mixture in petroleum is mostly comprised of different categories of hydrocarbons (alkanes, naphthenes, and aromatic compounds) with five- or six-carbon member rings and polar compounds. The main unfavourable impurity in petroleum oils is the presence of polar compounds containing hetero-atoms which are mostly composed of nitrogen, oxygen, and sulphur-containing species. To reach better quality of petroleum all these compounds must be removed, or their quantities reduced [2-4]. In crude oil, one of the most abundant constituents are sulphur-containing compounds such as thiols and heterocyclic compounds, and their detailed structural characterization is of particular interest. In some cases, the content of sulphur in crude oil can be as high as 10% [5]. The petroleum analysis is quite difficult due to sulphur-containing compounds which exhibit high reactivity, absorptivity, and adsorptivity. These components are also mainly responsible for catalyst poisoning and the corrosion of petroleum pipelines [6]. In the oil industry, their better identification and reduction could be helpful to achieve a higher quality of oil, as well as cheaper transportation processes and cost reduction achieved for refining. Besides that, sulphur-containing compounds have implications regarding environmental and human health presenting high exposure risk factors [4]. The main goal of present work is the detection and identification of five selected sulphur-containing hydrocarbons at sub-atmospheric pressure by IMS-MS at positive polarity. We are focusing on identification of the nature of positive ions and designating the limit of detection of all studied compounds.

2. Experimental part

In this work, the homemade ion mobility spectrometer (IMS) (Figure 1) with an atmospheric pressure chemical ionisation (APCI) source based on corona discharge (CD) has been used. The technical properties of the IMS are presented in Table 1. During measurements, the IMS was operated in the positive polarity mode and at sub-atmospheric pressure (680 mbar) due to simple sampling of volatile organic compounds by the capillary inlet. The sample flow rate was controlled by a micro-splitter valve (Supelco) and adjusted by a gas flow meter (Platon). As a drift gas in IMS, a laboratory air cleaned by our self-designed circulation vacuum system with additional moisture traps (Agilent) and containers filled with activated carbon and potassium permanganate-impregnated activated alumina spheres (Alphasorb) was used.

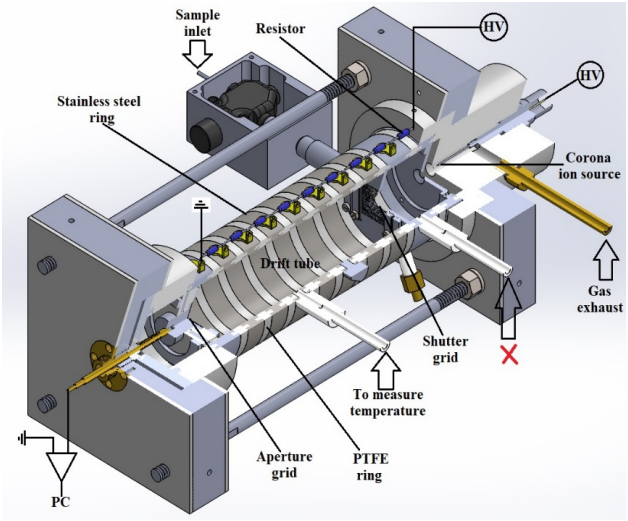

Fig. 1. Scheme of the IMS spectrometer: The described IMS was operated in reverse gas flow mode.

Tab. 1. Parameters of IMS used in the experiment.

Operating Parameters	Unit
IMS drift tube length	11.9 cm
Electric field intensity	672 $V.cm^{-1}$
IMS operating pressure	680 mbar
IMS operating temperature	373 K
Drift gas flow	800 $mL.min^{-1}$
Sample gas flow	10 $mL.min^{-1}$
CD current	10 µA
Shutter grid pulse width	80 µs
Shutter grid frequency	50 Hz

The vapours of the investigated compounds were introduced into the reaction region of the IMS through a sample inlet. The thiophenes were placed in a glass syringe (about 3 mg, 1 drop) to determine the LOD value. To achieve an equilibrium between the gas and the liquid phase we waited at least 20 minutes. Afterward, the syringe was connected via capillary with the sample inlet and using a syringe pump (Kent Scientific), the sample was introduced into the reaction region of the IMS with a pre-set flow rate. The reactant ions (RI) generated in CD were $H_3O^+ (H_2O)_n$ (n=2,3) and in a very low concentration $NO^+(H_2O)_n$ (n=2,3). The IMS has been operated in reverse gas flow mode.

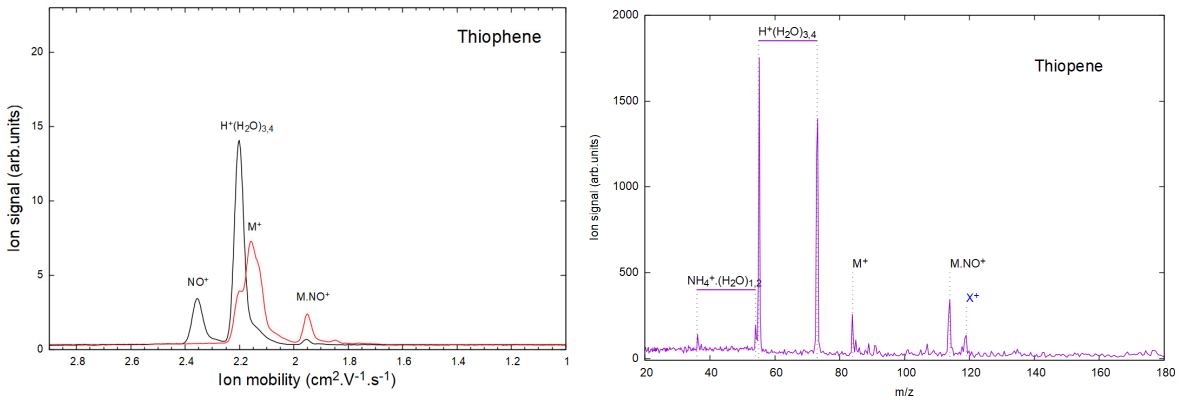

Fig. 2. The positive IMS and the MS spectrum of Thiophene at 373K.

Figure 2 shows the positive IMS and MS spectra of the ambient air with Thiophene at 373K. In the IMS spectrum the Thiophene has two strong peaks at K_0 = 2.15 $cm^2.V^{-1}.s^{-1}$ and K_0 = 1.95 $cm^2.V^{-1}.s^{-1}$ which correspond to monomer ions of sample M^+ and $M.NO^+$ respectively confirmed by MS spectrum with ion mass m/z = 84 and 114. The other investigated compounds form mainly ions with H^+. The limit of detection for all investigated compounds was under 2.2 ppm.

Acknowledgments

The presented research was partially supported by Slovak grant agency VEGA within the project nr. 1/0489/21, by Slovak Research and Development Agency within project nr. APVV-19-0386 and APVV-17-0318.

3. References

[1] Acter, T., Solihat, N.N., Kim, S. et al. Application of silver-assisted laser desorption ionization ultrahigh-resolution mass spectrometry for the speciation of sulfur compounds. *Anal Bioanal Chem* **412,** 243–255 (2020).
[2] Li, S.-m.; Pang, X.-q.; Jin, Z.-j.; Li, M.-w., Characteristics of NSO compounds in sediment and their geochemical significance. *Diqiu Huaxue* 2001, **30** (4), 347-352.
[3] Farrington, J. W.; Quinn, J. G., Petroleum hydrocarbons in Narragansett Bay. I. Survey of hydrocarbons in sediments and clams. (Mercenaria mercenaria). *Estuarine Coastal Mar. Sci*. 1973, **1** (1), 71-9.
[4] Hossein Maleki, Samaneh Ghassabi Kondalaji, Mahdiar Khakinejad, and Stephen J. Valentine Structural Assignments of Sulfur-Containing Compounds in Crude Oil Using Ion Mobility Spectrometry-Mass Spectrometry Energy & Fuels 2016 **30** (11), 9150-9161
[5] Hua, R. X.; Wang, J. H.; Kong, H. W.; Liu, J.; Lu, X.; Xu, G. W., Analysis of sulfur-containing compounds in crude oils by comprehensive two-dimensional gas chromatography with sulfur chemiluminescence detection. Journal of Separation Science 2004, **27** (9), 691-698
[6] Liu, J.-p.; Deng, W.-a., Corrosion problems caused by high sour and acid crude oil processing and corrosion inhibition countermeasures. Shandong Huagong 2010, **39** (4), 44-49.

DETECTION OF NO_2 GENERATED BY APPJ IN ARGON USING IMS

Emanuel Maťaš[1], Ladislav Moravský[1], Martin Sabo[2], Štefan Matejčík[1]

[1]*Department of Experimental Physics, Comenius University, Mlynská dolina F2, 84245 Bratislava, Slovakia*

[2]*MaSa Tech s.r.o., Sadová 3018/10 91501 Stará Turá, Slovak Republic*

E-mail: emauel.matas@fmph.uniba.sk

Ion mobility spectrometry (IMS) was applied for detection of NO_2 generated by the kHz driven DBD atmospheric pressure plasma jet (APPJ) in Ar. The reactive oxygen and nitrogen species are efficiently generated in the APPJ, which are widely used in various biological and technological applications. The efficient detection of these species is of great importance for many fields of science and engineering. Using IMS, we achieved fast and sensitive detection of NO_2 with the limit of detection of 200 ppb. The highest production of NO_2 (3.7 ppm) generated by APPJ was achieved at Ar flow rate of 100 mL/min.

1. Introduction and Methodology

Reactive oxygen and negative species (RONS) play an important role in many biochemical, physiological, and pathological processes. Some of RONS like O_3, OH, NO_2, NO_3, N_2O_5 etc can be generated using atmospheric pressure plasma jet (APPJ) in Argon. The production of controlled RONS by the APPJ is frequently used in the fields of biomedicine for wound healing, cancer treatment, immune cell activation [1–4] surface treatment and sterilization [5]. Several techniques are used to diagnose RONS, Fourier-transform infrared (FTIR) spectroscopy, chemical and semiconductor gas sensors etc [6,7]. In present study, we applied ion mobility spectrometry (IMS) as a new method for diagnosis of NO_2 generated by the APPJ.

The IMS is very fast (ms – s range), highly sensitive (ppb – ppt level), and powerful analytical technique based on the measurement of the mobility in gaseous environment and presence of electric field [8–10]. The IMS instrument consisting of several parts, the ion source, the reactive region, the shutter grid, the drift tube and the detector [8]. The IMS can be used for direct sampling of gaseous substances, for headspace sampling of vapours of liquids and also for thermal or laser desorption of substances from surfaces. It can be applied for monitoring of the ambient air or for online monitoring of different plasma processes producing neutral molecules. The spectrometer can be operated in both positive and negative polarity. The corona discharge is usually used as a source of reactant ions (RI) (H_3O^+ in positive and O_2^- CO_2 in negative polarity). The RI are further used to ionise the neutral particles of sample injected into the reactive region. The NO_2 and other RONS can be detected in negative mode polarity.

Detection of NO_2 was carried out for the APPJ developed at the Department of Experimental Physic at Comenius University Bratislava [11]. APPJ plasma was generated in a glass capillary with an internal diameter of 0.5 mm by a hollow needle electrode. The Ar (purity 4.6, Hastex spol. s.r.o., Slovakia) flow through the needle at flow rates 50, 100 and 200 mL/min. The high voltage of 3.5 kV amplitude and frequency 10 kHz was applied to the needle electrode. The other electrode of cylindrical geometry, located outside of the glass capillary was grounded. The IMS used in this study for monitoring of NO_2 generated by the APPJ was developed by MaSa Tech Company (Slovakia). The electric field intensity in the drift tube of IMS was 547.6 $V.cm^{-1}$, drift gas flow was set to 700 mL/min. The IMS drift tube was operated at a pressure 700 mbar and temperature 373K. The sample flow of IMS was set to 20 mL/min.

2. Results and Discussion

Prior the experiments, the IMS was calibrated for NO_2 detection. A standard mixture (100 ppm NO_2 diluted in N_2, Messer Tatragas s.r.o., Slovakia) was used for the calibration process. The standard mixture was further diluted to concentrations in range of 0.1 – 20 ppm by Ar using mass flow controllers (MKS Instruments, Inc.). The dilution of the NO_2 standard by Ar was related to the APPJ.

The IMS spectra for different concentration of NO_2 are presented in Figure 1. The signal intensity of the 2.49 $cm^2.V^{-1}.s^{-1}$ peak depends on the concentration of NO_2 in the mixture. The RI were used for ionisation of NO_2, therefore the intensity of the RI peak decreases with increasing NO_2 concentration. On the other hand, the intensity of the NO_2^- was increasing with increasing NO_2 concentration. The ionization of neutral NO_2 species was carried out using the negative chemical ionization method, with RI:

$$O_2^- \cdot CO_2 \cdot (H_2O)_{0,1,2} + NO_2 \rightarrow NO_2^- + O^2 + CO_2 + n\,H_2O \quad (1)$$

The electron transfer reaction ionizes molecules with electron affinities, exceeding the bond energy of the electron in the reactant ions $O_2^-{\cdot}CO_2{\cdot}(H_2O)_{0,1,2}$, which is about 1.36 eV [12]. This condition is valid for NO_2 (electron affinity of NO_2 is 2.273 eV [13]). The dependence of RI and NO_2^- intensities on NO_2 concentration are plotted in Figure 2. The linearity of the NO_2^- scale was observed below 5 ppm. The limit of detection for the NO_2 detection is about 200 ppb. At low NO_2 concentrations, the NO_2^- background was observed, related to the NO_2 generated in the CD.

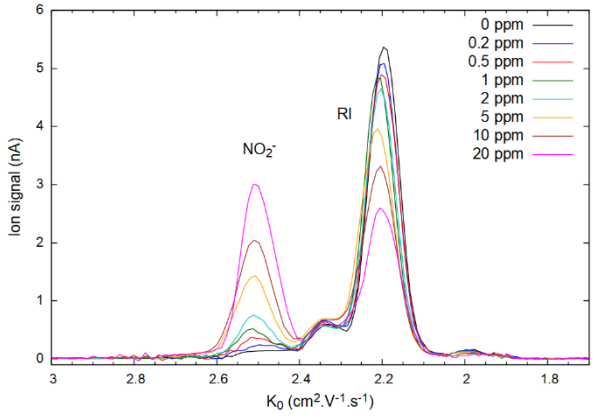

Fig. 1. The IMS spectra of NO_2 standard mixtures for different concentrations.

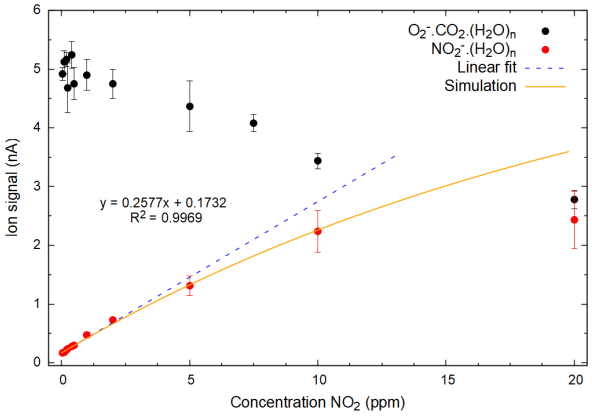

Fig. 2. RI and NO_2^- intensities for NO_2 mixtures (0 – 20 ppm). Linearity range 0.2 – 5 ppm (blue dashed line). Calculated NO_2^- intensities (yellow line) using rate coefficient 0.97 $cm^3.s^{-1}$.

In the plasma generated by the APPJ in Ar many reactive species are formed (e, Ar^+, exited Ar), of which the metastable states of Ar (Ar*) are very important, as their life time in the plasma jet is long. The excitation energy of Ar* is 11.6 eV [14]. Ar* undergoes dissociative reaction with N_2, O_2 or H_2O [15]. These gases are sucked into the Ar plasma beam from air. The NO_2 can be formed via following reactions [15–17].

$$O + O_2 + M \rightarrow O_3 + M \quad (2)$$

$$N + OH \rightarrow NO + H \quad (3)$$

$$NO + O_3 \rightarrow NO_2 + O_2 \quad (4)$$

The negative polarity IMS spectrum of the Ar following through the APPJ (on discharge) is presented in Figure 3 (black line). The dominant peak with reduced ion mobility of 2.20 $cm^2.V^{-1}.s^{-1}$ is assigned to RI ($O_2^-.CO_2.(H_2O)_{0,1,2}$) formed in the IMS. After applying AC (10 kHz) high voltage power to the needle, the APPJ plasma was generated, and its products were detected by the IMS (Figure 3 red line). The intensity of RI depends strongly on the concentration of electronegative species in the plasma. With the increasing of the discharge power, the concentration of the electronegative species is increasing and the RI intensity is rapidly decreasing and four new peaks with reduce mobilities 2.49, 2.24, 2.18 and 1.93 $cm^2.V^{-1}.s^{-1}$ appear in the IMS spectrum. These ion mobilities were assigned by mass spectrometry method to NO_2^-, NO_3^-, $N_2O_3^-$ and $NO_3^-.(HNO_3)$. In this study, we have focused on the first peak (ion mobility 2.49 $cm^2.V^{-1}.s^{-1}$), related to NO_2.

In present work the formation of NO_2 in the APPJ was studied for different Ar gas flows (50, 100 and 200 mL/min). The highest voltage amplitude was kept constant for all flows. The NO_2 intensity in the gas was measured for different distance between the APPJ outlet and the IMS inlet (separation 2 to 100 mm). In the Figure 4 we display the dependence of the NO_2 concentration as a function of APPJ-IMS separation for tree different Ar gas flows. The highest concentrations of NO_2 3.3 ± *0.09*, 3.7 ± *0.1*, and 2.9 ± 0.12 ppm were observed at shortest distance (2 mm) for gas flows 50, 100 and 200 mL/min, respectively. The present results yield values comparable to those of *Adhikari et al.*, who measured a concentration of 3.1 ppm at an AC voltage of 4 kV @ 28 kHz and an Ar flow of 350 mL/min [4]. The concentration of NO_2 decreases with the increasing APPJ-IMS distance. This can be due to losses of NO_2 from the gas flow into the surrounding environment.

The highest NO_2 concentration was observed for Ar flow rate 100 mL/min, the lowest productions was recorded at a flow rate of 200 mL/min. Most probably the discharge power density (ratio of applied voltage to flow rate) is important parameter for the production of NO_2. Substantial changes of NO_2 concentration are visible in the separation rage 2 to 50 mm. At larger distance (up to 100 mm) the production of NO_2 concentration is stable (~ 0.5 ppm).

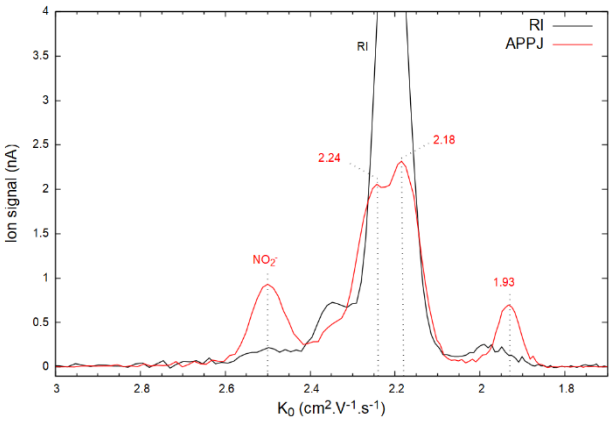

Fig. 3. IMS spectra of reactant ions (RI) and APPJ generated in Ar at 3.5 kV @ 10 kHz, 50 mL/min gas flow and 2 mm distance.

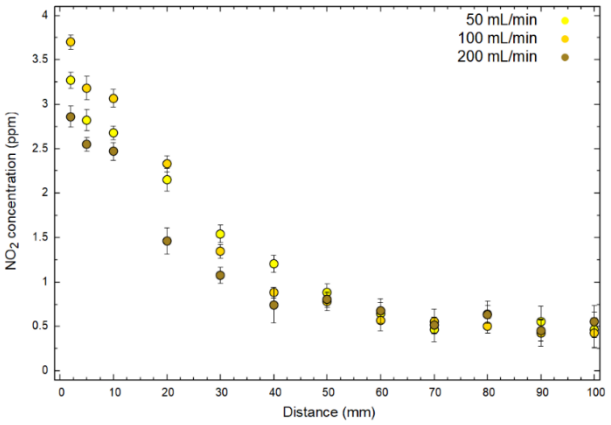

Fig. 4. Evaluation of axial concentration of NO_2 for distances 2 to 100 mm from the APPJ.

3. Conclusion

In this study we applied IMS for NO_2 detection generated by the APPJ in Ar. The value of reduced ion mobility for NO_2^- was 2.49 $cm^2.V^{-1}.s^{-1}$. The calibration of the linear scale using an NO_2 standerd indicated linearity of the method in the range 0.2 to 5 ppm. The NO_2 concentration was measured as a function as Ar gas flow and APPJ-IMS distance for constant high voltage amplitude (3 kV) of 10 kHz voltage power supply. The highest production of NO_2 for each flow rate was achieved at distance 2 mm, where NO_2 could achieve concentration up to 3.7 ppm NO_2. In the future we plan to study influence of more parameters on NO_2 production (discharge power, gas flow, axial and radial profiles and admixture of small amount of N_2, O_2 into Ar gas). We plan as well to detect additional produce of the APPJ NO_3, N_2O_3, $NO_3(HNO_3)$.

Acknowledgments. The present studies were supported by the Slovak Grant Agency for Science VEGA Nr. 1/0489/21, Slovak Research and Development Agency under project Nr. APVV-19-0386 and SK-SRB-21-0004

4. References

[1] Brandenburg R, Lange H, von Woedtke T, Stieber M, Kindel E, Ehlbeck J and Weltmann K D 2009 Antimicrobial effects of UV and VUV radiation of nonthermal plasma jets *IEEE Transactions on Plasma Science* **37** 877–83

[2] Laroussi M 2015 Low-Temperature Plasma Jet for Biomedical Applications: A Review *IEEE Transactions on Plasma Science* **43** 703–12

[3] Moravský L, Klas M, Machová E, Pisklová K and Matejčík Š 2015 Influence of a plasma jet on the viability of Candida albicans *Open Chem* **13** 257–62

[4] Adhikari B C, Lamichhane P, Lim J S, Nguyen L N and Choi E H 2021 Generation of reactive species by naturally sucked air in the Ar plasma jet *Results Phys* **30**

[5] Penkov O v., Khadem M, Lim W S and Kim D E 2015 A review of recent applications of atmospheric pressure plasma jets for materials processing *J Coat Technol Res* **12** 225–35

[6] Yi H, Cazaunau M, Gratien A, Michoud V, Pangui E, Doussin J F and Chen W 2021 Intercomparison of IBBCEAS, NitroMAC and FTIR analyses for HONO, NO2 and CH2O measurements during the reaction of NO2 with H2O vapour in the simulation chamber CESAM *Atmos Meas Tech* **14** 5701–15

[7] Fischer S, Pohle R, Farber B, Proch R, Kaniuk J, Fleischer M and Moos R 2010 Method for detection of NOx in exhaust gases by pulsed discharge measurements using standard zirconia-based lambda sensors *Sens Actuators B Chem* **147** 780–5

[8] Eiceman G A and Karpas Z 2005 *Ion Mobility Spectrometry* vol 350 (CRC Press)

[9] Sabo M, Páleník J, Kučera M, Han H, Wang H, Chu Y and Matejčík Š 2010 Atmospheric Pressure Corona Discharge Ionisation and Ion Mobility Spectrometry/Mass Spectrometry study of the negative corona discharge in high purity oxygen and oxygen/nitrogen mixtures *Int J Mass Spectrom* **293** 23–7

[10] Sabo M and Matejčík Š 2012 Corona discharge ion mobility spectrometry with orthogonal acceleration time of flight mass spectrometry for monitoring of volatile organic compounds *Anal Chem* **84** 5327–34

[11] Horváth G, Moravský L, Krčma F and Matejčík Š 2013 Characterization of a low-cost kilohertz-driven plasma pen operated in Ar gas *IEEE Transactions on Plasma Science* **41** 613–9

[12] Moravský L, Borkhari A F, Adamov A Y, Sysoev A A, Papp P and Matejčík Š 2022 Negative Atmospheric Pressure Chemical Ionization of Chlorinated Hydrocarbons Studied by Ion Mobility Spectrometry (IMS) and IMS-MS Techniques *J Am Soc Mass Spectrom* **33** 1569–76

[13] P.J. Linstrom and W.G. Mallard 2022 NIST Chemistry WebBook, NIST Standard Reference Database Number 69

[14] Nayak G, Simeni Simeni M, Rosato J, Sadeghi N and Bruggeman P J 2020 Characterization of an RF-driven argon plasma at atmospheric pressure using broadband absorption and optical emission spectroscopy *J Appl Phys* **128**

[15] Schmidt-Bleker A, Winter J, Bösel A, Reuter S and Weltmann K D 2015 On the plasma chemistry of a cold atmospheric argon plasma jet with shielding gas device *Plasma Sources Sci Technol* **25**

[16] Atkinson R, Baulch D L, Cox R A, Hampson R F, Kerr Chairman J A and Troe J 1989 Evaluated Kinetic and Photochemical Data for Atmospheric Chemistry: Supplement III. IUPAC Subcommittee on Gas Kinetic Data Evaluation for Atmospheric Chemistry *J Phys Chem Ref Data* **18** 881–1097

[17] Kossyi I A, Kostinsky A Y, Matveyev A A and Silakov V P 1992 Kinetic scheme of the non-equilibrium discharge in nitrogen-oxygen mixtures Related content Kinetic scheme of the *Plasma Sources Sci Technol* **1** 207–20

DISSOCIATIVE ELECTRON ATTACHMENT TO FLUORO-, CHLORO-, AND BROMOSILANES

Peter Papp[1], Bartosz Michalczuk[2], Dušan Mészáros[1], Barbora Stachová[1], Wiesława Barszczewska[2], Štefan Matejčík[1]

[1]*Department of Experimental Physics, Faculty of Mathematics, Physics and Informatics, Comenius University in Bratislava, Mlynská dolina F2, 842 48 Bratislava*
[2] *Faculty of Sciences, Siedlce University, 3 Maja 54, 08-110 Siedlce, Poland*
E-mail: peter.papp@uniba.sk

Low-energy electron processes on halogenated silanes are presented. We compare the dissociative electron attachment in the gas phase to chloro-trimethyl silane, dichloro-dimethyl silane, tetrachloro silane, tetrafluoro silane and tetrabromo silane.

1. Introduction

Electron attachment processes are usually one of the initial steps of silanes and halogen derivatives of silanes in the plasma processing industry. In most of the cases, electron attachment leads to the fragmentation of molecules into radicals and ions. These, in turn, are the components that perform the plasma processing. Thus, data on the interaction of low-energy electrons with silanes are important for plasma-assisted processes: cleaning [1], deposition [2] or etching [3].

2. Results

At the Comenius University in Bratislava we are focusing on dissociative electron attachment (DEA) studies with the CEMBIA apparatus [4] (a gas phase mass spectrometer equipped with trochoidal electron monochromator), in this work on chloro-trimethyl silane, dichloro-dimethyl silane, tetrachloro silane, tetrafluoro silane and tetrabromo silane. The halogen elements (X) in each of these compounds plays a special role in DEA process, due to their high electron affinity the main DEA product is the X^- ion, as expected for tetrachloro silane [5], tetrafluoro silane [6] and tetrabromo silane [6]. Within our collaboration with Siedlce University in Poland we have focused on a group of different chloro-, fluoro-, and bromo- silanes (methyls, ethyls…), trying to support the swarm experiments on these molecules performed in Siedlce. We will present the DEA result to these first group of measured molecules, compare the energetics of DEA leading to X^- fragments, associated with first step quantum chemical calculations based on DFT methods. The preliminary results show that these processes can act at very low electron energies (0-2 eV) for chlorinated or bromo- compounds, however at significantly higher energies close around 10 eV for the fluorinated compounds.

3. Acknowledgement

This work was supported by the Slovak Research and Development Agency contract no. APVV-19-0386, SK-PL-21-0025 and the Slovak Grant Agency for Science contract no. VEGA 1/0552/22. The project is co-financed by the Polish National Agency for Academic Exchange.

4. References

[1] Lieberman M A, Lichtenberg A J. *Principles of Plasma Discharges and Materials Processing, 2nd Edition*. New Jersey: John Wiley & Sons, INC; 2005.
[2] Lieberman M A 2009 *Plasma Sources Science and Technology*. **18(1)** 014002.
[3] Chen F F 1995 *Physics of Plasmas.* **2(6)** 2164-2175.
[4] Papp, P. et al. 2006 *J. Chem. Phys.* **125**, 204301.
[5] Ragesh, R. K. et al. 2018 *Int. J. Mass Spectrom.* **426**, 12–28.
[6] Bjarnason E H et al. 2013 *Int. J. Mass Spectrom.* **339–340**, 45–53.
[7] Ómarsson, F. H. et al. 2014 *Int. J. Mass Spectrom.* **365–366**, 275–280.

LOW ENERGY ELECTRON ATTACHMENT BY FLUOROSILANES

Bartosz Michalczuk[1], Peter Papp[2], Dušan Mészáros[2], Ladislav Moravský[2], Wiesława Barszcewska[1]

[1]*Faculty of Sciences, Siedlce University, 3 Maja 54, 08-110 Siedlce, Poland*
[2] *Department of Experimental Physics, Faculty of Mathematics, Physics and Informatics, Comenius University in Bratislava, Mlynská dolina, 842 48 Bratislava, Slovakia*
E-mail: bartosz.michalczuk@uph.edu.pl

The results of thermal electron attachment for (difluoromethyl)trimethylsilane in the gas phase are reported. The fundamental parameters such as rate coefficients and activation energy for the electron capture processes were determined. Results were obtained using Pulsed Townsend technique. Measurements were carried out in the temperature range 298K to 348K. The obtained rate coefficients depended on temperature in accordance to Arrhenius equation. From the fit to the experimental data points with function ln (k) = ln (A)-E_a /k_BT the activation energy (E_a) was determined.

1. Introduction

Silanes and halogen derivatives of silanes play an important role in plasma technologies that are widely used in the plasma processing industry. In such technologies, the electron capture process is usually the initial step that ultimately leads to the breakdown of molecules into radicals and ions. These, in turn, are the components that perform the plasma processing. Thus, data on the interaction of electrons with halogenated silanes can be used to control important components in plasma in many technologies, primarily in the microelectronics industry. The modern microelectronics industry is largely dependent on plasma-assisted processes such as cleaning, etching and deposition [1-3].

2. Experiment and results

The aim of the conducted research was to determine the kinetic parameters (rate constants and activation energy) for the process of electron capture by selected fluorine derivatives of silanes. The experiments were carried out in the gas phase, using the electron swarm method with photochemical generation of electrons using a Nd:YAG laser operating in the fourth harmonic mode, at a wavelength of 266 nm and a frequency of 10 Hz [4].

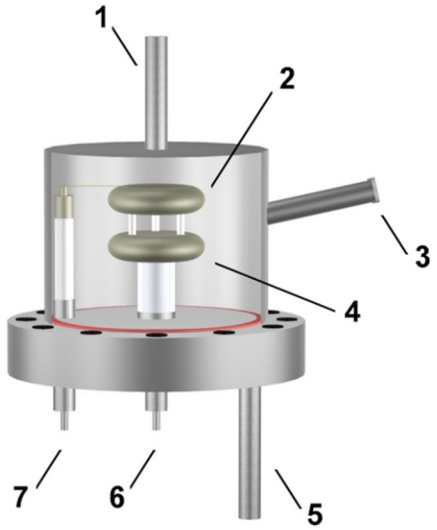

Fig. 1. The reaction chamber of the SWARM method: 1- laser beam entry, 2- anode, 3- connection to vacuum line and pumps 4- cathode, 5- baratron connector, 6- HV power supply, 7- preamplifier.

Under the influence of a uniform electric field, electrons drift towards the anode, inducing an increase in its voltage. Determination of the rate constant of the electron capture process is based on the numerical analysis of the shape of the voltage pulse. Thanks to the small volume of the reaction chamber (0.7 dm^3), it is possible to heat it and precisely control the temperature inside it, which enables measurements to be carried out at different temperatures and determination of the activation energy of the capture process.

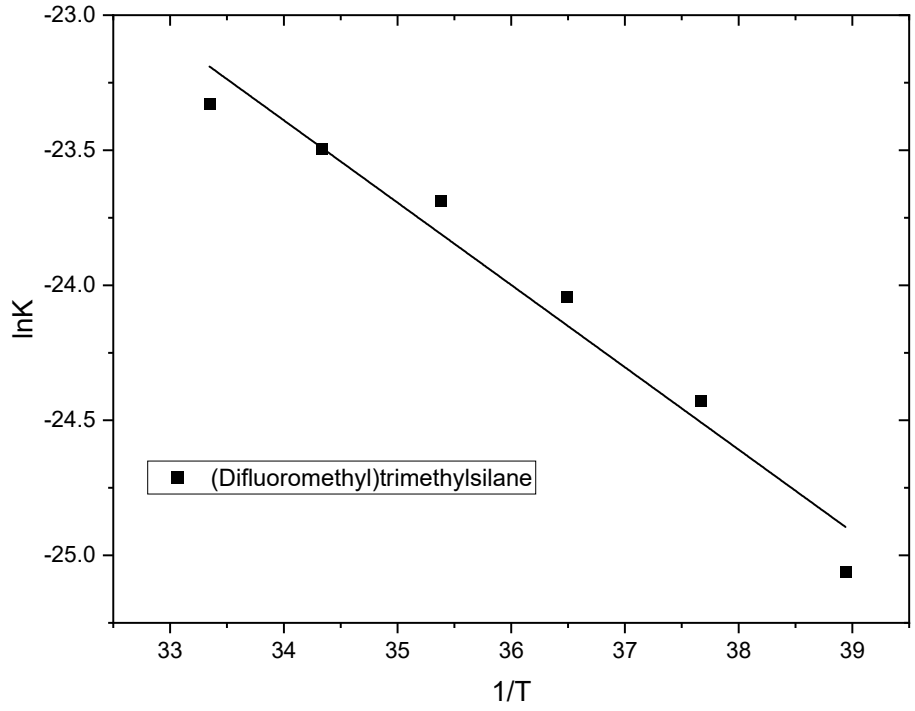

Fig. 2 Dependence of natural logarithm of k versus 300 K/T for (difluoromethyl)trimethylsilane.

We have measured rate coefficients k in the temperature range 298–348 K for (difluoromethyl) trimethylsilane. The rate coefficient at 298 K is equal to 1.89 x 10^{-11} cm^3s^{-1}. Activation energy was obtained from the slope of the curve in Figure 2 and is equal to 0.30 eV. For few past years in laboratory at Siedlce University using SWARM method were conducted studies on many compounds, such as chlorine, fluorine and bromine derivatives of hydrocarbons, alcohols and ethers. Thanks to the results of these studies, it was possible to find relationships between the number and position of substituents and the rate constant of the electron capture process as well as the activation energy. The results presented here are an introduction to analogous studies on the influence of substituents on the capture of low-energy electrons in the gas phase for silanes.

3. Acknowledgement

The project is co-financed by the Polish National Agency for Academic Exchange, by the Slovak Research and Development Agency bilateral contract no. SK-PL-21-0025 and the Slovak Grant Agency for Science contract no. VEGA 1/0552/22.

4. References

[1] Lieberman M A, Lichtenberg A J. *Principles of Plasma Discharges and Materials Processing, 2nd Edition*. New Jersey: John Wiley & Sons, INC; 2005.
[2] Chen F F 1995 *Physics of Plasmas.* **2(6)** 2164-2175.
[3] Lieberman M A 2009 *Plasma Sources Science and Technology.* **18(1)** 014002.
[4] J. Kopyra, J. Wnorowska, M. Foryś, and I. Szamrej 2007 *International Journal of Mass Spectrometry*. **268(1)** 60-65.

SIMULATION STUDIES OF SURGICAL ELECTRODE DESIGN TO PREVENT SPARKING ENHANCED BURNS

Marija Radmilović-Radjenović, Nikola Bošković, Branislav Radjenović

Institute of Physics, University of Belgrade, Pregrevica 118, 11080 Belgrade, Serbia
E-mail: marija@ipb.ac.rs

Proper care and handling of electrosurgical equipment are essential to patient and personnel safety. Burns that destroy layers of the patient's skin often linked to a medical mistake are largely preventable. This paper is dealing with the design of surgical electrodes as one of the extremely important factors for the formation of burns during standard procedures.

1. Introduction

The main mechanism responsible for skin burns during electrocautery is the electrical breakdown characterized by a voltage that electrically breaks down gas in the interelectrode gap enabling current flow through the ionized gas. The breakdown voltage usually obeys the standard scaling law. Further development of the discharge depends on several parameters such as the geometry of the electrode arrangements and the gap spacing. Results of extensive studies reveal that various electrode configurations correspond to different electric field distributions although the same voltage is applied leading to the dissimilar breakdown voltages.

2. Method

In the past few decades, computer modeling and simulations have evolved into very effective tools for studying sparking during various *electrosurgical* procedures and for developing new instrument designs. In this paper, the effects of the electrode shape on the sparking have been studied by using software package COMSOL [1] based on the multi-component plasma fluid model. Our goal was to determine both a minimum voltage necessary for sparking and locations where sparks start as crucial factors for the formation of burns during electrocautery. For that purpose, calculations were carried out for DC argon discharges having in mind that the main advantage of argon coagulation is constant, a minimum depth of the thermal effect. The emphasis was put on generations of sparks between various electrode arrangements (cylinder-cylinder, sphere-sphere cylinder-sphere, cylinder-cone, sphere-cone, and cone-cone). Electrosurgical sparks have been distinguished both for the positive and negative cycles. It was found that mechanisms of electrical spark formation are not equal in both directions introducing the electrical asymmetries.

3. Results

The obtained simulation results shown in Figure 1 agree well with the experimental data taken from literature [2] revealing that the sparking formation is strongly affected by the electrode configuration. Sparking occurs most easily when both electrodes are cylindrical and the most difficult when one electrode is a cone. The highest voltages are required for triggering sparks between arrangements with one cone electrode. It was found that the field is more uniform in the cylinder-cylinder configuration, while highly non-uniform in the cylinder-cone configuration. For a configuration with one or two spherical electrodes, breakdown voltages are higher up to 10 V and 8 V, respectively. When one electrode is a cone, the breakdown voltage is higher from 4 V up to 46 V.

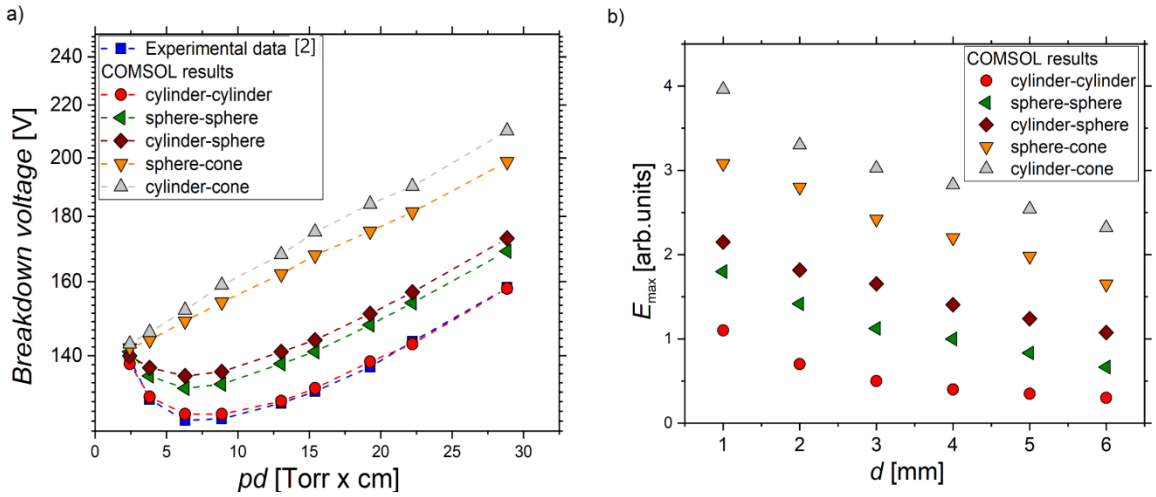

Figure 1. a) The breakdown voltage curves and b) maximum electrical field for various electrode configurations. The experimental data [2] are presented by blue squares.

This study was supported by the Science Fund of the Republic of Serbia, The Program IDEAS, GRANT No. 7739583, SimSurgery.

4. References

[1] COMSOL Multiphysics. Stockholm,Sweden, www.comsol.com.
[2] Meek JM and Craggs JD 1953. *Electrical breakdown of gases*. (Oxford, UK: Oxford Press).